UNIVERSITY of CALIFORNIA

Santa Barbara

Redox-Enhanced Electrochemical Capacitors:

Electrolyte Design and Device Engineering

A dissertation submitted in partial satisfaction of the

requirements for the degree

Doctor of Philosophy

in Materials

by

Brian William Evanko

Committee in charge:

Professor Galen Stucky, Co-Chair

Professor Martin Moskovits, Co-Chair

Professor Ram Seshadri

Professor Fred Wudl

January 2018

The dissertation of Brian William Evanko is approved.

_____

Professor Fred Wudl

_____

Professor Ram Seshadri

_____

Professor Martin Moskovits, Committee Co-Chair

_____

Professor Galen Stucky, Committee Co-Chair

September 2017

Redox-Enhanced Electrochemical Capacitors:

Electrolyte Design and Device Engineering

by

Brian William Evanko

ACKNOWLEDGEMENTS

There are a number of individuals that I wish to thank for their help in completing this work.

• My committee members, **Professors Galen Stucky, Martin Moskovits, Ram Seshadri and Fred Wudl**. Thank you for your advice throughout this project and teaching me how to approach difficult problems. Thank you also for being such excellent people, and showing by example how we should treat others as we advance in our careers.

• **Celia Wrathall**, for her help in navigating the intricacies of the university and her guidance on the writing and submitting of manuscripts.

• My high school teachers, particularly **Jan Bryson and Jeremy Blincoe,** who went out of their way to not just teach me, but to challenge me.

• **Professor Alan Weimer, Professor Janet deGrazia, Dr. Victoria Aston, and Dr. Chris Muhich**, my mentors at CU Boulder, whose encouragement and mentorship prepared me for graduate school and gave me a foundation in academic research.

• My postdoctoral mentors, **Dr. Sylvia Joun Lee, Dr. Juan Antonio Macia-Agullo, Professor Young-Si Joun, Dr. David Vonlanthen, and Professor Syed**

Mubeen, who helped me to get started in the lab at the very beginning of the Ph.D. program. Your kindness, patience, and insight were invaluable.

• Members of the ARPA-E project team, **Professor Galen Stucky, Professor Shannon Boettcher, Professor David Ji, Dr. David Auston, Professor Sang-Eun Chun, Dr. Seung Joon Yoo, and Dr. Xingfeng Wang, and Jane Kittle**. This project defined my Ph.D., and working with this group was a privilege.

• The ARPA-E Program Managers, **Professor Ping Liu, Dr. Susan Babinec, Dr. Grigorii Soloveichik, and Dr. Aron Newman**. Thank you for keeping us focused, sharing your expertise, and helping us to complete our project.

• UCSB Undergraduate Researchers, **Jason Lipton, Monica Romelczyk, Marzieh Tousi, and Nicholas Parker.** Working with all of you in the lab was one of the most enjoyable parts of research, and I truly appreciate all of the time, effort, and ideas that you volunteered.

• **Daniel Lubin,** for all of your help and enthusiasm, and reminding me that science is meant to be fun.

• Stucky and Moskovits Group Members, **Jose Navarrete, Tracy Chuong, Will Elliot, Chi Nguyen, Katie Mackie, and Katherine Kanipe**. Thank you all for making it enjoyable to come to work. I could not have asked for a better group of lab mates, and facing the challenges of graduate school was so much easier together.

• The MRL Battery Group, including **Professor Kimberly See, Dr. Jeff Gerbec, Dr. Megan Butala, Professor Vicky Doan-Nguyen, Dr. Max Radin, Julija Vinckviciute, Molleigh Preefer, Nicole Schauser**, and many others. You taught me a great deal about building batteries, understanding electrochemistry, and how to navigate this field.

• **Jocelyn Guzman**, for excellent academic advising and answering every question I could think of.

• Funding agencies: The Advanced Research Projects Agency-Energy (**ARPA-E**), Southern California Electrochemical Energy Storage Association (**SCEESA**), and the **UCSB Materials Department** for providing research funding over the past 5 years.

• The **2012 Materials Class**. The individuals in this group are not just great scientists, but also fascinating people. Going through a year in San Clemente, two years of classes, and five years of grad school together was a wonderful experience.

• **Dan, John, Will, Sean, Stefan, Humberto, Mitchell, Dez, and Laura**. Thank you for your friendship and the time that we have shared together in Santa Barbara.

• **My family, especially my grandparents and my sister Lisa,** for their constant love and encouragement.

• To **my parents**, I am truly grateful that you taught me to love learning when I was a child, have always cared first about my happiness, and been supportive no matter what path I choose.

• Finally, to **Carol**. During the most difficult and overwhelming parts of the Ph.D., you were always there to listen and help. I could not have done this without you.

Curriculum Vitae

Brian William Evanko

Education

2012–2017	Ph.D. in Materials, University of California, Santa Barbara, CA, USA
2007–2011	B.S. in Chemical Engineering, University of Colorado, Boulder, CO, USA (cum laude)

Publications

11. **B. Evanko**, et al., "Stackable bipolar pouch cells with metal-free current collectors for high-power electrochemical energy storage with corrosive aqueous electrolytes," in preparation.
10. **B. Evanko**, S. W. Boettcher, S. J. Yoo and G. D. Stucky. "Redox-Enhanced Electrochemical Capacitors: Status, Opportunity, and Best Practices for Performance Evaluation," ACS Energy Lett. 11, 2581, 2017.
9. S. J. Yoo, **B. Evanko**, X. Wang, M. Romelczyk, A. Taylor, X. Ji, S. W. Boettcher, and G. D. Stucky, "Fundamentally Addressing Bromine Storage through Reversible Solid-State Confinement in Porous Carbon Electrodes: Design of a High-Performance Dual-Redox Electrochemical Capacitor," J. Am. Chem. Soc. 29, 9985, 2017.

8. W. Lee, J. Navarrete, **B. Evanko**, G. D. Stucky, S. Mubeen, and M. Moskovits, "A plasmonic liquid junction photovoltaic cell with greatly improved power conversion efficiency," Chem. Commun. 52, 13460, 2016.
7. **B. Evanko**, S. J. Yoo, S.-E. Chun, X. Wang, X. Ji, S. W. Boettcher, and G. D. Stucky, "Efficient Charge Storage in Dual-Redox Electrochemical Capacitors through Reversible Counterion-Induced Solid Complexation," J. Am. Chem. Soc. 138, 9373, 2016.
6. S.-E. Chun, **B. Evanko**, X. Wang, D. Vonlanthen, X. Ji, G. D. Stucky, and S. W. Boettcher, "Design of aqueous redox-enhanced electrochemical capacitors with high specific energies and slow self-discharge," Nat. Commun. 6, 7818, 2015.
5. X. Wang, R. S. Chandrabose, S.-E. Chun, T. Zhang, **B. Evanko**, Z. Jian, S. W. Boettcher, G. D. Stucky, and X. Ji, "High Energy Density Aqueous Electrochemical Capacitors with a KI-KOH Electrolyte," ACS Appl. Mater. Interfaces 7, 19978, 2015.
4. X. Liang, **B. Evanko**, A. Izar, D. M. King, Y.-B. Jiang, and A. W. Weimer, "Ultrathin highly porous alumina films prepared by alucone ABC molecular layer deposition (MLD)," Microporous Mesoporous Mater. 168, 178, 2013.

3. P. Lichty, X. Liang, C. Muhich, **B. Evanko**, C. Bingham, and A. W. Weimer, "Atomic layer deposited thin film metal oxides for fuel production in a solar cavity reactor," Int. J. Hydrogen Energy 37, 16888, 2012.
2. Z. Shang, R. L. Patel, **B. Evanko**, and X. Liang, "Encapsulation of supported metal nanoparticles with an ultra-thin porous shell for size-selective reactions.," Chem. Commun. (Camb). 49, 10067, 2013.
1. C. L. Muhich, **B. Evanko**, K. C. Weston, P. Lichty, X. Liang, J. Martinek, C. B. Musgrave, and A. W. Weimer, "Efficient generation of H2 by splitting water with an isothermal redox cycle.," Science 341, 540, 2013.

Intellectual Property

1. G. D. Stucky, B. Evanko, N. Parker, D. Vonlanthen, D. Auston, S. W. Boettcher, S.-E. Chun, X. Ji., B. Wang, X. Wang, R. S. Chandrabose, "Energy storage device including a redox-enhanced electrolyte" U. S. Patent 9,728,344, August 8, 2017.

Abstract

Redox-Enhanced Electrochemical Capacitors:

Electrolyte Design and Device Engineering

by

Brian William Evanko

Electrochemical energy storage is increasingly important as the world decarbonizes and electrifies. Research in this area requires compromise between properties that are often mutually exclusive, including power, energy, lifetime, efficiency, operating temperature, safety, and cost. Electric double layer capacitors (EDLCs) exhibit high power and outstanding cycle life compared to secondary batteries, but have low specific energy, limiting applications. Redox-enhanced electrochemical capacitors (redox ECs) are a class of augmented electric double-layer capacitors utilizing reversible redox reactions of soluble redox couples in the electrolyte to add faradaic charge storage. These systems offer increased energy density, efficient power delivery, and simple construction.

We study a range of redox-active electrolytes to clarify operating mechanisms and formalize design rules for high-performance. Our investigations focus on dual-redox ECs, which attain higher energy density by employing a pair of distinct redox couples, with each operating at a different electrode. Simplicity is important both in terms of the mechanistic aspects of the electrochemical redox chemistry and for system cost considerations. A single ionic molecular entity that intrinsically delivers both distinct redox couples is preferable over two separate redox-active electrolytes. In this context, we have identified specific viologen bromide salts as particularly promising aqueous redox-active electrolytes for dual-redox ECs. While charging, Br^- is oxidized to Br_3^- at the positive electrode and the viologen dication (V^{2+}) is reduced to the stable monocation radical ($V^{+\bullet}$) at the negative electrode. The reverse processes occur during discharge, providing a high-capacity faradaic discharge plateau and attaining an energy density of ~20 Wh/L.

The viologen bromide system shows unusually high Coulombic efficiency and low self-discharge rates for an aqueous redox-EC. This was initially attributed to strong adsorption of the Br_3^- and $V^{+\bullet}$ to the activated carbon electrodes, but a more detailed analysis confirms that the behavior is due to two electroprecipitation mechanisms. In these mechanisms, each ion acts as a charge-storing redox couple at one electrode and as a complexing agent at the other

electrode. The processes are highly reversible and cells show negligible capacity fade even after 20,000 cycles. The devices use conventional activated carbon electrodes, and because crossover is not a concern and self-discharge is suppressed, a simple inexpensive cellulose separator is sufficient and more costly ion-selective membranes are not required.

Based on our understanding of solid complexation in redox ECs, we studied in detail the confinement of charged redox species in porous electrodes with liquid-to-solid phase transitions to mitigate self-discharge. We demonstrate that in addition to viologens, tetrabutylammonium cations induce reversible solid complexation of Br_2/Br_3^-. This mechanism slows cross-diffusion of Br_3^-, stabilizes the reactive bromine generated during charging, and can be broadly used as a positive electrode to balance the capacity of a wide variety of pseudocapacitive or battery-type negative electrodes.

In the final component of this work we consider the challenges of scaling up these systems for practical application. We address corrosion of metallic current collectors, which is a common device design challenge for high-power aqueous electrochemical energy storage devices, by designing a bipolar pouch cell using electrochemically stable carbon-polymer composite current collectors. In order to show the versatility of this approach, we construct a high-power redox EC/battery hybrid using a zinc metal anode and an activated carbon cathode with

tetrabutylammonium-complexed bromide catholyte. This system achieves excellent power and energy performance, with negligible capacity degradation over more than 3000 cycles.

Throughout the dissertation we compare the performance and properties of our dual redox ECs to those of the current state-of-the-art conventional energy storage systems and other redox-enhanced energy storage systems and we close with comments on economic analysis and the future of redox enhanced electrochemical capacitors.

Contents

List of Figures

List of Tables

Chapter 1

Introduction

The contents of this chapter have substantially appeared in the following reference: B. Evanko, S. W. Boettcher, S. J. Yoo and G. D. Stucky. "Redox-Enhanced Electrochemical Capacitors: Status, Opportunity, and Best Practices for Performance Evaluation," *ACS Energy Lett*. 11, 2581, 2017

Redox-Enhanced Electrochemical Capacitors

Energy production and consumption is rapidly changing worldwide to create sustainable energy systems. The displacement of coal on the electric grid by solar and wind power is well underway and the replacement of petroleum in the transportation sector with electric vehicles is beginning. These changes offer the possibility to waste less energy as heat in inefficient thermodynamic cycles, prevent combustion products from accumulating in the atmosphere, and simplify energy distribution by sending electrons over the grid instead of moving chemical fuels. One core technology needed to realize the efficiency improvements, environmental benefits, and economic advantages of these changes is improved electrochemical energy storage.

Secondary batteries are well-suited for storing energy, but many applications require higher power than batteries can deliver. Electrochemical capacitors (ECs), members of the capacitor family that use liquid electrolytes in place of solid dielectrics, are more suitable for high power applications. Electric double-layer capacitors (EDLCs), interchangeably referred to as supercapacitors or ultracapacitors, are the most-commercialized subset of ECs. EDLCs consist of two high-surface-area electrodes coated onto metallic foil current collectors, placed on either side of a porous, electron-insulating separator, and saturated with an aqueous, organic, or ionic liquid electrolyte. During charging, the positive and

negative electrodes accumulate oppositely charged ions at the interfaces between the electronic conductors (e.g., high-surface-area carbon) and the ionic conductor (the electrolyte) and create electric double-layers that store energy in the resulting electric fields. This charging mechanism based on electrostatic interaction enables EDLCs to fully charge or discharge in seconds with device-level specific power as high as 10 kW/kg.[1] EDLCs also have calendar lifetimes on the order of decades and can cycle millions of times with minimal performance loss. These advantages compare favorably with secondary batteries, which typically have low specific power (<0.5 kW/kg) due to the inherent diffusion and kinetic limitations of bulk solid-state electrode materials as well as limited cycle life.[2] Several excellent reviews of EDLCs can be found elsewhere.[3–5]

The combination of high power and long-term stability makes EDLCs useful in a wide array of applications ranging from utility-scale grid services to hybrid vehicles to consumer electronics.[6] Future applications, however, are constrained by the low specific energy of EDLCs (power and energy density for EDLCs and secondary batteries are compared in the Ragone plot in Figure 1). The high power, low energy performance of EDLCs locates them in the quadrant opposite to batteries in the Ragone plot. EDLCs and batteries are thus sometimes integrated in tandem in modules, with the former providing power and the latter providing energy. Constructing these systems requires at least three components

– an EDLC, a battery, and power conversion electronics to independently manage the two electrochemical energy storage devices. Because a multi-component system increases design and manufacturing complexity, costs more, and has higher mass and volume, current research in ECs aims to achieve battery-level energy combined with capacitor-level power and cycle life in a single device. Such ECs could transition from augmenting battery systems to displacing them. In an automotive engine start-stop application, for example, the ideal system would not only start the engine reliably for many years, but also store sufficient energy to run auxiliary devices while the engine is off – fully supplanting the traditional battery. Other applications are expected to arise if advanced ECs are developed that occupy the empty, valuable positions in the high-power, high-energy region of the Ragone plot.

In order to increase the energy storage of ECs, a number of systems have been developed that utilize different charge storage mechanisms beyond electric double-layer capacitance. The most common approach is the incorporation of solid-state electrode materials that employ fast faradaic redox reactions.[7–9] These materials include redox-active polymers, transition metal oxides and hydroxides, which are created using a wide array of synthetic routes to achieve different nanostructures. Collectively, ECs utilizing these materials are known as pseudocapacitors.

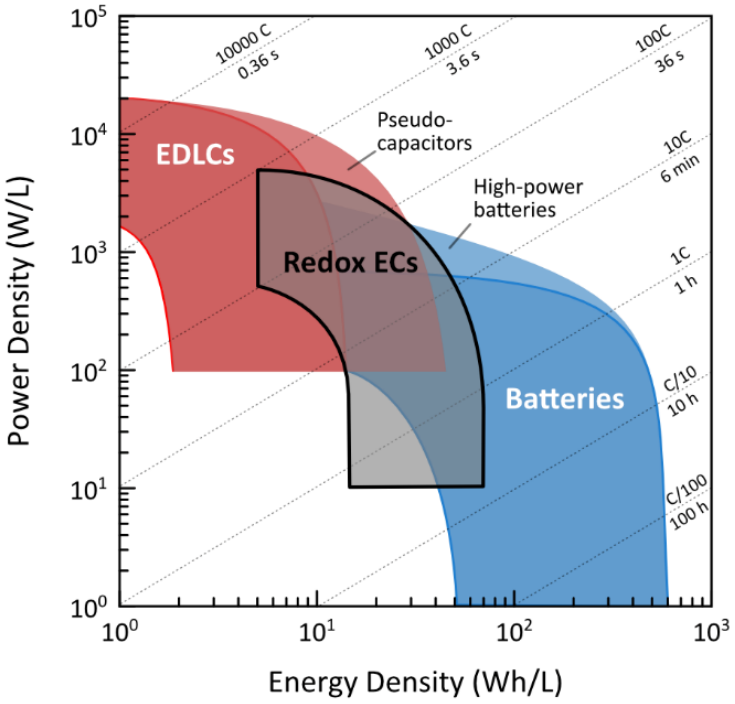

Figure 1. Ragone plot of electrochemical energy storage devices. Device-level power and energy density for electric double-layer capacitors (EDLCs), pseudocapacitors, secondary batteries, and redox-enhanced electrochemical capacitors (Redox ECs). Diagonal lines correspond to different charge/discharge times and the corresponding C-rates.

The successful development of solid-state redox-active electrode materials has inspired the expansion of the concept to include *liquid-state redox-active electrolytes*. Redox-active electrolytes augment the 'electrochemically inert' electrolyte of a conventional EDLC with soluble redox couples to add faradaic

charge storage in addition to electric-double layer capacitance. These redox-enhanced electrochemical capacitors (redox ECs) utilize the dead weight of the inert electrolyte and wasted pore volume in the electrodes as a reservoir for redox couples to supply extra capacity and enhance the energy density of ECs.

The utilization of liquid redox-active materials has several advantages: (1) The approach is easily scalable because active materials are simply dissolved into the existing electrolyte. (2) Simple-to-fabricate electrodes, such as commercially-available activated carbon, can be used, avoiding complex synthesis of nanostructured solid-state redox-active electrode materials. (3) High-power performance is maintained because the redox reactions occur over a large electrode surface area and are not limited by solid-state diffusion. (4) With the design of custom organic redox-active molecules, one can tune the solubility and redox potential by changing the chemical structure.

This chapter provides a brief introduction to the emerging field of redox ECs. We highlight some notable successes, discuss outstanding problems, and present recent developments in the context of the different strategies used to suppress self-discharge and improve Coulombic and energy efficiency. Finally, we comment on best practices for device characterization and performance evaluation, and examine future directions for the field.

Operational principles of redox ECs

Redox-ECs store energy through electric double-layer capacitance, like EDLCs, but add additional capacity using faradaic redox reactions of soluble redox couples at the electrode/electrolyte interface on high-surface-area electrodes. As redox ECs charge, a redox-active electrolyte at the positive electrode (catholyte) is oxidized, and a redox-active electrolyte at the negative electrode (anolyte) is reduced, as shown in Figure 2a. During discharge the reverse processes occur (Figure 2b). Electrons flow to or from the redox couples across the electrode/electrolyte interface, and current moves in and out of the device via current collectors. The separator is placed to provide electronic insulation between the two electrodes but maintain ionic conductivity. In many cases the electrolyte is homogeneous in the discharged state, with anolyte and catholyte fully miscible throughout the entire cell.

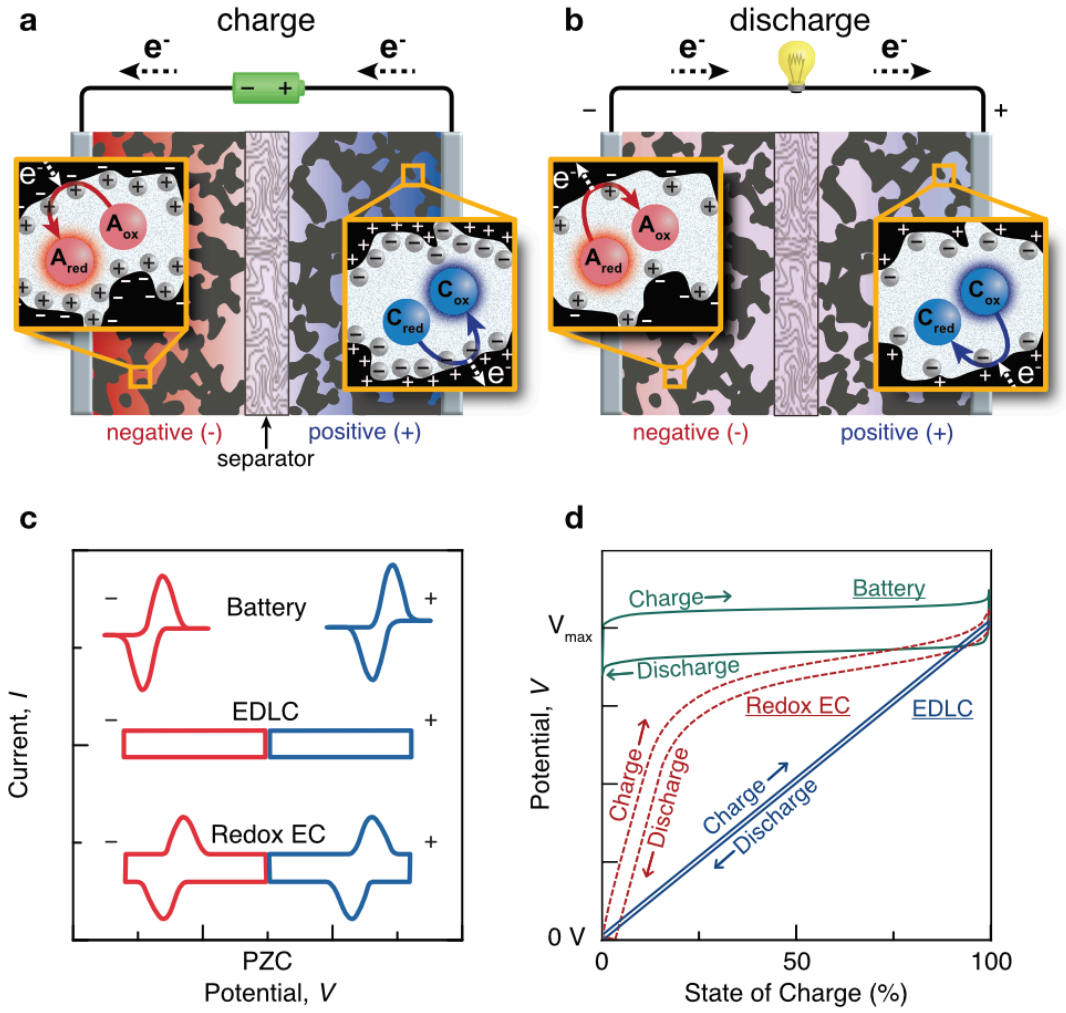

Figure 2. Energy storage mechanisms in a redox EC. Redox EC under (a) charge and (b) discharge conditions utilizing the electric double-layer for capacitive charge storage, as well as reduction and oxidation of the anolyte (A) and catholyte (C) redox couples in the electrolyte for faradaic charge storage. Comparison of the theoretical (c) 3-electrode cyclic voltammograms and (d) 2-electrode galvanostatic charge/discharge potential profiles of a battery, an EDLC, and a redox EC. (a) and (b) are modified from Reference 30, with permission.

Figure 2c shows a comparison of the typical 3-electrode cyclic voltammograms (CVs) of a traditional secondary battery, an EDLC, and a redox-EC. The CVs highlight notable differences in the operating mechanisms that result in the different galvanostatic charge/discharge (GCD, often referred as constant-current charge/discharge) potential profiles shown in Figure 2d. Secondary batteries have well-defined redox peaks from the anode and cathode redox half-reactions in the CV. The potential difference between the two redox half-reactions gives rise to a relatively constant cell potential (E_{cell}) in the GCD potential profile. In contrast, EDLCs have a characteristic rectangular CV, due to the electrostatic accumulation of ions at the electrode/electrolyte interface, that translates to a linearly rising (charging) or falling (discharging) GCD potential profile. Importantly, the CV for redox ECs exhibits features of both a secondary battery and an EDLC simultaneously. Redox ECs therefore exhibit both linear and plateau regions in the GCD potential profile, reflecting the presence of both capacitive and faradaic charge storage mechanisms in a single system. Because redox ECs have well-defined redox peaks on the CV as well as a non-linear GCD potential profile, they are not considered to be pseudocapacitors and should be defined as hybrid systems.[10,11]

The different operating mechanisms of electrochemical energy storage devices influence their respective power-energy performance. Figure 3 compares

the two-electrode discharge profiles of an EDLC and a redox EC. Energy delivered is proportional to the area under the time-voltage curve (and equal to the area under the time-power curve) under constant-current discharge conditions. The redox EC has a higher specific energy compared to an EDLC. In addition to increased energy, a redox EC can provide a steadier power output. Instantaneous power, P_{inst}, as opposed to average power or matched impedance power, is the product of current and voltage ($P = I \times V$) and therefore varies at different points in the discharge process.[12] An EDLC has a linear potential-time response, so power decreases steadily with time under constant-current conditions. As most energy storage applications demand constant power, an EDLC must supply increasing current as it discharges to compensate for the continuously dropping potential.[6] Once an EDLC has discharged below 50% of its maximum voltage, the remaining capacity is essentially unusable because of limitations on the power electronics and increasing IR drop associated with the high currents needed to maintain constant power. As a result, ~25% of the EDLC's theoretical energy is not practically useful.[13] Unlike EDLCs, redox-ECs maintain a flatter voltage plateau with a potential equal to the difference between the faradaic half reactions of the catholyte and anolyte (Figure 3). The steady output voltage allows redox ECs to provide more-constant power for most of the discharge profile, which is a significant advantage over EDLCs that would

require a DC–DC converter to modify their output voltage. Additionally, the unusable fraction of the energy at low voltage is a much smaller fraction of the total energy for redox ECs. These characteristics make redox-ECs an easier drop-in replacement for applications currently using secondary batteries, and simplifies the design of, or eliminates, the need for power-conversion electronics.

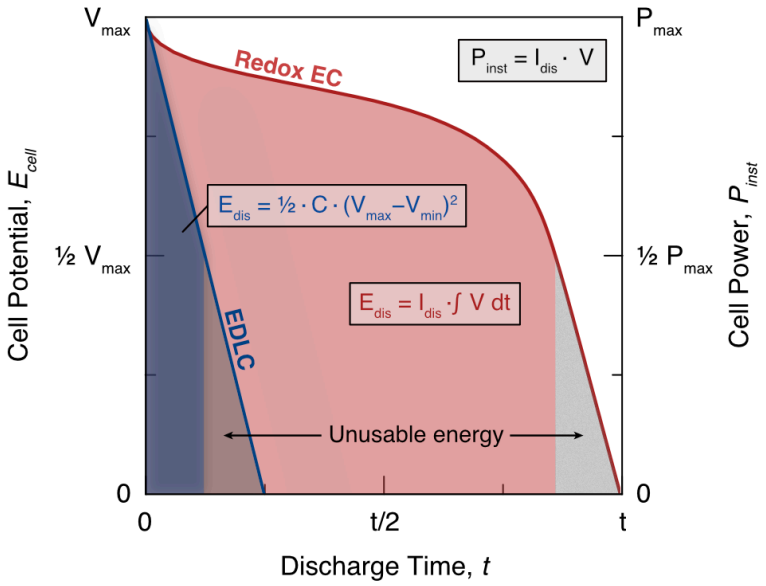

Figure 3. Discharge profiles of an ideal EDLC and redox EC. As the devices discharge, the power produced by the EDLC steadily decreases while the power from the redox EC remains relatively constant. At low voltages, the remaining energy is difficult to usefully extract, so the practically available energy (shaded areas) is lower than the theoretical stored energy (the full area under each discharge curve). In this figure, it is assumed that both devices are constructed with identical electrodes and discharged at the same rate.

Demonstrated state of the art

To date, most redox-active electrolytes have been aqueous. Aqueous electrolytes offer high power (high ionic conductivity), safety (non-flammable), and simple manufacture (aqueous devices do not require dry rooms for fabrication). The disadvantage of aqueous systems is a low operating potential (the thermodynamic electrochemical stability window of water is 1.23 V and ~ 1.5 V in practice due to slow water oxidation/reduction kinetics).[14,15] Redox-active electrolytes can compensate for this low voltage by providing a high capacity. The first reported redox-active electrolytes for aqueous redox ECs were alkali metal iodide salts, which perform well in both neutral and alkaline conditions.[16–18] Other early work explored hydroquinone (HQ) in sulfuric acid, followed shortly thereafter by methylene blue.[19,20] Many other families of redox-active molecules have been investigated in aqueous redox ECs, including halides, transition metals (Cu, V, Fe, etc.), inorganic and organometallic complexes (metal bipyridine complexes, ferricyanide, etc.), and organic molecules (viologens, quinones, etc.).[21–23] A summary of select reported redox-active electrolytes and the corresponding redox potentials is presented in Figure 4.

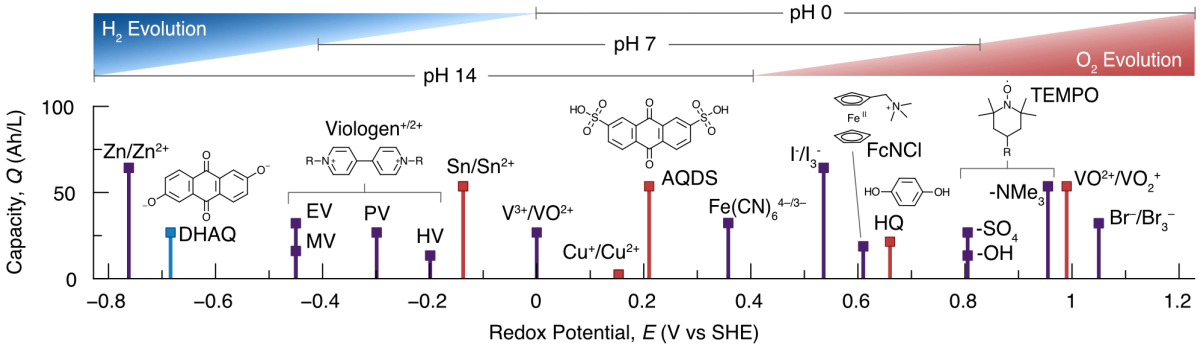

Figure 4. Reduction potential and demonstrated volumetric capacity for selected aqueous redox couples used in redox ECs, flow batteries, and redox batteries. The redox-active electrolytes illustrated in red, purple, and blue operate in acidic[24–27], neutral[28–37], or basic[38] conditions, respectively. The thermodynamic stability window of water at different pH values is provided for reference. Chemical abbreviations: DHAQ, 2,6-dihydroxyanthraquinone[38]; EV, ethyl viologen[32]; MV, methyl viologen[30]; PV, pentyl viologen[31]; HV, heptyl viologen[30]; AQDS, 9,10-anthraquinone-2,7-disulphonic acid[25]; FcNCl, (ferrocenylmethyl)trimethylammonium chloride[33]; HQ, hydroquinone[26]; TEMPO, 2,2,6,6-tetramethylpiperidin-1-oxyl [(-OH), 4-hydroxy-TEMPO[34]; ($-SO_4$), TEMPO-4-sulfate[36]; ($-NMe_3$), 4-trimethylammonium-TEMPO[35]]. All organic molecules are shown in the discharged state.

When a single redox couple (either catholyte or anolyte) is added to the electrolyte, device performance improvement tends to be modest in comparison to EDLCs. Although one electrode has excellent capacity owing to the added redox-active electrolyte, the counter electrode is still a purely capacitive EDLC with lower capacity that limits overall device performance. If both electrodes

have equivalent mass, the potential of the capacitive counter electrode will reach the edge of the electrolyte voltage stability window before the redox-enhanced electrode is fully charged (Figure 5a, left). If the capacitive electrode is significantly oversized to match the capacity of the redox-enhanced electrode, the increased device mass (or volume) will decrease the mass-normalized energy (as well as the energy density). Therefore, in order to truly realize the promise of redox-active electrolytes, redox ECs must concurrently utilize two separate redox couples, a catholyte and an anolyte, each of which acts at a different electrode and matches the redox activity of the other. This configuration is known as a *dual-redox EC* (Figure 5a, right). It is also possible to match a redox EC electrode with a battery-type or pseudocapacitive counter electrode in a hybrid device.[29,39]

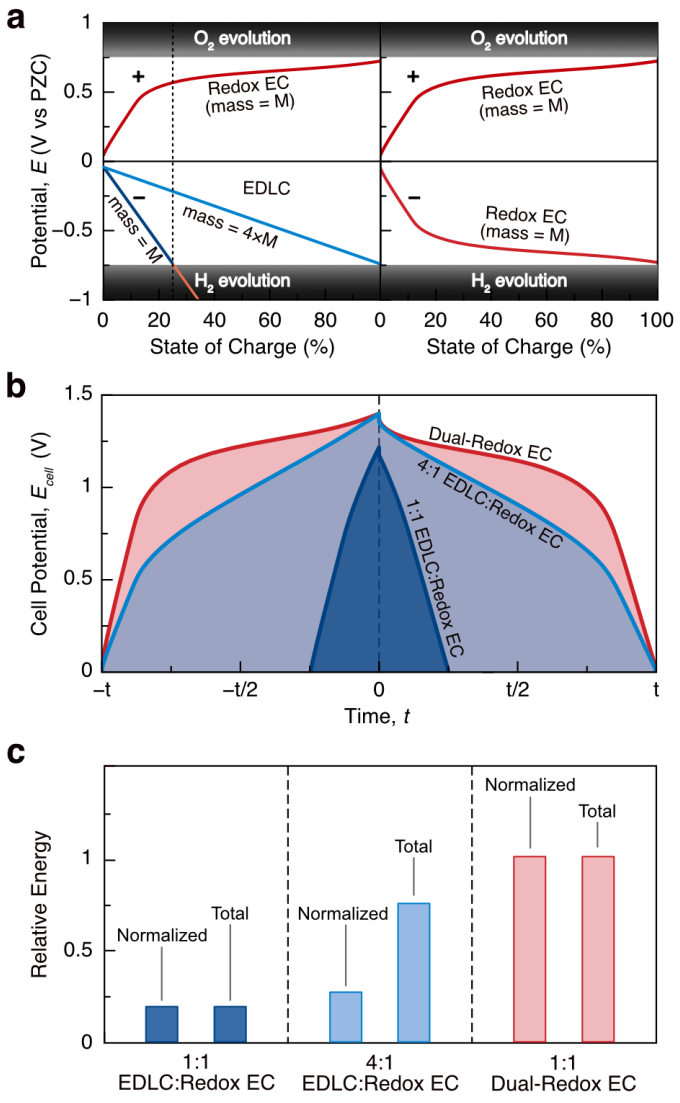

Figure 5. Balancing the capacity of a redox EC electrode. (a) Galvanostatic charging potential profiles for a redox EC electrode with an EDLC counter electrode of equal mass, an EDLC counter electrode with four times higher mass, or another redox EC electrode of equal mass (dual-redox EC). (b) The energy stored by each combination is proportional to the area under the resulting full-cell potential profiles. (c) The relative total and normalized (gravimetric or volumetric) energy stored by systems with an EDLC counter electrode is much less than the dual-redox EC configuration.

The most important principle for designing dual-redox ECs should be the selection of redox-active electrolytes. Briefly, these redox couples should have (1) high solubility, (2) reversible electron-transfer kinetics, (3) compatibility when intermixed, (4) long-term cycling stability, and, ideally, (5) a standard redox potential close to the oxygen evolution potential (for the catholyte) and near the hydrogen evolution potential (for the anolyte). The first report of a dual-redox EC used $VOSO_4$ as a redox-active anolyte and KI as a redox-active catholyte.[28] Other notable dual-redox EC examples use anolyte/catholyte pairs of viologen/bromide,[30–32,40] tin/vanadium,[24,41] and hydroquinone/methylene blue.[42] Three-electrode GCD profiles for select systems (Figure 6) show electrochemical behavior that transitions from capacitive to faradaic at both positive and negative electrodes during charging/discharging. Typically, single-redox ECs have a specific energy of 10-30 Wh/kg, while dual-redox ECs range from 40-80 Wh/kg (based on the mass of electrodes only). These examples support the idea that energy optimization through redox-active electrolyte engineering is best-achieved using dual-redox EC systems.

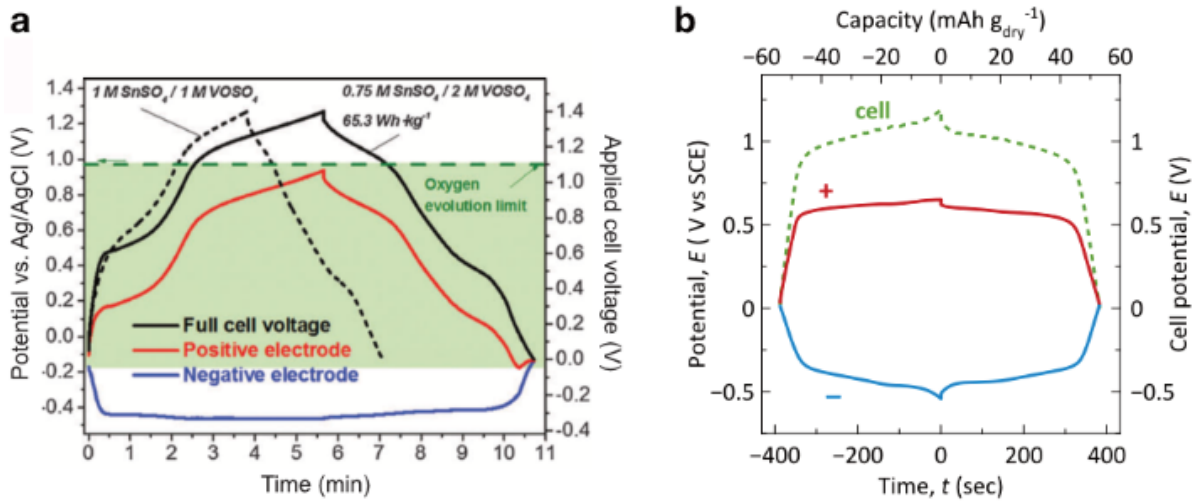

Figure 6. Experimental GCD potential profiles of reported devices. Literature reports of dual-redox ECs with (a) 0.75 M $SnSO_4$ anolyte/2 M $VOSO_4$ catholyte and (b) 1 M $PVBr_2$/3 M NaBr ($PVBr_2$; pentyl viologen dibromide) mixed anolyte/catholyte electrolyte. Potential profiles from 3-electrode cells show a transition from capacitive to faradaic charging for the positive electrode, negative electrode, and total (full) cell. Reprinted with permission from (a) Reference 41 – Published by the Royal Society of Chemistry and (b) from Reference 31. Copyright 2016 American Chemical Society.

Critical challenges facing the realization of high-performance redox ECs

Despite the many literature reports and the advantages stated above, redox ECs have not been commercialized and there are significant hurdles to overcome. In fact, the primary advantage of redox ECs, i.e., the storage of energy by soluble redox couples, presents a major challenge for practical applications. Large amounts of stored energy can quickly dissipate as the dissolved charged redox species diffuse across the cell and shuttle charge between the dissimilarly charged electrodes by exchanging electrons with the electrode surface or other redox couples (redox shuttling). These effects result in self-discharge, as illustrated in Figure 7. Many redox-active electrolytes, such as hydroquinone/benzoquinone or ferricyanide/ferrocyanide, improve specific energy during high-rate cycling tests, but are unable to hold significant amounts of charge for long periods of time (beyond seconds to minutes).[30,43] This electrolyte behavior severely limits practical applications, causing low Coulombic efficiency, fast self-discharge, and irreversible side reactions when oxidized catholyte and reduced anolyte intermix during mutual cross-diffusion. In order to fundamentally address these issues, the suppression of cross diffusion and redox shuttling is critically important. To date,

several design strategies for selective separation of catholyte and anolyte and mitigation of self-discharge have been developed, as discussed in detail below.

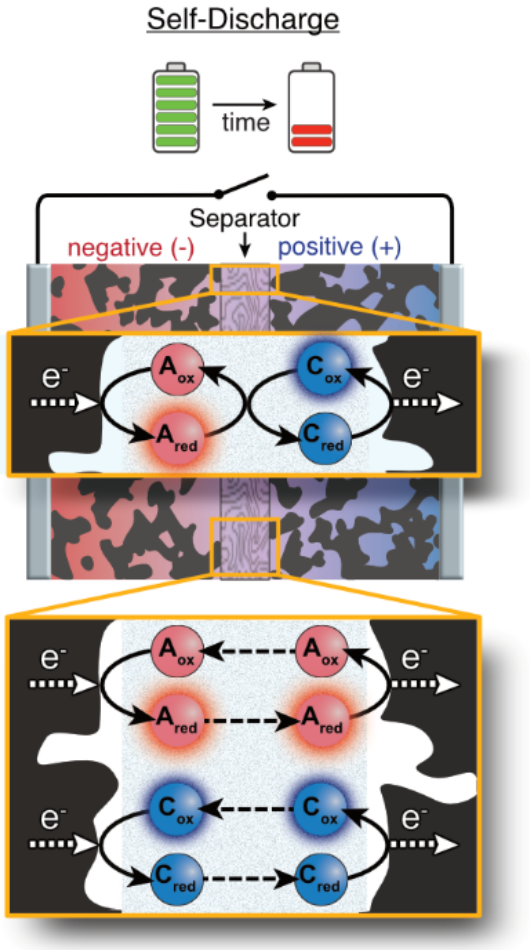

Figure 7. Schematic illustration of self-discharge mechanisms. Self-discharge is caused by cross-diffusion and redox shuttling of charged redox couples (anolyte and/or catholyte) between the oppositely polarized electrodes in the cell. This unfavorable electron transfer can occur both at the electrode/electrolyte interface and between charged redox species in solution.

Ion exchange membranes. In order to avoid rapid self-discharge, most redox-active electrolytes require an ion exchange membrane (IEM) to separate the two half cells. Examples include $VOSO_4/SnSO_4$ (anion exchange membrane), $K_3Fe(CN)_6$ (cation exchange membrane), hydroquinone (Nafion), and $KI/VOSO_4$ (Nafion).[28,37,41,42] This strategy is commonly used with redox flow batteries, as IEM's provide an effective solution to block the migration of the "liquid" redox-active electrolyte. However, although redox ECs are similar to redox flow batteries in the sense that electric charge is stored by redox processes in a redox-active electrolyte, this approach is not currently practical for (non-flow) redox ECs due to the different system architectures and cost issues. For example, the economics of IEMs may be acceptable for flow batteries because the cost of other passive materials (i.e., pumps, storage tanks, flow meters, etc.) are comparable and the cost of the IEM is normalized by the energy of a large volume of redox-active electrolyte. However, this cost justification does not apply to redox ECs, constituting a significant hurdle for commercial development. We base this claim on calculations for a hypothetical device with generous performance assumptions. This device is comprised of two electrodes, each with a mass loading of 25 mg/cm^2 and specific energy of 100 Wh/kg, normalized to the combined mass of both electrodes (for reference, typical electrode mass loading is <10 mg/cm^2 and the highest reported energy for a redox EC is ~75 Wh/kg).

Such a device would store energy with an areal density of 5 mWh/cm^2. Anion exchange membranes currently cost approximately \$50/m^2 and Nafion cation exchange membranes cost approximately \$500/m^2, so these membranes alone would contribute \$1000/kWh to \$10,000/kWh, respectively, to the cost of a redox EC.[34,44] Therefore, in view of practical applications, ignoring this exorbitant cost of separators will result in significantly underestimating the true cost (in \$/kWh) of reported devices. However, given the effectiveness of ion-selective membranes in suppressing cross-diffusion, this approach remains promising if inexpensive membranes can be developed. Membrane improvement is therefore an ongoing challenge for both redox ECs and redox flow batteries.

Electrostatic attraction and physical adsorption. Following the first dual-redox EC work on KI/$VOSO_4$ electrolyte with an ion-selective separator, we studied a similar system with cellulose filter paper replacing Nafion as the separator.[45] We found that the cell does not need the ion-selective membrane as a separator for short-time-scale energy storage. We proposed that the charge-storing products of I^- oxidation (I_3^-) and VO^{2+} reduction (V^{3+}) remain electrostatically attracted to their respective positively and negatively charged electrodes, suppressing cross-diffusion.

We later studied the self-discharge mechanisms in more detail, comparing the behavior of redox-active electrolytes with varying chemical structure and electrical charge.[30] For example, we found exceptionally slow self-discharge rates for iodide (I^-/I_3^-) and bromide (Br^-/Br_3^-) catholytes in comparison to more-negatively charged ferrocyanide ($Fe(CN)_6^{4-/3-}$) at the positive electrode. Similarly, methyl viologen ($MV^{2+}/MV^{+\bullet}$) anolyte had much slower self-discharge rates than more-positively charged ruthenium hexamine ($Ru(NH_3)_6^{3+/2+}$) at the negative electrode. These comparative studies show that retarded self-discharge cannot be explained purely by electrostatics. Further adsorption tests with activated carbon suggested that physical adsorption of the charged form of the redox couples onto the electrodes was the primary mechanism preventing self-discharge. This work is detailed in Chapter 2.

Tuning the pore size of activated carbon electrodes can further slow self-discharge with an iodide catholyte.[29] The ideal pore size for an iodide catholyte was found to be 7-8 Å, and the concept of optimizing porosity for other redox couples is likely possible. In the past decade, a significant finding for EDLCs was that matching micropore size to desolvated ion radius improved capacitance.[46] A similar advance may now be possible with redox ECs, this time to improve self-discharge performance rather than capacitance.

Solid complexation. In 2014, the concept of using an immobilized redox-ion on the electrode surface to limit self-discharge was proposed using the Cu^{2+}/Cu couple.[43] We explored a related concept of reversible solid complexation, which prevents redox shuttling by causing oxidized catholyte or reduced anolyte to precipitate as a solid.[31] We chose viologen (V) and bromide redox species and found that during charging at the positive electrode the oxidized bromide (Br_3^-) forms an insoluble complex with the viologen dication (V^{2+}), and at the negative electrode the reduced viologen cation radical ($V^{+\bullet}$) forms an insoluble complex with a bromide anion (Br^-). Upon discharge, these solid complexes dissolve back into the electrolyte. Understanding this process enabled the design of system with high Coulombic efficiency (99.9 %) and a slow self-discharge rate (77 % energy retention after 6 h at open circuit) with a pentyl viologen/bromide electrolyte without using a costly ion-selective separator. Because the electrolyte is homogenous throughout the cell in the discharged state and the two electrodes are identical, the symmetric cell can be charged in either polarity, i.e., "backwards" without damaging the device. This V/Br system is therefore resistant to over-discharge, which is important when stacking individual cells into packs or modules. This system is presented in Chapter 3.

In the following work, detailed in Chapter 4, we proposed a simple and general approach to utilize high-performance bromide catholyte using a non-

redox-active tetrabutylammonium cation (TBA^+). Our study shows that the charged Br_3^- is efficiently retained inside carbon pores as a [$TBA^+ \cdot Br_3^-$] solid complex. Compared to the uncomplexed case without TBA^+, this approach slowed self-discharge of cells using bromide catholyte dramatically, increasing the energy remaining after 10 h at open circuit from 1% to 50%. This combination of catholyte and complexing agent should be widely applicable for use with other anolytes and anodes, acting as a platform for future devices using redox-active electrolytes.

Other approaches and future strategies. There are other methods to suppress self-discharge beyond identifying redox-couples that strongly adsorb or precipitate in the charged state. One report used a size exclusion membrane (volume-selective semi-permeable dialysis tubing) as the separator with bulky polymer redox couples (sulfonated polyaniline).[47] Another concept uses a biredox ionic liquid where a large organic anion and cation are functionalized with anthraquinone and TEMPO moieties, respectively, as redox-active electrolyte.[48] This system minimizes self-discharge and leakage current by retaining the bulky redox couples in the pores with the help of a highly viscous electrolyte. Finally, there is redox EC work where the charge-storage mechanisms likely prevent redox shuttling but the self-discharge was not

reported. One such example is the use of a Cu^{2+}/Cu^{+} redox couple in nitric acid, where Cu^{+} reversibly binds to the electrode by complexing with a Cl^{-} anion and a carbonyl group on the carbon surface.[27] Revisiting this and other past work to analyze self-discharge suppression may be useful.

Despite these strategies, the self-discharge rates of redox ECs in general are still non-negligible. It is critical that researchers in this area continue to investigate new and innovative self-discharge suppression mechanisms that forgo the use of the expensive ion-selective membrane and extend energy retention into the days-to-weeks range.

Best practices for performance evaluation

All electrochemical energy storage research is based on compromises between competing properties. Correct evaluation is critical to realize the limitations of these technologies and target areas for further development. A brief discussion of important performance metrics and our perspectives on making meaningful measurements for redox ECs are presented below.

(1) Self-Discharge. Although self-discharge is an important performance metric in a redox EC, it is not always measured consistently and is sometimes not reported at all in the literature. The most common method to evaluate self-discharge is to leave a charged cell in the open-circuit condition and monitor the voltage decay over time. This method is useful for analyzing the self-discharge mechanism, where a linear relationship between open-circuit voltage (V_{OC}) and ln(t) implies activation control, and a linear relationship between V_{OC} and $t^{1/2}$ implies diffusion control.[49] This measurement can also estimate energy retention for EDLCs, as the theoretical remaining energy is equal to $\frac{1}{2} \cdot C \cdot (V_{OC})^2$. Unlike EDLCs, however, redox ECs do not have a linear relationship between V_{OC} and state of charge, and the open-circuit voltage measurement does not give practical information on the amount of energy remaining in the device as a function of time (Figure 8). We have therefore suggested that additional tests be done where

the full cell is discharged after different periods of time at open circuit, t, to quantify how quickly stored energy is lost over time. We normalize the discharge energy at each time point, $E_{dis}(t)$, to the initial discharge energy with no open-circuit period, $E_{dis}(0)$, giving an open-circuit energy efficiency, $\eta_R = E_{dis}(t)/E_{dis}(0)$.[30] For half-cells investigating a single electrode instead of a full device, an experiment measuring Coulombic efficiency versus resting time may be preferable.[29]

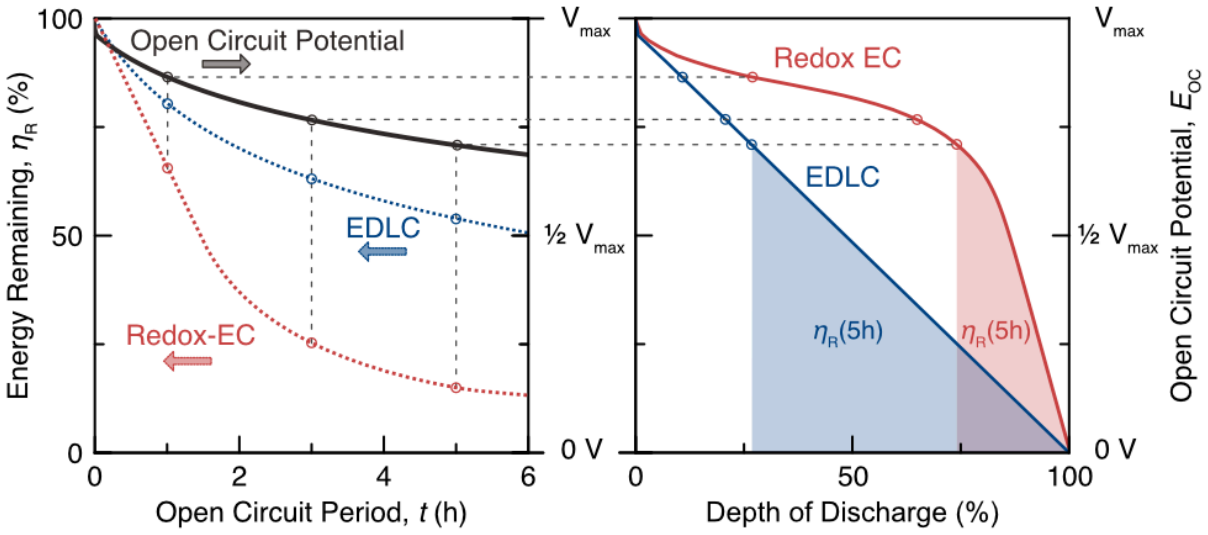

Figure 8. Proper self-discharge rate evaluation for redox ECs. The open-circuit potential of a redox EC undergoing self-discharge (black line, left) cannot accurately predict the remaining energy in the cell. The actual energy remaining is shown (dashed red line, left), which can be derived by matching the open circuit potential at a given time to the redox EC potential profile (solid red line,

right) and determining what fraction (remaining area under the curve) of the initial energy (total area under the curve) is retained. Also shown is the remaining energy that would be calculated (dashed blue line, left) under the mistaken assumption that the redox EC energy retention can be calculated using the same principles as an EDLC with a linear potential profile (solid blue line, right). Several tie lines are included for reference, and the remaining energies for the correct and incorrect case at $t = 5$ h are shaded to visually illustrate the derivation of a pair of η_R values.

(**2) Power and Energy.** There are many best practices established for determining power and energy performance in electrochemical energy storage systems. We briefly re-emphasize some of the important points, which are reported in detail elsewhere:

• Instead of extrapolating performance metrics from 3-electrode cyclic voltammetry results, it is preferable to construct a complete device and use galvanostatic cycling. 3-electrode tests with EDLCs can overestimate energy by up to a factor of 2 compared to a 2-electrode cell, and for a redox EC the larger supply of excess redox-active electrolyte can further inflate the measured values.[50]

• Realistic active material mass loadings of 1-10 mg/cm^2 are recommended so that the mass of the electrodes are significant relative to that of current collectors

and other cell components.[51] At very low loading, transport properties within each electrode are much faster, resulting in unrealistically high performance measurements.

• Capacitance should not be used to describe redox ECs (Wh and mAh are more meaningful than Farads).[10,11] As discussed above, redox ECs are distinct from pseudocapacitors.

• Energy needs to be calculated by integration of the galvanostatic charge/discharge potential profile and not using the formula $E = \frac{1}{2} \cdot C \cdot V^2$, which is only applicable for EDLCs (see Figure 3 above).[22]

(3) Performance Normalization. Interpreting performance correctly requires choosing the appropriate denominator when normalizing power or energy. Research test cells are much heavier than commercial cells, so performance is normally calculated based on the electrode mass only. For redox ECs, the electrolyte contributes to the total mass and contains active material but is often overlooked when calculating specific energy or power. In order to address this issue, the electrolyte mass (including solvent, redox couples, and supporting electrolyte) should be included, and excess electrolyte should be eliminated using volume-limiting cells.[30] In practice, however, electrolyte mass is difficult to measure and minimize because test cells always contain some extra volume. This

situation makes it difficult to compare redox ECs performance to that of EDLCs because redox ECs are "penalized" by the inclusion of the redox-active electrolyte mass, even though EDLCs contain an equivalent mass of inert electrolyte that is not considered in typical normalization. Volumetric reporting avoids these issues entirely, so we recommend evaluating performance on a volumetric basis in addition to a gravimetric basis. A reasonable estimate of volume is the geometric area of the electrodes, A, multiplied by the thickness of the cell stack (electrode/separator/electrode), d, and one should specifically indicate whether or not current collectors and packaging are also included in the calculation. Volumetric values are also easier to compare between different systems and more meaningful for many applications where space is more of a constraint than mass.

(4) Efficiency. High-power devices with poor energy efficiency will present thermal management issues in practical application, because all unrecovered energy must be dissipated as heat. The heat generation is so critical that we suggest reporting energy efficiency (EE) at different rates in addition to Coulombic efficiency (CE), as is typically done in redox-flow-battery literature. Voltage efficiency (VE) can be reported as well, using the relationship VE = EE/CE.

(5) Cycle Life. It is now common to see stable cycling over 5,000-20,000 cycles for redox ECs.[23] High-rate GCD tests are needed to demonstrate that the electrode materials can survive the stresses of repeated cycling and that redox reactions are highly reversible. However, the number of completed cycles does not provide a full picture of stability. At fast rates, the test duration is short and thousands of cycles are completed in hours or days. The cell spends little cumulative time at its maximum potential, where most degradation occurs. A more demanding test is a constant voltage hold at the maximum cell voltage.[52,53] This test is similar to a trickle charging or float condition that devices would be subjected to in practical application. It has been demonstrated in a redox EC with KI electrolyte that a 200 h voltage hold at 1.2 V causes equivalent degradation as cycling 110,000 times at a 1 A/g rate.[54] Performing this test on redox ECs gives more information on long-term stability because this condition allows more time for charged redox couples to diffuse away from the immediate vicinity of the electrode and interact with the separator, other redox couples, or the opposite electrode. It is also a more-relevant test for high voltage aqueous systems (1.5 - 2 V) where fast cycling may be the only factor limiting water splitting and gas evolution.[14]

References

1. Burke, A. R&D considerations for the performance and application of electrochemical capacitors. *Electrochim. Acta* **53,** 1083–1091 (2007).

2. Pandolfo, T., Ruiz, V., Sivakkumar, S. & Nerkar, J. in *Supercapacitors: Materials, Systems, and Applications* (eds. Beguin, F. & Frackowiak, E.) 69–109 (Wiley-VCH, 2013).

3. Salanne, M. *et al*. Efficient storage mechanisms for building better supercapacitors. *Nat. Energy* **1,** 16070 (2016).

4. Wang, Y., Song, Y. & Xia, Y. Electrochemical capacitors: mechanism, materials, systems, characterization and applications. *Chem. Soc. Rev.* **451,** 652–657 (2016).

5. Béguin, F., Presser, V., Balducci, A. & Frackowiak, E. Carbons and electrolytes for advanced supercapacitors. *Adv. Mater.* **26,** 2219–2251 (2014).

6. Miller, J. R. Engineering electrochemical capacitor applications. *J. Power Sources* **326,** 726–735 (2016).

7. Frackowiak, E. in *Supercapacitors: Materials, Systems, and Applications* (eds. Lu, M., Beguin, F. & Frackowiak, E.) 207–237 (Wiley-VCH, 2013).

8. Yan, J., Wang, Q., Wei, T. & Fan, Z. Recent Advances in Design and Fabrication of Electrochemical Supercapacitors with High Energy Densities. *Adv. Energy Mater.* **4,** 1300816 (2014).

9. Augustyn, V., Simon, P. & Dunn, B. Pseudocapacitive oxide materials for high-rate electrochemical energy storage. *Energy Environ. Sci.* **7,** 1597–1614 (2014).

10. Brousse, T., Belanger, D. & Long, J. W. To Be or Not To Be Pseudocapacitive? *J. Electrochem. Soc.* **162,** 5185–5189 (2015).

11. Simon, P., Gogotsi, Y. & Dunn, B. Where do batteries end and supercapacitors begin? *Science* **343,** 1210–1 (2014).

12. Burke, A. & Miller, M. The power capability of ultracapacitors and lithium batteries for electric and hybrid vehicle applications. *J. Power Sources* **196,** 514–522 (2011).

13. Burke, A. & Miller, M. Testing of electrochemical capacitors: Capacitance, resistance, energy density, and power capability. *Electrochim. Acta* **55,** 7538–7548 (2010).

14. Ratajczak, P., Jurewicz, K., Skowron, P., Abbas, Q. & Béguin, F. Effect of accelerated ageing on the performance of high voltage carbon/carbon electrochemical capacitors in salt aqueous electrolyte. *Electrochim. Acta* **130,** 344–350 (2014).

15. Gao, Q., Demarconnay, L., Raymundo-Piñero, E. & Béguin, F. Exploring the large voltage range of carbon/carbon supercapacitors in aqueous lithium sulfate electrolyte. *Energy Environ. Sci.* **5,** 9611–9617 (2012).

16. Lota, G. & Frackowiak, E. Striking capacitance of carbon/iodide interface. *Electrochem. commun.* **11,** 87–90 (2009).

17. Fic, K., Meller, M. & Frackowiak, E. Interfacial Redox Phenomena for Enhanced Aqueous Supercapacitors. *J. Electrochem. Soc.* **162,** A5140–A5147 (2015).

18. Wang, X. *et al.* High Energy Density Aqueous Electrochemical Capacitors with a KI-KOH Electrolyte. *ACS Appl. Mater. Interfaces* **7,** 19978–19985 (2015).

19. Roldán, S., Blanco, C., Granda, M., Menéndez, R. & Santamaría, R. Towards a further generation of high-energy carbon-based capacitors by using redox-active electrolytes. *Angew. Chemie Int. Ed.* **50,** 1699–701 (2011).

20. Roldán, S., Granda, M., Menéndez, R., Santamaría, R. & Blanco, C. Supercapacitor modified with methylene blue as redox active electrolyte. *Electrochim. Acta* **83,** 241–246 (2012).

21. Senthilkumar, S. T., Selvan, R. K. & Melo, J. S. Redox additive/active electrolytes: a novel approach to enhance the performance of supercapacitors. *J. Mater. Chem. A* **1,** 12386–12394 (2013).

22. Akinwolemiwa, B., Peng, C. & Chen, G. Z. Redox Electrolytes in Supercapacitors. *J. Electrochem. Soc.* **162,** A5054–A5059 (2015).

23. Chen, G. Z. & Akinwolemiwa, B. Dissolved redox species for the improvement of the performance of supercapacitors. *Curr. Top. Electrochem.* **19,** 47–65 (2017).

24. Lee, J. *et al.* Asymmetric tin–vanadium redox electrolyte for hybrid energy storage with nanoporous carbon electrodes. *Sustain. Energy Fuels* **1,** 299–307 (2017).

25. Huskinson, B. *et al.* A metal-free organic–inorganic aqueous flow battery. *Nature* **505,** 195–198 (2014).

26. Roldán, S., Granda, M., Menéndez, R., Santamaría, R. & Blanco, C. Mechanisms of energy storage in carbon-based supercapacitors modified with a quinoid redox-active electrolyte. *J. Phys. Chem. C* **115,** 17606–17611 (2011).

27. Mai, L.-Q. *et al.* Synergistic interaction between redox-active electrolyte and binder-free functionalized carbon for ultrahigh supercapacitor performance. *Nat. Commun.* **4,** 2923 (2013).

28. Frackowiak, E., Fic, K., Meller, M. & Lota, G. Electrochemistry serving people and nature: high-energy ecocapacitors based on redox-active electrolytes. *ChemSusChem* **5,** 1181–5 (2012).

29. Lee, J. *et al.* Nanoconfinement of redox reactions enables rapid zinc iodide energy storage with high efficiency. *J. Mater. Chem. A* **5,** 12520–12527 (2017).

30. Chun, S.-E. *et al.* Design of aqueous redox-enhanced electrochemical capacitors with high specific energies and slow self-discharge. *Nat. Commun.* **6,** 7818 (2015).

31. Evanko, B. *et al.* Efficient Charge Storage in Dual-Redox Electrochemical Capacitors through Reversible Counterion-Induced Solid Complexation. *J. Am. Chem. Soc.* **138,** 9373–9376 (2016).

32. Yoo, S. J. *et al*. Fundamentally Addressing Bromine Storage through Reversible Solid-State Confinement in Porous Carbon Electrodes: Design of a High-Performance Dual-Redox Electrochemical Capacitor. *J. Am. Chem. Soc*. **139,** 9985–9993 (2017).

33. Hu, B., Debruler, C., Rhodes, Z. & Liu, T. A Long Cycling Aqueous Organic Redox Flow Battery (AORFB) towards Sustainable and Safe Energy Storage. *J. Am. Chem. Soc*. **139,** 1207–1214 (2016).

34. Liu, T., Wei, X., Nie, Z., Sprenkle, V. & Wang, W. A Total Organic Aqueous Redox Flow Battery Employing a Low Cost and Sustainable Methyl Viologen Anolyte and 4-HO-TEMPO Catholyte. *Adv. Energy Mater*. **6,** 1501449 (2016).

35. Janoschka, T., Martin, N., Hager, M. D. & Schubert, U. S. An Aqueous Redox-Flow Battery with High Capacity and Power: The TEMPTMA/MV System. *Angew. Chem. Int. Ed. Engl*. **55,** 14427–14430 (2016).

36. Winsberg, J. *et al*. Aqueous TEMPO Catholytes for a High Capacity and High Current Density Oxygen-Insensitive Hybrid-Flow Battery. *ACS Energy Lett*. **2,** 411–416 (2017).

37. Lee, J., Choudhury, S., Weingarth, D., Kim, D. & Presser, V. High Performance Hybrid Energy Storage with Potassium Ferricyanide Redox Electrolyte. *ACS Appl. Mater. Interfaces* **8,** 23676–23687 (2016).

38. Lin, K. *et al*. Alkaline quinone flow battery. *Science (80-.).* **349,** 1529–1532 (2015).

39. Hwang, J. Y. *et al*. Boosting the capacitance and voltage of aqueous supercapacitors via redox charge contribution from both electrode and electrolyte. *Nano Today* **15,** 15–25 (2017).

40. Sathyamoorthi, S., Kanagaraj, M., Kathiresan, M., Suryanarayanan, V. & Velayutham, D. Ethyl viologen dibromide as a novel dual redox shuttle for supercapacitors. *J. Mater. Chem. A* **4,** 4562–4569 (2016).

41. Lee, J. *et al*. Tin/vanadium redox electrolyte for battery-like energy storage capacity combined with supercapacitor-like power handling. *Energy Environ. Sci*. **9,** 3392–3398 (2016).

42. Zhong, J. *et al*. Improved energy density of quasi-solid-state supercapacitors using sandwich-type redox-active gel polymer electrolytes. *Electrochim. Acta* **166,** 150–156 (2015).

43. Chen, L., Bai, H., Huang, Z. & Li, L. Mechanism investigation and suppresion of self-discharge in active electrolyte enhanced supercapacitors. *Energy Environ. Sci.* **7,** 1750–1759 (2014).

44. Ha, S. & Gallagher, K. G. Estimating the system price of redox flow batteries for grid storage. *J. Power Sources* **296,** 122–132 (2015).

45. Wang, B. *et al*. A Hybrid Redox-Supercapacitor System with Anionic Catholyte and Cationic Anolyte. *J. Electrochem. Soc.* **161,** A1090–A1093 (2014).

46. Chmiola, J. *et al*. Anomalous increase in carbon capacitance at pore sizes less than 1 nanometer. *Science* **313,** 1760–3 (2006).

47. Chen, L. *et al*. Electrochemical supercapacitor with polymeric active electrolyte. *J. Mater. Chem. A* **2,** 10526–10531 (2014).

48. Mourad, E. *et al*. Biredox ionic liquids with solid-like redox density in the liquid state for high-energy supercapacitors. *Nat. Mater.* **16,** 446–453 (2016).

49. Andreas, H. A. Self-Discharge in Electrochemical Capacitors: A Perspective Article. *J. Electrochem. Soc.* **162,** A5047–A5053 (2015).

50. Stoller, M. D. & Ruoff, R. S. Best practice methods for determining an electrode material's performance for ultracapacitors. *Energy Environ. Sci.* **3,** 1294 (2010).

51. Gogotsi, Y. & Simon, P. Materials science. True performance metrics in electrochemical energy storage. *Science* **334,** 917–8 (2011).

52. Ruch, P. W., Cericola, D., Foelske-Schmitz, A., Kötz, R. & Wokaun, A. Aging of electrochemical double layer capacitors with acetonitrile-based electrolyte at elevated voltages. *Electrochim. Acta* **55,** 4412–4420 (2010).

53. Weingarth, D., Foelske-Schmitz, A. & Kötz, R. Cycle versus voltage hold

– Which is the better stability test for electrochemical double layer capacitors? *J. Power Sources* **225,** 84–88 (2013).

54. Frackowiak, E., Meller, M., Menzel, J., Gastol, D. & Fic, K. Redox-active electrolyte for supercapacitor application. *Faraday Discuss*. **172,** 179–198 (2014).

Chapter 2

Design of aqueous redox-enhanced electrochemical capacitors with high specific energies and slow self-discharge

---

The contents of this chapter have substantially appeared in the following reference: S.-E. Chun, B. Evanko, X. Wang, D. Vonlanthen, X. Ji, G. D. Stucky, and S. W. Boettcher, "Design of aqueous redox-enhanced electrochemical capacitors with high specific energies and slow self-discharge," Nat. Commun. 6, 7818, 2015

Introduction

Electric double-layer capacitors (EDLCs) store electrical energy at the interface between a solid electrode (e.g. high-surface-area activated carbon) and a liquid electrolyte[1-4]. They are used in commercial applications requiring high power density and long-term cycle stability, e.g., in load-leveling and in electric vehicles[5-7]. These characteristics are enabled by a double-layer charging mechanism which relies only on physical ion adsorption/desorption in the Helmholtz layer of the liquid electrolyte and does not require driving slower solid-state ion insertion/de-insertion reactions as in, e.g. Li-ion batteries[1,8,9], which also lead to electrode volume change and thus capacity fade with cycling[10-12]. To attain specific energies of 5-10 Wh kg^{-1}, commercial EDLCs require organic electrolytes that operate at high potentials near 3 V. The disadvantages of these electrolytes are (1) low-to-moderate volumetric and gravimetric energy density, (2) high cost, (3) the requirement for high-purity activated carbon (needed to reduce self-discharge at the high voltages)[13], and (4) safety concerns associated with using flammable organic electrolytes[4]. These disadvantages limit the wide application of EDLCs[1,5].

One primary challenge in increasing the energy density of EDLCs is the mass of the electrolyte[14,15]. High-surface area carbons typically have large pore volumes that fill with inert electrolyte, reducing the cell-level specific energy[14].

A number of hybrid and pseudocapacitive devices incorporate solid-state or surface-redox functionality into electrodes to increase the specific energy of EDLCs[16-23].

In "redox ECs" the inert electrolyte is replaced with a redox-active one, thereby adding faradaic charge storage mechanisms to the underlying capacitive ones while ideally maintaining high power and cyclability (Figure 9)[24-31]. This approach enables the use of aqueous (aqueous) electrolytes (where high redox couple solubility results in high capacity) and less-expensive carbons (due to lower operating voltage windows). The disadvantages include the possibility of internal self-discharge via shuttling and cross-diffusion of mobile redox species, diffusion overvoltage losses, and cycling instability due to the intermixing redox couples[26,30,32]. The work in this chapter shows that these challenges can be simultaneously mitigated by understanding the underlying electrochemical processes and rationally choosing appropriate redox couples.

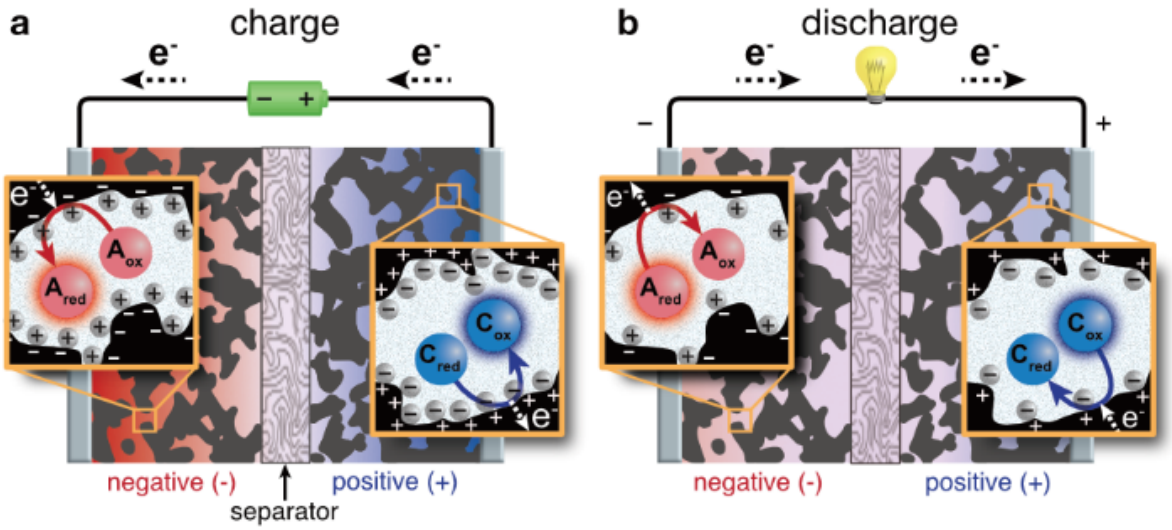

Figure 9. Charge storage mechanisms for redox ECs. Schematic showing capacitive and faradaic charge-storage processes. The redox couple used at the positive electrode (which is oxidized upon charging, and reduced upon discharge) is labeled as C_{red}/C_{ox} (catholyte), and the couple used at the negative electrode (which is reduced upon charging, and oxidized upon discharge) as A_{red}/A_{ox} (anolyte).

A number of soluble couples have been studied in redox ECs including halides, vanadium complexes, copper salts, methylene blue, phenylenediamine, indigo carmine, and quinones[25-28,30,33,34]. The performance to date of complete devices has been low and the underlying electrochemical processes poorly understood. The most substantial work is by Frackowiak and co-workers, who developed aqueous KI and $VOSO_4$ "catholyte" and "anolyte", respectively, separated by a Nafion membrane in two cell compartments[4,29]. Although specific

energy > 20 Wh kg^{-1} and specific power > 2000 W kg^{-1} were reported,[29] these metrics are normalized to the mass of the electrodes alone[14,35-37]. While such normalization is common, it is inappropriate for redox ECs where the electrolyte contributes directly to faradaic storage. Accounting for electrolyte reduces performance metrics by at least a factor of three. Further, the prohibitive cost of the Nafion cation-exchange membrane, which is used to prevent self-discharge via redox shuttling, needs to be addressed[4,29,32]. Stucky and co-workers studied a related system containing KI/$VOSO_4$ electrolyte without an ion-selective separator[34]. They proposed an electrostatic mechanism to account for self-discharge times on the order of 1 h, which was somewhat longer than expected given the separator used.

More-substantial progress has been prevented by the demands on the redox couples needed for the electrolyte. (1) The couples must be soluble at high concentrations, ideally > 1 M, to contribute substantially to the capacity. (2) The electron-transfer kinetics must be sufficiently fast to minimize voltage loss during charge/discharge. (3) The solution behavior of the charged redox couples must be such that self-discharge is slow, without the use of expensive ion-selective membranes. (4) During charging, the catholyte couple (C_{red}/C_{ox}) must be oxidized at the positive electrode while the anolyte couple (A_{red}/A_{ox}) must be reduced at the negative electrode. The relevant redox potentials of the two species

should be near the electrolyte decomposition window to maximize the voltage output. In water at near-neutral pH, appropriate couples could span > 1.5 V as the water oxidation and reduction kinetics are slow relative to those of one-electron couples[38].

This chapter explores a redox-active electrolyte containing viologen and bromide salts that was optimized with respect to the above criteria by systematic study of the underlying electrochemical phenomena. A device with 0.4 M KBr and 0.1 M heptyl viologen (HV) provides a specific energy of 11 Wh kg^{-1} and a specific power of 122 W kg^{-1} (normalized to the total mass of both electrodes and electrolyte, with each electrode having a high mass loading of 12.9 mg cm^{-2}), shows negligible fade over 20,000 cycles, and slow self-discharge rates superior to conventional aqueous control EDLCs without redox-active electrolyte. A related system employing methyl viologen (MV) instead of HV provides higher energy density (~14 Wh kg^{-1}) due to higher solubility, but also faster self-discharge and lower cycling stability. The self-discharge mechanisms are studied by comparing the behavior of individual redox electrolytes with varying chemical structure and molecular charge. Adsorption of the viologen and Br redox species to the activated carbon following charging is found to be important, and this effect enables 90 % (HV) retention of stored energy after 6 h at open circuit. In addition to good electrochemical performance, the cells use aqueous electrolyte,

are simple to prepare under ambient conditions, and likely safer for application than those using flammable organics[4,17]. The new system is thus appealing as a low-cost aqueous capacitor/battery hybrid.

Materials and Methods

Activated Carbon. Nanoporous carbon was prepared by CO_2 activation from high-purity carbon powder (Donacarbo S-241, Osaka Gas Co.). Carbon precursor (1 g) positioned in the center of a tube furnace was heated to 890 °C under flowing CO_2 (100 mL min^{-1}) for 22.5 h, which resulted in burn-off of 73.2 % of the carbon mass and resulted in a BET surface area of 2470 m^2 g^{-1}. Pore size distribution of the prepared activated carbon is characterized in Figure 10.

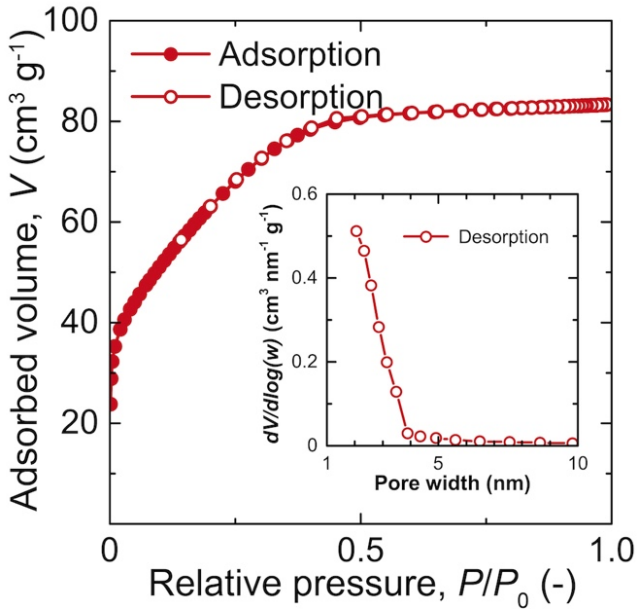

Figure 10. Pore analysis data on CO_2-activated Donacarbo. N_2 gas isotherm (adsorption/desorption) graph measured at 77 K and (inset) the pore size distribution (PSD) curved based on BJH theory from the desorption isotherm.

In activated carbon electrodes, micropores (< 2 nm) are often not accessible to large solvated ions and molecules, so N_2 adsorption isotherms can overestimate the available surface area. A better measurement of practically useful surface area is provided by methylene blue adsorption isotherms. This test was performed using standard procedures described elsewhere.[39] Methylene blue (MB) was dissolved into Millipore 18.2 MΩ cm water. Samples of activated carbon were massed and mixed with MB solutions in 250 mL and 500 mL Erlenmeyer flasks. The mixtures were stirred at 25ºC for 24 h to reach equilibrium adsorption. Samples of the supernatant from the flasks were centrifuged to remove any activated carbon, and the concentration of MB was determined with an Agilent UV-Visible spectrophotometer at 664 nm.

The data were fit using the linear form of the Langmuir adsorption isotherm model:

$$\frac{C_e}{q_e} = \frac{1}{Q_0 * b} + \left(\frac{1}{Q_0}\right) * C_e \qquad (2.1)$$

where C_e is the equilibrium concentration of MB in the liquid phase (mg/L), q_e is the equilibrium concentration of MB in the solid phase (mg/g), Q_0 is the theoretical maximum MB concentration in the solid phase, corresponding to the formation of a complete monolayer (mg/g), and b is the adsorption energy constant (mg^{-1}).

The linear fit gives a slope of 1.57 mg/mg ($1/Q_o$), an intercept of 2.67 mg/L ($1/(Q_o \bullet b)$), and a correlation coefficient of $R^2 = 0.998$, as shown in Figure 11. This gives b = 0.589 mg^{-1} and the theoretical maximum MB adsorption Q_0 = 636 mg/g. Assuming 1.35 nm^2 per MB molecule, the sample has a MB-accessible SSA of 1620 m^2/g,[40] somewhat lower than the BET surface area of 2470 $m^2\ g^{-1}$.

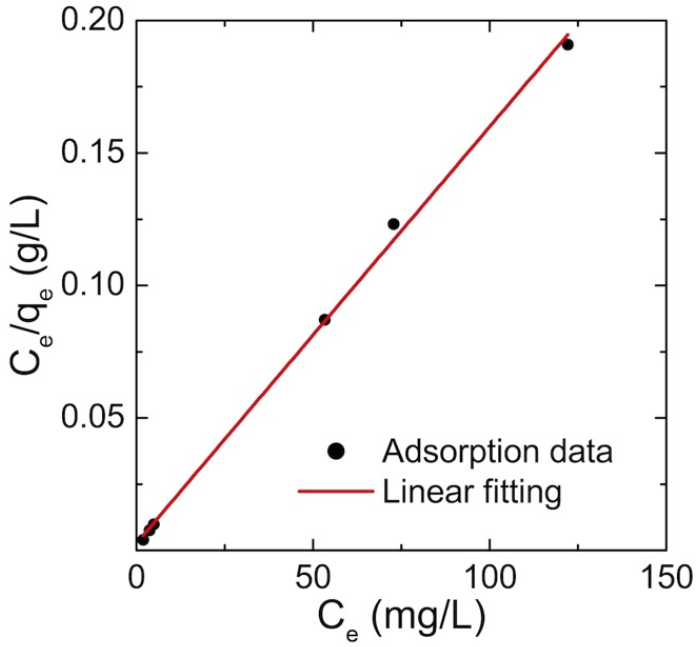

Figure 11. Methylene blue adsorption isotherm measured from Donacarbo CO_2-activated carbon.

The elemental composition (inductively coupled plasma analysis) is shown in Table 1 (Only elements with over 1/1000 wt.% were shown). Further details of the activated carbon preparation are reported elsewhere[41].

Table 1. Inductively coupled plasma (ICP) elemental analysis result of activated carbon.

Al	S	Ca	Fe	Zn
0.001 wt.%	0.001 wt.%	0.004 wt.%	0.009 wt.%	0.001 wt.%

Electrodes. To construct the freestanding electrodes, activated carbon, polytetrafluoroethylene (PTFE) binder, and acetylene black conductive additive were mechanically mixed with a 90:5:5 weight ratio. A 10-mm-diameter electrode pellet was fabricated from ~ 10 mg (~22 m^2 per pellet) of the mixture by hydraulic pressing at 2000 psi. To enhance the wetting of the electrode, the electrode pellets were immersed in excess electrolyte under vacuum for 10 min (to remove the air in the void space), and then pressurized with N_2 at 150 psi to force electrolyte into the pores (see Chapter 3). The process was carried out twice to ensure the electrolyte was thoroughly infiltrated.

Electrolytes. The electrolytes were prepared by either dissolving redox-reactive or electrochemically inert salts in 18.2 MΩ water. The salts were obtained as follows: potassium iodide (KI, 99 %, Alfa Aesar), potassium bromide (KBr, 99.999 %, Alfa Aesar), methyl viologen dichloride hydrate, $MVCl_2$ (1,1′-Dimethyl-4,4′-bipyridinium dichloride, 98 %, Sigma Aldrich), heptyl viologen

dibromide, $HVBr_2$ (1,1′-Diheptyl-4,4′-bipyridinium dibromide, 98 %, TCI AMERICA), potassium sulfate (K_2SO_4, 99.99 %, Alfa Aesar), potassium ferrocyanide ($K_4[Fe(CN)_6 \cdot 3H_2O]$, Mallinckrodt), hexaammineruthenium (III) chloride ($Ru(NH_3)_6Cl_3$, 99%, Strem Chemicals). Tris(2,2′-dipyridyl)dichlorocobalt ($Co(Bpy)_3Cl_2$) was prepared by literature methods[42].

Analytical electrochemistry. All electrochemical measurements were performed with a potentiostat/galvanostat (SP-300, Bio-logic). Redox-active electrolytes were first studied using a standard three-electrode configuration with a Pt or GC working electrode. Electrode discs were hand-polished for 30 s using 0.25 μm alumina/water slurry on Buehler microcloth. The electrode was then rinsed and sonicated in 18.2 MΩ water for 30 s. A coiled Pt wire and saturated calomel electrode (SCE, Fisher Scientific) served as the counter and reference, respectively. Test solutions (10 ml) were sparged with N_2 for 10 min to remove dissolved O_2.

Cell design and quantitative performance analysis. In order to quantitatively analyze charge-discharge and performance data, two custom cells were designed and built. The first was a T-shaped three-electrode Swagelok cell that incorporated a reference electrode with the tip placed at the edge of the separator. This enabled the study of the electrochemical processes at both electrodes simultaneously (Figure 12a). Insulated glassy carbon (GC) current

collectors were used to avoid background current that might be associated with metallic current collectors. These Swagelok-type cells were flooded with excess electrolyte (~500 μL) and thus the specific energy and power were calculated based on the combined "dry" electrode mass (indicated as g_{dry}) from the discharge data (as is typical and discussed below)[43,44].

We also designed a two-electrode cell with a "volume-limiting" geometry, where the electrolyte is confined within a precisely machined cavity and sandwiched between two GC plates in contact with the activated carbon (Figure 12b). For the volume-limiting cell the mass of both electrodes and all electrolyte were used to calculate the specific energy, power, and capacity (indicated as g_{wet}). The polycarbonate separator mass (0.9 mg) was ignored as it is only ~ 1 % of the total cell mass. Performance metrics based on the total "wet" cell mass are practically relevant, whereas the "dry" metrics are useful only for comparison to other systems where electrolyte mass has been ignored.

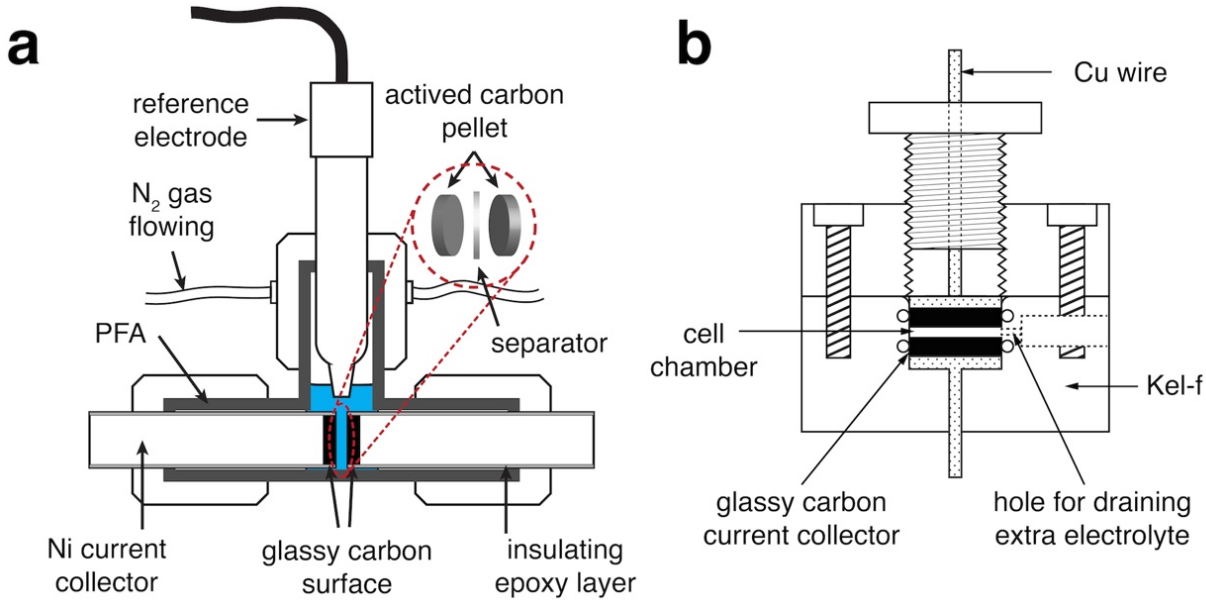

Figure 12. Schematic of electrochemical test cells. (a) the three-electrode Swagelok cell and (b) custom two-electrode volume-limiting cell with limited chamber volume to contain electrodes and minimal excess electrolyte

Three-electrode cell design. The three-electrode cell was built from a perfluoroalkoxy (PFA) T-shaped Swagelok fitting and used insulated GC current collectors (Figure 12a). Between the activated carbon pellets, a paper separator (Whatman qualitative filter paper, Grade 1) was inserted to prevent direct electrical contact between electrodes. The electrodes/separator were soaked in test electrolyte (de-aerated by flowing N_2 gas for 10 min prior to use), and pressed in-between two current-collector rods. The cell was then flooded with 0.4-0.5 ml of excess electrolyte. The rods were made of a GC plate (3 mm thick, type 2, Alfa Aesar) bonded to a Ni (Nickel Alloy 200, McMaster) body with the sides

insulated with non-conducting epoxy (Stycast 1266, Emerson and Cuming). Before each test, the GC surface was polished as with the analytical electrochemistry. The use of GC avoids potential complications due to background corrosion of, e.g., stainless steel current collectors often used in Swagelok cells. A SCE reference electrode placed with the tip at the edge of the separator was incorporated to allow for independent measurement of the absolute potential at each electrode. The cell exterior was purged with wet N_2 during voltammetry and constant-current charge/discharge cycling.

Two-electrode cell design for specific energy and power measurements. An 11.3-mm-wide cylindrical chamber machined from inert plastic (Kel-F) served as the cell housing (Figure 12b). Two GC discs tightly fit with o-ring seals and back-contacted with Cu wire served as the current collectors. The separator (Polycarbonate membrane filter, STERLITECH) was cut into a disc with an identical diameter as the chamber. The electrodes were 10-mm-diameter pellets, fabricated as described above.

Control/comparison devices. Two commercial EDLCs using an aqueous and an organic electrolyte were characterized to evaluate the electrochemical behavior and self-discharge rate of commercial devices as a benchmark. One capacitor utilizes organic electrolyte with a specified 2.7 V of working potential

range (BACP0010 P270 T01, Maxwell Technologies). The other (CLG03P025L12, Cellergy) utilizes aqueous electrolyte, and the operating potential is specified at 3.5 V (presumably obtained using approx. three cells in series). For an additional comparison, a lab-made EDLC cell was tested with the manufactured CO_2 activated carbon electrodes and non-redox active electrolyte (0.5 M K_2SO_4, 99.99 % pure).

Galvanostatic charge/discharge cycling was performed on each system by applying appropriate current based on the device capacity. All three kinds of EDLC show linearly changing potential with time, indicating pure double-layer capacitive charging. For the lab-made EDLCs, the specific capacity and energy density were normalized in two ways based either on combined electrodes mass ("dry", as is typical) or on the integrated mass of electrodes and electrolyte (i.e. "wet").

Definition and evaluation of performance metrics. The specific capacity at discharge, Q_{dis} (mAh g^{-1}), is defined as

$$Q_{dis}=I_{dis}/m_{cell}\cdot t_{dis} \tag{2.2}$$

where I_{dis} is the constant discharge current in mA, m_{cell} is the mass of the cell components (as indicated above either "dry" or "wet"), and t_{dis} is the discharge time. The specific energy density at discharge, E_{dis} (Wh kg^{-1}), is calculated by integrating the instantaneous specific power

$$E_{\mathrm{dis}} = \int_0^{t_{\mathrm{dis}}} I_{\mathrm{dis}}/m_{\mathrm{cell}} \cdot V(t)\mathrm{d}t \tag{2.3}$$

where $V(t)$ is the time varying voltage output of the cell. The average specific power, P_{dis} (W kg^{-1}), is calculated by dividing the energy by the discharge time[15,44,45]

$$P_{\mathrm{dis}} = E_{dis}/t_{dis} \tag{2.4}$$

We define the coulombic efficiency, $\eta_{\mathrm{C}}(\delta)$, after a specific self-discharge period δ (in min, where the cell is left at open circuit) as

$$\eta_{\mathrm{C}}(\delta) = Q_{\mathrm{dis}} / Q_{\mathrm{ch}} \tag{2.5}$$

where Q_{ch} is the total charge passed during the charging cycle (analogous to Q_{dis} defined in Eq. 2.2). We define the energy efficiency $\eta_{\mathrm{E}}(\delta)$ after a specific self-discharge time as

$$\eta_{\mathrm{E}}(\delta) = E_{\mathrm{dis}} / E_{\mathrm{ch}} \tag{2.6}$$

where E_{ch} is the total energy expended during the charging cycle (analogous to E_{dis} defined in Eq. 2.3). Finally, we define the energy retention efficiency, $\eta_{\mathrm{R}}(\delta)$, which is the ratio of the energy obtained after a self-discharge period δ compared to that where $\delta = 0$, as

$$\eta_{\mathrm{R}}(\delta) = \eta_{\mathrm{E}}(\delta) / \eta_{\mathrm{E}}(0) \tag{2.7}$$

Self-discharge was studied by measuring η_{C} and η_{E} as a function of δ. First, the cell was charged to the specific potential by applying a constant current (0.5 A g_{dry}^{-1}). Then, while monitoring the cell potential decay, the cell was left at

various periods of open circuit: 0 min, 1 min, 2 min, 5 min, 10 min, 20 min, 30 min, 60 min, 120 min, and 360 min. After each open circuit period, the cell was discharged to 0 V by extracting the same constant current density (-0.5 A g_{dry}^{-1}). For each self-discharge test, at each time, the coulombic and energy efficiency (%) were obtained. We use the "half-life" of the specific energy $t_{½\cdot E_{max}}$ where $\eta_R(t_{½\cdot E_{max}}) = 0.5$ as well as η_R(6 h) to compare the different self-discharge rates of the cells. When $t_{½\cdot E_{max}}$ was longer than the test duration (6 h), the experimental η_R data was fit to a linear decay to estimate $t_{½\cdot E_{max}}$.

Electrolyte mass is especially important for devices with redox-active electrolytes. To develop significant faradaic energy storage, a sufficient supply of redox-active ions is required. The volume of electrolyte available is determined by the free volume in the porous electrodes and the separator[15]. This volume, along with the concentration of the redox-active species, determines the maximum possible number of ions available for faradaic charging. For each electrode, the total electrode volume is as a sum of the volume of each component:

$$V_{el} = m_{el}\left(\frac{f_{binder}}{\rho_{binder}} + \frac{f_{ACskeleton}}{\rho_{ACskeleton}} + \frac{f_{CarbonBlack}}{\rho_{CarbonBlack}}\right) + V_{free,el} \quad (2.8)$$

where f_x and ρ_x represent the mass fraction and density, respectively, of each component, m_{el} represents the total electrode mass, V_{el} represents the total

electrode apparent volume, and $V_{free,el}$ represents the free pore volume that will be filled with electrolyte upon device assembly. The solid skeleton of many activated carbons, carbon blacks, and other materials with graphitic domains has a density of approximately 2.1 g/cm^3 and PTFE has a density of 2.2 g/cm^3 [46-48]. The free volume of the separator is also straightforward to calculate, with:

$$A_{\text{sep}} * t_{\text{sep}} * P_{\text{sep}} = V_{\text{free,sep}} \quad (2.9)$$

where A_{sep} and t_{sep} are the area and thickness, respectively, of the separator, P_{sep} is the separator porosity, and $V_{free,sep}$ is the separator free volume. Cellulosic separators have a porosity near 0.7, while glassy fiber separators have a porosity closer to 0.9 [49]. Some popular polyethylene separators, such as Celgard 3501, have a porosity of 0.55. The separator and the electrodes are the only porous components in a complete device, so the electrolyte volume, $V_{electrolyte}$, will simply be the sum of $V_{pore,el}$ for both electrodes and $V_{free,sep}$:

$$V_{\text{electrolyte}} = V_{\text{pore,p}} + V_{\text{pore,n}} + V_{\text{free,sep}} \quad (2.10)$$

Activated carbon adsorption measurements for redox-active electrolytes. In these experiments, concentrations of oxidized and reduced redox couples in an electrolyte were measured with and without the presence of activated carbon (AC). All experiments were performed in 1.5 mL centrifuge tubes. The tubes were filled with 1.5 mL of ~10 mM analyte solution and capped to exclude oxygen immediately after adding reagents and/or 5 mg of AC. A vortex mixer

was used to agitate the centrifuge tubes at the beginning and end of a 10-minute waiting period. After this time, the tubes were centrifuged and a 10 uL sample of the supernatant was diluted by a factor of 200 into 1.99 mL of Millipore 18.2 MΩ.cm water in a quartz cuvette. The cuvette was shaken vigorously for 20 s to ensure a homogeneous analyte. The concentration of each analyte was determined with an Agilent UV-Vis spectrophotometer.

Methyl Viologen adsorption. For MV^{2+}, the analyte was prepared by directly dissolving $MVCl_2$ salt into 18.2 MΩ.cm water. For the MV^{+} analyte, chemical reduction of the MV^{2+} solution was performed in the centrifuge tubes with excess zinc powder (8 um) with and without AC. In the cuvette, direct measurement of dilute MV^{+} is difficult due to background reaction with dissolved oxygen, so the reduced viologen in the diluted sample was allowed to completely reoxidize and the concentration of the resulting MV^{2+} was measured instead. To ensure there was no effect due to reaction time, all spectra were repeated after 20 min. Very little deviation was observed between 10 and 20 min intervals.

Heptyl Viologen adsorption. The adsorption of heptyl viologen ($HVBr_2$) was investigated using the same procedures as with MV. Because zinc powder did not perform well as a reducing agent for HV, 15 mg sodium dithionite ($Na_2S_2O_4$) was used instead.[50] It should be noted that even without activated carbon, some

of the reduced HV^+ precipitates, suggesting the HV^+ radical is much less soluble than the MV^+ radical.

Bromide and Bromine/Tribromide adsorption. For Br^-, the analyte was prepared by directly dissolving KBr salt into 18.2 MΩ.cm water. Because Br_2 and Br_3^- are stable in air, these oxidation products can be measured directly and these species were generated *ex-situ*, unlike the viologen radicals. Liquid bromine is volatile and difficult to handle and precisely measure, so bromine and tribromide were generated using the following chemical reactions[51]:

$$NaBrO_3 + 5\ Br^- + 6\ H^+ \rightarrow 3\ Br_{2(aq)} + 3\ H_2O \qquad (2.11)$$

$$Br_{2(aq)} + Br^- \rightleftharpoons Br_3^- \quad (K_{eq} = 16.1\ M^{-1}) \qquad (2.12)$$

To increase the conversion of the sodium bromate and drive the equilibrium products towards Br_3^-, the oxidation was performed in a solution containing 0.1 M KBr and 0.1 M HBr with $NaBrO_3$ as the limiting reagent. This reaction, if completed, produces a total bromine concentration of 10 mM (before adsorption to AC):

$$[Br_2]_T = [Br_2] + [Br_3^-] = 0.01\ M \qquad (2.13)$$

Like other species investigated by UV-vis, the supernatant from the Br^- tests was diluted by a factor of 200 in Millipore 18.2 MΩ cm water. Samples from the oxidized Br_2/Br_3^- species, however, were diluted with a 0.1 M KBr solution. This ensured that the equilibrium did not shift from Br_3^- back towards Br_2 in the

cuvette, which has a much lower molar absorptivity coefficient, making it harder to accurately measure by UV-vis. The total concentration of oxidized bromide species in solution remaining, $[Br_2]_T$ is proportional to the absorption at λ_{max} = 266 nm, and can be calculated by combining equations (2.12) and (2.13) [51]:

$$A_{266} = \frac{(\epsilon_{Br_3^-})K_{eq}[Br^-][Br_2]_T}{1+K_{eq}[Br^-]} \quad (2.14)$$

with $\epsilon_{Br_3^-} = 40{,}900\ M^{-1}cm^{-1}$. For Br^-, the analysis is simpler. No chemical equilibrium considerations are necessary and λ_{max} = 191 nm with $\epsilon_{Br^-} = 13{,}000\ M^{-1}cm^{-1}$.

Ferrocyanide/Ferricyanide adsorption. For the ferrocyanide and ferricyanide analytes, no chemical oxidation or reduction was required. Instead, the 10 mM ferrocyanide solution and the 10 mM ferricyanide solution were prepared separately directly from $K_4Fe(CN)_6$ and $K_3Fe(CN)_6$ salts, respectively.

Results and Discussion

Redox-active electrolytes for the positive electrode (catholyte).

Redox species at the positive electrode are reduced during discharge ($C_{ox} + e^- \rightarrow C_{red}$) and thus referred to as the "catholyte". The catholyte should have a reduction potential near, or slightly more positive than, the oxygen evolution potential to maximize energy density. The halogens iodide and bromide are promising as they are inexpensive and highly soluble (> 1 M)[52,53]. The aqueous reduction potentials of iodine ($E^{\circ}_{I_3^-/I^-} = 0.3$ V vs. SCE) is within the water stability window while that of bromine ($E^{\circ}_{Br_3^-/Br^-} = 0.81$ V vs. SCE) is located above the thermodynamic oxygen evolution potential at pH 7 (0.58 V vs. SCE)[54].

Figure 13a shows the galvanostatic cycling profiles of candidate catholytes tested in a three-electrode Swagelok cell. For 1 M KI, the positive electrode potential narrowly varied between 0.02 V and 0.19 V vs. SCE, indicating oxidation of I^- to I_3^- (the difference between the observed plateau potential and $E^{\circ}_{I_3^-/I^-} = 0.3$ V vs. SCE is discussed below)[54]. The negative electrode potential varied linearly with charge between and 0.02 V and -0.81 V vs. SCE indicating a double-layer charging mechanism with inert K^+.

For 1 M KBr electrolyte, the positive electrode shows two distinct charging regimes. For the first 60 s, the electrode potential depends linearly on the charge added, indicating capacitive charging with Br^- in the double layer. For the next 60 s the potential increase slows and plateaus at ~ 0.7 V vs. SCE, indicating oxidation of Br^- to Br_3^- [54]. The negative electrode showed purely capacitive charging. The high redox potential of Br^-/Br_3^- is advantageous for increasing energy density, as discussed below.

EDLC self-discharge is commonly studied by monitoring the potential decay at open circuit[55-57]. However, because the charge is not linear with potential for redox ECs, we measured energy retention η_R by complete discharge at each time point in Figure 14. The self-discharge profiles of KI and KBr show η_R of 76 % and 43 % after 6 h, respectively. Remarkably, the self-discharge rate of the KI cell is slower than that of the control K_2SO_4 cell when also charged to 1 V (η_R = 67 % after 6 h). Given the lack of an ion-selective membrane, the slow self-discharge of the halogen cells is unexpected. After charging the KI cell, a large concentration gradient of I_3^- and I^- between the positive and negative electrode is present that would normally be expected drive diffusive transport across the cell resulting in fast self-discharge.

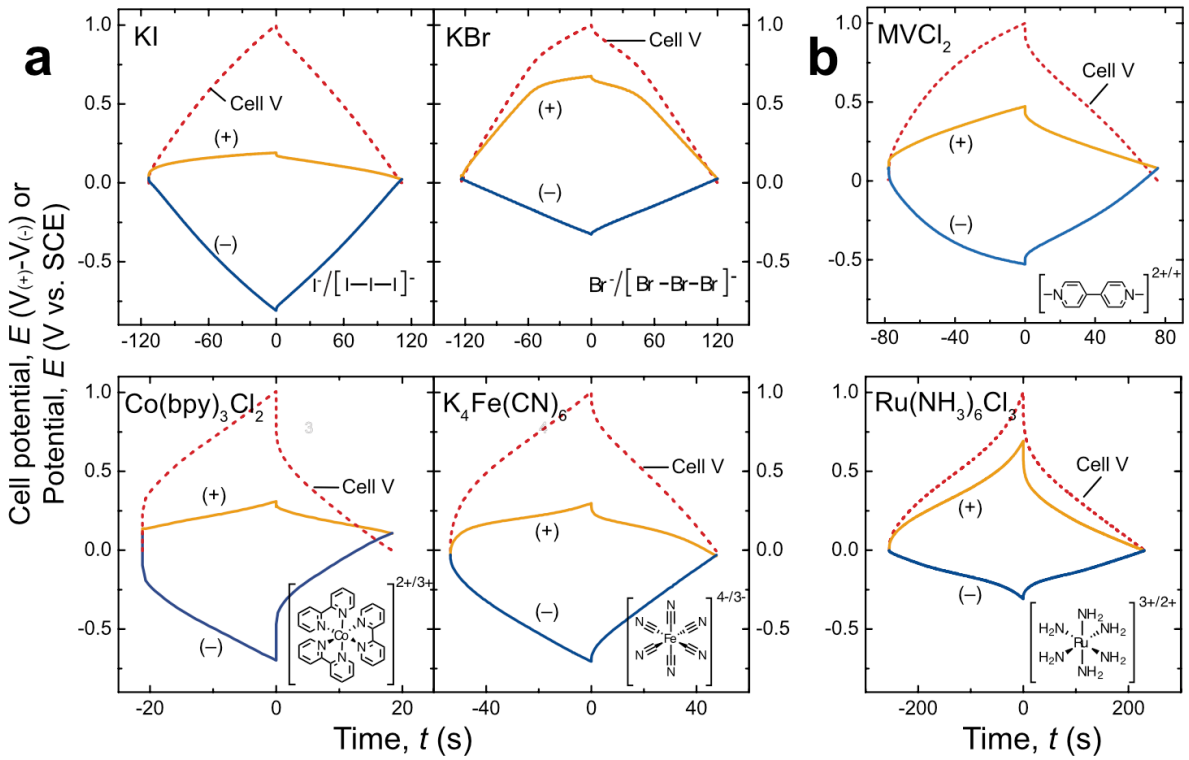

Figure 13. **Asymmetric cells with a single redox couple.** The galvanostatic charge/discharge profiles are shown for asymmetric cells with the candidate (a) catholyte and (b) anolyte redox couples. The cells were charged/discharged at a rate of 1 A $g^{-1}_{(+)\text{ electrode}}$ (normalized to the mass of the positive electrode only to a total cell voltage of 1 V. In (a), the slope of the potential-time curve for the negative electrode is smaller for the KBr cell than for the KI cell because the negative electrode had three times the mass of the positive electrode so that the positive electrode was able to reach the Br^- oxidation potential with a total cell potential of 1 V, which was not possible with a symmetric cell.

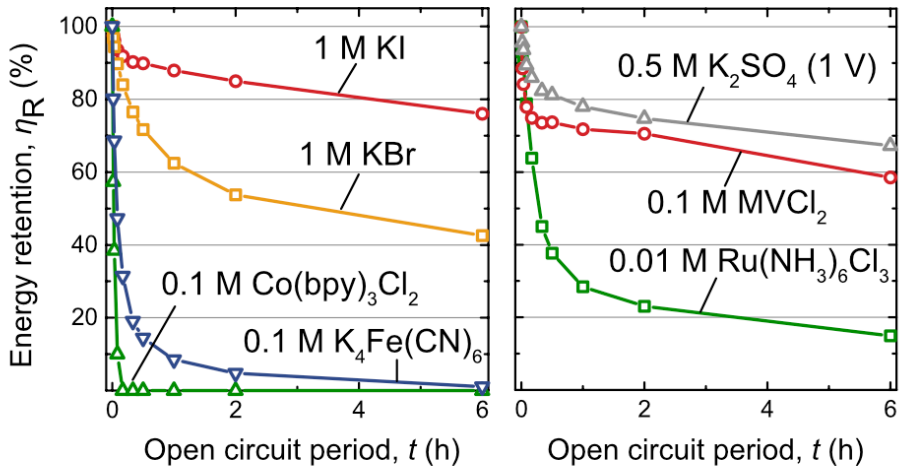

Figure 14. Self-discharge rates of selected redox-active electrolytes. Energy retention η_R for each cell was collected by charging the cell, allowing it to sit at open circuit for a given time, then discharging the cell completely.

$K_4Fe(CN)_6$ and $Co(bpy)_3Cl_2$ cells show galvanostatic charging behavior at the positive electrode similar to the KI cell with the electrode potential pinned near the standard potential of the couple (Figure 13a). The negative electrodes show capacitive (linear potential-time) response on charging, while upon discharging an additional potential loss is measured that is associated with the low ionic conductivity of the 0.1 M redox-active electrolytes. The $Co(bpy)_3Cl_2$ and $K_4Fe(CN)_6$ cells have 89.5 % and 90.8 % coulombic efficiency, respectively –lower than the 99.9 % and 98.8 % measured for the KI and KBr cells, respectively. The $Co(bpy)_3Cl_2$ cell loses half of its energy in 1 min, while for the $K_4Fe(CN)_6$ cell this takes 5 min. This data is consistent with electrostatics

contributing to the self-discharge in the case of $Co(bpy)_3^{2+/3+}$ and retarding it in the case of $Fe(CN)_6^{4-/3-}$, and for the halides. However, despite the larger negative charge of $Fe(CN)_6^{4-/3-}$ its self-discharge rate is still roughly 100 times faster than that of I_3^-/I^-. The retarded self-discharge for the halides cannot be explained purely by electrostatics.

A mechanism to explain the slow self-discharge of the halides is physical adsorption of the oxidized species within the activated carbon surface preventing cross-diffusion. Halides are known to adsorb on carbon electrodes[58-60] and we confirmed the strong adsorption of Br_3^- on activated carbon using UV-VIS spectroscopy, evidenced by the decrease of the concentration of Br_3^- in solution after the addition of activated carbon (Figure 15) . In contrast, Br^-, $Fe(CN)_6^{4-}$, and $Fe(CN)_6^{3-}$ do not adsorb. We also note that for both the KBr and KI cells the observed potential plateau at the positive electrode (Figure 13a) is ~0.1 V less positive than the standard potential of the respective couples. This is also consistent with specific adsorption stabilizing the oxidized halide, thus shifting the formal potential within the activated carbon negative of the standard potential. These results show physical adsorption is the primary mechanism preventing self-discharge and electrostatic effects are secondary.

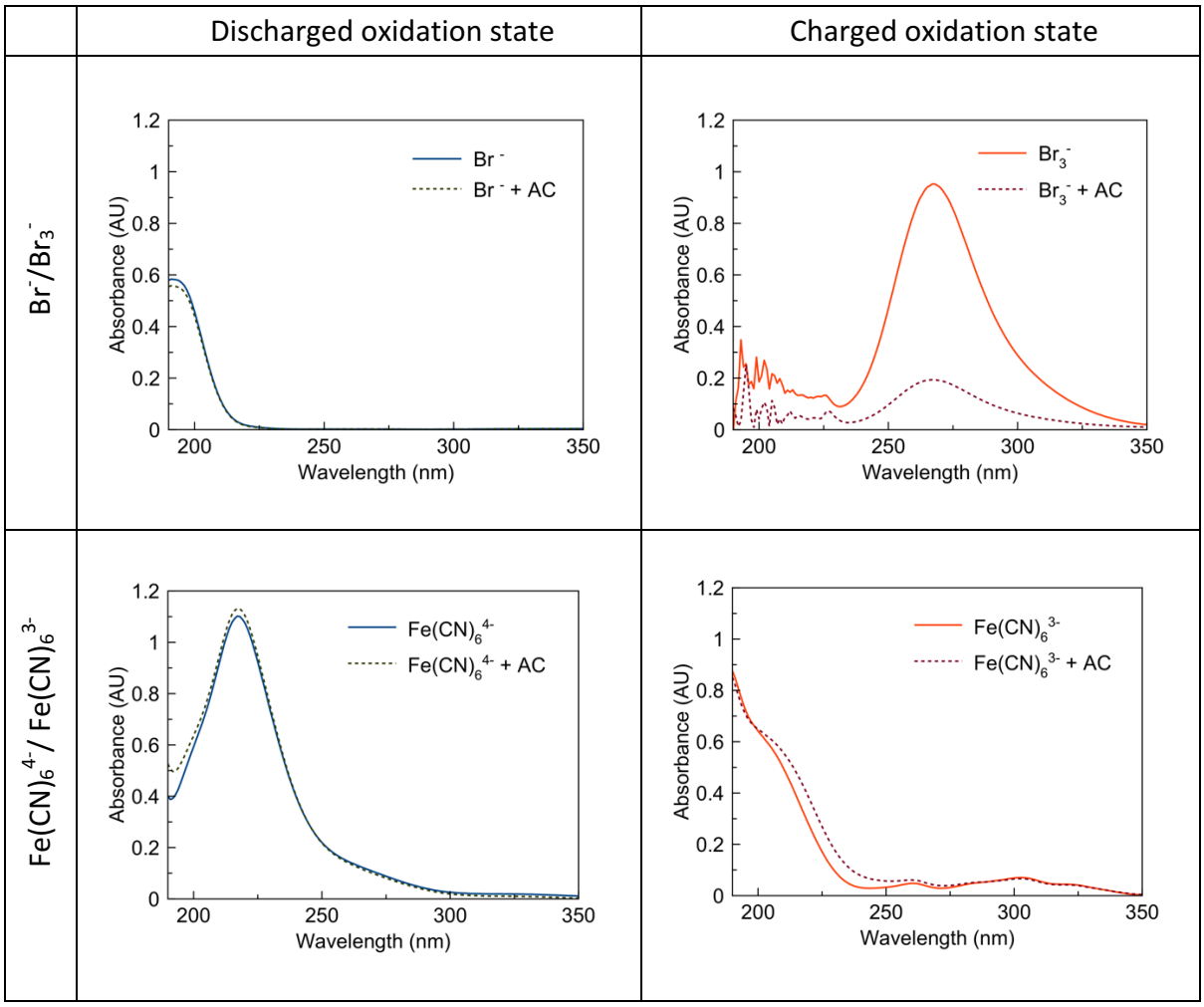

Figure 15. Adsorption of catholyte couples to activated carbon. UV-VIS spectra measuring concentration of charged or discharged catholyte redox couples in solution with and without the addition of activated carbon.

Redox-active electrolytes for the negative electrode (anolyte).

Redox couples for the negative electrode A_{red}/A_{ox} should have standard potentials at or slightly more-cathodic than the hydrogen evolution potential, as well as high solubility and solution compatibility with the catholyte. Based on the observations above, A_{red}/A_{ox} should have a positive charge and physically adsorb on activated carbon following charging to prevent self-discharge.

Viologen dications (4,4'-dipyridinium compounds) are positively charged, highly soluble redox couples, with formal potentials negative of the hydrogen potential and fast, reversible, kinetics[61-67]. Methyl viologen dichloride ($MVCl_2$) was studied first due to its negative potential (E^o = -0.69 V vs. SCE), commercial availability, and low cost (< \$5 kg^{-1} in bulk, used for agriculture)[65,68-70]. Being a nearly co-planar π-π conjugated ring system, $MVCl_2$ also adsorbs on activated carbon surfaces[71]. Stronger adsorption is expected after reduction of MV^{2+} to MV^+ due to decreased charge density and increased co-planarity of the two adjacent rings.

In order to study the viologen electrochemistry in the absence of a redox-active electrolyte at the positive electrode, a 4:1 mass ratio for the positive:negative electrode was used (the Cl^- counter ion is inert over the accessible potential range). During galvanostatic charging, the positive electrode potential varied nearly linearly with time while the negative electrode potential

curves substantially with time near ~ -0.5 V vs. SCE (Figure 13b), consistent with the reduction MV^{2+} to MV^{+}. The self-discharge rate of the $MVCl_2$ electrolyte was measured (Figure 14) and found comparable to that of the EDLC with 0.5 M K_2SO_4, suggesting that the redox couple does not contribute substantially to self-discharge via redox shuttling.

To understand the self-discharge processes, a ruthenium hexamine dichloride electrolyte was also studied (Figure 13b). $Ru(NH_3)_6^{3+}/Ru(NH_3)_6^{2+}$ is cationic, like MV^{2+}/MV^{+}, but is unlikely to specifically absorb on the activated carbon surface because of its near-spherical molecular shape. The $Ru(NH_3)_6Cl_3$ cell shows double-layer charging with Cl^- on the positive electrode and some faradaic charging on the negative electrode with a slight plateau near -0.2 V consistent with the reduction of ruthenium hexamine (E^o ~ -0.14 V vs. SCE)[72]. The self-discharge rate (Figure 14), however, is significantly faster for $Ru(NH_3)_6Cl_3$ than for $MVCl_2$, providing further evidence that electrostatic effects are not sufficient to prevent self-discharge and that MV^{+}, like the oxidized halides, adsorbs on the carbon electrode[73]. UV-VIS spectroscopy supports this mechanism, showing weak adsorption of MV^{2+} and stronger adsorption of MV^{+} (Figure 16).

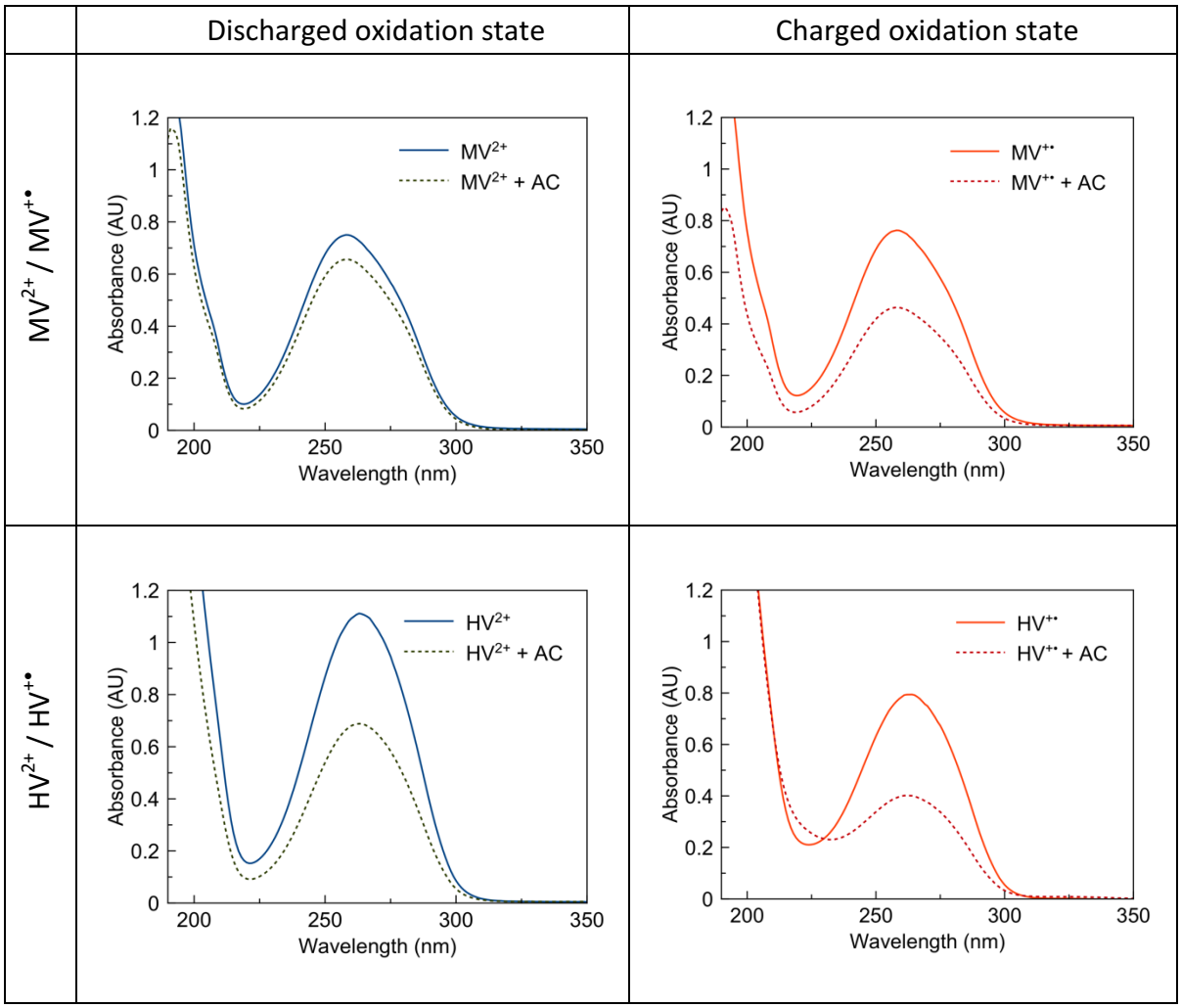

Figure 16. Adsorption of anolyte couples to activated carbon. UV-VIS spectra measuring concentration of charged or discharged anolyte redox couples in solution, with and without the addition of activated carbon.

Combined electrolyte systems.

For high performance, the redox-active electrolytes for the positive and negative electrodes must be combined to make a dual redox EC where the catholyte and anolyte have a matched capacity. All species in both redox states (A_{red}, A_{ox}, C_{red}, C_{ox}) should be stable in the same electrolyte to reduce manufacturing complexity and relax demands on the separator. Based on the results from studying the individual couples, we targeted mixed halogen/viologen electrolytes. We first studied $MVCl_2$/KI, which was stable in the uncharged state but formed $MV^{\bullet+}$-I^- precipitate upon charging, leading to irreversible capacity loss[64,74]. In contrast, $MVCl_2$/KBr solutions showed highly reversible redox behavior of both redox-ions in analytical voltammetry cells (Figure 17). Br^- benefits from a more positive oxidation potential compared to I^-, thus providing increased specific energy, but is more reactive/corrosive as Br_2 or Br_3^- compared to I_3^-.

Cells with 1 M KBr/0.1 M $MVCl_2$ electrolyte were tested by voltammetry and galvanostatic cycling to probe the charging mechanism (Figure 18). Voltammograms collected with a 1 V window are rectangular indicating a capacitive charging mechanism at both electrodes. As the Br/MV cell was cycled beyond 1 V, current peaks were observed at the positive and negative electrodes corresponding to Br^- oxidation to Br_3^- and MV^{2+} reduction to MV^+, respectively.

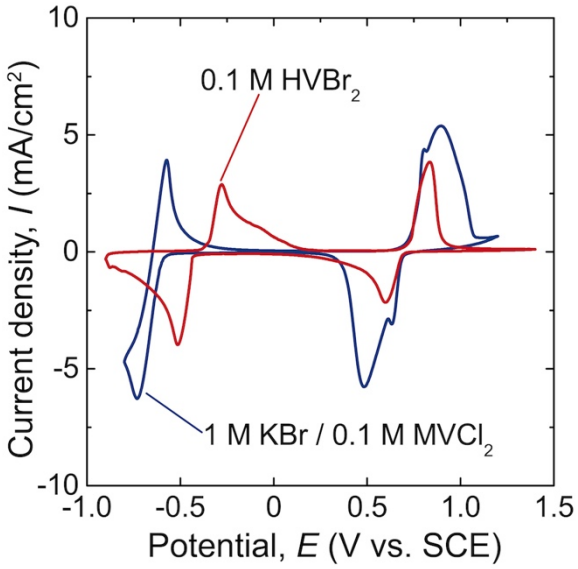

Figure 17. Cyclic voltammograms of viologen/bromide half-cells. Cyclic voltammograms of the mixed solution of 1 M KBr/0.1 M $MVCl_2$ and 1 M KBr/0.1 M $HVBr_2$ collected at 5 mV s^{-1}. A three-electrode half-cell configuration was used, with GC disc working, coiled Pt counter and SCE reference electrode. Both solutions show the redox process between Br^-/Br_3^- near 0.72 V vs. SCE. Other redox processes from MV^{2+}/MV^+ at -0.64 V and HV^{2+}/HV^+ at -0.40 V vs. SCE are observed in 1 M KBr/0.1 $MVCl_2$ and 0.1 $HVBr_2$ solution, respectively. Both solutions show reversible redox behavior for both redox couples, without irreversible interaction between them.

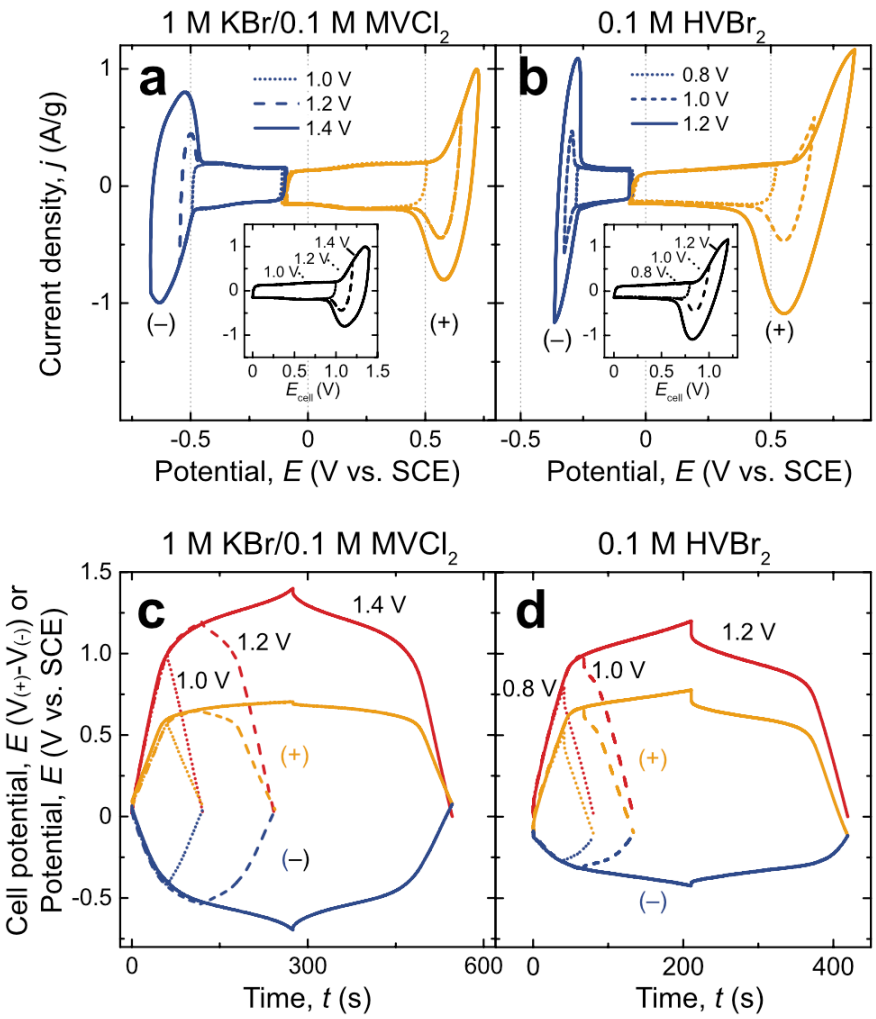

Figure 18. Electrochemical characterization of cells with combined electrolytes. (a) and (b) show voltammograms for complete cells collected at 5 mV s^{-1} (inset) with the voltages for the positive and negative electrodes separately recorded. (c) and (d) show the galvanostatic charge/discharge profiles at 0.5 A g_{dry}^{-1} to a total cell potential between 0.8 and 1.4 V.

Figure 18c shows the galvanostatic charging of the same cell to different total cell voltages. At both the positive and negative electrodes an initial capacitive (linear) voltage-time response is observed followed by a faradaic

response as the electrode potential approaches the reduction potential of the couple. Figure 19 shows that the self-discharge rate for the 1 M KBr/0.1 M $MVCl_2$ cell charged to 1.4 V ($t_{½\cdot E_{max}}$ = 170 min) is similar to the commercial Cellergy control capacitor ($t_{½\cdot E_{max}}$ = 140 min), but still faster than the commercial non-aqueous Maxwell cell and the KI or KBr aqueous cells ($t_{½\cdot E_{max}}$ > 6 h), suggesting the MV^{2+}/MV^{+} is a contributor to the self-discharge reaction under these conditions.

To further improve the self-discharge (and cycle stability as discussed below) we explored different viologens. Heptyl viologen (HV) is known to form a strongly bonded solid on electrodes following its reduction in aqueous solution in the presence of Br^- or I^-, as evidenced by voltammetry and UV-VIS spectroscopy[63,65,75-78]. This adsorption/insolubility could be useful to impede internal shunting as long as the adsorption process is highly reversible. We first tested $HVBr_2$ (the chloride salt is not commercially available) in cells in an identical fashion as described above for the KBr/$MVCl_2$ cells. The results are similar with the exception that HV^{2+} has a more-positive reduction potential (E^o = -0.60 V vs. SCE) than MV^{2+} leading to a lower plateau voltage[64,65]. The galvanostatic charge-discharge curves (Figure 18d) also show evidence of higher ionic resistance due to the lower ion concentration used in this particular cell.

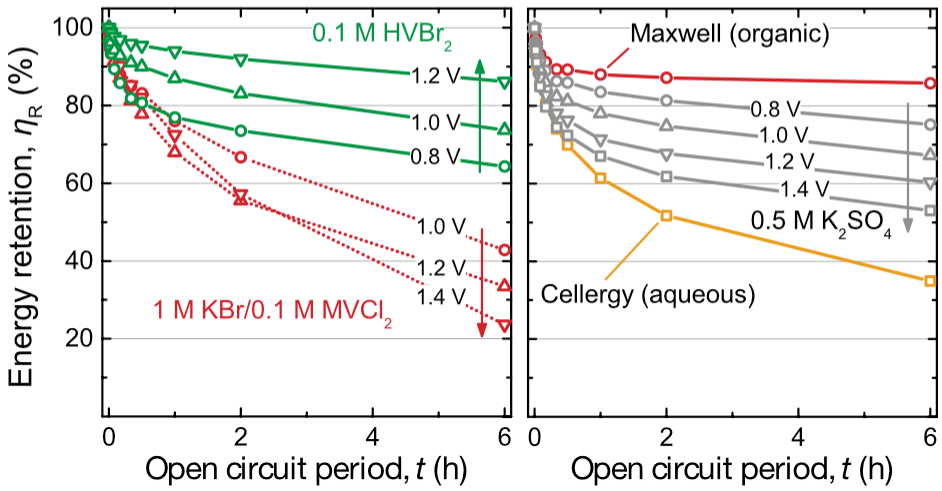

Figure 19. Self-discharge rates in viologen bromide dual redox ECs and control devices. (left) Energy retention η_R for the cells with redox-active electrolyte demonstrating substantial differences in the self-discharge rate between cells with HV and those with MV. (right) Energy retention η_R for the commercial and lab-built control EDLC cells tested with inert (non-redox-active) electrolyte.

The self-discharge rate of the $HVBr_2$ electrolyte, however, is substantially lower than for KBr /$MVCl_2$. Further, the self-discharge rate for $HVBr_2$ decreases as the charging voltage is increased, whereas it increases with voltage for $MVCl_2$/KBr. This data is consistent with the strong adsorption / precipitation of the HV^+ onto the activated carbon following charging. The weaker-adsorbing MV^+ apparently contributes substantially to self-discharge when large concentrations build up at high states of charge. The formation of the HV^+ films was confirmed by voltammetry and visual observation on a GC electrode in an

analytical half-cell. In addition, the thin $HV^{+}\bullet Br^{-}$ layer formed on the electrode might partially block the $Fe^{2+/3+}$ impurity transport, which has been reported to be a significant self-discharge path in aqueous EDLCs with inert electrolyte[55]. We also note that the adsorption/precipitation process was completely reversible with the $HVBr_2$ cell showing nearly 100% coulombic efficiency.

Impedance spectra were also measured for the 0.4 M KBr/0.1 M $HVBr_2$ cell at multiple potentials during charging/discharging (Figure 20). At lower operating potentials (0-0.6 V), the impedance spectra look like those of a traditional EDLC. With increasing operating potential above ~1 V, the faradic reaction with the Br^{-}/HV^{2+} becomes evident with the formation of a semi-circle associated with a small charge-transfer resistance. As the cell becomes completely charged at 1.2 V, the "knee" in the Nyquist plot (i.e. the right side of the first semicircle) moves to higher impedance indicating an increase in the charge transfer resistance relative to that at 1 or 1.1 V (due to consumption of available redox couple which adsorbs on the carbon surface after charging). The intercept with the real axis at high frequency also increased above 1 V, indicating higher series resistance associated with the absorbed redox couple. These impedance spectra are thus consistent with $HV^{+}\bullet Br^{-}$ precipitation on the carbon electrode.

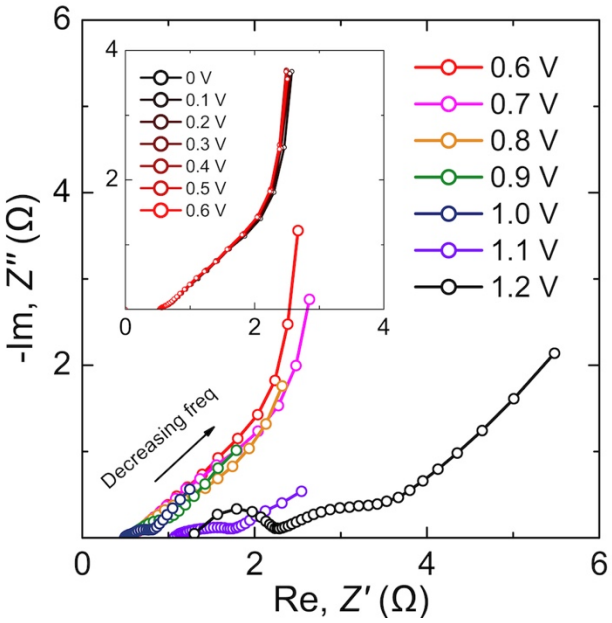

Figure 20. Nyquist impedance spectra of the 0.4 M KBr/0.1 M $HVBr_2$ cell. Spectra were measured at different applied potential in the frequency range of 1 MHz - 0.1 Hz.

The specific capacity and energy density of the redox-enhanced cells were evaluated based on galvanostatic cycling profiles at multiple potentials (Table 2). These data were collected in the Swagelok cell with excess electrolyte and therefore the performance metrics were normalized to the mass of the electrodes only and do not include the electrolyte (as is typically done). These results are further analyzed via an electrochemical model below. The dramatic effect of the added faradaic reaction is apparent; the 1 M KBr/0.1 M $MVCl_2$ cell at 1.4 V (driving faradaic + capacitive charging) stores over four times more charge than at 1.0 V (capacitive charging only), and has eight times larger energy density.

Table 2. Performance metrics obtained using three-electrode Swagelok cells.

Performance metric	1 M KBr/0.1 M $MVCl_2$			0.1 M $HVBr_2$		
	1.0 V	1.2 V	1.4 V	0.8 V	1.0 V	1.2 V
Specific capacity*, Q_{dis} (mAh g_{dry}^{-1})	9.2	18.0	37.9	4.0	9.0	32.1
Specific energy*, E_{dis} (Wh kg_{dry}^{-1})	5.2	14.5	38.7	1.3	4.8	26.4
Coulombic efficiency, η_C (0)	98.8%	99.0%	98.8%	99.9%	99.4%	99.9%
Energy efficiency, η_E (0)	99%	92%	92%	63%	80%	87%
Energy retention, η_R (6 h)	43%	33%	24%	64%	64%	86%

*Normalized to carbon electrode mass only

Performance quantification and optimization.

To increase energy density as well as minimize ionic resistance, higher redox-active electrolyte concentrations are needed. In addition, the practical specific energy and power must be evaluated based on both electrode and electrolyte mass, as they are both integral to the charge storage process[14]. $MVCl_2$ is highly soluble in water (> 2 M), where-as the $HVBr_2$ solubility is limited to < 0.2 M[79]. 1.0 M KBr/0.5 $MVCl_2$ and 0.4 M KBr/0.1 $HVBr_2$ were tested in a two-electrode "volume-limiting" cell, which accommodates a precise quantity of electrolyte. Thin polycarbonate film (9 μm) instead of Whatman paper (180 μm) was used as a separator to minimize excess electrolyte mass.

Performance parameters measured from galvanostatic cycling at 0.5 A g_{dry}^{-1} in volume-limiting cells are given in Table 3. The mass-based metrics are reported normalized to both the total active-material mass (electrodes + electrolytes) and, in parentheses, the electrode mass only (as is more-typically reported). The specific energies achieved for the KBr/$MVCl_2$ system are ~14 Wh kg_{wet}^{-1} or 50 Wh kg_{dry}^{-1} (16.8 Wh l^{-1}). The specific energies achieved for the

KBr/$HVBr_2$ system are ~11 Wh kg_{wet}^{-1} or 39 Wh kg_{dry}^{-1} (12.7 Wh l^{-1}). A highly concentrated MV^{2+} cell (1 M KBr/1 M $MVCl_2$) was also assembled to further increase the energy density, but the cell showed lower coulombic efficiency with $\eta_C(0) \sim 90$ %.

Table 3. Performance metrics for electrolyte-volume-limited cells.

Redox-active species	1 M KBr/0.5 M $MVCl_2$	0.4 M KBr/0.1 M $HVBr_2$
Electrode masses (mg) (including binder and conductive additive)	Cathode: 20.7 mg; Anode: 20.6 mg	Cathode: 10.0 mg; Anode: 10.0 mg
Electrolyte mass (mg)	110.1 mg	53.1 mg
$m_{electrode}/m_{electrolyte}$	1:2.69 ± 0.02	1:2.67 ± 0.07
Operating voltage (V)	1.4 V	1.2 V
Specific capacity*, Q_{dis}	13.3 mAh g_{wet}^{-1} (48.8 mAh g_{dry}^{-1})	12.1 mAh g_{wet}^{-1} (44.0 mAh g_{dry}^{-1})
Specific energy*, E_{dis}	13.9 Wh kg_{wet}^{-1} (51.0 Wh kg_{dry}^{-1})	10.8 Wh kg_{wet}^{-1} (39.3 Wh kg_{dry}^{-1})
Power density*, P_{dis}	142 W kg_{wet}^{-1} (521 W kg_{dry}^{-1})	122 W kg_{wet}^{-1} (447 W kg_{dry}^{-1})

*The performance data were normalized by both electrodes and electrolyte mass and, in parenthesis, by electrode mass only.

We also measured the relationship between energy and power in the redox EC devices and compared the performance to control aqueous K_2SO_4 devices and published reference data on a Ragone plot (Figure 21). The metrics estimated for both devices are promising as they fill a gap between high-power batteries and traditional EDLCs using simple, potentially low-cost, aqueous chemistry. Additional optimization and cell engineering (discussed below) would be expected to significantly further improve both power (reduced internal resistance) and specific energy.

To study degradation/fading, several cells were cycled at 0.5 and 2.5 A g_{dry}^{-1} (Figure 21 inset). The energy density of the KBr/$MVCl_2$ cell fades over the

course of several hundred cycles. This degradation is likely due to irreversible polymerization of MV^{+} in the aqueous electrolyte[64,65]. In comparison, the KBr/$HVBr_2$ cell shows no fading over 2,000 cycles (0.5 A g_{dry}^{-1}) and 20,000 cycles (2.5 A g_{dry}^{-1}) and its specific energy and power are largely limited by the low solubility of HV^{2+}. The Br/HV cell is practically promising due to slow self-discharge, cycle stability, and relatively high specific energy. There are hundreds of viologen derivatives that can be synthesized and it is likely that the appropriate combination of solubility and stability can be found[65,80,81]. This search is the central topic in Chapter 3 of this thesis.

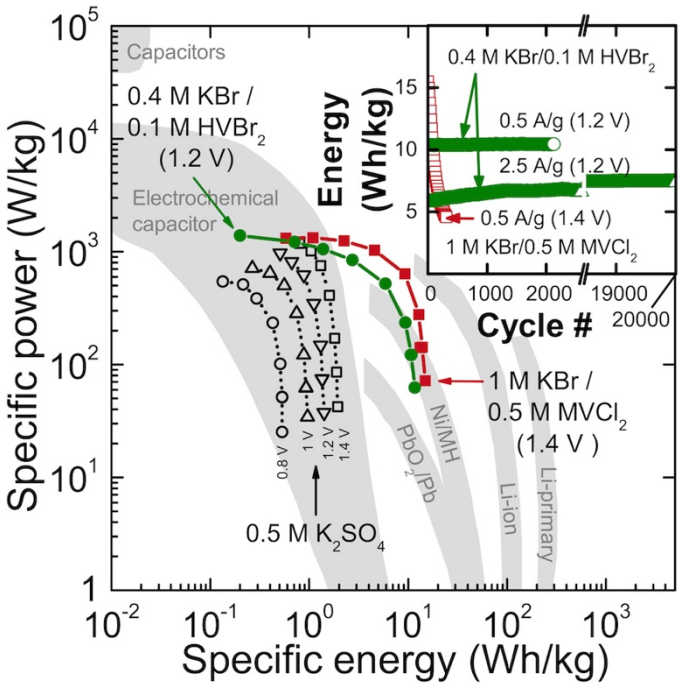

Figure 21. Ragone plot of redox EC performance from volume-limiting cells. Power-energy data for 1 M KBr/0.5 M $MVCl_2$ and 0.4 M KBr/0.1 M $HVBr_2$ electrolytes are shown in red and green, respectively, are overlaid on the performance of various electrochemical devices from Ref [2]. The redox EC performance metrics were normalized to the mass of both electrodes and electrolyte. The inset shows the long-term cycling performance of both cells obtained by galvanostatic cycling at 0.5 A g_{dry}^{-1} and 0.25 A g_{dry}^{-1} (every 10th cycle marked). Higher current was used to speed up the 20,000 cycle test and the HV/Br cell showed no degradation after 2,000 cycles at 0.5 A/g or after the 20,000 cycles at 2.5 A/g.

Comparison to related systems

There has been previous work aimed at enhancing conventional EDLCs using faradaic charging from soluble redox species. Previous cells often rely on a single

redox process at one electrode coupled with capacitive charging at the other, but this capacity mismatch lowers cell-level performance[26-28,30,82-84]. Balancing the capacity with different redox-species at each electrode has been demonstrated, but the potential difference between the couples has been small, leading to low specific energy when electrolyte weight is considered, and the cells have required an ion-selective Nafion separators[29]. The Br/viologen cell in this work was designed and optimized to achieve high energy density considering all *active* components (electrode and electrolyte) and simultaneously shows much better specific energy and self-discharge behavior than typical redox-enhanced EDLCs.

It is also useful to compare these redox EDLCs to flow batteries[60,85]. While both store charge through oxidation and reduction of soluble couples, the underlying design principles and applications are quite different. Flow batteries can use relatively expensive separators, such as ion-selective Nafion membranes, because the separator is a small component of the total flow-battery system cost (that includes pumps, automated controls, and large storage tanks with redox electrolyte). In EDLCs, the separators must be inexpensive because they are identical in size to the large-area activated carbon electrodes. The redox couples in the catholyte and anolyte must also be stable together, as it would be practically challenging in a redox EDLC to prevent crossover by sealing the catholyte from the anolyte compartments. Redox EDLCs require careful control and

optimization of the carbon porosity, as the carbon serves as the reservoir for the redox electrolyte and also contributes substantial capacitive energy storage capability (see below). Practically, flow batteries find application in grid-scale energy storage, where-as the redox EDLCs are more appealing for high power applications, for example in transportation.

Electrochemical model and predicted performance limits

To better understand the system and predict performance limits we developed an electrochemical model. To model the total energy storage of the system, the contributions from capacitive energy storage and faradaic energy storage are treated as separate processes occurring simultaneously. At every state of charge, the amount of capacitive and faradic charge passed to (or from) one electrode is a function of the electrode potential E_{el}. The capacitive contribution to the charge q_{cap} is

$$q_{\mathrm{cap}} = C_{\mathrm{sp}} \cdot m_{\mathrm{el}} \cdot \left| E_{\mathrm{el}} - E_{\mathrm{el,0}} \right| \tag{2.15}$$

where C_{sp} is the specific electrode capacitance, m_{el} is the electrode mass, and $E_{el,0}$ is the electrode potential in the discharged state – also known as the point of zero charge (PZC). The faradaic contribution is derived from the Nernst equation (i.e. assuming fast electrode kinetics).

$$E_{\mathrm{el}} = E^{\circ'} - \frac{RT}{nF} * \ln(Q) \tag{2.16}$$

E_{el} is the electrode potential, R is the gas constant, T is the temperature in Kelvin, n is the number of electrons involved in the electrochemical half-reaction, and $E^{0'}$ is the formal potential for the redox half-reaction. Q is the reaction quotient for the general redox half-reaction, $x\mathrm{X} + n\mathrm{e}^- \rightarrow y\mathrm{Y}$, and is a function of the total charge transferred through redox reactions q_{red}, the initial redox-species concentration, and the electrolyte volume:

$$Q = \frac{[\mathrm{Y}]^{\mathrm{y}}}{[\mathrm{X}]^{\mathrm{x}}} = \frac{\left(\frac{\frac{q_{\mathrm{red}}}{F} * \frac{\mathrm{y}}{n}}{V_{\mathrm{electrolyte}}}\right)^{\mathrm{y}}}{\left(\frac{[\mathrm{X}_0] * V_{\mathrm{electrolyte}} - \frac{q_{\mathrm{red}}}{F} * \frac{\mathrm{x}}{n}}{V_{\mathrm{electrolyte}}}\right)^{\mathrm{x}}} \tag{2.17}$$

Where $[\mathrm{X}_0]$ is the initial concentration of the anolyte or catholyte. It should be noted that no activity coefficients are included here. These are incorporated into $E^{0'}$, the experimentally determined formal potential. In a more advanced treatment, $E^{0'}$ would be dependent on the SOC instead of being treated as a constant, as the ionic strength of the electrolyte changes with time. Combining Equation 2.16 and 2.17 and solving gives q_{red} as a function of E_{el}.

The total faradaic charge passed through the electrode q_{far} at a potential E_{el} is:

$$q_{\mathrm{far}} = q_{\mathrm{red}}[\mathrm{E}_{\mathrm{el}}] - q_{\mathrm{red}}\left[E_{\mathrm{el},0}\right] \tag{2.18}$$

The total charge passed for an electrode is the sum of faradaic q_{far} and capacitive q_{cap} components.

$$q_{\mathrm{el}} = q_{\mathrm{far}} + q_{\mathrm{cap}} \tag{2.19}$$

The complete cell operates under the constraints that the total charge passed q_{cell} is equal to the charged passed at the positive q_{p} and negative q_{n} electrodes.

$$q_{\mathrm{cell}} = q_{\mathrm{p}} = q_{\mathrm{n}}\ ,\ V_{\mathrm{cell}} = E_{\mathrm{p}} - E_{\mathrm{n}} \tag{2.20}$$

The above set of equations are solved numerically using the Mathematica code shown in Appendix 1 over the range of $V_{\mathrm{cell,min}}$ to $V_{\mathrm{cell,\,max}}$ to generate charge-discharge profiles for the redox ECs, which are overlaid on experimental data in Figure 22. With this model, it is also possible to find the total energy and capacity of the device, the charge/discharge profiles of the anode and cathode, and even the degree of conversion of each redox couple.

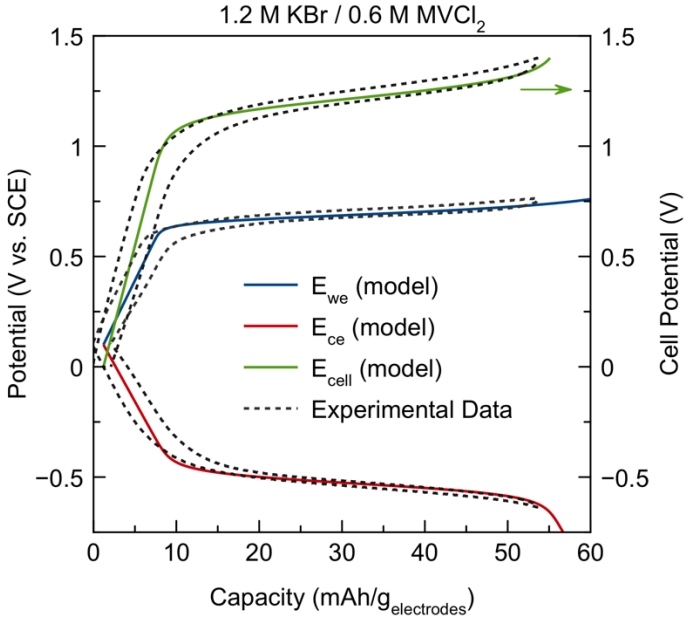

Figure 22. Model calculations compared to experimental data for galvanostatic charge/discharge profiles. The experimental data (dashed lines) was for a 1 M KBr/0.5 M $MVCl_2$ (nominal) cell cycled to 1.4 V at 0.5 A g_{dry}^{-1}. The experimental charge and discharge curves are overlaid to illustrate the hysteresis and coulombic efficiency of the real cell. The model parameters that best fit the experimental data are: $C_{sp,+}$ = 95 F g^{-1}, $C_{sp,-}$ = 105 F g^{-1}, $\boldsymbol{E^{\circ\prime}_{Br_3^-/Br^-}}$ = 0.70 V vs. SCE, $\boldsymbol{E^{\circ\prime}_{MV^{2+}/MV^{+}}}$ = -0.53 V vs. SCE, [KBr] = 1.2 M, and [$MVCl_2$] = 0.6 M. All other values, such as electrode mass and dimensions, electrolyte density, free volume available to electrolyte, and $E_{el,0}$ were measured experimentally or calculated directly from experimental measurements.

Comparing the model to experimental data provides insight into the device operation. The formal potential of $MV^{2+}/MV^{+\bullet}$ (in the activated carbon) is found to be -0.53 V vs. SCE, less negative than the standard potential of -0.69 V vs. SCE[64,65]. From the electrochromics literature it is known that, for certain electrode/viologen/anion combinations, viologen dications are reversibly reduced to form an adsorbed $[V^{+\bullet}][X^-]$ layer on the electrode at potentials less negative than the standard potential[63,64,74,86,87]. This precipitation of HV^+ with Br^- is consistent with the measured impedance spectra that show increased series resistance after HV^+ adsorption (Figure 20). A similar mechanism occurs at the positive electrode, where the formal potential for Br^-/Br_3^- from the model is 0.70 V vs. SCE, less positive than the standard potential of 0.81 V vs. SCE[54]. The formal potentials obtained from the model thus indicate strong adsorption at both electrodes, consistent with the separate self-discharge and adsorption measurements described earlier.

Because the electrolyte volume and total faradaic charge passed through the cell are known, it is also possible to calculate the initial concentration of redox-active species. Electrodes soaked in 1 M KBr / 0.5 M $MVCl_2$ before cell assembly end up with an effective MV^{2+} concentration close to 0.6 M and electrodes soaked in 1 M KBr/ 0.1 M $MVCl_2$ with a MV^{2+} concentration close to 0.4 M. Submerging the electrodes in excess electrolyte during fabrication apparently leads to

concentration of the viologen in the activated carbon due to physical adsorption, an effect observed by others[71]. Additionally, the vacuum steps during electrolyte filling cause some electrolyte evaporation, increasing the concentration of all species by 18 ± 8 %.

The agreement between experiment and simulation indicate the redox EC operates as outlined in the above electrochemical model. The simulation thus enables predication of performance limits. By adjusting variables including electrode density, which determines the free volume available for redox-active electrolyte, and the concentration of redox-active species, we calculated the performance of different cell configurations (Figure 23). The simulations suggest that by finding a viologen with the stability of heptyl viologen and the high solubility of methyl viologen, a specific energy 2-3 times higher than what is reported here is experimentally possible.

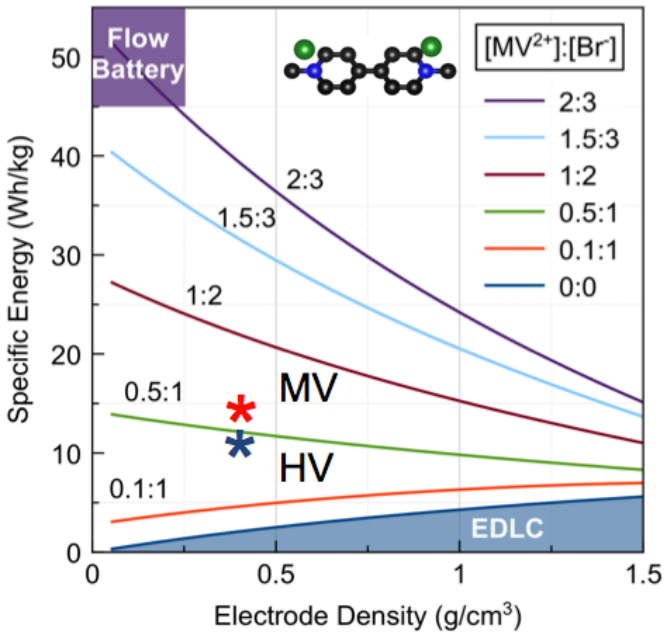

Figure 23. Specific energy predictions using the electrochemical model for the KBr/$MVCl_2$ system. The numbers indicate different concentrations (in mol/L) of redox-active species in the electrolyte for a range of activated carbon electrode densities. The specific energy is normalized to the mass of electrodes and electrolyte and the specific capacitance of each electrode is modeled as 100 F/g. For very low electrode density, the performance is determined only by the redox-active electrolyte (somewhat akin to a "static" flow battery). Without redox-active species the pure EDLC behavior is recovered, as indicated by the blue region at the bottom of the plot. The experimental data for the 0.5 M $MVCl_2$/1 M KBr (nominal) cell with a density of 0.42 g/cm^3 and capacitance of 108 F/g is indicated by the red star.

Conclusions

This chapter introduced redox ECs with new viologen couples and high specific energies of 14 Wh kg_{wet}^{-1} (1 M KBr/0.5 $MVCl_2$) and 10 Wh kg_{wet}^{-1} (0.4 M KBr/0.1 $HVBr_2$) when accounting for the complete electrolyte and electrode mass. Because redox-active ions compose the electrolyte, the approach converts the "dead" weight of a conventional EDLC electrolyte into an active element for charge storage. The cells use neutral-pH electrolyte, can be assembled without a dry-room or glove box, and have slow self-discharge similar to commercial non-aqueous cells – without the use of an ion-selective membrane separator that is needed in other systems. By studying related redox electrolytes, we showed that the slow self-discharge is due to adsorption of the charged form of the redox couples (e.g. Br^{3-} and MV^{+}/HV^{+}) onto the activated carbon and that simple electrostatic effects were unable to prevent self-discharge. Our electrochemical model quantitatively describes the measurements and demonstrates that, with targeted design of new couples, the energy density could be further improved by a factor of three to near 50 Wh kg^{-1}. These systems may thus find use in applications requiring energy and power performance in-between that of batteries and traditional electrochemical capacitors.

References

1 Conway, B. E. *Electrochemical Supercapacitors: Scientific Fundamentals and Technological Applications*. (Springer US, 1999).

2 Simon, P. & Gogotsi, Y. Materials for electrochemical capacitors. *Nat. Mater.* **7**, 845-854 (2008).

3 Beguin, F. & Frackowiak, E. *Carbons for Electrochemical Energy Storage and Conversion Systems*. (Taylor & Francis, 2009).

4 Lu, M., Beguin, F. & Frackowiak, E. *Supercapacitors: Materials, Systems and Applications*. (Wiley, 2013).

5 Miller, J. R. & Simon, P. Electrochemical capacitors for energy management. *Science* **321**, 651-652 (2008).

6 Miller, J. R. & Burke, A. F. Electrochemical capacitors: challenges and opportunities for real-world applications. *Electrochem. Soc. Interf.* **17**, 53 (2008).

7 Miller, J. R., Outlaw, R. A. & Holloway, B. C. Graphene double-layer capacitor with ac line-filtering performance. *Science* **329**, 1637-1639 (2010).

8 Winter, M. & Brodd, R. J. What are batteries, fuel cells, and supercapacitors? *Chem. Rev.* **104**, 4245-4270 (2004).

9 Zhang, L. L. & Zhao, X. S. Carbon-based materials as supercapacitor electrodes. *Chem. Soc. Rev.* **38**, 2520-2531 (2009).

10 van Schalkwijk, W. & Scrosati, B. *Advances in Lithium-Ion Batteries*. (Springer, 2002).

11 Huggins, R. *Advanced Batteries: Materials Science Aspects*. (Springer, 2008).

12 Reddy, T. *Linden's Handbook of Batteries*. 4th edn, (McGraw-Hill Education, 2010).

13 Weinstein, L. & Dash, R. Supercapacitor carbons. *Mater. Today* **16**, 356-357, (2013).

14 Gogotsi, Y. & Simon, P. True performance metrics in electrochemical energy storage. *Science* **334**, 917-918 (2011).

15 Merrill, M. D. *et al*. Optimizing supercapacitor electrode density: achieving the energy of organic electrolytes with the power of aqueous electrolytes. *RSC Adv*. **4**, 42942-42946 (2014).

16 Amatucci, G. G., Badway, F., Du Pasquier, A. & Zheng, T. An asymmetric hybrid nonaqueous energy storage cell. *J. Electrochem. Soc*. **148**, A930-A939 (2001).

17 Long, J. W. *et al*. Asymmetric electrochemical capacitors—Stretching the limits of aqueous electrolytes. *MRS Bull*. **36**, 513-522 (2011).

18 Augustyn, V. *et al*. High-rate electrochemical energy storage through Li+ intercalation pseudocapacitance. *Nat. Mater*. **12**, 518-522 (2013).

19 Yan, J., Wang, Q., Wei, T. & Fan, Z. Recent advances in design and fabrication of electrochemical supercapacitors with high energy densities. *Adv. Energy Mater*. **4**, 1300816 (2014).

20 Vonlanthen, D., Lazarev, P., See, K. A., Wudl, F. & Heeger, A. J. A stable polyaniline-benzoquinone-hydroquinone supercapacitor. *Adv. Mater*. **26**, 5095-5100 (2014).

21 Tomai, T., Mitani, S., Komatsu, D., Kawaguchi, Y. & Honma, I. Metal-free aqueous redox capacitor via proton rocking-chair system in an organic-based couple. *Sci. Rep*. **4** (2014).

22 Yan, J. *et al*. Fast and reversible surface redox reaction of graphene–MnO2 composites as supercapacitor electrodes. *Carbon* **48**, 3825-3833 (2010).

23 Mai, L.-Q. *et al*. Hierarchical MnMoO4/CoMoO4 heterostructured nanowires with enhanced supercapacitor performance. *Nat. Commun*. **2**, 381 (2011).

24 Lota, G. & Frackowiak, E. Striking capacitance of carbon/iodide interface. *Electrochem. Commun*. **11**, 87-90 (2009).

25 Lota, G., Fic, K. & Frackowiak, E. Alkali metal iodide/carbon interface as a source of pseudocapacitance. *Electrochem. Commun*. **13**, 38-41 (2011).

26 Roldán, S., Blanco, C., Granda, M., Menéndez, R. & Santamaría, R. Towards a further generation of high-energy carbon-based capacitors by using redox-active electrolytes. *Angew. Chem. Int. Ed.* **50**, 1699-1701 (2011).

27 Roldán, S. *et al*. Redox-active electrolyte for carbon nanotube-based electric double layer capacitors. *Electrochim. Acta* **56**, 3401-3405 (2011).

28 Roldán, S., Granda, M., Menéndez, R., Santamaría, R. & Blanco, C. Mechanisms of energy storage in carbon-based supercapacitors modified with a quinoid redox-active electrolyte. *J. Phys. Chem. C* **115**, 17606-17611 (2011).

29 Frackowiak, E., Fic, K., Meller, M. & Lota, G. Electrochemistry serving people and nature: high-energy ecocapacitors based on redox-active electrolytes. *ChemSusChem* **5**, 1181-1185 (2012).

30 Senthilkumar, S. T., Selvan, R. K. & Melo, J. S. Redox additive/active electrolytes: a novel approach to enhance the performance of supercapacitors. *J. Mater. Chem. A* **1**, 12386-12394 (2013).

31 Senthilkumar, S. T., Selvan, R. K., Lee, Y. S. & Melo, J. S. Electric double layer capacitor and its improved specific capacitance using redox additive electrolyte. *J. Mater. Chem. A* **1**, 1086-1095 (2013).

32 Chen, L., Bai, H., Huang, Z. & Li, L. Mechanism investigation and suppression of self-discharge in active electrolyte enhanced supercapacitors. *Energy Environ. Sci.* **7**, 1750-1759 (2014).

33 Mai, L.-Q. *et al*. Synergistic interaction between redox-active electrolyte and binder-free functionalized carbon for ultrahigh supercapacitor performance. *Nat. Commun.* **4** (2013).

34 Wang, B. *et al*. A hybrid redox-supercapacitor system with anionic catholyte and cationic anolyte. *J. Electrochem. Soc.* **161**, A1090-A1093 (2014).

35 Liu, C., Yu, Z., Neff, D., Zhamu, A. & Jang, B. Z. Graphene-based supercapacitor with an ultrahigh energy density. *Nano Lett.* **10**, 4863-4868 (2010).

36 Zhang, L. *et al*. Porous 3D graphene-based bulk materials with exceptional high surface area and excellent conductivity for supercapacitors. *Sci. Rep.* **3** (2013).

37 Zhang, L. *et al*. High-performance supercapacitor electrode materials prepared from various pollens. *Small* **9**, 1342-1347 (2013).

38 Gao, Q., Demarconnay, L., Raymundo-Pinero, E. & Beguin, F. Exploring the large voltage range of carbon/carbon supercapacitors in aqueous lithium sulfate electrolyte. *Energy Environ. Sci.* **5**, 9611-9617 (2012).

39 Hameed, B. H., Din, A. T. M. & Ahmad, A. L. Adsorption of methylene blue onto bamboo-based activated carbon: Kinetics and equilibrium studies. *Journal of Hazardous Materials* **141**, 819-825 (2007).

40 Yang, X., Cheng, C., Wang, Y., Qiu, L. & Li, D. Liquid-Mediated Dense Integration of Graphene Materials for Compact Capacitive Energy Storage. *Science* **341**, 534-537 (2013).

41 Maciá-Agulló, J. A., Moore, B. C., Cazorla-Amorós, D. & Linares-Solano, A. Activation of coal tar pitch carbon fibres: Physical activation vs. chemical activation. *Carbon* **42**, 1367-1370 (2004).

42 Sapp, S. A., Elliott, C. M., Contado, C., Caramori, S. & Bignozzi, C. A. Substituted polypyridine complexes of cobalt(II/III) as efficient electron-transfer mediators in dye-sensitized solar cells. *J. Am. Chem. Soc.* **124**, 11215-11222, doi:10.1021/ja027355y (2002).

43 Zhu, Y. *et al*. Carbon-based supercapacitors produced by activation of graphene. *Science* **332**, 1537-1541, doi:10.1126/science.1200770 (2011).

44 Xu, Y. *et al*. Holey graphene frameworks for highly efficient capacitive energy storage. *Nat. Commun.* **5** (2014).

45 Yu, D. *et al*. Scalable synthesis of hierarchically structured carbon nanotube-graphene fibres for capacitive energy storage. *Nat. Nanotechnol.* **9**, 555-562 (2014).

46 Purewal, J. J., Kabbour, H., Vajo, J. J., Ahn, C. C. & Fultz, B. Pore size distribution and supercritical hydrogen adsorption in activated carbon fibers. *Nanotechnology* **20**, 204012 (2009).

47 Zhang, J. *et al*. Sustainable, heat-resistant and flame-retardant cellulose-based composite separator for high-performance lithium ion battery. *Sci. Rep*. **4** (2014).

48 Donnet, J. B. *Carbon Black: Science and Technology, Second Edition*. (Taylor & Francis, 1993).

49 Daniel, C. & Besenhard, J. O. *Handbook of Battery Materials*. (Wiley, 2012).

50 Monk, P. M. S., Hodgkinson, N. M. & Ramzan, S. A. Spin pairing ('dimerisation') of the viologen radical cation: kinetics and equilibria. *Dyes Pigm*. **43**, 207-217 (1999).

51 Wang, T. X., Kelley, M. D., Cooper, J. N., Beckwith, R. C. & Margerum, D. W. Equilibrium, Kinetic, and UV-Spectral Characteristics of Aqueous Bromine Chloride, Bromine, and Chlorine Species. *Inorg. Chem*. **33**, 5872-5878 (1994).

52 Hiegel, G. A., Abdala, M. H., Burke, S. V. & Beard, D. P. Methods for preparing aqueous solutions of chlorine and bromine for halogen displacement reactions. *J. Chem. Educ*. **64**, 156 (1987).

53 Goldstein, S. W. The iodide-iodine solubility relation. *J. Am. Pharm. Assoc*. **41**, 333-335 (1952).

54 Bard, A. J., Parsons, R. & Jordan, J. *Standard Potentials in Aqueous Solution*. (Taylor & Francis, 1985).

55 Andreas, H. A., Lussier, K. & Oickle, A. M. Effect of Fe-contamination on rate of self-discharge in carbon-based aqueous electrochemical capacitors. *J. Power Sources* **187**, 275-283 (2009).

56 Zhang, Q., Rong, J., Ma, D. & Wei, B. The governing self-discharge processes in activated carbon fabric-based supercapacitors with different organic electrolytes. *Energy Environ. Sci*. **4**, 2152-2159 (2011).

57 Lewandowski, A., Jakobczyk, P., Galinski, M. & Biegun, M. Self-discharge of electrochemical double layer capacitors. *Phys. Chem. Chem. Phys*. **15**, 8692-8699, (2013).

58 Faita, G., Fiori, G. & Mussini, T. Electrochemical processes of the bromine/bromide system. *Electrochim. Acta* **13**, 1765-1772 (1968).

59 Mastragostino, M. & Gramellini, C. Kinetic study of the electrochemical processes of the bromine/bromine aqueous system on vitreous carbon electrodes. *Electrochim. Acta* **30**, 373-380 (1985).

60 Weber, A. *et al*. Redox flow batteries: a review. *J. Appl. Electrochem.* **41**, 1137-1164 (2011).

61 Michaelis, L. & Hill, E. S. The viologen indicators. *J. Gen. Physiol.* **16**, 859-873 (1933).

62 Elofson, R. M. & Edsberg, R. L. Polarographic behavior of the viologen indicators. *Can. J. Chem.* **35**, 646-650 (1957).

63 van Dam, H. T. & Ponjeé, J. J. Electrochemically generated colored films of insoluble viologen radical compounds. *J. Electrochem. Soc.* **121**, 1555-1558 (1974).

64 Bird, C. L. & Kuhn, A. T. Electrochemistry of the viologens. *Chem. Soc. Rev.* **10**, 49-82 (1981).

65 Monk, P. M. S. *The Viologens: Physicochemical Properties, Synthesis, and Applications of the Salts of 4,4'-Bipyridine*. (Wiley, 1998).

66 Yang, H.-H. & McCreery, R. L. Effects of surface monolayers on the electron-transfer kinetics and adsorption of methyl viologen and phenothiazine derivatives on glassy carbon electrodes. *Anal. Chem.* **71**, 4081-4087 (1999).

67 Monk, P., Mortimer, R. & Rosseinsky, D. *Electrochromism and Electrochromic Devices*. (Cambridge University Press, 2007).

68 Ito, M. & Kuwana, T. Spectroelectrochemical study of indirect reduction of triphosphopyridine nucleotide: I. Methyl viologen, ferredoxin-TPN-reductase and TPN. *J. Electroanal. Chem. Interfac.* **32**, 415-425, (1971).

69 Xiao, L., Wildgoose, G. G. & Compton, R. G. Investigating the voltammetric reduction of methylviologen at gold and carbon based electrode materials. Evidence for a surface bound adsorption mechanism

leading to electrode 'protection' using multi-walled carbon nanotubes. *New J. Chem.* **32**, 1628-1633, (2008).

70 Deloitte Access Economics. Vol. 2013 (Syngenta Australia Pty Ltd, 2013).

71 Nakamura, T. *et al.* Adsorption removal of paraquat and diquat onto activated carbon at different adsorption temperature. *Toxicol. Environ. Chem.* **70**, 275-280, (1999).

72 Bard, A. J. & Faulkner, L. R. *Electrochemical Methods: Fundamentals and Applications, 2nd Edition.* (Wiley Global Education, 2000).

73 Datta, M., Jansson, R. E. & Freeman, J. J. In situ resonance raman spectroscopic characterization of electrogenerated methyl viologen radical cation on carbon electrode. *Appl. Spectrosc.* **40**, 251-258 (1986).

74 Lezna, R. O. & Centeno, S. A. Spectroelectrochemistry of methyl viologen/iodide solutions at mercury film electrodes. *Langmuir* **12**, 4905-4908 (1996).

75 Bewick, A., Lowe, A. C. & Wederell, C. W. Recrystallisation process in viologen-based electrochromic deposits: voltammetry coupled with rapid time-resolved spectroscopy. *Electrochim. Acta* **28**, 1899-1902 (1983).

76 Compton, R. G., Waller, A. M., Monk, P. M. S. & Rosseinsky, D. R. Electron paramagnetic resonance spectroscopy of electrodeposited species from solutions of 1,1'-bis-(p-cyanophenyl)-4,4'-bipyridilium (cyanophenyl paraquat, CPQ). *J. Chem. Soc., Faraday Trans.* **86**, 2583-2586 (1990).

77 Rosseinsky, D. R., Monk, P. M. S. & Hann, R. A. Anion-dependent aqueous electrodeposition of electrochromic 1,1'-bis-cyanophenyl-4,4'-bipyridilium (cyanophenylparaquat) radical cation by cyclic voltammetry and spectroelectrochemical studies. *Electrochim. Acta* **35**, 1113-1123 (1990).

78 Rosseinsky, D. R. & Monk, P. M. S. Electrochromic cyanophenylparaquat (CPQ: 1,1'-bis-cyanophenyl-4,4'-bipyridilium) studied voltammetrically, spectroelectrochemically and by ESR. *Sol. Energy Mater. Sol. Cells* **25**, 201-210 (1992).

79 Milne, G. W. A. *Gardner's Commercially Important Chemicals: Synonyms, Trade Names, and Properties*. (Wiley, 2005).

80 Wardman, P. Reduction potentials of one-electron couples involving free radicals in aqueous solution. *J. Phys. Chem. Ref. Data* **18**, 1637-1755 (1989).

81 Lieder, M. & Schlapfer, C. W. Synthesis and electrochemical properties of new viologen polymers. *J. Appl. Electrochem.* **27**, 235-239 (1997).

82 Roldán, S., Granda, M., Menéndez, R., Santamaría, R. & Blanco, C. Supercapacitor modified with methylene blue as redox active electrolyte. *Electrochim. Acta* **83**, 241-246 (2012).

83 Senthilkumar, S. T., Selvan, R. K., Ponpandian, N., Melo, J. S. & Lee, Y. S. Improved performance of electric double layer capacitor using redox additive (VO^{2+}/VO_2^{+}) aqueous electrolyte. *J. Mater. Chem. A* **1**, 7913-7919 (2013).

84 Park, J., Kim, B., Yoo, Y.-E., Chung, H. & Kim, W. Energy-density enhancement of carbon-nanotube-based supercapacitors with redox couple in organic electrolyte. *ACS Appl. Mater. Interfaces* **6**, 19499-19503 (2014).

85 Huskinson, B. *et al*. A metal-free organic-inorganic aqueous flow battery. *Nature* **505**, 195-198 (2014).

86 Heyrovský, M. & Novotný, L. Interfacial interactions and the heterogeneous one-electron reduction of methyl viologen. *Collect. Czech. Chem. Commun.* **52**, 1097-1114 (1987).

87 Sagara, T., Fujihara, Y. & Tada, T. Molecular structure dependence of the phase transition spike response of viologens at an HOPG electrode using bisviologen and carboxylated viologen. *J. Electrochem. Soc.* **152**, E239-E246 (2005).

Chapter 3

Efficient charge storage in dual-redox electrochemical capacitors through reversible solid complexation

---

The contents of this chapter have substantially appeared in the following reference: B. Evanko, S. J. Yoo, S.-E. Chun, X. Wang, X. Ji, S. W. Boettcher, and G. D. Stucky, "Efficient Charge Storage in Dual-Redox Electrochemical Capacitors through Reversible Counterion-Induced Solid Complexation," J. Am. Chem. Soc. 138, 9373, 2016.

Introduction

Commercial electric double layer capacitors (EDLCs) provide specific power as high as 20 kW/kg for millions of cycles, but have a low energy density compared to other energy storage systems of ca. 6 Wh/kg (8 Wh/L). [1,2] To increase the energy density of EDLCs, research has focused on developing pseudocapacitive systems that add faradaic energy storage. [3–10] One recent approach is to replace the traditional solid-state pseudocapacitive materials with soluble redox couples. [11–16] Such redox-enhanced electrochemical capacitors (redox ECs) provide high power density and increased specific energy without the need for nanostructured metal oxide/nitride electrodes and allow for good performance in aqueous (aqueous) electrolytes. However, they are challenged by cycle stability and internal self-discharge due to cross-diffusion of redox-active electrolytes. [17,18] For efficient redox ECs, the redox couples used should exhibit fast and reversible electron transfer and be retained inside the porous electrodes in their charged states (i.e. oxidized catholyte or reduced anolyte) to eliminate self-discharge. [19]

Heptyl viologen/bromide (HV/Br), discussed in detail in Chapter 2, is a promising dual-redox-active electrolyte for aqueous redox ECs (Figure 24a). [20] The system maintains cycling stability over 20,000 cycles and has a slow self-discharge rate without using a costly ion-selective membrane as a separator.

However, due to the low solubility of HV (<0.2 M), the specific energy is limited to ca. 30 Wh/kg_{dry}, i.e. normalized to the dry mass of both the positive electrode (cathode) and negative electrode (anode). Substituting HV with highly soluble methyl viologen (MV) increases specific energy to 50 Wh/kg_{dry}, but energy density fades rapidly over the course of several hundred cycles (Figure 24b) and the self-discharge rate increases.[12] One critical challenge is to attain high energy density, stable cycling, and minimal self-discharge in a single device.

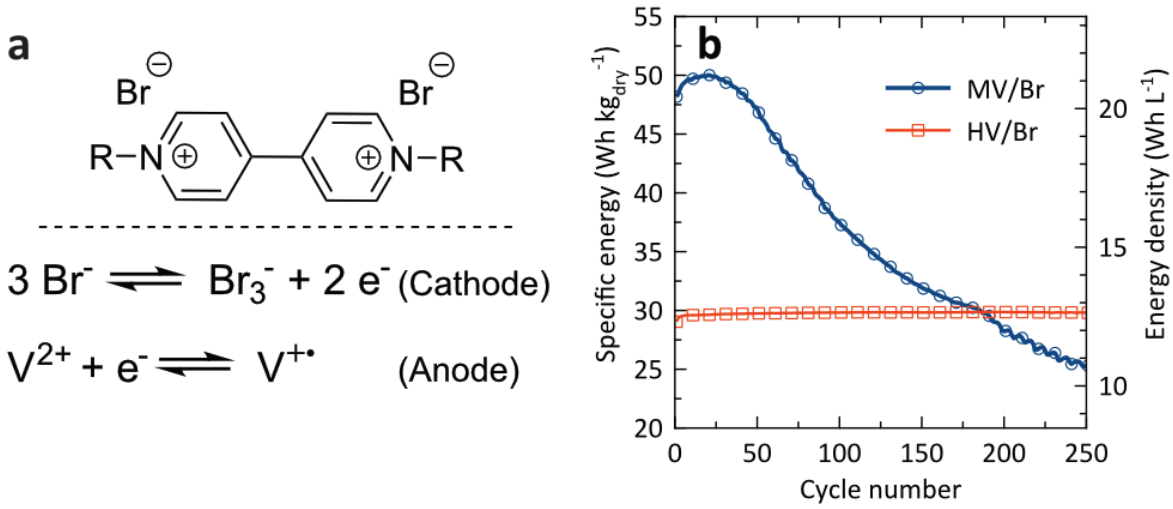

Figure 24. Viologen/bromide redox ECs. (a) Viologen dibromide and faradaic energy storage reactions of bromide and viologen (denoted as V). (b) Cycling stability of redox ECs. Cells are charged to 1.4 V (0.5 M $MVCl_2$/1 M KBr) and 1.2 V (0.1 M $HVBr_2$/0.4 M KBr), at 0.5 A/g_{dry} in custom Swagelok cells.

In this chapter, we investigated viologen/bromide dual-redox ECs to elucidate the mechanisms underlying the observed cycling behavior. We find that the stability of the HV/Br system is due to the effective retention of charged redox products through reversible electrodeposition/precipitation at the electrode surface. Based on fundamental understanding of the electrolyte chemistry, we rationally design an electrolyte system that incorporates pentyl viologen (PV) as anolyte and bromide as catholyte. This system combines the cycling stability of HV with the solubility of MV to produce a high specific energy of 48.5 Wh/kg_{dry} (20 Wh/L) at 0.5 A/g_{dry} (average specific discharge power of 0.44 kW/kg_{dry}) and maintains stability with 97 % energy retention over 10,000 cycles at 2.5 A/g (2.0 kW/kg_{dry}). In addition, we show that the redox EC allows completely symmetric operation without failure or instability when operated with reversed polarity.

Materials and Methods

Materials. All reagents and starting materials were obtained commercially and used as received without any further purification:

n-bromobutane, *n*-bromopentane, *n*-bromohexane, sodium bromide (NaBr), sodium dithionite ($Na_2S_2O_4$), and polytetrafluoroethylene (60 weight % aqueous dispersion) were purchased from Sigma-Aldrich. Acetonitrile, heptyl viologen, and 4,4'-bipyridine were purchased from TCI America. Methyl viologen and hydrobromic acid (HBr) were purchased from Acros Organics. Sodium bromate ($NaBrO_3$) was purchased from J. T. Baker Chemical Co., isopropanol was purchased from VWR, and potassium bromide (KBr) was purchased from EMD Chemicals Inc. Water was from a Milli-Q Simplicity™ 185 system with resistivity ≥ 18.2 MΩ•cm (if not specified, all solutions in the following paragraphs refer to aqueous solutions.)

Activated carbon. Activated carbon was prepared by physical CO_2 activation of high-purity coal tar pitch-based carbon fibers (Donacarbo S-241, Osaka Gas Co., 13 μm OD x 130 μm long).[21] Carbon fibers (1 g) were heated in a tube furnace at 890 ºC under flowing CO_2 (100 SCCM) for 22.5 h. The resulting activated carbon had a 26.8 % yield (73.2 % burn-off), a Brunauer-Emmett-Teller (BET) specific surface area of 2,470 m^2g^{-1}, and a methylene-blue-accessible specific surface area of 1,620 m^2g^{-1}. Additional details, including elemental

composition and pore size distribution are reported in the literature and in the Materials and Methods section of Chapter 2.[20]

Viologen bromide salts. Symmetric viologens were synthesized by N-alkylation of 4,4'-bipyridine with various alkyl halides under microwave irradiation conditions.

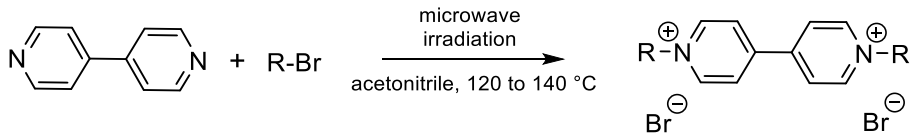

For the synthesis of pentyl viologen (1,1'-dipentyl-4,4'-bipyridinium dibromide), 700 mg of 4,4'-bipyridine (1 equiv) was dissolved in 7.5 mL of acetonitrile, and 5 mL of excess 1-bromopentane (ca. 10 equiv) was added in a 20 mL microwave reactor vial. The reaction was carried out in three stages in a Biotage Initiator Classic Microwave Synthesizer as follows: 2 min. at 120 ºC, 20 min. at 135ºC, and 10 min. at 140 ºC, with stirring at 600 rpm. Reaction progress was monitored by TLC (10 % water/20 % methanol/70% acetic acid as an eluent) until the reaction was terminated when the starting 4,4'-bipyridine was consumed and the mono-substituted byproduct disappeared. After the reaction, the reaction mixture was filtered, washed with acetonitrile several times, and dried for 2 days under vacuum at room temperature. Pentyl viologen (1.5 g; 3.3 mmol; 73 % yield), was obtained as a yellow crystalline solid whose spectral properties matched those reported in the literature.[22] The same procedure was used for butyl

viologen (1,1'-dibutyl-4,4'-bipyridinium dibromide) and hexyl viologen (1,1'-dihexyl-4,4'-bipyridinium dibromide) with slight modifications: For butyl viologen, 700 mg of 4,4'-bipyridine was dissolved in 5 mL acetonitrile and 5 mL 1-bromobutane. For hexyl viologen, 700 mg of 4,4'-bipyridine was dissolved in 5 mL acetonitrile and 7.5 mL 1-bromohexane. All spectroscopic data were consistent with those reported for these compounds.[3]

Tribromide (Br_3^-) solution. Bromine and Br_3^- were generated using the following chemical reactions: [23]

$$NaBrO_3 + 5\ Br^- + 6\ H^+ \rightarrow 3\ Br_{2(aq)} + 3\ H_2O$$

$$Br_{2(aq)} + Br^- \rightleftharpoons Br_3^- \qquad (K_{eq} = 16.1\ M^{-1})$$

To produce a 10 mL stock solution of 120 mM Br_3^-, 3 mL of 2 M HBr, 3 mL of 2 M KBr, and 4 mL of 0.1 M $NaBrO_3$ were combined in a glass vial and stirred for 10 minutes. The resulting Br_3^- solution is dark orange.

Fabrication of redox-enhanced electrochemical capacitors (redox ECs)

Carbon electrodes. 0.056 g of polytetrafluoroethylene (PTFE) binder (60 weight % aqueous dispersion), 0.033 g of acetylene black conductive additive (Vulcan® XC72R), and 4 mL isopropanol were combined and mixed in a 10 mL mixing cup for 2 minutes on a vortex mixer followed by 5 minutes on a FlackTek high shear mixer at 2000 rpm. Next, 600 mg of activated carbon was added to the

resulting slurry and the mixing steps were repeated. The resulting material was rolled with a PTFE rolling pin and folded over itself 5-10 times until a single freestanding film was formed. This film was dried overnight at 160 ºC in air, ground into a powder through mesh sieve, and then dried again under high vacuum at room temperature. The resulting electrode material contained activated carbon, carbon black conductive additive, and PTFE binder in a 90:5:5 mass ratio, respectively. Freestanding 10 mg electrode pellets were pressed from the powder in a 1 cm die (MTI Corporation) on a Carver hydraulic press under an applied uniaxial force of 2 tons, applied 3 times. Electrodes were 1 cm in diameter and 300 ± 5 um thick, for a total volume of 0.024 cm^3, density of 0.42 g/cm^3, and areal mass loading of 12.7 mg/cm^2.

Building the cell stack. To build each symmetric cell, two electrodes were placed in a glass cup and immersed in 1.5 mL of electrolyte. To infiltrate the hydrophobic electrodes with aqueous electrolyte, vacuum and nitrogen (150 psi) were alternately applied for 5 minute intervals, 10 times (Figure 25). The process was carried out twice to ensure the electrolyte was thoroughly infiltrated. Electrodes were removed from the excess electrolyte and assembled into a cell stack by placing them on either side of an electrolyte-wetted, 12 mm diameter

filter paper or polycarbonate separator (Whatman #1 or Sterlitech PCT069030, respectively).

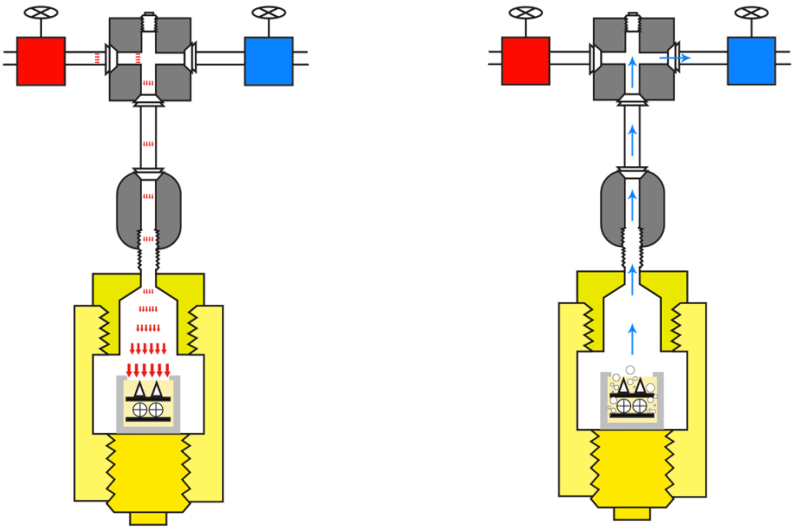

Figure 25. Vacuum-Pressure setup for electrolyte infiltration. Electrodes are submerged in cups of electrolyte and placed into a pressure chamber made of brass pipe fittings. Pressure (left) is applied with 150 psi N_2 and vacuum (right) is applied with a roughing pump. Alternate exposure to vacuum and pressure causes improved wetting of the electrodes and infiltrates the hydrophobic micropores with electrolyte solution.

Cell assembly. Cell bodies were formed by boring out the center of ½" Swagelok PFA Unions. Current collectors were formed by bonding 3-mm-thick type 1 glassy carbon discs (Alfa Aesar) to the ends of 12 mm diameter stainless steel rods (McMaster-Carr) with silver epoxy (CW2400 - Chemtronics), and encapsulating the sides of the disc and rod in electrically insulating and chemically protective epoxy (Stycast 1266 – Emmerson and Cumming). The cell

stack was placed between the two glassy-carbon-capped current collectors inside the cell body. The assembly was held together by tightening the PFA nuts and ferrules while applying ~50 psi of pressure on the stack through the current collectors. This differs from many electrochemical cells (e.g. Li-ion coin cells) that contain springs, and instead relies on the elasticity of the thick electrodes to maintain pressure. For the three-electrode configuration tests, a T-shaped Swagelok PFA union was used with an Ag/AgCl reference electrode (Fisher Scientific™accumet™) placed with the tip at the edge of the separator with 0.5 mL of excess electrolyte added to submerge the reference electrode frit. Cell assemblies are shown in Figure 26.

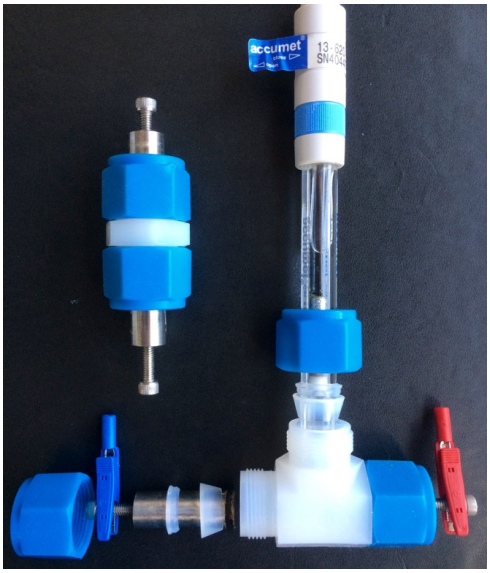

Figure 26. Custom Swagelok Cells. Two PFA Swagelok cells are shown: a fully assembled two-electrode cell (left) and a partially assembled three-electrode cell (lower-right).

Electrochemical characterization of redox ECs. All galvanostatic charge/discharge cycling (GCD) tests were performed on a Bio-logic VMP3 potentiostat/galvanostat at a temperature of 25 ± 1 ºC. Glassy carbon surfaces of the current collectors were polished using polishing alumina (0.05 μm) and then washed with water and methanol prior to any measurements. The applied current, I, for GCD testing was normalized to the dry mass (activated carbon, carbon black, and PTFE binder) of both positive and negative electrodes (denoted as A/g_{dry}) – e.g. a current of ±20 mA was applied to cycle a cell with symmetric 10 mg electrodes at a rate of 1 A/g_{dry}.

Voltage, V, is measured as a function of time, t, and charging or discharging stops when V reaches V_{max} (i.e., 1.2 V) for charging or V_{min} (i.e., 0 V) for discharging, respectively. The following equations are used for calculating device performance:

Charge capacity, Q_{ch} (mAh)	$Q_{ch} = I_{ch} \cdot t_{ch}$	(3.1)
Discharge capacity, Q_{dis} (mAh)	$Q_{dis} = I_{dis} \cdot t_{dis}$	(3.2)
Coulombic efficiency, η_C	$\eta_C = Q_{dis}/Q_{ch}$	(3.3)
Charge energy, E_{ch} (Wh)	$E_{ch} = \int_0^{t_{ch}} I_{ch} \cdot V(t)\, dt$	(3.4)
Discharge energy, E_{dis} (Wh)	$E_{dis} = \int_0^{t_{dis}} I_{dis} \cdot V(t)\, dt$	(3.5)

Energy efficiency, η_E $\eta_E = E_{dis}/E_{ch}$ (3.6)

Average power, P_{dis} (W) $P_{dis} = E_{dis}/t_{dis}$ (3.7)

Energy reported in the manuscript indicates discharge energy, E_{dis}, which is normalized to the *dry mass of both positive and negative electrodes* to get specific energy (Wh/kg_{dry}), or to the combined volume of both electrodes to get energy density (Wh/L).

The GCD procedure was modified for discharge rate tests and self-discharge tests as follows:

Discharge rate tests were performed by repeatedly charging the cell to 1.2 V at 0.5 A/g_{dry} and discharging it to 0 V for 5 cycles each at 0.5 A/g_{dry}, 1 A/g_{dry}, 2.5 A/g_{dry}, 5 A/g_{dry}, 7.5 A/g_{dry}, and 10 A/g_{dry}, respectively. The self-discharge rate was studied based on the decay of discharge energy as a function of open circuit time, δ. First, the cell was charged to 1.2 V by applying a constant current (0.5 A/g_{dry}). Then, while monitoring the cell potential decay, the cell was left at open circuit for 6 h. After the open circuit period, the cell was discharged to 0 V by extracting the same constant current density (0.5 A/g_{dry}). Energy retention, η_R, after time δ at open circuit is defined and calculated by the following formula:

$$\eta_R(\delta) = E_{dis}(\delta)/E_{dis}(0) \quad (3.8)$$

Normalized performance metrics and theoretical capacity

Performance normalization. Electrodes and electrolyte from a 1 M $PVBr_2$/3M NaBr 2-electrode cell massed before and after cycling were 82 mg. Based on this mass and the electrolyte density of 1.41 g/cm^3, the electrolyte volume and the relative mass of the different electrolyte components were calculated and summarized in Table 4. The cell performance was then normalized to the total masses of electrodes only (indicated as g_{dry}), and electrodes plus electrolyte (indicated as g_{wet}).

Table 4. Properties of a 1 M $PVBr_2$/3M NaBr electrolyte in a cell with symmetric 10 mg electrodes

Electrolyte density	1.41 g/cm^3
Electrolyte mass	62 mg
a. $PVBr_2$	20 mg
b. NaBr	14 mg
c. H_2O	28 mg
Electrolyte volume	44 μL

Additional analytical measurements

Cyclic voltammetry of viologens. The cyclic voltammetry experiments were carried out in a conventional three electrode cell using a Potentiostat 600C (CH Instruments, Austin, TX). A glassy carbon disc (CH Instruments, 3 mm diameter) served as the working electrode and a platinum wire as the counter electrode. The glassy carbon disc electrode was polished using polishing alumina (0.05 μm) and the Pt disc electrode was rinsed first with acetonitrile followed by water and methanol, and then dried before each experiment. A saturated calomel reference electrode (SCE, CH Instruments) was used. The supporting electrolyte was 0.5 M KBr dissolved in ultrapure water obtained from a Milli-Q Simplicity™ 185 system with resistivity ≥ 18.2 MΩ•cm.

UV-Vis measurements for testing complexation of viologens and Br_3^-. The UV-Vis spectra were acquired on an Agilent 8453 UV-Vis spectrophotometer equipped with a cuvette holder. All spectra were recorded under ambient conditions with a 1 cm light-path.

To generate spectra of uncomplexed viologen dications, 0.5 mL of each 60 mM viologen solution was combined with 1 mL water in 1.5 mL centrifuge tubes. Tubes were agitated with a vortex mixer for 1 min and left to sit overnight. Before UV-Vis measurements, tubes were centrifuged for 5 min at 4,000 rpm and then

a 5 uL sample of the solution was diluted 400 times into 1.995 mL water in a quartz cuvette. The capped cuvette was shaken to ensure a homogeneous analyte.

To generate spectra of the viologens after complexation with Br_3^-, each 0.5 mL of 60 mM viologen solution was combined with 0.5 mL water and 0.5 mL of 120 mM Br_3^- solution. Prepared samples were processed with the same methods stated above before UV-Vis measurements.

Optical absorption data for both complexed and uncomplexed viologen samples were normalized to the absorbance at the absorption maxima for the uncomplexed sample.

Results and Discussion

In aqueous electrolytes, the 1,l'-substituents of the viologens (1,1'-disubstituted-4,4'-bipyridinium dications) significantly affect the solubility of the cation radical. [24] With bromide as the counterion, viologen dications with alkyl substituents R ≥ 5 (*n*-pentyl) precipitate as the [$V^{+\bullet}$•Br^-] salt at the electrode surface when reduced. [25,26] Solubility tests of $HV^{+\bullet}$ and $MV^{+\bullet}$ in the presence of KBr indeed show that HV precipitates as the [$HV^{+\bullet}$•Br^-] salt and [$MV^{+\bullet}$•Br^-] remains dissolved in solution (Figure 27).

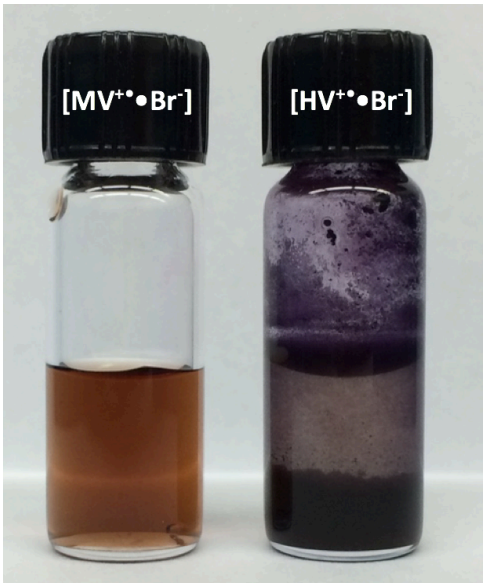

Figure 27. Complexation of viologen radicals. Complexation of ($V^{+\bullet}$) by the bromide anion (Br^-) to generate [$V^{+\bullet}$•Br^-] complex. (left) [$MV^{+\bullet}$•Br^-] and (right) [$HV^{+\bullet}$•Br^-] formed by reducing a solution of 60 mM V^{2+} in the presence of 0.1 M KBr with excess sodium dithionite ($Na_2S_2O_4$).

We first investigated whether the difference in solubility of the [$V^{+\bullet}$•Br^-] salt at the anode affects the overall cycling stability of the cell (Figure 24), noting that the *soluble* $MV^{+\bullet}$ could be susceptible to irreversible reactions (e.g., polymerization).[20] To study the degradation mechanism, we built two asymmetric EC cells, one with the $MV^{2+}/MV^{+\bullet}$ redox couple (0.1 M $MVCl_2$) and the other with the Br^-/Br_3^- redox couple (1 M KBr) for comparison, without any other electrolyte. Counter electrodes were ruled out as a source of fading by oversizing them so that charge storage was only via double-layer capacitance. Galvanostatic charge/discharge cycling (GCD) potential profiles are shown in Figure 28.

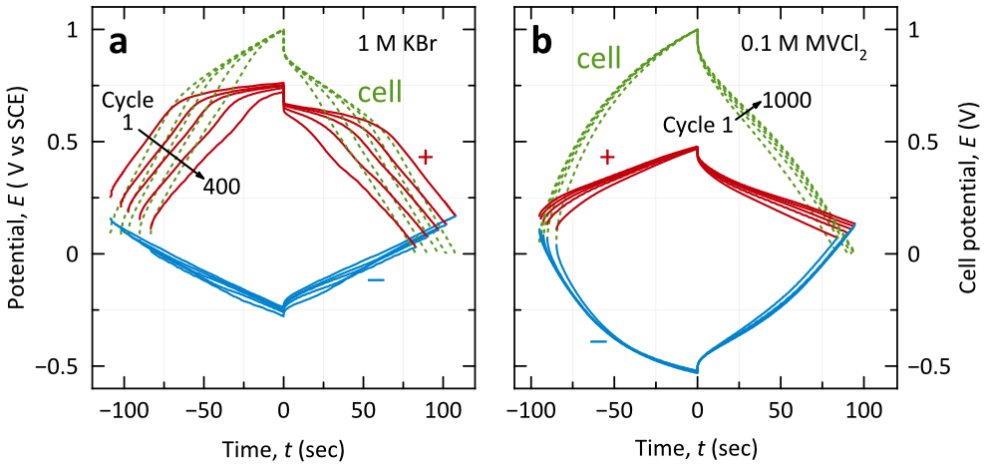

Figure 28. Asymmetric cells testing anolyte and catholyte stability. GCD potential profiles for the cathode (+), anode (–), and total cell for (a) first 400 cycles of Br^- catholyte with an EDLC anode (6:1 anode to cathode mass ratio), and (b) first 1000 cycles of MV^{2+} anolyte with an EDLC cathode (3:1 cathode to anode mass ratio).

The KBr cell degrades rapidly, and over the course of 400 cycles nearly all faradaic charging at the cathode disappears (Figure 28a). The $MVCl_2$ cell, however, maintains consistent GCD potential profiles for both cathode and anode and even exhibits slight performance improvement over 1000 cycles (Figure 28b). The stability of the asymmetric $MVCl_2$ cell suggests that although soluble $MV^{+\bullet}$ leads to low coulombic efficiency and high self-discharge, the $MV^{2+}/MV^{+\bullet}$ redox couple is stable and does not contribute to cell fading. Extended cyclic voltammetry (CV) scans of $MVCl_2$/KBr electrolyte at cathodic potentials confirm the reversible redox behavior of MV^{2+} anolyte (Figure 29), and indicate that no significant degradation products accumulate on the electrode surface. With the evidence suggesting that degradation likely occurs at the cathode, we next focused on understanding why the Br^-/Br_3^- redox reaction causes instability when operating alone or in the presence of MV, but remains stable when paired with HV.

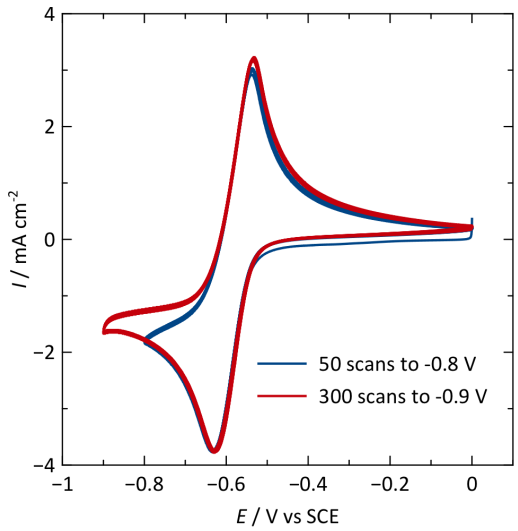

Figure 29. Extended cyclic voltammetry of MV/Br electrolyte. Repeated cyclic voltammograms of 50 mM $MVCl_2$/0.2 M KBr electrolyte are shown for 50 scans to -0.8 V followed by 300 scans to -0.9 V at a scan rate of 10 mV/s.

Bromide is an efficient catholyte in electrochemical energy storage systems,[27] particularly in aqueous redox flow batteries.[28] However, bromine is corrosive, volatile, and intercalates graphitic carbons to cause electrode degradation.[29] To address these issues, quaternary ammonium salts are used in flow batteries to complex Br_2/Br_3^-, reducing the reactivity and vapor pressure.[30,31] Because viologens are structurally similar to these quaternary ammonium salts, they may also complex Br_2/Br_3^- in redox ECs. We hypothesized that (1) V^{2+} complexes Br_3^- at the cathode, (2) the length of the alkyl substituent determines the solubility of the complex, and (3) HV effectively complexes Br_3^- into an insoluble salt, suppressing its reactivity and cross-diffusion.

To determine if HV is better at precipitating Br_3^- as a solid complex than MV, 20 mM aqueous MV^{2+} or HV^{2+} was measured by ultraviolet-visible spectroscopy (UV-Vis) with and without 40 mM Br_3^-. After mixing, 4.0 mM MV^{2+} remained dissolved in solution as compared to 0.6 mM HV^{2+}. The MV solution also retains a yellow tint from dissolved Br_3^-, while the HV solution turns clear (Figure 30). Greater precipitation of the nominally [HV^{2+}•$2Br_3^-$] complex compared to the MV complex is likely driven by the increased hydrophobicity of HV imparted by its longer alkyl substituents.[32] The formation of solid [HV^{2+}•$2Br_3^-$] in the cathode should thus suppress the reactivity and diffusion of Br_3^-, allowing the HV/Br cell to cycle stably while the MV/Br cell fades due to the presence of free Br_3^-.

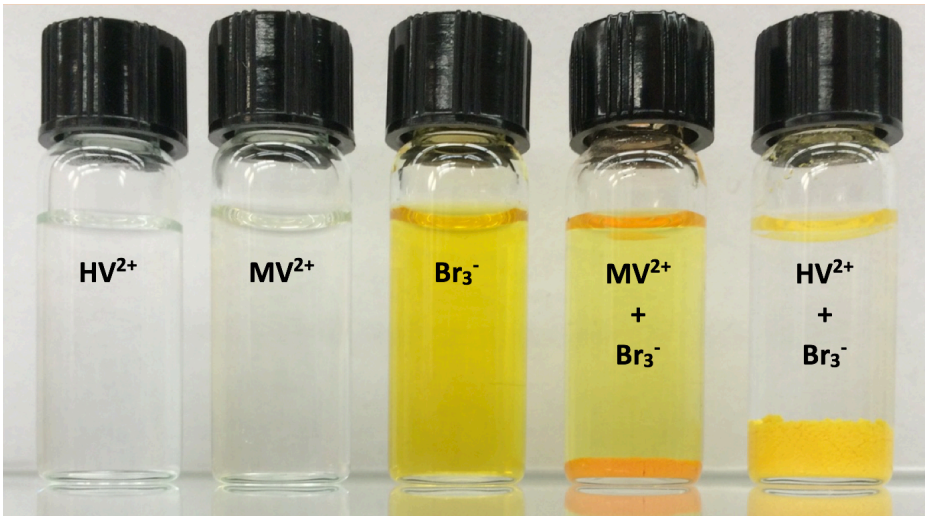

Figure 30. Complexation of Br_3^- by methyl and heptyl viologen dications. 20 mM $MVCl_2$ or $HVBr_2$ (left) and 40 mM Br_3^- (center) form solid complexes of [MV^{2+}•$2Br_3^-$] or [HV^{2+}•$2Br_3^-$] (right) when mixed in aqueous solution. The degree of complex precipitation is higher for HV than for MV. In the case of MV, a

significant amount of Br_3^- remains dissolved in solution, which can be visually observed as a yellow tint compared to the clear HV/Br_3^- solution.

To confirm the role of viologen in complexing Br_3^- and stabilizing the redox ECs, we constructed a cell with higher concentrations of the MV/Br electrolyte (i.e. increasing from 0.5 M $MVCl_2$/1 M KBr to 1 M $MVCl_2$/4 M NaBr). The cell GCD cutoff potential for the concentrated cell was reduced from 1.4 V to 1.3 V. Both cells therefore store nearly equal energy, but the concentrated cell has excess Br^- present at the cathode after charging, which facilitates the formation of Br_3^-, and an increased concentration of MV^{2+}, which supports efficient complexation and precipitation of Br_3^-. Over 450 cycles, stability significantly improved from a 62 % capacity loss in the original cell to only 17 % in the concentrated cell (Figure 31). This result supports the proposed operating mechanism by confirming that cell degradation slows when Br_3^- is more efficiently complexed.

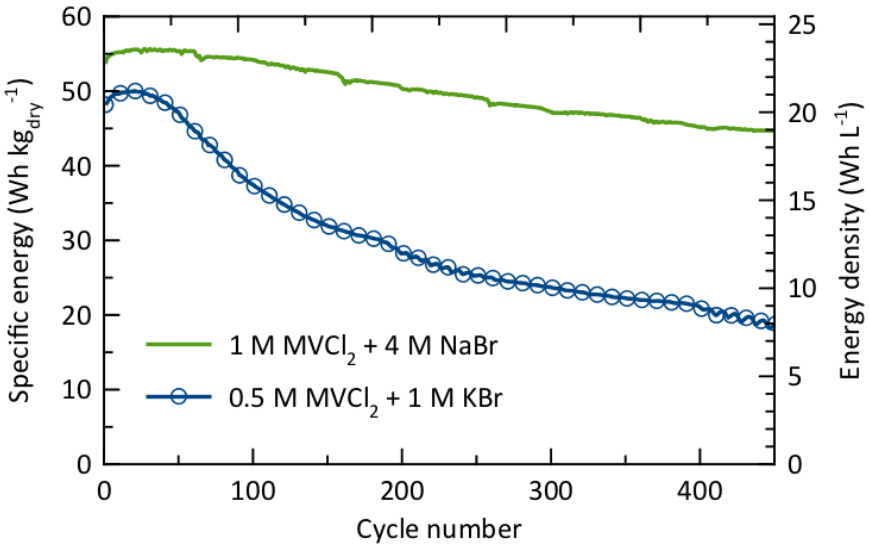

Figure 31. Cycling stability for concentrated MV/Br cell. A 1 M $MVCl_2$/4 M NaBr cell and a 0.5 M $MVCl_2$/1 M KBr cell are cycled at 0.5 A/g_{dry} to 1.3 V and 1.4 V, respectively. The highly concentrated cell exhibits significantly less capacity fade over 450 charge/discharge cycles.

Previously, the slow self-discharge of the halides could not be explained purely by electrostatics and was attributed to the physical adsorption of Br_3^- at the electrode surface suppressing cross-diffusion in the charged state.[13,20] We show here that retention of Br_3^- is driven by the formation of the [HV^{2+}•$2Br_3^-$] solid complex at the cathode. Together with the simultaneous generation of the [$HV^{+\bullet}$•Br^-] solid complex at the anode,[26] the charged products ($HV^{+\bullet}$ and Br_3^-) are immobilized within the porous hydrophobic electrodes, suppressing cross-diffusion (Scheme 1 and Figure 32). Microscopic electrodeposition/precipitation occurring at *both* electrodes is consistent with the exceptionally low self-

discharge (energy retained after 6 h at open circuit, η_R(6 h) = 86 %) and high coulombic efficiency (99.9 %) of the HV/Br device. Therefore, in order to improve the specific energy of viologen/bromide redox ECs without compromising on self-discharge or stability, electrolyte design must account for and optimize the dual complexation/precipitation effect.

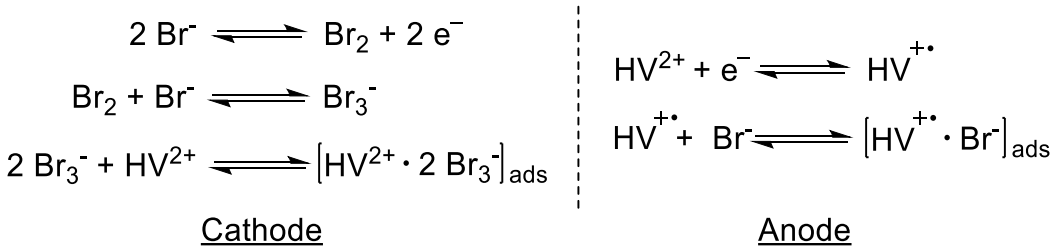

Scheme 1. Charge/discharge mechanism of the HV/Br system with dual reversible solid complexation. Each ion acts as a charge-storing redox couple at one electrode and as a complexing agent at the other.

For redox ECs, high redox-active electrolyte concentrations are advantageous to maximize faradaic energy storage while minimizing electrolyte volume. New viologens to replace MV or HV must (1) be easy to synthesize, (2) have high solubility (≥1 M, *for energy density*), (3) precipitate as a solid complex when reduced at the anode (*for high coulombic efficiency and slow self-discharge*), and (4) form an insoluble complex with Br_3^- at the cathode (*for stability, coulombic efficiency and slow self-discharge*). Meeting these criteria is challenging because

the long hydrophobic alkyl chains that enhance (3) and (4) work against (2) in aqueous systems.

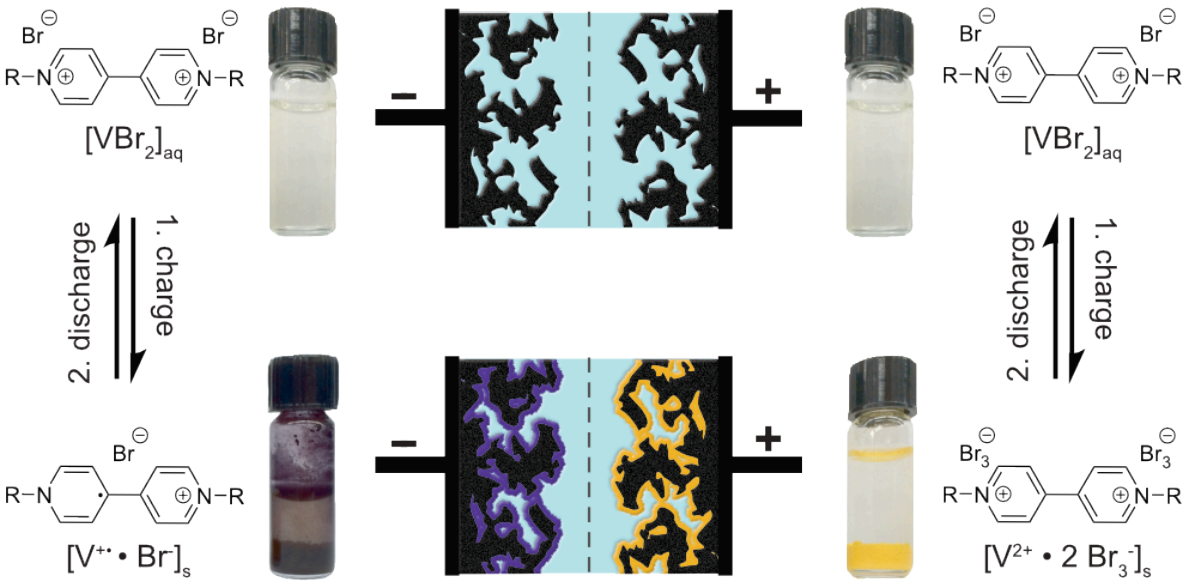

Figure 32. Dual redox ECs with reversible solid complexation. The viologen bromide system uses a single, homogeneous electrolyte with a non-ion-selective separator. One organic salt dissociates into anionic and cationic species that act as redox-active catholyte and anolyte, respectively. Each species acts as a charge-storing redox couple at one electrode and as a complexing agent at the other electrode. By optimizing the functional group, reversible electroprecipitation of a solid complex at each electrode is possible, improving cycling stability and decreasing self discharge. The solid films forms in the charged state (below), and redissolves into the electrolyte in the discharged state (above).

We synthesized a series of alkyl-substituted viologens with R ≥ 5, as viologens with shorter alkyl chains do not precipitate with Br^- upon reduction (Scheme 2 and Table 4).[24] Although not expected to precipitate, butyl viologen was synthesized as well for comparison. Hexyl viologen exhibits insufficient solubility (<0.5 M) in the presence of NaBr, but butyl viologen (BV) and pentyl viologen (PV) are highly soluble (>1.5 M).

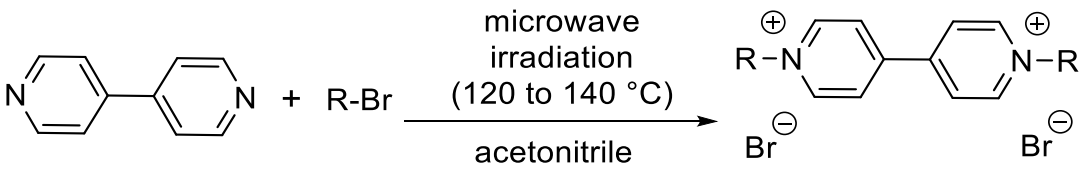

Scheme 2. Synthesis scheme for alkyl viologens

Table 5. Redox potential and solubility for synthesized viologens

	R (units of CH_2)	$E_{1/2}$ (V vs SCE)	Solubility (in 2 M NaBr solution)
n-Butyl[a]	4	-0.60	>1.5 M
n-Pentyl	5	-0.54	>1.5 M
n-Hexyl	6	-0.50	<0.5 M
n-Heptyl	7	-0.44	<0.2 M

[a] Butyl viologen is synthesized as well for comparison.

Cyclic voltammograms for the synthesized viologens in the potential range of the negative electrode are shown in Figure 33a, demonstrating a trend of increasingly anodic reduction potentials as alkyl chain length increases. BV and PV were tested for solid complexation with Br_3^- by UV-Vis and compared to MV and HV (Figure 33b). The addition of Br_3^- decreased the concentration of both PV and HV dissolved in the solution by ca. 97%, indicating that PV forms a solid complex as effectively as HV. BV shows similar complexing capacity to MV.

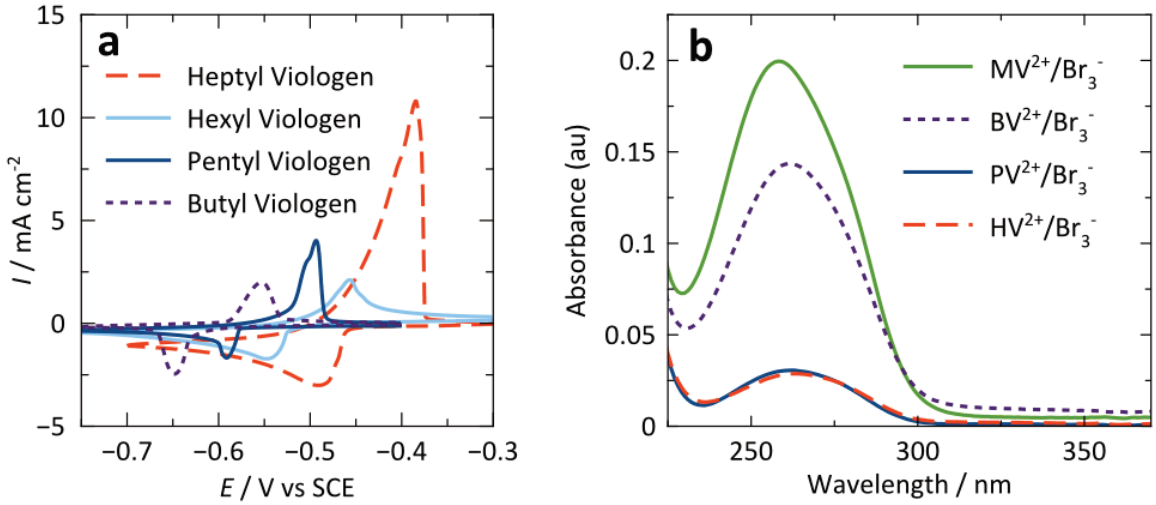

Figure 33. Screening synthesized viologens. (a) Cyclic voltammograms were recorded at a scan rate of 5 mV/s with 20 mM viologen in 0.5 M KBr electrolyte. (b) UV-Vis absorption spectra quantifying V^{2+} remaining dissolved in the supernatant after 20 mM V^{2+} complexes and precipitates with 40 mM Br_3^-. Spectra are normalized to absorption maxima of 20 mM V^{2+} solutions without Br_3^-, thus absorbance peak values here translate to the fraction of the initial V^{2+} that remains uncomplexed.

With both high solubility and good complexing capacity, we selected PV for further study in dual-redox ECs. A three-electrode cell (Figure 34a) and a two-electrode cell (Figure 34b and Figure 35) with a 1 M $PVBr_2$/3 M NaBr electrolyte, paper separator, and symmetric activated carbon electrodes with a 12.7 mg/cm^2 mass loading were assembled and tested by GCD. The 2-elecrode cell produced 48.5 Wh/kg_{dry} at 0.5 A/g_{dry} (0.44 kW/kg_{dry}) with slow self-discharge (η_R(6 h) = 77 %). The PV/Br cell delivers ca. *75 % higher* specific energy than the HV/Br cell over a wide range of discharge rates (Figure 34b, from 0.44 kW/kg_{dry} at 0.5 A/g_{dry} to 4.2 kW/kg_{dry} at 10 A/g_{dry}). Performance metrics were also calculated for the wet stack mass, taking into account the electrolyte contribution, as shown in Table 6.

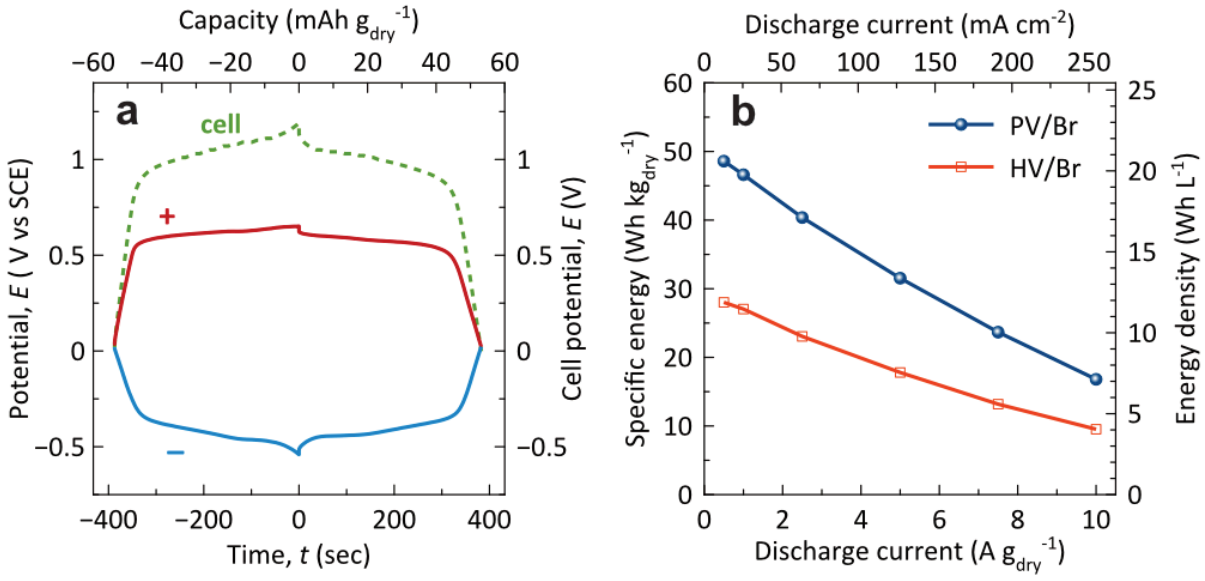

Figure 34. Performance of 1 M $PVBr_2$/3 M NaBr cells. (a) GCD potential profiles for the cathode (+), anode (–), and total cell cycled at 0.5 A/g_{dry}. During charging, the electrochemical behavior transitions from capacitive to faradaic. (b) Specific energy of PV/Br and HV/Br cells at different discharge rates in a 2-electrode volume limiting cells. Both cells were charged to 1.2 V at 0.5 A/g_{dry} and discharged at rates from 0.5 A/g_{dry} to 10 A/g_{dry}.

Table 6. Performance metrics normalized to different cell components

	Dry electrodes	**Wet electrodes**
Normalization mass (mg)	20 mg Cathode: 10 mg Anode: 10 mg	82 mg Electrolyte: 62 mg Electrodes: 20 mg
Specific energy (Wh/kg)	48.5 (Wh/kg_{dry})	11.8 (Wh/kg_{wet})
Specific capacity (mAh/g)	55.6 (mAh/g_{dry})	13.6 (mAh/g_{wet})
Specific power (W/kg)	437 (W/kg_{dry})	107 (W/kg_{wet})

Theoretical capacity. Based on Scheme 1, we can write the half-reactions and overall reaction for a cell with pentyl viologen bromide electrolyte:

Cathode half-reaction: $6\ Br_{aq}^{-} + PV_{aq}^{2+} \rightleftharpoons [PV^{2+} \bullet 2\ Br_3^{-}]_s + 4\ e^{-}$

Anode half-reaction: $PV_{aq}^{2+} + Br_{aq}^{-} + e^{-} \rightleftharpoons [PV^{+\bullet} \bullet Br^{-}]_s$

Overall: $\mathbf{5}\ [\boldsymbol{PVBr_2}]_{\boldsymbol{aq}} \rightleftharpoons\ \mathbf{4}\ [\boldsymbol{PV^{+\bullet} \bullet Br^{-}}]_{\boldsymbol{s}} +\ [\boldsymbol{PV^{2+} \bullet 2\ Br_3^{-}}]_{\boldsymbol{s}}$

The overall reaction can be balanced without the use of the NaBr supporting electrolyte. This reaction shows that if all of the pentyl viologen in the electrolyte is utilized, 80 % will be used for faradaic energy storage and 20 % will be used as a complexing agent for Br_3^-. Based on the calculated mass of $PVBr_2$ in the cell, the theoretical faradaic specific capacity is 47 mAh/g_{dry} (after accounting for the 20 % of PV^{2+} needed for complexing Br_3^-). Combined with an additional 9 mAh/g_{dry} of capacitive charging, the total theoretical specific capacity is 56 mAh/g_{dry}. The measured capacity of 55.6 mAh/g_{dry} very closely matches the theoretical value, however the theoretical capacity may be slightly underestimated because additional viologen can be adsorbed to the electrode surface during the electrolyte soaking step of cell fabrication. For the theoretical capacity calculated here, this adsorption was not accounted for because its effect should be minor for solutions with high viologen concentrations.[20]

In addition to reaching high specific capacity and energy, the pentyl viologen cells maintain stability with 97 % energy retention over 10,000 cycles when tested at 2.5 A/g_{dry} (2.0 kW/kg_{dry}) (Figure 35a). These results indicate that pentyl viologen achieves the goal of simultaneously matching the high specific energy of methyl viologen redox ECs and the excellent cycling stability of heptyl viologen redox ECs.

The viologen bromide redox EC system is a hybrid between a supercapacitor and a battery, but unlike batteries, it is not damaged upon polarity reversal. Due to its symmetric nature, fully mixed anolyte/catholyte, and reversible dual solid complexation (i.e. the solids formed at each electrode during charging completely redissolve on discharge), the cell functions identically when operated "backwards" (Figure 35b). The chemistry is therefore tolerant to overdischarge or improper assembly and use, which is important when stacking individual cells into battery packs.[33]

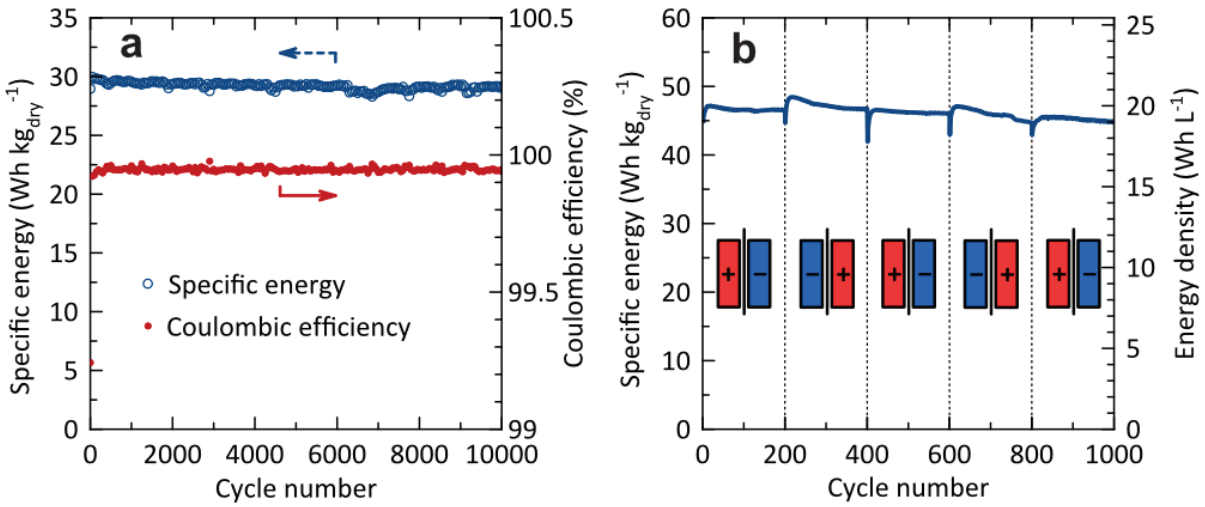

Figure 35. Stability of 1 M $PVBr_2$/3 M NaBr cells. (a) Cycling stability and coulombic efficiency of PV/Br cell cycled at 2.5 A/g_{dry}. Energy retention is 97% over 10,000 cycles with 99.9% coulombic efficiency. After 10,000 cycles, the cell achieves the same specific energy at 0.5 A/g_{dry}, showing no degradation after long-term cycling at higher current. (b) Stable cycling with the leads switched every 200 cycles (at 1 A/g_{dry}), repeatedly reversing the polarity.

For additional characterization, equivalent series resistance (R_{ES}) was measured by both IR drop and electrochemical impedance spectroscopy (EIS) methods. The equivalent series resistance (R_{ES}) is commonly estimated by two different methods: IR drop and electrochemical impedance spectroscopy (EIS).[2] For the IR drop method, the voltage drop is measured when the current switches between charging and discharging values (without dwelling at the peak potential) and used in the equation $R_{ES} = \Delta V / \Delta I$ where ΔV and ΔI are the changes in voltage and current of the IR drop, respectively. For the EIS method, R_{ES} is taken

as the real part of the complex impedance found by extrapolating the low-frequency region of a Nyquist plot to Im(Z) = 0. Both of these measurements were performed on a 1 M $PVBr_2$/3 M NaBr cell in the fully charged state (100 % state of charge (SOC), 1.2 V) and in the fully discharged state (0 % SOC, 0 V). The data are shown in Figure 36 and the calculated R_{ES} values are summarized in Table 7. When the cell is fully charged, the R_{ES} calculated by both methods is ca. 2 times higher than in the fully discharged state. This suggests that the precipitated solid complexes formed during charging have low electrical conductivity, as they increase the total resistance of the cell by ca. 190 % (IR drop method) to 225 % (EIS method).

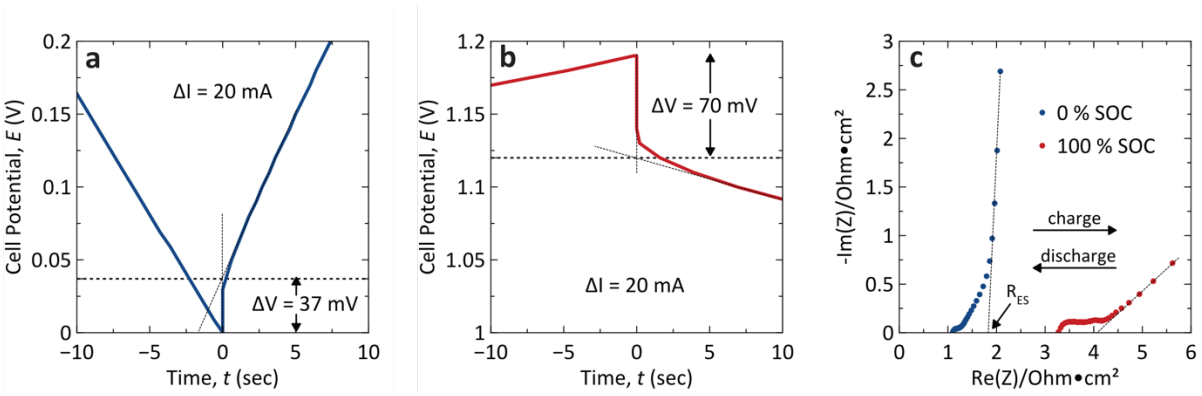

Figure 36. Measuring equivalent series resistance (R_{ES}). IR drop for a 1 M $PVBr_2$/3 M NaBr cell immediately after (a) discharging and (b) charging at ± 10 mA, as well as (c) Nyquist impedance spectra from 0.2 MHz to 0.1 Hz for the fully discharged (0 % SOC) and fully charged (100 % SOC) conditions. The increase in R_{ES} in the charged state is evidenced by the larger IR drop, contact resistance, and charge transfer resistance. This behavior is related to the formation of precipitated solid complexes with low electrical conductivity at both electrodes, and consistent with the operating mechanism of the cell.

Table 7. Equivalent series resistance (R_{ES}) of a 1 M $PVBr_2$/3 M NaBr cell

	IR drop method	**EIS method**
Discharged (0% SOC)	1.85 Ω (1.45 Ω•cm^2)	2.32 Ω (1.82 Ω•cm^2)
Charged (100% SOC)	3.50 Ω (2.75 Ω•cm^2)	5.18 Ω (4.07 Ω•cm^2)

Conclusions

Challenges to maximize the performance of redox ECs are (1) to suppress the diffusion of redox couples in the charged state to prevent side reactions and self-discharge, and (2) to balance the capacity of the electrodes using a catholyte and anolyte that are compatible when intermixed. The strategy outlined in this chapter of utilizing *dual redox couples*, each of which participates in a faradaic reaction at one electrode and acts as a complexing agent at the other, solves the main problems associated with redox ECs. With reversible solid complexation of highly soluble PV/Br redox-active electrolytes, the redox EC device retains charged products efficiently, produces a record specific energy with stable cycling, and, unlike other batteries and pseudocapacitors, operates symmetrically. The cells are easy to assemble in air and use simple inexpensive aqueous redox electrolytes, which suggests they may be manufacturable at low cost and impact applications where performance in-between batteries and traditional supercapacitors is desired.

References

1. Burke, A. R&D considerations for the performance and application of electrochemical capacitors. *Electrochim. Acta* **53,** 1083–1091 (2007).

2. Zhang, S. & Pan, N. Supercapacitors Performance Evaluation. *Adv. Energy Mater.* **5,** 1401401 (2015).

3. Yan, J., Wang, Q., Wei, T. & Fan, Z. Recent Advances in Design and Fabrication of Electrochemical Supercapacitors with High Energy Densities. *Adv. Energy Mater.* **4,** 1300816 (2014).

4. Ghidiu, M., Lukatskaya, M. R., Zhao, M.-Q., Gogotsi, Y. & Barsoum, M. W. Conductive two-dimensional titanium carbide 'clay' with high volumetric capacitance. *Nature* **516,** 78–81 (2014).

5. Conway, B. E., Birss, V. & Wojtowicz, J. The role and utilization of pseudocapacitance for energy storage by supercapacitors. *J. Power Sources* **66,** 1–14 (1997).

6. Li, W. *et al.* Nitrogen-containing carbon spheres with very large uniform mesopores: The superior electrode materials for EDLC in organic electrolyte. *Carbon N. Y.* **45,** 1757–1763 (2007).

7. Kim, S. Y. *et al.* Nickel oxide encapsulated nitrogen-rich carbon hollow spheres with multiporosity for high-performance pseudocapacitors having extremely robust cycle life. *Energy Environ. Sci.* **8,** 188–194 (2015).

8. Augustyn, V., Simon, P. & Dunn, B. Pseudocapacitive oxide materials for high-rate electrochemical energy storage. *Energy Environ. Sci.* **7,** 1597–1614 (2014).

9. Lang, X., Hirata, A., Fujita, T. & Chen, M. Nanoporous metal/oxide hybrid electrodes for electrochemical supercapacitors. *Nat. Nanotechnol.* **6,** 232–236 (2011).

10. Rauda, I. E., Augustyn, V., Dunn, B. & Tolbert, S. H. Enhancing Pseudocapacitive Charge Storage in Polymer Templated Mesoporous

Materials. *Acc. Chem. Res.* **46,** 1113–1124 (2013).

11. Frackowiak, E. in *Supercapacitors: Materials, Systems, and Applications* (eds. Lu, M., Beguin, F. & Frackowiak, E.) 207–237 (Wiley-VCH, 2013).

12. Sathyamoorthi, S., Kanagaraj, M., Kathiresan, M., Suryanarayanan, V. & Velayutham, D. Ethyl viologen dibromide as a novel dual redox shuttle for supercapacitors. *J. Mater. Chem. A* **4,** 4562–4569 (2016).

13. Wang, B. *et al.* A Hybrid Redox-Supercapacitor System with Anionic Catholyte and Cationic Anolyte. *J. Electrochem. Soc.* **161,** A1090–A1093 (2014).

14. Fic, K., Meller, M. & Frackowiak, E. Strategies for enhancing the performance of carbon/carbon supercapacitors in aqueous electrolytes. *Electrochim. Acta* **128,** 210–217 (2014).

15. Frackowiak, E., Fic, K., Meller, M. & Lota, G. Electrochemistry serving people and nature: high-energy ecocapacitors based on redox-active electrolytes. *ChemSusChem* **5,** 1181–5 (2012).

16. Wang, X. *et al.* High Energy Density Aqueous Electrochemical Capacitors with a KI-KOH Electrolyte. *ACS Appl. Mater. Interfaces* **7,** 19978–19985 (2015).

17. Frackowiak, E., Meller, M., Menzel, J., Gastol, D. & Fic, K. Redox-active electrolyte for supercapacitor application. *Faraday Discuss.* **172,** 179–198 (2014).

18. Chen, L., Bai, H., Huang, Z. & Li, L. Mechanism investigation and suppresion of self-discharge in active electrolyte enhanced supercapacitors. *Energy Environ. Sci.* **7,** 1750–1759 (2014).

19. Akinwolemiwa, B., Peng, C. & Chen, G. Z. Redox Electrolytes in Supercapacitors. *J. Electrochem. Soc.* **162,** A5054–A5059 (2015).

20. Chun, S.-E. *et al.* Design of aqueous redox-enhanced electrochemical capacitors with high specific energies and slow self-discharge. *Nat. Commun.* **6,** 7818 (2015).

21. Maciá-Agulló, J. A., Moore, B. C., Cazorla-Amorós, D. & Linares-Solano, A. Activation of coal tar pitch carbon fibres: Physical activation vs. chemical activation. *Carbon N. Y.* **42,** 1367–1370 (2004).

22. Lin, R.-L., Li, J.-Q., Liu, J.-X. & Kaifer, A. E. The Binding Interactions between Cyclohexanocucurbit[6]uril and Alkyl Viologens Give Rise to a Range of Diverse Structures in the Solid and the Solution Phases. *J. Org. Chem.* **80,** 10505–10511 (2015).

23. Wang, T., Kelley, M. & Cooper, J. Equilibrium, kinetic, and UV-spectral characteristics of aqueous bromine chloride, bromine, and chlorine species. *Inorg. Chem.* **33,** 5872–5878 (1994).

24. Bird, C. & Kuhn, A. Electrochemistry of the viologens. *Chem. Soc. Rev.* **10,** 49–82 (1981).

25. Monk, P. *The Viologens: Physicochemical Properties, Synthesis and Applications of the Salts of 4,4'-Bipyridine*. (John Wiley and Sons Ltd., 1999).

26. van Dam, H. T. & Ponjeé, J. J. Electrochemically Generated Colored Films of Insoluble Viologen Radical Compounds. *J. Electrochem. Soc.* **121,** 1555 (1974).

27. Zhao, Y. *et al*. A reversible Br2/Br– redox couple in the aqueous phase as a high-performance catholyte for alkali-ion batteries. *Energy Environ. Sci.* **7,** 1990 (2014).

28. Soloveichik, G. L. Flow Batteries: Current Status and Trends. *Chem. Rev.* **115,** 11533–11558 (2015).

29. Fabjan, C. & Drobits, J. in *Handbook of Battery Materials: Second Edition* (eds. Daniel, C. & Besenhard, J. O.) 197–217 (Wiley-VCH, 2011).

30. Lancry, E., Magnes, B.-Z., Ben-David, I. & Freiberg, M. New Bromine Complexing Agents for Bromide Based Batteries. *ECS Trans.* **53,** 107–115 (2013).

31. Jeon, J. D., Yang, H. S., Shim, J., Kim, H. S. & Yang, J. H. Dual function of quaternary ammonium in Zn/Br redox flow battery: Capturing the

bromine and lowering the charge transfer resistance. *Electrochim. Acta* **127,** 397–402 (2014).

32. Hoshino, K., Oikawa, Y., Sakabe, I. & Komatsu, T. Reversible polycolour change of viologens from violet through transparent to white. *Electrochim. Acta* **55,** 165–170 (2009).

33. Doughty, D. H. in *Handbook of Battery Materials: Second Edition* (eds. Daniel, C. & Besenhard, J. O.) 905–938 (Wiley-VCH, 2011).

Chapter 4

Bromine storage through solid complexation in porous carbon electrodes[4]

The contents of this chapter have substantially appeared in the following reference: S. J. Yoo, B. Evanko, X. Wang, M. Romelczyk, A. Taylor, X. Ji, S. W. Boettcher, and G. D. Stucky, "Fundamentally Addressing Bromine Storage through Reversible Solid-State Confinement in Porous Carbon Electrodes: Design of a High-Performance Dual-Redox Electrochemical Capacitor," J. Am. Chem. Soc. 29, 9985, 2017.

Introduction

Electric double-layer capacitors (EDLCs), interchangeably referred to as supercapacitors or ultracapacitors, are capable of storing and discharging energy quickly due to a physical ion adsorption/desorption mechanism in the Helmholtz layer.[1,2] Compared to EDLCs using non-aqueous electrolytes, EDLCs with nonflammable aqueous electrolytes are in principle safer, and provide higher power density due to their having a lower ionic resistance.[1,3-5] However, the energy density of aqueous EDLCs is limited by the narrow electrochemical potential window of water compared to counterparts with organic electrolytes or ionic liquids.[6-8] The grand challenge for aqueous EDLCs is to increase specific energy without compromising specific power and cycling stability. A number of hybrid and pseudocapacitive systems have been developed that utilize different charge storage mechanisms in addition to, and/or in place of, electric double-layer capacitance to increase energy density.[9-15]

One such approach to enhance the energy density is to replace the inert electrolytes of conventional EDLCs with redox-active electrolytes that enable faradaic charge storage.[16-23] Compared with the construction of nanostructured solid-state redox-active electrode materials, liquid-state redox-active electrolytes are easier to prepare and be scaled up, and should be compatible with the carbon electrodes that are currently mass-produced for commercial EDLCs.

In order to design redox-active electrolyte systems, redox couples should exhibit fast and reversible electron transfer and not engage in irreversible side reactions and/or degradation over repeated charge/discharge cycles. Additionally, the cross-diffusion of soluble redox couples that causes low Coulombic efficiency and fast self-discharge must be eliminated. The use of ion-selective membrane separators to mitigate self-discharge has been reported,[24] but such membranes are costly, and primarily for that reason are not practical for commercial applications. Electrostatic attraction has also been proposed as a mechanism to retain redox couples at the surface of oppositely charged electrodes, but was shown to have only a minor effect on the suppression of self-discharge rates.[25,26]

Halogens (I^- and Br^-) are promising aqueous redox-active species as they are inexpensive, electrochemically reversible redox couples with high solubility.[22,25,27-31] In comparison to iodide, bromide has a higher standard reduction potential (0.81 V vs SCE; $E^o_{I_3^-/I^-} = 0.3$ V) that further increases energy density. However, this advantage is offset by the corrosive and volatile nature of bromine generated at the positive electrode. Furthermore, soluble Br_3^- diffuses to the negative electrode, which causes low Coulombic efficiency and fast self-discharge, as well as possible irreversible oxidation or bromination of the anode or anolyte.[32,33] In aqueous bromine flow batteries, asymmetric quaternary

ammonium salts such as methyl ethyl pyrrolidinium bromide (MEPBr; 1-ethyl-1-methylpyrrolidinium bromide) or methyl ethyl morpholinium bromide (MEMBr; 4-ethyl-4-methylmorpholinium bromide) are commonly used to complex Br_2/Br_3^- as an oily-liquid phase.[34,35] This complexation reduces the reactivity and vapor pressure of bromine while maintaining a mobile, liquid state for flow-system compatibility. However, this approach does not address the cross-diffusion and poor Coulombic efficiency.[32] Standard bromine flow batteries avoid these limitations by storing the charged liquid complex in a separate tank away from the cell stack, but this practice is not feasible for non-flow systems, such as in redox-enhanced electrochemical capacitors (redox ECs). Alternatively, ion-exchange membrane separators can be used, but these materials are expensive and require addressing significant sealing challenges to be effective in a practical device. In short, a fundamental need is to store Br_3^- in non-flow energy storage systems in a manner that (1) reduces the unwanted chemical reactivity and vapor pressure of bromine but at the same time (2) suppresses cross-diffusion and self-discharge by (3) a simple and affordable mechanism.

In the present work, we introduce for the first time tetrabutylammonium-induced, reversible solid complexation of the Br^-/Br_3^- redox couple in aqueous redox ECs. Systematic studies show that this solid complex is retained in the

pores of the high-surface-area carbon electrodes upon charging, dramatically improving cycling stability and self-discharge relative to traditional oily-liquid-phase bromine complex. Furthermore, we reveal the underlying cause of the irreversible capacity loss that occurs when the uncomplexed Br^-/Br_3^- redox couple is used in aqueous redox ECs with activated carbon electrodes.

Building upon these findings, we design a high-performance and stable aqueous redox EC. High-energy redox ECs must concurrently utilize a catholyte and an anolyte (dual-redox enhanced electrochemical capacitors; dual-redox ECs) to maximize faradaic energy storage.[19,23,25,26,36] In aqueous systems, these redox couples should have a standard redox potential close to the oxygen evolution potential (for the catholyte) and near the hydrogen evolution potential (for the anolyte), respectively, to widen the operating voltage of the device, as well as good solution compatibility when intermixed.[26] To demonstrate the utility of bromide catholyte and our complexation strategy in such a system, we use a highly soluble ethyl viologen (EV) as an anolyte and investigate the compatibility and comparative Br_3^- complexing capacity. With the use of readily available tetrabutylammonium bromide as an additive, a dual-redox EC that utilizes bromide and ethyl viologen (EV) produces a specific energy of ~64 W·h/kg (normalized to the dry mass of both positive and negative electrode, and maintains stability over 7000 cycles.

Materials and Methods

Chemicals. All reagents and starting materials were obtained commercially and used as received without any further purification.

Sodium bromide (NaBr), sodium sulfate (Na_2SO_4), tetrabutylammonium bromide (TBABr), 1-ethyl-1-methylpyrrolidinium bromide (methyl ethyl pyrrolidinium bromide; MEPBr), and ethyl viologen dibromide ($EVBr_2$) were purchased from Sigma-Aldrich. Hydrobromic acid (HBr) was purchased from Acros Organics, tetrabutylammonium tribromide was purchased from Alfa Aesar, sodium bromate ($NaBrO_3$) was purchased from J. T. Baker Chemical Co., sodium hydroxide (NaOH) was purchased from Fisher Chemical, and potassium bromide (KBr) was purchased from EMD Chemicals Inc. Water was from a Milli-Q Simplicity™ 185 system with resistivity ≥ 18.2 MΩ·cm (if not specified, all solutions in the SI and text refer to aqueous solutions).

Carbon electrodes. Activated carbon was prepared by CO_2 activation of high-purity carbon fibers (Donacarbo S-241, Osaka Gas Co., ~13 μm OD x 130 μm long) in a tube furnace at 890 ºC under flowing CO_2 (100 SCCM) for 22.5 h. Detailed characterization data, including specific surface area, elemental composition and pore size distribution are reported in Chapter 2.[26]

For the preparation of electrodes, activated carbon, polytetrafluoroethylene (PTFE) binder (60 weight % aqueous dispersion from Sigma-Aldrich), and

acetylene black conductive additive (Vulcan® XC72R) were mechanically mixed with a 90:5:5 mass ratio with isopropanol, and the resulting slurry was rolled into a single freestanding film with a PTFE rolling pin. This film was dried overnight at 160 ºC in air, ground into a powder through a mesh sieve, and further dried under high vacuum at room temperature for two days. Freestanding electrode pellets were pressed from the powder in a 1-cm-diameter die (MTI Corporation) on a Carver hydraulic press under an applied uniaxial force of 2 tons, applied 3 times. Electrodes were 1 cm in diameter and 300 ± 5 μm thick, for a total volume of 0.024 cm^3, and density of 0.42 g/cm^3.

Electrolytes. The electrolytes were prepared by dissolving $EVBr_2$ and/or bromide salts in 18.2 MΩ water.

Tribromide (Br_3^-) solution. Bromine and Br_3^- were generated using the following chemical reactions:[36]

$$NaBrO_3 + 5\ Br^- + 6\ H^+ \rightarrow 3\ Br_{2(aq)} + 3\ H_2O$$

$$Br_{2(aq)} + Br^- \rightleftharpoons Br_3^- \qquad (K_{eq} = 16.1\ M^{-1})$$

Cell design and assembly. The construction of the redox-enhanced electrochemical capacitor (redox EC) cell including cell housing, current collectors, and the cell stack with two electrodes and a separator is described in detail in Chapters 2 and 3.[36] Briefly, a two-electrode cell was built from a perfluoroalkoxy (PFA) Swagelok fitting with glassy-carbon-capped current collectors. For the preparation of each cell stack, two electrodes were soaked in 1.5 mL of test electrolyte, and vacuum and N_2 (150 psi) were alternately applied to infiltrate the hydrophobic carbon electrodes with test aqueous electrolyte. Electrodes were then placed on either side of an electrolyte-wetted, 12-mm-diameter filter paper separator (Whatman™ #1). Thereafter, the cell stack was pressed between the two glassy-carbon-capped current collectors inside the cell body. For the three-electrode configuration tests, a T-shaped Swagelok PFA union was used with an Ag/AgCl reference electrode (Fisher Scientific™accumet™) placed with the tip at the edge of the separator with ~0.5 mL of excess test electrolyte added to submerge the reference electrode frit.

Electrochemical studies

All electrochemical experiments (cyclic voltammetry, controlled potential electrolysis, and galvanostatic charge/discharge cycling tests) were performed on a Bio-logic VMP3 potentiostat/galvanostat.

Analytical voltammetry. The cyclic voltammetry experiments were carried out in a conventional three-electrode cell with either a glassy carbon (CH Instruments, 3-mm-diameter) or activated carbon pellet (identical to carbon electrode used in cells; pasted on a carbon cloth with conducting grease) working electrode, a Pt wire counter electrode, and an Ag/AgCl reference electrode (CH Instruments). The glassy carbon electrode was polished using polishing alumina (0.05 μm), and the Pt wire electrode was rinsed first with acetone followed by water and methanol, and then dried before each experiment. Test solutions were purged with N_2 for 10 mins prior to each measurement.

Controlled potential electrolysis. Electrolysis experiments were performed in an open beaker-type cell with 6 mL of test electrolyte, i.e., 1 M KBr/0.2 M TBABr solution. Either carbon cloth, graphite rod or an activated carbon pellet (identical to carbon electrode used in cells; pasted on a carbon cloth with conducting grease) served as working electrodes and a platinum wire served as the counter electrode. An Ag/AgCl electrode was used as the reference electrode.

Electrochemical characterization of redox ECs. All galvanostatic charge/discharge (GCD) cycling tests were performed at a temperature of 25 ± 1 ºC, or in a temperature chamber for temperature-dependent studies. The applied

current for GCD cycling tests was normalized to the combined dry mass (activated carbon, carbon black, and PTFE binder) of both positive and negative electrodes. Potential limits were applied with the voltage range from 0 V (for discharging) to various V_{max} values (for charging). Energy and power reported in the text indicate discharge energy (E_{dis}) and average discharge power (P_{dis}), which are normalized to the *dry mass of both positive and negative electrodes* to get specific energy (W·h/kg) and specific power (W/kg), respectively. The following equations are used for calculating device performance (I = applied current, t = time, and V = voltage):

Charge capacity, Q_{ch} (mAh)	$Q_{\mathrm{ch}} = I_{\mathrm{ch}} \cdot t_{\mathrm{ch}}$	(4.1)
Discharge capacity, Q_{dis} (mAh)	$Q_{\mathrm{dis}} = I_{\mathrm{dis}} \cdot t_{\mathrm{dis}}$	(4.2)
Coulombic efficiency, η_C	$\eta_{\mathrm{C}} = Q_{\mathrm{dis}}/Q_{\mathrm{ch}}$	(4.3)
Charge energy, E_{ch} (Wh)	$E_{\mathrm{ch}} = \int_0^{t_{\mathrm{ch}}} I_{\mathrm{ch}} \cdot V(t)\, dt$	(4.4)
Discharge energy, E_{dis} (Wh)	$E_{\mathrm{dis}} = \int_0^{t_{\mathrm{dis}}} I_{\mathrm{dis}} \cdot V(t)\, dt$	(4.5)
Energy efficiency, η_E	$\eta_E = E_{\mathrm{dis}}/E_{\mathrm{ch}}$	(4.6)
Average power, P_{dis} (W)	$P_{\mathrm{dis}} = E_{\mathrm{dis}}/t_{\mathrm{dis}}$	(4.7)

The self-discharge rate was quantified based on the remaining discharge energy as a function of open-circuit time, δ. An open-circuit energy efficiency, η_R, is defined as the ratio of the energy retained after time δ at open circuit to the initial discharge energy and calculated by the following formula:

Open-circuit energy efficiency, η_R $\quad \eta_R(\delta) = E_{dis}(\delta)/E_{dis}(0)$ (4.9)

Normalized performance metrics

When the performance of devices including redox ECs is reported, normalizing to the dry mass of both positive and negative electrodes is the common practice in the literature. Therefore, we evaluated cell performance normalized by dry mass in the text so that direct comparisons can be made. However, we note that the redox couples in the electrolyte significantly contribute to the capacity through faradaic energy storage for the redox ECs. To clarify and address this discrepancy of the performance normalization, we also normalize energy, power, and capacity to both masses, i.e., performance metrics based on "wet" cell mass (electrodes plus electrolyte) and "dry" cell mass (electrodes only).

Performance normalization. Electrodes and electrolyte from a 1.2 M $EVBr_2$/0.12 M TBABr/2.88 M NaBr two-electrode cell massed before and after

cycling weighed 90 mg. The cell performance was then normalized to the total masses of electrodes only (indicated as g), and electrodes plus electrolyte (indicated as g_{wet}).

Other characterization methods

The UV-vis spectra were acquired on an Agilent 8453 UV-vis spectrophotometer equipped with a cuvette holder. All spectra were recorded under ambient conditions with a 1 cm light-path. Contact angle measurements were taken on a DataPhysics OCA 15Pro system using an automatic elliptical fitting program, and the images were recorded with a charge-coupled device (CCD) camera horizontal to the drop to allow measurements of the test electrolytes' contact angles on the sample surface. Raman spectroscopy was performed on a Horiba JY Aramis Raman microscope equipped with a CCD detector thermoelectrically cooled to -70 °C. Raman spectra were recorded with the incident laser of 0.86 mW, 600-μm hole, 400-μm slit width and a 600 lines/mm grating. The structure/morphology changes of carbon materials were observed through electron microscopes of a FEI Titan operating at 300 kV in scanning TEM mode, a FEI Quanta 600 SEM, and a FEI TECNAI™ T20 high-resolution transmission electron microscope (TEM) operating at 200 kV. The elemental compositions of positive electrodes and carbon pellets were analyzed

by energy-dispersive X-ray spectroscopy (EDX) at an accelerating voltage of 24.4 kV.

Contact-angle measurements. Aqueous solutions of 1 M KBr, 1 M MEPBr, and 1 M TBABr were prepared, and an activated carbon pellet (identical to carbon electrode used in cells) was used as a test surface. A 2-μL liquid droplet of test electrolyte was gently placed on the surface with a syringe, and the needle was withdrawn immediately to minimize any inconsistency that might be caused by solution evaporation prior to image capture. The contact angle was determined by using an automatic elliptical fitting program.

Controlled potential electrolysis, scanning transmission electron microscopy (STEM), and energy-dispersive X-ray spectroscopy (EDX). To demonstrate the electrochemical generation of the [$TBA^+ \cdot Br_3^-$] solid complex, anodic oxidation of bromide was carried out with a carbon cloth as working electrode. To an open beaker-type cell was added 6 mL of 1 M KBr/0.2 M TBABr solution, and controlled potential electrolysis at 1.2 V (vs Ag/AgCl reference electrode; a Pt wire counter electrode) was performed until yellow solids were clearly visible on the working electrode. Following electrolysis, the working electrode was photographed.

To investigate solid-state confinement of electrochemically generated [$TBA^+ \cdot Br_3^-$] solid complex in the pores of the high-surface-area carbon electrode, analysis of carbon surface/pores was conducted using STEM following electrolysis. For the electrolysis, a high-surface-area activated carbon pellet was pasted and pressed on a carbon cloth with conducting grease. The remaining area of the carbon cloth was masked with electrochemical tape to block its exposure to the electrolyte. As a control, an identical activated carbon pellet was separately prepared. Both pellets were immersed in the 1 M KBr/0.2 M TBABr solution, and vacuum/N_2 (150 psi) were alternately applied to infiltrate the hydrophobic carbons with this aqueous electrolyte. Electrolysis was performed with the first pellet (electrolyzed C pellet) as the working electrode in an open beaker-type cell with 1 M KBr/0.2 M TBABr solution at a set potential of 0.6 V (vs Ag/AgCl reference electrode; a Pt wire counter electrode). The potential increased incrementally to 1.2 V before the electrolysis was terminated after a charge of 10.4 C was passed. For the full duration of electrolysis, the control pellet (control C pellet) was immersed in a separate 1 M KBr/0.2 M TBABr solution.

Both carbon pellets were removed from the solutions and each surface was washed with water, soaked in 10 mL of water for 7 h, and dried in air at room temperature for 24 h. Samples for STEM analysis were prepared by sonicating (10 mins) small pieces of each pellet in isopropanol and drop-casting the

dispersion onto lacey-carbon TEM grids. The samples were imaged by STEM with the signal being acquired using a high-angle annular dark-field detector (HAADF-STEM). In addition, elemental analysis by EDX of the electrolyzed C pellet and control C pellet were performed.

UV-vis measurements for testing complexation of ethyl viologen dication (EV^{2+}) and Br_3^-. To generate spectra of uncomplexed EV^{2+}, 20 mM $EVBr_2$ solution was prepared in a 1.5 mL centrifuge tube, and the solution was agitated with a vortex mixer for 1 min followed by centrifugation for 5 min at 4,000 rpm (Eppendorf® MiniSpin Plus Centrifuge). Then, a 5 μL sample of the 20 mM $EVBr_2$ solution was diluted 400 times into 1.995 mL of water in a quartz cuvette. The capped cuvette was shaken to ensure a homogeneous analyte before UV-vis measurements.

In order to generate spectra of the EV^{2+} after complexation with Br_3^-, 500 μL of 60 mM $EVBr_2$ solution was combined with equal volumes of 120 mM Br_3^- solution and water. Then, EV remaining dissolved in the supernatant after the addition of Br_3^- was processed with the same methods stated above before UV-vis measurements. Optical absorption data for both uncomplexed and complexed EV^{2+} samples were normalized to the absorbance at the absorption maxima (λ_{max} = 260 nm) for the uncomplexed EV^{2+} sample.

UV-vis measurements for testing complexation of EV^{2+} and Br_3^- in the presence of methyl ethyl pyrrolidinium bromide (MEPBr) and tetrabutylammonium bromide (TBABr). To generate spectra of the EV^{2+} in the presence of Br_3^- and MEPBr or TBABr, respectively, to test competitive Br_3^- complexation between EV^{2+} and these quaternary ammonium cations, 500 μL of 60 mM $EVBr_2$ solution was combined with equal volumes of 120 mM Br_3^- solution and 120 mM quaternary ammonium bromide solution in a 1.5 mL centrifuge tube. Then, EV remaining dissolved in the supernatant was processed with the same methods stated above before UV-vis measurements. Each spectrum was normalized by the absorption maxima measured for uncomplexed EV^{2+} samples (in a solution containing the corresponding concentrations of MEPBr and TBABr, respectively, but without Br_3^-).

Control/comparison devices. An aqueous EDLC cell (1 M Na_2SO_4 electrolyte) and commercial nonaqueous device (BCAP0001 P270 T01, Maxwell Technologies) were tested to provide reference performance data in comparison to the EV/TBA/Br dual-redox EC. The 1 M Na_2SO_4 cell was assembled with the same cell housing, current collectors, electrodes, and separator as the EV/TBA/Br cell. The commercial cell was tested with a specified 2.7 V of working potential range. To report specific energy and specific power of the Maxwell cell

normalized to the dry mass of both positive and negative electrodes, the device was disassembled after GCD cycling tests. The extracted cell stack was placed in 20 mL aqueous NaOH solution to dissolve the aluminum foil current collector and isolate the electrodes. Thereafter, the electrodes were soaked in ~20 mL of doubly distilled water and dried in an oven at 160 °C until the mass remained constant.

Results and Discussion

Properties of Br_3^- complexing agents

In order to support the efficient use of the Br^-/Br_3^- redox couple for aqueous redox ECs, we selected and compared two differently-structured quaternary ammonium salts as complexing agents for Br_3^- (complexing agent refers to Br_3^- complexing agent throughout). Asymmetric cyclic methyl ethyl pyrrolidinium bromide (MEPBr), a commonly used complexing agent for aqueous bromine flow batteries, forms a separate oily-phase with Br_3^- while the symmetric and more hydrophobic tetrabutylammonium bromide (*n*-Bu_4NBr; TBABr) is known to form a solid complex.[34,37] We studied how each complexing agent affects the overall performance of the redox ECs relative to a control system without either additive.

Three asymmetric EC cells were constructed, all utilizing the Br^-/Br_3^- redox couple at the positive electrode, with (1) no complexing agent (1.2 M KBr electrolyte), (2) methyl ethyl pyrrolidinium bromide (MEPBr; 1 M KBr + 0.2 M MEPBr), and (3) tetrabutylammonium bromide (TBABr; 1 M KBr + 0.2 M TBABr), respectively. The negative counter electrode was purely capacitive and oversized to increase capacity so that the positive electrode could reach the Br^- oxidation potential with a total applied cell voltage of 1 V.

The influence of each complexing agent on the electrochemical behavior of the bromide catholyte in redox ECs was determined by galvanostatic charge/discharge (GCD) cycling tests of each asymmetric cell in a three-electrode configuration (Figure 37).

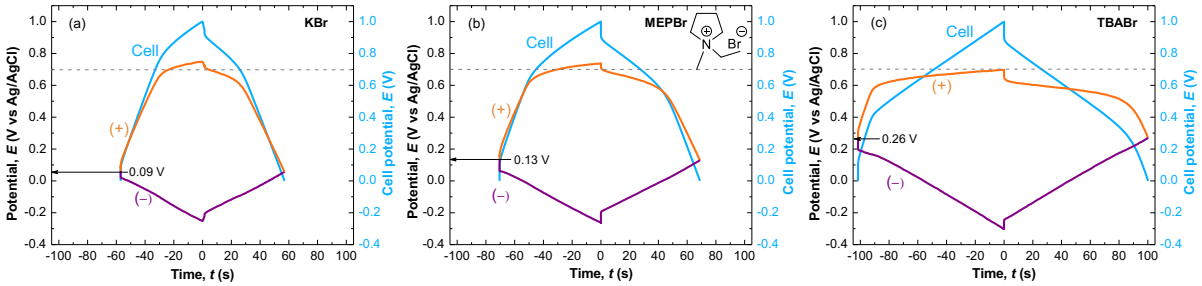

Figure 37. Galvanostatic charge/discharge potential profiles with different bromine complexing agents. The full asymmetric cells (blue curves) can be divided into contributions from the positive electrode (orange curves) and the negative electrode (purple curves), referenced to the centrally placed Ag/AgCl reference electrode. The cells were charged/discharged at a rate of 2 A/g (based on the mass of positive electrode only) to 1 V, with a 4:1 negative to positive electrode mass ratio; the aqueous electrolytes were (a) 1.2 M KBr, (b) 1 M KBr + 0.2 M MEPBr, and (c) 1 M KBr + 0.2 M TBABr.

All cells show electrochemical behavior that transitions from capacitive to faradaic energy storage at the positive electrode (orange curve), indicating oxidation of Br^- to Br_3^-, and only a capacitive (linear potential vs time/charge) response at the negative electrode (purple curve) during charging. Notably, there

are differences when TBABr is present as a complexing agent as compared to the KBr and KBr/MEPBr cells. For example, a greater potential of zero charge (PZC) was observed for the KBr/TBABr cell (0.26 V) compared to the KBr (0.09 V) and KBr/MEPBr (0.13 V) cells. The more positive PZC with KBr/TBABr electrolyte allows bromide oxidation to occur earlier in the charging stage and increases the ΔV for the capacitive negative electrode, which translates to greater faradaic charge storage at the positive electrode before the arbitrary cell cutoff potential of 1 V is reached (Figure 37; orange curves). Considering the amphiphilic nature of the tetrabutylammonium cation (TBA^+),[38,39] we reasoned that TBABr acts as a surfactant and TBA^+ adsorbs at the porous carbon electrodes. To verify this hypothesis, contact-angle measurements were conducted. The contact angle for the carbon electrode with a droplet of aqueous TBABr solution is ~24° smaller compared to a droplet of aqueous KBr solution (138°; Figure 38). This surfactant behavior may increase wettability of hydrophobic electrodes, and thus facilitate infiltration of hydrophilic bromide catholyte into the porous carbon electrode.[39]

Figure 38. Contact angle of test electrolyte on the surface of a porous activated carbon pellet. (left) aqueous KBr solution droplet; (middle) aqueous MEPBr solution droplet; (right) aqueous TBABr solution droplet.

We also observed that the onset point of the faradaic plateau at the positive electrode is a function of the complexing agent used. The horizontal grey dashed line drawn at 0.7 V in Figure 37 reflects the largest negative shift in the Br^-/Br_3^- redox potential for the KBr/TBABr cell. Additional cyclic voltammetry shows a redox potential that is consistent with the above GCD potential profile result, as well as a reversible redox reaction in the presence of TBABr (Figure 39).

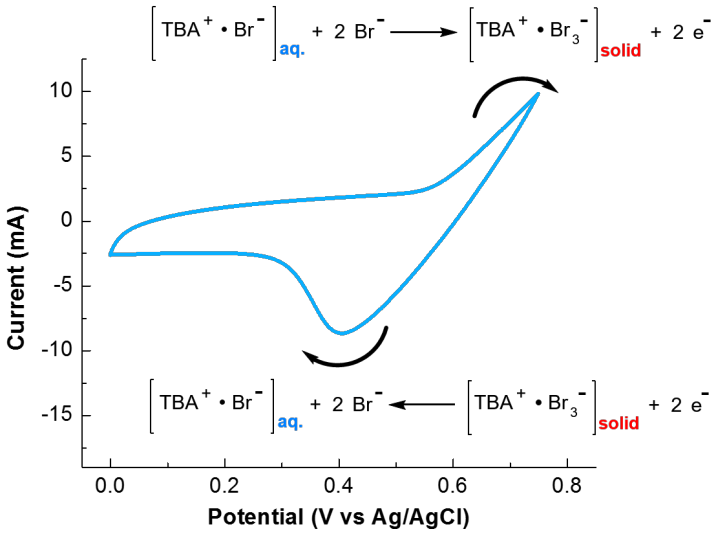

Figure 39. Cyclic voltammogram of 1 M KBr/0.2 M TBABr. An activated carbon pellet pasted on carbon cloth served as working electrode and a Pt wire as counter electrode. As reference, an Ag/AgCl electrode was used. The scan rate was 10 mV/s.

The observed electrochemical behavior can be explained by the reversible formation of [$TBA^+ \cdot Br_3^-$] solid complex that decreases the Br_3^- concentration at the interface between the electrolyte and the high-surface-area electrode. Both chemical (Figure 40a) and electrochemical (Figure 40b) methods confirm the generation of a [$TBA^+ \cdot Br_3^-$] solid complex. The image (Figure 40a; right vial) visually shows that after complexation induced by TBA^+, Br_3^- is almost entirely removed from the solution. Notably, the solutions with MEPBr (middle vial) and KBr (left vial) retain a yellow tint, demonstrating that a significant concentration of Br_3^- remains dissolved due to insufficient complexation by MEP^+ (and K^+,

respectively). Figure 40b shows electrochemical generation of a solid complex on the surface of a carbon cloth by passing anodic current in a KBr/TBABr electrolyte. The Raman spectrum taken of this solid exhibits an intense band at 169 cm^{-1}, which corresponds to symmetric stretching vibration of Br_3^-,[40,41] and its spectrum is identical to the Raman spectrum of commercial [$TBA^+ \cdot Br_3^-$] solid complex (Figure 40c). Further characterization of the electrochemically generated [$TBA^+ \cdot Br_3^-$] solid complex in an aqueous system is well-documented elsewhere.[37]

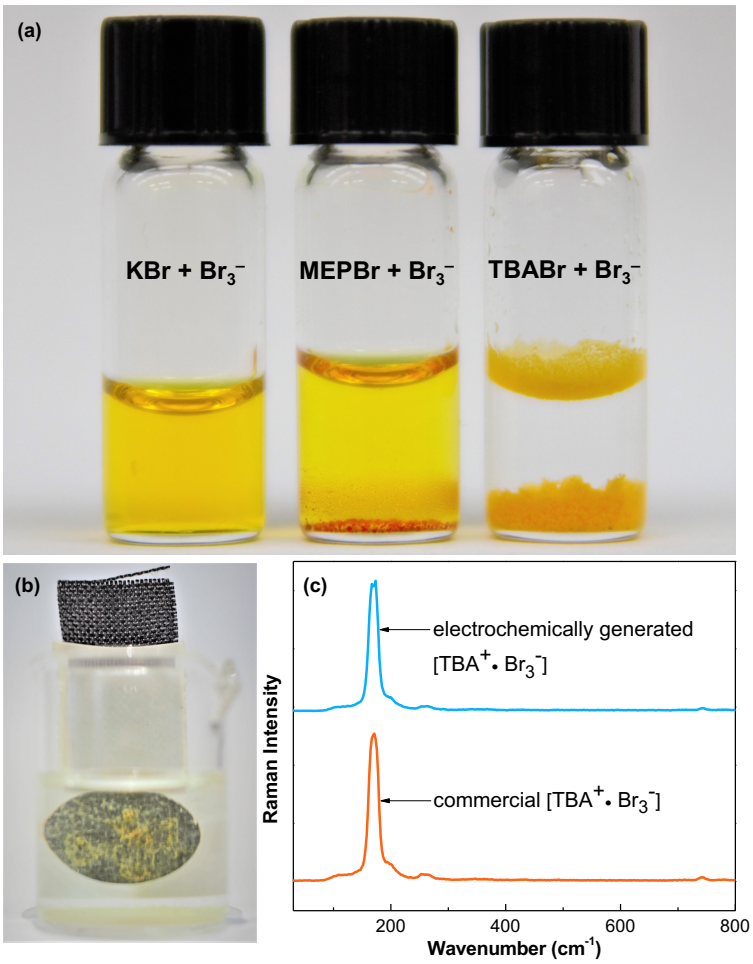

Figure 40. Complexation of tribromide with different quaternary ammonium species. (a) Complexation of chemically generated Br_3^- by the addition of potassium bromide (left), MEPBr (middle), and TBABr (right). (b) Electrochemically generated [$TBA^+ \cdot Br_3^-$] solid complex by controlled potential electrolysis. (c) Raman spectra of the electrochemically generated [$TBA^+ \cdot Br_3^-$] solid complex (blue curve) and commercial [$TBA^+ \cdot Br_3^-$] solid complex (orange curve).

Strong adsorption of the charged products within the electrodes has been found to be an effective mechanism to prevent cross-diffusion in a full redox EC cell.[26] We hypothesize that our complexation strategy may suppress cross-diffusion and redox shuttling even more effectively if the [$TBA^+ \cdot Br_3^-$] solid complex is retained *in the pores of the high-surface-area carbon electrodes*, instead of being formed and precipitating to the bulk solution upon charging. In order to investigate this hypothesis, controlled potential electrolysis with 1 M KBr/0.2 M TBABr solution was performed with an activated porous carbon pellet as the working electrode (denoted as electrolyzed C pellet) to provide a relevant, yet extreme charged state. As a control, an identical activated carbon pellet (denoted as the control C pellet) was separately prepared and infiltrated with same electrolyte solution through repeated vacuum/N_2 steps. No electrolysis was performed with this control carbon and hence no [$TBA^+ \cdot Br_3^-$] solid complex should be present in the sample.

Both carbon surfaces were analyzed by scanning TEM (STEM) with the signal being acquired using a high-angle annular dark-field detector (HAADF-STEM). In this imaging mode, the signal contrast scales linearly with sample thickness, and as the square of average atomic number (Z) of atoms in the sample.[42,43] Therefore, for our sample analysis, the higher average atomic number of the bromine-containing [$TBA^+ \cdot Br_3^-$] solid complex compared to that for

porous carbon may ensure that such complexes confined in the pores appear as bright regions in the image (Z-contrast imaging). Figure 41a shows a scanning TEM (STEM) image of the electrolyzed C pellet. The material displays clear contrast with nm-scale bright clusters that were hypothesized to contain the element Br. Subsequent elemental analysis by energy-dispersive X-ray spectroscopy (EDX) confirms the presence of Br in the carbon sample (Table 8). In contrast, the STEM image from the control C pellet displayed no high-contrast spots (Figure 41b), showing that infiltrated Br^- from KBr/TBABr solution is effectively removed during washing steps. Consistent with the STEM image, elemental analysis by EDX of the control carbon did not detect a Br signal (Table 8). This control experiment strongly supports the hypothesis that the bright regions observed by STEM of the electrolyzed C pellet (Figure 41a) originate from the high-Z insoluble bromide-containing [$TBA^+ \cdot Br_3^-$] complex that persists after washing, and not by Br^- from the solution which is easily removed. In sum, these data show that the [$TBA^+ \cdot Br_3^-$] solid complex generated in-situ during electrolysis is contained in the pores of the high-surface-area carbon. This complexation approach combined with porous carbon electrodes being used for EDLCs may lead to enhanced stability and slower self-discharge of the bromide-based redox ECs, without using ion-exchange membranes. We note that if a non-

porous electrode is used, precipitation of the [$TBA^+ \cdot Br_3^-$] solid complex away from the electrode can occur, which would cause irreversible capacity loss.

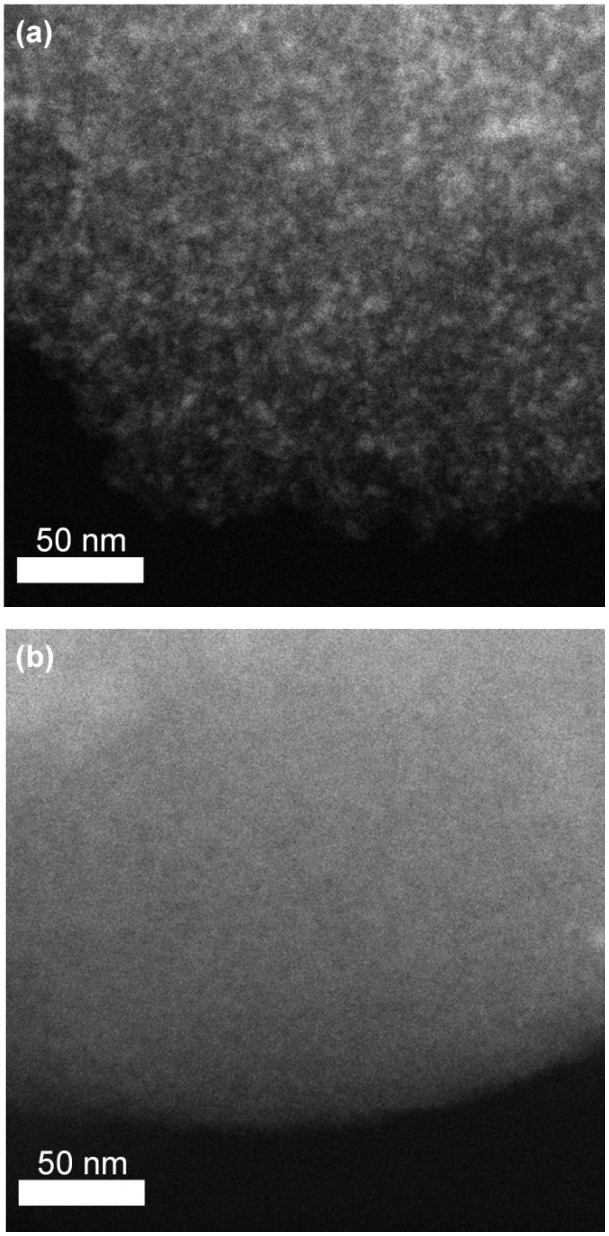

Figure 41. Imaging the [$TBA^+ \cdot Br_3^-$] solid complex in activated carbon pores. Scanning transmission electron microscopy images of (a) electrolyzed C pellet, and (b) the control C pellet, collected by a high-angle annular dark-field (HAADF) detector.

Table 8. Elemental analysis by EDX of electrolyzed and control C pellets

Sample	C	Br
Electrolyzed C pellet	28	72
Control C pellet	100	0

(relative atomic ratio of C to Br present in the sample; calculation based on the atom %)

In order to test stability and self-discharge rates, asymmetric cells were constructed in the two-electrode cell configuration with a paper separator (Whatman™ #1). In cycling stability tests, the KBr cell lost ~20% of its specific energy over 500 cycles. In contrast, the KBr/TBABr and KBr/MEPBr cells show no fading over the course of 500 cycles, and produce ~80% and ~40% higher energy density compared to the KBr cell, respectively (Figure 42a). Significant differences between the cells are further evident from self-discharge tests. The self-discharge rate determined by the open circuit energy efficiency, η_R, of the KBr/TBABr cell was substantially lower than that for KBr and KBr/MEPBr cells, retaining 50% of its energy after 10 h at open circuit, $\eta_R(10\text{ h}) = 50\%$, compared to $\eta_R(10\text{ h})$ of only 1% and 14% for the KBr and KBr/MEPBr cells, respectively (Figure 42b). Importantly, when the KBr cell was charged to 1.2 V to attain a higher capacity, which is closer to that of the KBr/TBABr cell, an even faster

self-discharge rate was observed (Figure 42b, solid blue vs dashed blue). This result implies that the self-discharge problem with uncomplexed Br^-/Br_3^- redox couple is worsened at higher states of charge, limiting its application in high-performance redox EC devices. The problems with cycling stability and self-discharge are much aggravated at 40 °C for the KBr and KBr/MEPBr cells relative to the KBr/TBABr cell, suggesting that the increased diffusivity of soluble Br_3^- at high temperatures accelerates the redox shuttle self-discharge mechanism (Figure 42c and d; results for self-discharge tests from 0 °C to 40 °C are summarized in Table 9).

Table 9. Open-circuit energy efficiency (η_R) for asymmetric cells

Open circuit energy efficiency, $\eta_R(\delta h)$	**1.2 M KBr cell**			**1 M KBr/0.2 M MEPBr cell**			**1 M KBr/0.2 M TBABr cell**		
	0 °C	**25 °C**	**40 °C**	**0 °C**	**25 °C**	**40 °C**	**0 °C**	**25 °C**	**40 °C**
η_R(2 h) (%)	43	40	8	63	66	44	80	79	70
η_R(6 h) (%)	20	5	0	44	34	9	67	62	49
η_R(10 h) (%)	10	1	0	32	14	2	59	50	37

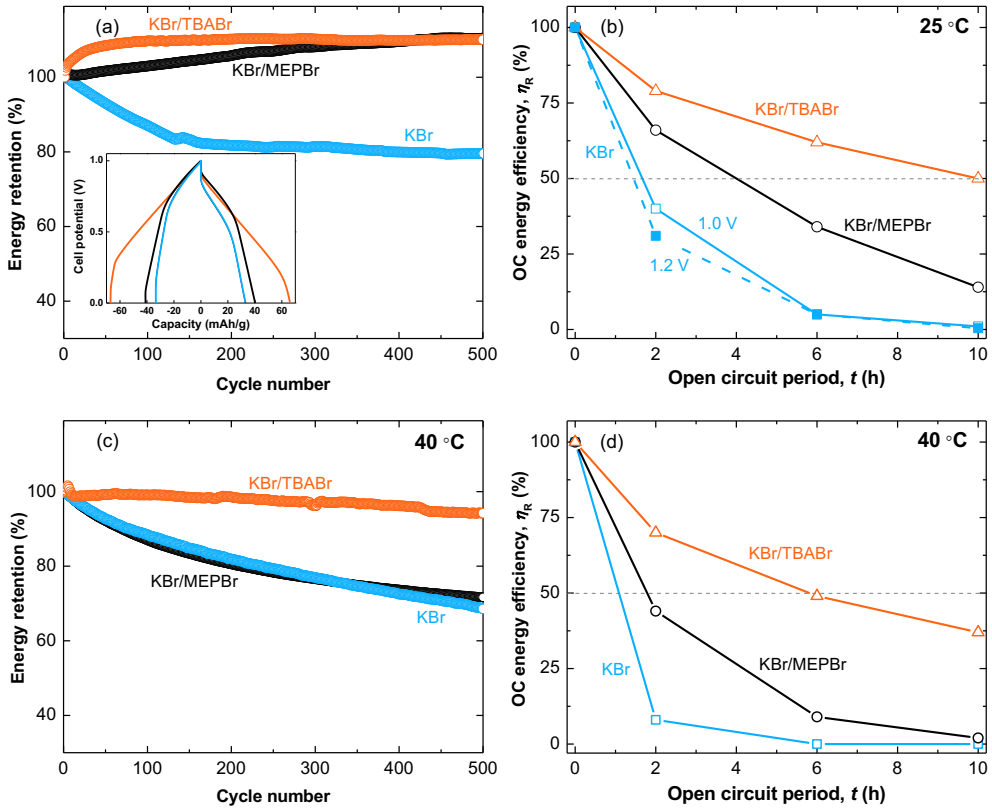

Figure 42. Stability and Self Discharge of two-electrode asymmetric cells with bromide catholyte. Cells were constructed with aqueous electrolytes of 1.2 M KBr (blue curve), 1 M KBr/0.2 M MEPBr (black curve), and 1 M KBr/0.2 M TBABr (orange curve), respectively. The cells were charged/discharged at a rate of 2 A/g (based on the mass of positive electrode only) to 1 V, with a 4:1 negative to positive electrode mass ratio. (a) Cycling stability of each cell tested at 25 °C; the inset shows two-electrode potential profiles vs capacity. (b) Open circuit (OC) energy efficiency (η_R) for each cell at 25 °C. Each data point was collected by charging the cell, allowing it to sit at open circuit for 2, 6, or 10 h, then discharging the cell completely. For the KBr electrolyte, self-discharge was tested for both a 1 V charge (solid blue) and a 1.2 V charge (dashed blue). (c) Cycling stability of each cell tested at 40 °C. (d) η_R at a given time for each cell at 40 °C.

These studies demonstrate that charge retention of bromide catholyte, and the stability and self-discharge performances, depend on whether Br_3^- is uncomplexed, complexed with MEP^+ (liquid state), or complexed with TBA^+ (solid state). Our results suggest that [$TBA^+ \cdot Br_3^-$] solid complex generated within the electrode pores suppresses cross-diffusion of oxidized bromide and lowers the self-discharge rate. Meanwhile MEPBr, a common complexing agent for bromine flow batteries, barely shows improvement over a cell without a complexing agent. The molecular structure of MEP^+, which lacks hydrophobic substituents, appears to provide insufficient complexation/precipitation with Br_3^- ,[37] leaving high concentrations of free Br_3^- in the electrolyte solution.

The question as to whether the decrease in specific energy observed for KBr and KBr/MEPBr cells is temporary due to reversible shuttling/diffusion effects or irreversible fading from chemical reactions was addressed by disassembling tested cells and assessing changes to the structure/morphology of the filter paper separator and carbon-electrode cell components. The separator from the KBr/TBABr cell appeared identical to the pristine paper separator before cycling, while the separators from the other cells are covered with a black solid (Figure 43). Raman spectra collected of the separator from the KBr/TBABr cell shows no clear peaks, and are identical to the Raman spectrum obtained from a pristine separator (Figure 44a). However, Raman spectra of the separators from the KBr

and KBr/MEPBr cells show peaks at approximately 1340 cm^{-1} and 1610 cm^{-1} which can be assigned to the D band and G band, respectively, of activated carbon.[44] The same peaks are observed for the non-cycled carbon electrode, indicating that the black solid observed in the separator was shed from the electrode. A control experiment where a pristine separator is soaked in Br_2/Br_3^- solution (that mimics the charged state of the cell) demonstrated no color change of the separator in the absence of the carbon electrode.

Figure 43. Paper separators after GCD cycling. (left) separator from asymmetric KBr/TBABr cell; (middle) separator from asymmetric KBr/MEPBr cell; (right) separator from asymmetric KBr cell.

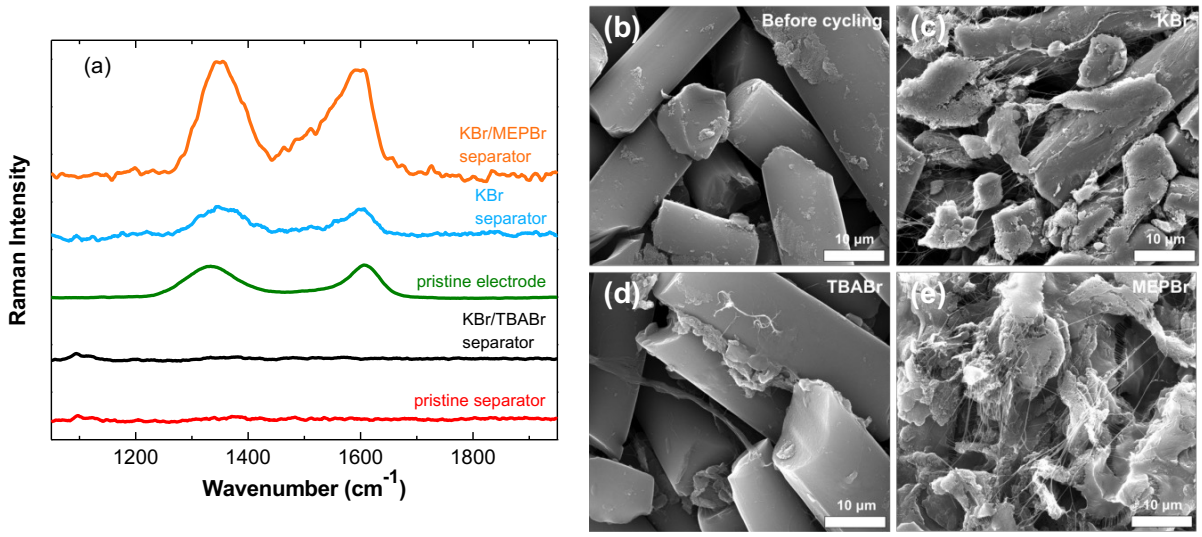

Figure 44. Analysis of paper separators after GCD cycling. (a) Raman spectra of the separators after cycling. Raman peaks for the non-cycled carbon electrode (green curve) are added to the plot for the comparison. (b to e) SEM images of positive electrodes. (b) Electrode before cycling. (c) Electrode from a KBr cell after cycling. (d) Electrode from a KBr/TBABr cell after cycling. (e) Electrode from a KBr/MEPBr cell after cycling.

Electron microscopy showed that the electrode exhibited little morphology change when cycled in a KBr/TBABr cell (Figure 44d). In contrast, we observe cracks and partial pulverization of carbon particulates on the electrode surface after cycling in KBr (Figure 44c) and KBr/MEPBr electrolytes (Figure 44e), providing evidence of carbon electrode degradation and its subsequent deposition onto the separator. Elemental analysis by EDX of the positive electrodes from

the KBr and KBr/MEPBr cells after cycling further confirm decreased carbon content (relative to F in the inert PTFE binder) compared to the electrode before cycling (Table 10).

Table 10. Elemental analysis by EDX of positive electrodes after cycling

Cells	C	F
Pristine activated carbon electrode	97	3
Electrode after cycling in a KBr cell	83	17
Electrode after cycling in a KBr/MEPBr cell	84	16
Electrode after cycling in a KBr/TBABr cell	98	2

(relative atomic ratio of C to F; calculation based on atom %)

Based on the experimental results, we propose that electrochemical intercalation induced by reactive bromine/polybromide causes permanent electrode degradation with time and thus irreversible fading of the KBr and KBr/MEPBr cells.[45,46] When TBA^+ is present, the concentration of non-complexed Br_2/Br_3^- is significantly reduced, thereby slowing irreversible side reactions and largely preventing electrode degradation upon repeated charge/discharge cycles. This TBA^+-induced solid complexation suppresses the permanent capacity loss mechanism. Overall, these results show an efficient way to utilize the bromide catholyte with readily available TBABr, the simple addition

of which simultaneously addresses the capacity loss as well as self-discharge problems for static bromide-enhanced redox ECs.

Designing a high-performance viologen/Br dual-redox EC with the addition of tetrabutylammonium complexing agent

For maximum faradaic energy storage, redox ECs should utilize redox-active electrolytes at both the positive electrode (catholyte) and negative electrode (anolyte) concurrently (dual-redox enhanced electrochemical capacitors; dual-redox ECs). We chose viologen (V) as a model anolyte to match the redox activity of the bromide catholyte and test the utility of tetrabutylammonium complexing agent in a full cell. While many families of redox-active anolytes should be compatible with the TBABr/Br^- catholyte, viologens have the advantage of an electrochemically reversible $V^{2+}/V^{\bullet+}$ redox couple.[36,47-49] In addition, V/Br cells typically have potential plateaus around 1.2 – 1.3 V, which coincides ideally with the thermodynamic stability window of water.

For the V/Br systems, (1) cycling stability largely depends on effective bromine storage in the positive electrode,[36] (2) only viologens with hydrophobic substituents, e.g., pentyl (PV)[36] or heptyl viologen (HV),[26] can function as an efficient Br_3^- complexing agent, limiting the capacity for faradaic energy storage due to their low solubility (e.g., < 0.2 M for HV), and thus (3) it is desirable to

enhance energy density by using highly soluble viologens to increase the available concentration of anolyte while finding other means to complex Br_3^- and maintain cycling stability. We envisioned that addition of TBABr to V/Br electrolytes should (1) suppress the fading mechanism at the positive electrode and (2) enable the use of more-soluble, short-alkyl-chain viologens at the negative electrode, in order to (3) maintain cycling stability while producing high energy density in a single device. To verify our hypothesis, readily available ethyl viologen (1,1′-diethyl-4,4′-bipyridinium dibromide; EV) was selected as an anolyte due to its high solubility (> 2 M) and the stability of $EV^{2+}/EV^{\bullet+}$ redox couple with a highly cathodic redox potential ($E_{1/2}$ = -0.64 V vs Ag/AgCl) in aqueous electrolytes.[50] Additionally, $EVBr_2$ shows good solution compatibility with a bromide catholyte (e.g., NaBr) in an analytical voltammetry cell (Figure 45).

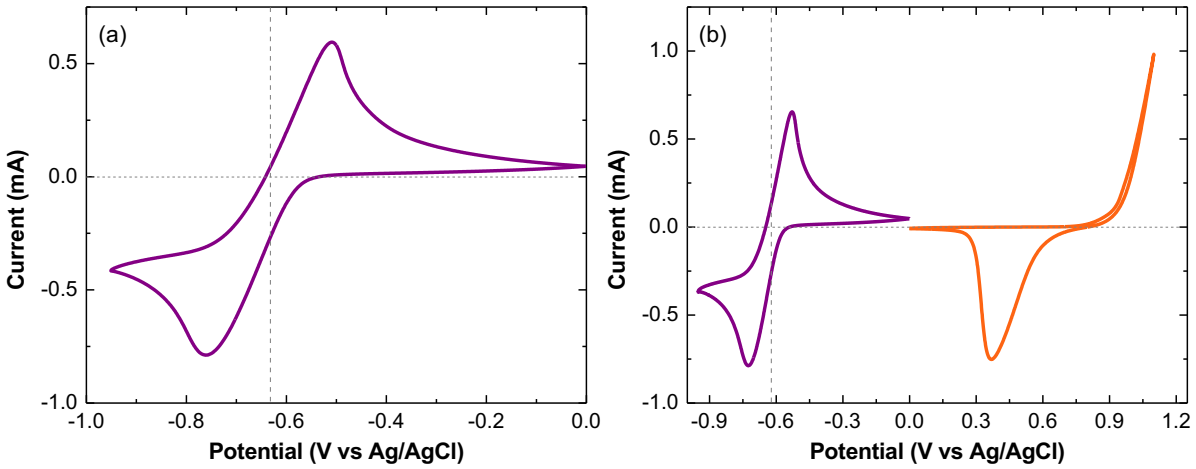

Figure 45. Cyclic voltammograms of $EVBr_2$ electrolytes. (a) 0.1 M $EVBr_2$ scanned from 0 V to -0.95 V and (b) 0.1 M $EVBr_2$/0.1 M NaBr scanned from 0 V to -0.95 V (purple curve) and 0 V to +1.1 V (orange curve), separately. Scan rate: 20 mV/s; Glassy carbon served as the working electrode and a Pt wire served as the counter electrode. As reference, an Ag/AgCl electrode was used.

First, a control cell with a readily soluble 1.2 M $EVBr_2$/3 M NaBr electrolyte, *without additional complexing agent*, was assembled and tested. Three-electrode GCD profiles show *dual* faradaic responses at both positive and negative electrodes, corresponding to Br^- oxidation to Br_3^- and EV^{2+} reduction to $EV^{\bullet+}$, respectively, upon charging (Figure 46a). This cell produced a specific energy of ~68 W·h/kg at 1 A/g, but the cell capacity faded and only retained 82% of the initial energy over 1000 cycles (Figure 46b). This poor cycle life confirms that short-alkyl-chain viologens do not effectively retain reactive Br_2/Br_3^-, which

decreases cell stability. To improve the cycle life of EV/Br redox ECs, electrolyte design must utilize a Br_3^- complexing agent that has stronger Br_3^- complexing capacity than EV.

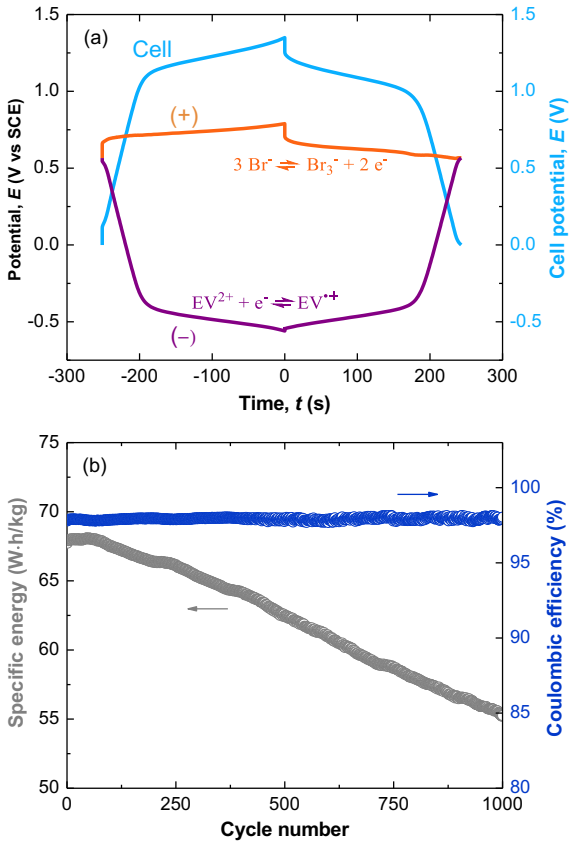

Figure 46. 1.2 M $EVBr_2$/3 M NaBr cells. (a) Three-electrode GCD potential profiles for the positive electrode (orange curve), negative electrode (purple curve), and total cell (blue curve) cycled to 1.35 V at 1 A/g. During charging, the electrochemical behavior transitions from capacitive to faradaic at both electrodes. (b) Specific energy, cycling stability and Coulombic efficiency of an EV/Br two-electrode cell cycled to 1.35 V at 1 A/g.

The degree of (solid) complexation of TBABr with Br_3^-, relative to EV, was tested by determining how much EV precipitates from an aqueous Br_3^- solution with and without this complexing agent additive. The amount of precipitated EV was indirectly quantified by measuring the concentration of the remaining viologen in solution with ultraviolet-visible spectroscopy (UV-vis).

Figure 47 shows that the addition of stoichiometric quantities of Br_3^- decreased the concentration of EV dissolved in the solution by ca. 83% due to precipitation of the nominally [EV^{2+}·$2Br_3^-$] solid complex (EV^{2+}; blue open-square curve vs EV^{2+}/Br_3^-; blue open-circle curve), which still leaves substantial free, non-complexed Br_3^- present in the solution, causing the poor cycling life of the EV/Br cell. Importantly, when TBABr was added together with Br_3^- and EV, EV remained completely dissolved (EV^{2+}; blue open-square curve vs $EV^{2+}/Br_3^-/TBA^+$; orange solid curve). These UV-vis results confirm that TBABr has a greater Br_3^- complexing capacity than EV^{2+} and that [TBA^+·Br_3^-] solid complex is preferentially formed. Notably, MEPBr, a common Br_2/Br_3^- complexing agent for aqueous flow battery systems, does not induce any additional complexation/precipitation with Br_3^- in the presence of EV^{2+} (EV^{2+}/Br_3^-; blue open-circle curve vs $EV^{2+}/Br_3^-/MEP^+$; black solid curve), which correlates with the poor stability and fast self-discharge results obtained for the previous asymmetric KBr/MEPBr cell. This relative interaction strength, i.e., MEP^+ <

EV^{2+} < TBA^{+}, is consistent with previous findings that indicate hydrophobicity enhances solid complexation,[36,37] and suggests that TBABr should be a suitable complexing agent for EV/Br dual-redox ECs.

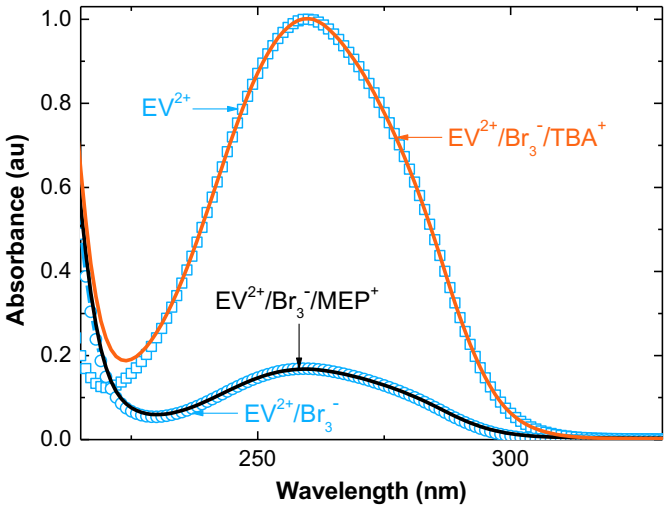

Figure 47. UV–vis absorption spectra quantifying the concentration of uncomplexed EV^{2+} in solution. Absorption maxima correspond to the concentration of EV^{2+} remaining dissolved in the supernatant without Br_3^- (EV^{2+}; blue open-square curve), with the addition of Br_3^- (EV^{2+}/Br_3^-; blue open-circle curve), with Br_3^- and TBABr ($EV^{2+}/Br_3^-/TBA^+$; orange solid curve), and with Br_3^- and MEPBr ($EV^{2+}/Br_3^-/MEP^+$; black solid curve), respectively. The spectra are normalized to the absorption maxima of the EV^{2+} (λ_{max} = 260 nm).

A two-electrode cell with a 1.2 M $EVBr_2$/2.88 M NaBr/0.12 M TBABr electrolyte (i.e., 10 mol % addition of TBABr based on the molar concentration of $EVBr_2$), paper separator, and symmetric activated carbon electrodes (areal

mass loading of 12.7 mg/cm^2) was assembled and tested by GCD. The concentration of EV and Br were set at 1.2 M and 3 M, respectively, for the comparison with standard EV/Br cell, and 10 mol % addition of TBABr ensures that this electrolyte concentration is readily soluble, thus providing simple solution preparation and lower viscosity. The cell (denoted as EV/TBA/Br) produced ~64 W·h/kg at 1 A/g with ~97% Coulombic efficiency and a high energy efficiency of ~84% when charged/discharged between 0 V and 1.35 V (full performance metrics summarized in Table 11). Most importantly, the specific energy of the cell degraded by only ~3% over 1000 cycles compared to 18% capacity loss of the cell without TBABr cycled under the same conditions (Figure 48a). For the long-term cycling test, the EV/TBA/Br cell maintained stability with 90% energy retention over 5000 cycles (charge/discharge at 2 A/g) and exhibited ~4% degradation over an additional 7000 cycles when operated from 0 V to 1.3 V at the same current density (Figure 48b). This stability increase shows that the superior performance of short-alkyl-chain viologens can be maintained without sacrificing lifetime through the addition of TBABr. Furthermore, the EV/TBA/Br cell shows good self-discharge characteristics. The EV/Br control cell has η_R (6 h) = 28% when charged to 1.35 V, due to gradual cross-diffusion of the charged Br_3^- and $EV^{\bullet+}$ species from the positive and negative electrodes, respectively. In contrast, the EV/TBA/Br cell, which is

designed to suppress the Br^-/ Br_3^- shuttle, shows improved self-discharge with η_R (6 h) = 53% when charged to 1.3 V and η_R (6 h) = 45% when charged to 1.35 V. For these two conditions the open circuit voltage losses are only 13% and 16%, respectively, comparable to other redox ECs that use costly ion-selective membrane separators (Figure 48c). The ability to forgo the use of the ion-selective membrane is made possible by the solid-state confinement of the bromine species in the porous carbon electrode.

Table 11. Performance metrics normalized to different cell components

	Dry electrodes	**Wet electrodes**
Normalization mass (mg)	20 mg Cathode: 10 mg Anode: 10 mg	90 mg Electrolyte: 70 mg Electrodes: 20 mg
Specific energy (W·h/kg)	63.6 W·h/kg	14.1 W·h/kg_{wet}
Specific capacity (mA·h/g)	66.6 mA·h/g	14.8 mA·h/g_{wet}
Specific power (W/kg)	970 W/kg	216 W/kg_{wet}

(cell was charged/discharged between 0 and 1.35 V at 1 A/g. Energy, capacity, and power reported here are from the 20th charge/discharge cycle.)

The Ragone plot in Figure 48d shows that the EV/TBA/Br cell provides a power performance higher than 3 kW/kg while still retaining ~15 W·h/kg energy density (based on the mass of dry electrodes). In order to provide further performance comparison, an aqueous EDLC (1 M Na_2SO_4 electrolyte) and a

commercial non-aqueous EDLC (BCAP0001 P270 T01, Maxwell Technologies) were tested as control/comparison devices. Figure 48d shows that the EV/TBA/Br cell produced specific energy well above the 1 M Na_2SO_4 cell (black curve) at all power rates. Compared to the commercial non-aqueous cell, this cell delivered as high as ~250% increased specific energy over a wide range of power rates up to ~3 kW/kg. Overall, these results further demonstrate that the EV/TBA/Br redox EC system substantially improves energy as well as power densities of aqueous EDLCs by adding dual faradaic reactions at both the positive and negative electrodes, without negatively impacting cycle life.

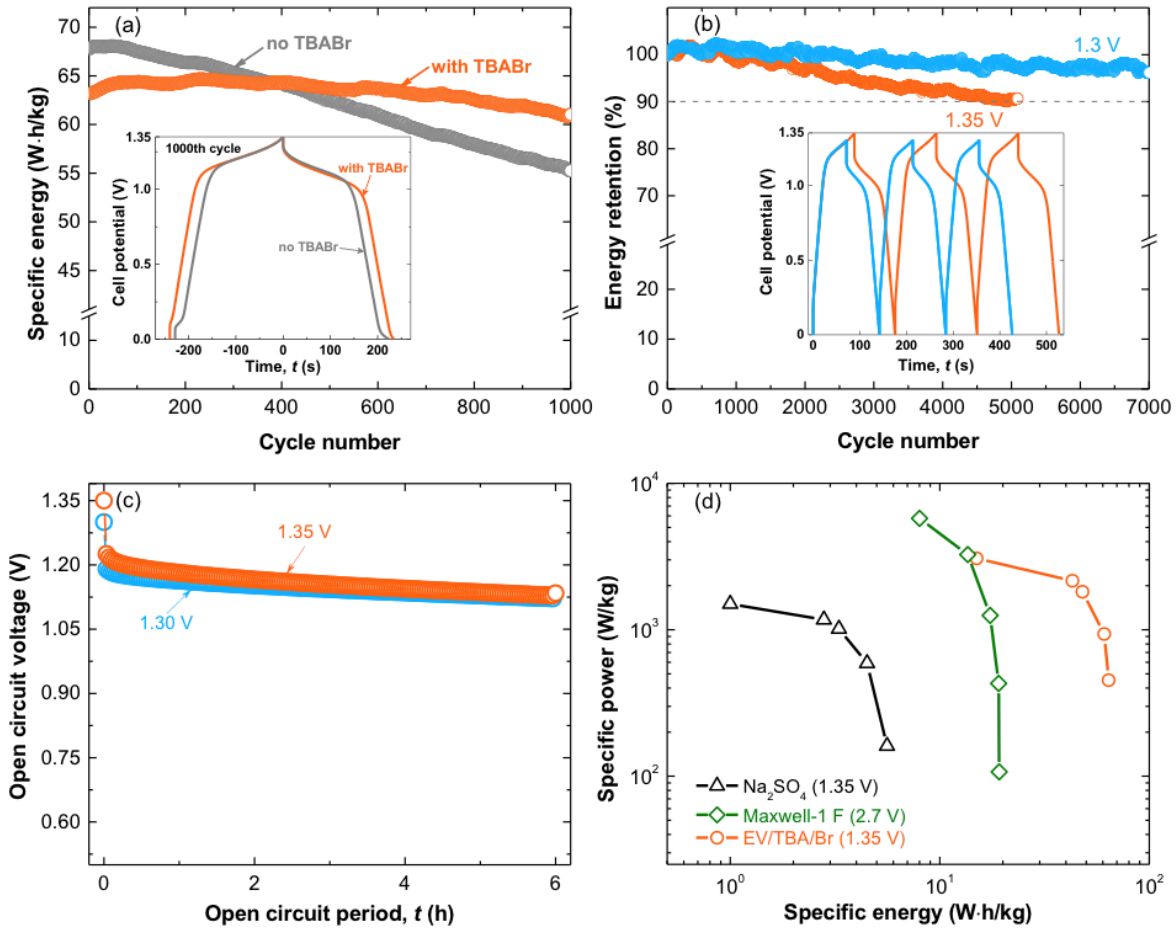

Figure 48. A 1.2 M $EVBr_2$/0.12 M TBABr/2.88 M NaBr cell. (a) Specific energy and cycling stability of EV/Br cells with and without TBABr; the inset shows GCD profiles at the 1000th cycle. (b) Long-term cycling stability of the EV/TBA/Br cell cycled at 2 A/g to 1.3 V, and to 1.35 V; the inset shows GCD profiles for the last 3 cycles. (c) Open circuit voltage for 6 h after charging the cell to 1.35 V (orange curve) and 1.3 V (blue curve), respectively. (d) Specific energy vs power of the EV/TBA/Br cell (orange curve) and its comparison to Na_2SO_4 (black curve) and commercial Maxwell (green curve) cells. Specific energy and power of all cells, including the commercial EDLC, were normalized to the dry mass of both positive and negative electrodes. Rate tests of the EV/TBA/Br cell were performed after the initial 1000 GCD cycles at 1 A/g.

Conclusions

We propose a shift away from the conventional use of a mobile, liquid state to complex Br_3^- and report a fundamentally different solution to complex/store Br_3^- for aqueous redox ECs. We demonstrate with microscopic-level evidence that reversible solid complexation of Br^-/Br_3^- redox couple induced by tetrabutylammonium bromide effectively stores reactive and diffusive bromine within the pores of the carbon electrodes. This mechanism suppresses unwanted chemical reactivity and cross-diffusion of Br_2/Br_3^- that results in improved cycling stability and self-discharge rates of redox ECs. We used this fundamental understanding of chemical and electrochemical processes at the electrolyte/electrode interface to develop a high-performance dual-redox EC. This dual-redox EC, which integrates TBABr with an ethyl viologen anolyte and a bromide catholyte, produces a record specific energy with stable cycling at high power levels: Addition of tetrabutylammonium improves all aspects of device performance including stability, energy and power density without adding complexity to the fabrication process. The system can be assembled without a dry room or glove box, uses *aqueous* electrolyte with readily available salts, and has a cost-effective paper separator that avoids the use of expensive ion-selective membranes. These attributes address hurdles to practical commercialization, and low costs of production may be possible. Our systematic approach to efficiently

utilize bromide catholyte with a non-redox-active cation and design of a high-performance dual-redox EC should be informative and promise to be readily applicable for a wide variety of energy storage applications, especially for the science of hybrid electrochemical energy-storage systems (e.g., pairing a high-performance bromide catholyte at positive electrode with faradaic battery-type or pseudocapacitive negative electrode).

References

1 Béguin, F., Presser, V., Balducci, A. & Frackowiak, E. Carbons and Electrolytes for Advanced Supercapacitors. *Adv. Mater.* **26**, 2219-2251 (2014).

2 Simon, P. & Gogotsi, Y. Materials for electrochemical capacitors. *Nat. Mater.* **7**, 845-854 (2008).

3 Burke, A. Ultracapacitors: why, how, and where is the technology. *J. Power Sources* **91**, 37-50 (2000).

4 Blomquist, N. *et al*. Metal-free supercapacitor with aqueous electrolyte and low-cost carbon materials. *Sci. Rep.* **7**, 39836 (2017).

5 Wang, Y., Song, Y. & Xia, Y. Electrochemical capacitors: mechanism, materials, systems, characterization and applications. *Chem. Soc. Rev.* **45**, 5925-5950 (2016).

6 Fic, K., Meller, M., Menzel, J. & Frackowiak, E. Around the thermodynamic limitations of supercapacitors operating in aqueous electrolytes. *Electrochim. Acta* **206**, 496-503 (2016).

7 Gao, Q., Demarconnay, L., Raymundo-Pinero, E. & Beguin, F. Exploring the large voltage range of carbon/carbon supercapacitors in aqueous lithium sulfate electrolyte. *Energy Environ. Sci.* **5**, 9611-9617 (2012).

8 Arbizzani, C. *et al*. Safe, high-energy supercapacitors based on solvent-free ionic liquid electrolytes. *J. Power Sources* **185**, 1575-1579 (2008).

9 Augustyn, V., Simon, P. & Dunn, B. Pseudocapacitive oxide materials for high-rate electrochemical energy storage. *Energy Environ. Sci.* **7**, 1597-1614 (2014).

10 Sheberla, D. *et al*. Conductive MOF electrodes for stable supercapacitors with high areal capacitance. *Nat. Mater.* **16**, 220-224 (2017).

11 Brezesinski, T., Wang, J., Tolbert, S. H. & Dunn, B. Ordered mesoporous [alpha]-MoO3 with iso-oriented nanocrystalline walls for thin-film pseudocapacitors. *Nat. Mater.* **9**, 146-151 (2010).

12 Lang, X., Hirata, A., Fujita, T. & Chen, M. Nanoporous metal/oxide hybrid electrodes for electrochemical supercapacitors. *Nat. Nanotechnol.* **6**, 232-236 (2011).

13 Yan, J., Wang, Q., Wei, T. & Fan, Z. J. Recent Advances in Design and Fabrication of Electrochemical Supercapacitors with High Energy Densities. *Adv. Energy Mater.* **4**, 1300816 (2014).

14 Muller, G. A., Cook, J. B., Kim, H.-S., Tolbert, S. H. & Dunn, B. High Performance Pseudocapacitor Based on 2D Layered Metal Chalcogenide Nanocrystals. *Nano Lett.* **15**, 1911-1917 (2015).

15 Boota, M., Chen, C., Becuwe, M., Miao, L. & Gogotsi, Y. Pseudocapacitance and excellent cyclability of 2,5-dimethoxy-1,4-benzoquinone on graphene. *Energy Environ. Sci.* **9**, 2586-2594 (2016).

16 Fic, K., Meller, M. & Frackowiak, E. Interfacial Redox Phenomena for Enhanced Aqueous Supercapacitors. *J. Electrochem. Soc.* **162**, A5140-A5147 (2015).

17 Frackowiak, E., Meller, M., Menzel, J., Gastol, D. & Fic, K. Redox-active electrolyte for supercapacitor application. *Faraday Discuss.* **172**, 179-198 (2014).

18 Roldán, S., Blanco, C., Granda, M., Menéndez, R. & Santamaría, R. Towards a Further Generation of High-Energy Carbon-Based Capacitors by Using Redox-Active Electrolytes. *Angew. Chem., Int. Ed.* **50**, 1699-1701 (2011).

19 Lee, J. *et al.* Tin/vanadium redox electrolyte for battery-like energy storage capacity combined with supercapacitor-like power handling. *Energy Environ. Sci.* **9**, 3392-3398 (2016).

20 Senthilkumar, S. T., Selvan, R. K. & Melo, J. S. Redox additive/active electrolytes: a novel approach to enhance the performance of supercapacitors. *J. Mater. Chem. A* **1**, 12386-12394 (2013).

21 Lee, J., Choudhury, S., Weingarth, D., Kim, D. & Presser, V. High Performance Hybrid Energy Storage with Potassium Ferricyanide Redox Electrolyte. *ACS Appl. Mater. Interfaces* **8**, 23676-23687 (2016).

22 Wang, X. *et al*. High Energy Density Aqueous Electrochemical Capacitors with a KI-KOH Electrolyte. *ACS Appl. Mater. Interfaces* **7**, 19978-19985 (2015).

23 Lee, J. *et al*. Asymmetric tin–vanadium redox electrolyte for hybrid energy storage with nanoporous carbon electrodes. *Sustainable Energy Fuels* **1**, 299-307 (2017).

24 Chen, L., Bai, H., Huang, Z. & Li, L. Mechanism investigation and suppression of self-discharge in active electrolyte enhanced supercapacitors. *Energy Environ. Sci.* **7**, 1750-1759 (2014).

25 Wang, B. *et al*. A Hybrid Redox-Supercapacitor System with Anionic Catholyte and Cationic Anolyte. *J. Electrochem. Soc.* **161**, A1090-A1093, (2014)

26 Chun, S.-E. *et al*. Design of aqueous redox-enhanced electrochemical capacitors with high specific energies and slow self-discharge. *Nat. Commun.* **6**, 7818 (2015).

27 Senthilkumar, S. T., Selvan, R. K., Lee, Y. S. & Melo, J. S. Electric double layer capacitor and its improved specific capacitance using redox additive electrolyte. *J. Mater. Chem. A* **1**, 1086-1095 (2013).

28 Tang, X., Lui, Y. H., Chen, B. & Hu, S. Functionalized carbon nanotube based hybrid electrochemical capacitors using neutral bromide redox-active electrolyte for enhancing energy density. *J. Power Sources* **352**, 118-126 (2017).

29 Li, Q. *et al*. Redox enhanced energy storage in an aqueous high-voltage electrochemical capacitor with a potassium bromide electrolyte. *J. Power Sources* **348**, 219-228 (2017).

30 Zhao, Y. *et al*. A reversible Br2/Br- redox couple in the aqueous phase as a high-performance catholyte for alkali-ion batteries. *Energy Environ. Sci.* **7**, 1990-1995 (2014).

31 Sankar, K. V. & Kalai Selvan, R. Improved electrochemical performances of reduced graphene oxide based supercapacitor using redox additive electrolyte. *Carbon* **90**, 260-273 (2015).

32 Biswas, S. *et al*. Minimal architecture zinc-bromine battery for low cost electrochemical energy storage. *Energy Environ. Sci*. **10**, 114-120 (2017).

33 Gerhardt, M. R. *et al*. Anthraquinone Derivatives in Aqueous Flow Batteries. *Adv. Energy Mater*. **7**, 1601488 (2017).

34 Lancry, E., Magnes, B.-Z., Ben-David, I. & Freiberg, M. New Bromine Complexing Agents for Bromide Based Batteries. *ECS Trans*. **53**, 107-115 (2013).

35 Poon, G., Parasuraman, A., Lim, T. M. & Skyllas-Kazacos, M. Evaluation of N-ethyl-N-methyl-morpholinium bromide and N-ethyl-N-methyl-pyrrolidinium bromide as bromine complexing agents in vanadium bromide redox flow batteries. *Electrochim. Acta* **107**, 388-396 (2013).

36 Evanko, B. *et al*. Efficient Charge Storage in Dual-Redox Electrochemical Capacitors through Reversible Counterion-Induced Solid Complexation. *J. Am. Chem. Soc*. **138**, 9373-9376 (2016).

37 Hoshino, K., Ando, M., Oikawa, Y., Okuma, M. & Murashiro, K. Reversible electrochromism between transparent and white using aqueous systems of tetrabutylammonium/bromide and tetrabutylphosphonium/bromide. *Sol. Energy Mater. Sol. Cells* **137**, 15-25 (2015).

38 Fic, K., Lota, G. & Frackowiak, E. Electrochemical properties of supercapacitors operating in aqueous electrolyte with surfactants. *Electrochim. Acta* **55**, 7484-7488 (2010).

39 Fic, K., Lota, G. & Frackowiak, E. Effect of surfactants on capacitance properties of carbon electrodes. *Electrochim. Acta* **60**, 206-212 (2012).

40 Chen, X. *et al*. Raman Spectroscopic Investigation of Tetraethylammonium Polybromides. *Inorg. Chem*. **49**, 8684-8689 (2010).

41 Zambounis, J. S., Kamitsos, E. I., Patsis, A. P. & Papavassiliou, G. C. Resonance Raman and far-infrared studies of n-Bu4NI3 and n-Bu4NBr3. *J. Raman Spectrosc*. **23**, 81-85 (1992).

42 Klein, N. D., Hurley, K. R., Feng, Z. V. & Haynes, C. L. Dark Field Transmission Electron Microscopy as a Tool for Identifying Inorganic Nanoparticles in Biological Matrices. *Anal. Chem*. **87**, 4356-4362 (2015).

43 Bals, S., Kabius, B., Haider, M., Radmilovic, V. & Kisielowski, C. Annular dark field imaging in a TEM. *Solid State Commun*. **130**, 675-680 (2004).

44 Genovese, M., Jiang, J., Lian, K. & Holm, N. High capacitive performance of exfoliated biochar nanosheets from biomass waste corn cob. *J. Mater. Chem. A* **3**, 2903-2913 (2015).

45 Gaier, J. R., Ditmars, N. F. & Dillon, A. R. Aqueous electrochemical intercalation of bromine into graphite fibers. *Carbon* **43**, 189-193 (2005).

46 Izumi, I., Sato, J., Iwashita, N. & Inagaki, M. Electrochemical intercalation of bromine into graphite in an aqueous electrolyte solution. *Synth. Met*. **75**, 75-77 (1995).

47 Janoschka, T., Martin, N., Hager, M. D. & Schubert, U. S. An Aqueous Redox-Flow Battery with High Capacity and Power: The TEMPTMA/MV System. *Angew. Chem., Int. Ed*. **55**, 14427-14430 (2016).

48 Hoshino, K., Oikawa, Y., Sakabe, I. & Komatsu, T. Reversible polycolour change of viologens from violet through transparent to white. *Electrochim. Acta* **55**, 165-170 (2009).

49 Liu, T., Wei, X., Nie, Z., Sprenkle, V. & Wang, W. A Total Organic Aqueous Redox Flow Battery Employing a Low Cost and Sustainable Methyl Viologen Anolyte and 4-HO-TEMPO Catholyte. *Adv. Energy Mater*. **6**, 1501449 (2016).

50 Sathyamoorthi, S., Kanagaraj, M., Kathiresan, M., Suryanarayanan, V. & Velayutham, D. Ethyl viologen dibromide as a novel dual redox shuttle for supercapacitors. *J. Mater. Chem. A* **4**, 4562-4569 (2016).

Chapter 5

Stackable bipolar pouch cells with metal-free current collectors for high-power electrochemical energy storage with corrosive aqueous electrolytes

Introduction

Aqueous electrochemical energy storage is currently under intense investigation and development due to the promise of low cost, environmental friendliness, high power, and safe operation.[1–6] Despite recent advances with active materials (i.e., electrodes and electrolytes) for aqueous electrochemical energy storage, successful translation of lab-scale test cells into practical applications remains scarce due to the lack of viable cell designs and the cost and technical difficulties of large-scale manufacturing. To facilitate commercialization of these nascent systems, it is important to look not just at active materials, but to also diagnose and solve problems related to entire cell components and device design. One example that fits into these categories is the current collector, an essential but often overlooked component in any electrochemical energy storage device that can have a significant impact on the viability of a scaled cell.

Current collectors provide mechanical support for the active materials in the electrode and a path for electrons to travel to and from the device terminals. A current collector (CC) designed for commercially viable high-power aqueous devices must be low-cost, electrically conductive, mechanically tough, and (electro)chemically stable in the electrolyte under a wide working potential range. Additionally, it must be thin and lightweight to avoid compromising cell-

level volumetric or gravimetric performance. Designing CCs that simultaneously meet all of these critical requirements is challenging. Metal foils, for example, provide high electronic conductivity, but aqueous electrolytes corrode most metals, limiting practical choices to stainless steel, nickel, or titanium.[2,7] Even these metals/alloys are unstable in acidic conditions, limiting their use to neutral-pH and alkaline chemistries.

Unlike metals, carbon allotropes are generally stable over a much wider range of electrolyte conditions.[8] Carbon has the additional advantage of better contact resistance with electrode materials due to the lack of a passivating oxide layer.[9] Further, it also suppresses hydrogen and oxygen evolution due to large kinetic overpotentials, which effectively widens the electrochemical stability window of aqueous electrolytes.[4] Consequently, the use of carbon as a current collector is well-explored. Expanded graphite foil has been shown to be a suitable current collector for aqueous electrochemical energy storage, but one drawback is its porous structure, which makes it permeable to electrolyte.[5,10–12] Carbon fiber and carbon nanotube papers and mats have also been used, but are again porous, fragile, and too resistive for practical application.[2,11] In flow batteries and fuel cells, rigid graphite or carbon/polymer composite plates are commonly employed as CCs, but these thick materials end up responsible for the majority of the cost, weight and volume of the stack, making them unattractive for use in compact,

portable (non-flow) cells.[13,14] Pyrolytic graphite has been considered for use with corrosive electrolytes, but it is not mechanically tough and its high cost quickly rules it out as a CC candidate for mass production.[15]

To address the limitations of existing metallic and carbon-based current collectors, we searched for alternative materials that could be widely applicable in a range of electrolytes for high-power aqueous energy storage. This chapter discusses the use of a carbon black/polyethylene composite film (CBPE) as a current collector material. This material is commercially available (mass-produced for antistatic packaging), low-cost, thin, and lightweight. We systematically investigate and demonstrate that CBPE exhibits a wide electrochemical stability window in a variety of aqueous electrolytes, but find that its insufficient conductivity prevents its use as a CC in a conventional cell architecture. To address this critical drawback, we developed a *bipolar pouch cell architecture* where current flows through-plane instead of in-plane, shortening the distance that it must travel through the CBPE CC. This configuration allows for the current collector material to have higher resistivity, and thus solves the low electrical conductivity issue of CBPE. Further, the flexible and heat-sealable CBPE composite serves simultaneously as the cell packaging and seal in addition to its role as a current collector, enabling the facile construction of stacked pouch cells with shared bipolar CCs. To test this conceptual platform for use in aqueous

electrochemical energy storage, we constructed non-flow zinc bromine batteries and demonstrated that the system operates in challenging conditions that combine a corrosive and acidic electrolyte with a wide operating voltage. These cells achieve a cell-level energy density of 50 Wh/L at a 10 C rate (0.5 kW/L), with less than 1% capacity loss over 500 cycles. This energy density is competitive with commercial Pb-acid batteries while the power density and stability are an order of magnitude better. Furthermore, a larger, 4-cell stack is built to illustrate that the pouch cells are scalable and stackable without sacrificing performance. The resulting device employs 3 bipolar CCs, operates in the range of 6-7 V, and has an internal self-balancing mechanism that prevents any individual cell in the stack from overcharging damage.

Materials and Methods

Materials. All reagents and starting materials were obtained commercially and used as received without any further purification. Sodium bromide (NaBr), sodium sulfate (Na_2SO_4), and tetrabutylammonium bromide (TBABr) were purchased from Sigma-Aldrich. Zinc bromide ($ZnBr_2$) was purchased from Fisher Chemical. Norit® A Supra activated carbon was purchased from Acros Organics. The carbon black/polyethylene composite film (CBPE) was purchased from Caplinq (Linqstat XVCF). Water was from a Milli-Q Simplicity™ 185 system with resistivity ≥ 18.2 MΩ·cm (if not specified, all solutions in the SI and text refer to aqueous solutions).

Cell design and assembly

Carbon electrodes. For the preparation of electrodes, activated carbon (Norit A Supra), polytetrafluoroethylene (PTFE) binder (60 weight % aqueous dispersion from Sigma-Aldrich), and acetylene black conductive additive (Vulcan® XC72R) were mechanically mixed in a 90:5:5 mass ratio with isopropanol, and the resulting slurry was repeatedly rolled and folded with a PTFE rolling pin. This mass was then rolled between sheets of PET plastic into a single freestanding film with a thickness of 165 ± 15 μm with an Emporio® Pasta Machine. Electrodes were cut from the film and dried overnight at 175 ºC

in air, and then further dried under high vacuum at room temperature for two days.

$ZnBr_2$ electrolyte. The electrolyte prepared for the cells in this chapter was 5 M $ZnBr_2$ + 1 M NaBr. To suppress dendrite formation, a polyethylene glycol (PEG, M.W. = 200) additive was included at 4.5% v/v.[16]

Pre-adsorption of TBABr complexing agent. TBABr does not dissolve in the $ZnBr_2$/NaBr electrolyte because tetrabromozincate anions, $[ZnBr_4]^{2-}$, will form and precipitate as an insoluble complex with TBA^+ out of solution.[17**] To solve this problem, the TBABr complexing agent was pre-adsorbed to the activated carbon by soaking the electrode in a solution of 0.25 M TBABr in the absence of $ZnBr_2$ (Figure 49). The electrodes were submerged in this solution for 4 h while vacuum and N_2 (150 psi) were alternately applied to infiltrate the hydrophobic carbon electrodes.

The quantity of TBABr adsorbed during this step was measured for one electrode by dabbing away excess electrolyte after soaking and then drying the

---

** This reference notes that a solid precipitate forms when mixing 1 M TBABr and 1 M $ZnBr_2$. We observed the same behavior when NaBr is present, but in the absence of NaBr we saw the formation of a separate highly viscous organic phase rather than solid precipitation.

sample for 2 days under high vacuum at room temperature instead of constructing a cell from the wet electrode. The dry electrode mass increased by 49% relative to the initial mass before soaking. Normalized to the mass of the activated carbon electrode, this amount of TBABr can form a quantity of $TBABr_3$ equivalent to 80 mAh/g of capacity. Additional formation of the weaker $TBABr_5$ or $TBABr_7$ complexes would correspond to even higher complexed capacities of 160 mAh/g or 240 mAh/g, respectively.[18,19]

$ZnBr_2$ Pouch cell Assembly. After the TBABr pre-adsorption/soaking step, the wet electrode is put into contact with a paper separator that has been saturated with a fixed volume of the $ZnBr_2$/NaBr electrolyte. The full cell assembly consists of the activated carbon positive electrode, a 180-μm-thick paper separator, and a plastic spacer between two CBPE current collectors. This cell assembly is heat-sealed to form a pouch and left to rest for 12 h before cycling/performance tests. As the $ZnBr_2$ diffuses into the electrode during this period, the TBA-bromozincate complex forms and adsorbs to the activated carbon surface (Figure 49). This mixing of the electrolyte with the aqueous TBABr solution in the electrode dilutes the $ZnBr_2$ electrolyte, decreasing the concentration from the initial 5 M in the separator to ~ 2.5-3 M in the final assembled cell.

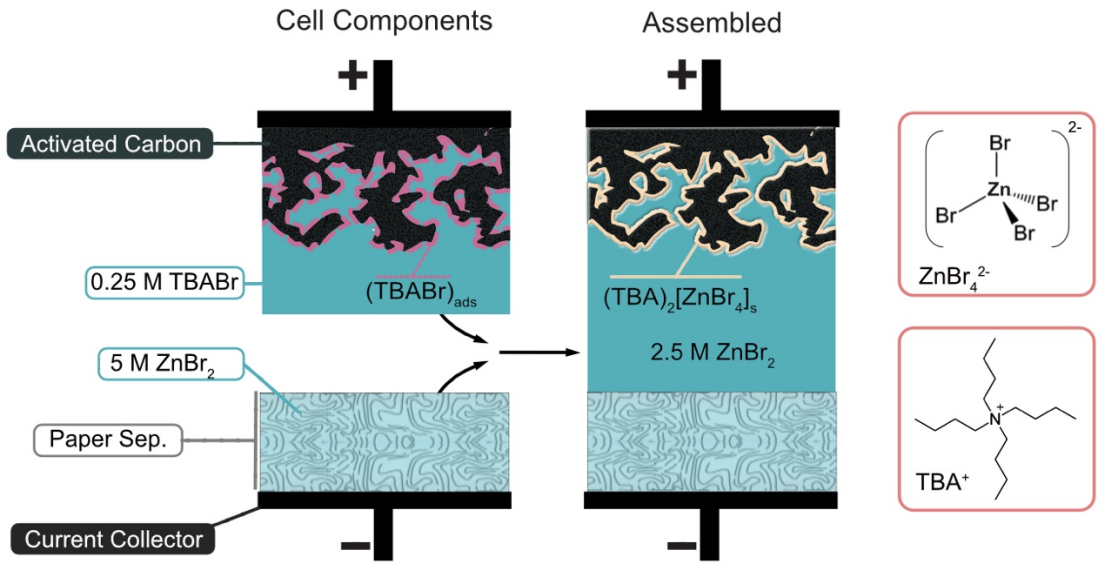

Figure 49. Zinc bromide cell construction. The activated carbon electrode is pre-soaked in a TBABr solution to pre-adsorb the Br_3^- complexing agent at the surface. Separately, the paper separator is wet with a fixed volume of the $ZnBr_2$ electrolyte. When the electrode is placed in contact with the separator in a cell assembly, bromozincate anions complex with TBA^+ and precipitate. This procedure ensures that both the complex and the TBA^+ it contains are retained in the high-surface-area pores of the electrode.

Pouch Preparation. To prepare the heat-sealed pouches, square pieces of CBPE current collector (Linqstat XVCF), paper separator (Whatman™ #1), and polyethylene spacer (90-μm-thick plastic bag) are cut according to the dimensions in Table 12.

Table 12. Dimensions of pouch cell components

	Individual Pouch	**Scaled Bipolar Stack**
Electrode(s)	1.0 cm × 1.0 cm	2.5 cm × 2.5 cm
Plastic Spacer(s)	Outer: 3 cm × 3 cm Inner: 1.1 cm × 1.1 cm	Outer: 4.5 cm × 4.5 cm Inner: 2.54 cm × 2.54 cm
Separator(s)	1.27 cm × 1.27 cm	3 cm × 3 cm
CBPE CC(s)	2.5 cm × 2.5 cm	4 cm × 4 cm
Electrolyte*	35 μL	195 μL (per cell)

*This represents the quantity of $ZnBr_2$ electrolyte added directly to the dry separator. Due to the additional aqueous TBABr in the positive electrode, the total electrolyte volume is ~60% higher after assembly.

After the pouch cell materials are cut, cell assembly is completed with a commercial heat sealer (KF-305 hand sealer, 12" × 5mm) with the following steps:

1. The plastic spacer is heat-sealed to all four edges of the negative CBPE CC. The paper separator is trapped between these layers at its edges and held in position laterally by the sealed edges (Figure 50a).
2. The positive CBPE CC is then heat-sealed to the other side of the plastic spacer on one edge to create a flexible flap (Figure 50b).
3. After adding $ZnBr_2$ electrolyte to the paper separator and placing the TBABr-soaked electrode on top of the separator, the flap is closed and the remaining three edges are sealed (Figure 50c).

For bipolar current collectors, instead of sealing a single CBPE CC onto the top of the pouch in Step 2, the new layer that becomes the flap is another CBPE CC/plastic spacer assembly, identical to that prepared in Step 1. In the scaled bipolar pouch cell, for example, there are four identical CBPE/plastic spacer assemblies before assembly (one negative CC and 3 bipolar CCs) and one CBPE positive CC (Figure 50d). For each new cell added to the top of the stack, steps 2 and 3 are repeated.

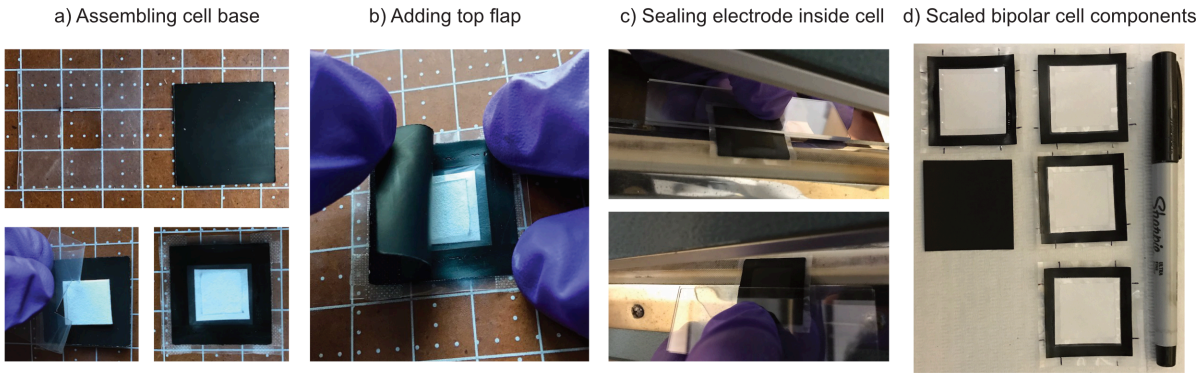

Figure 50. Assembly of pouch cells. (a) The plastic spacer is heat-sealed to all four edges of the negative CBPE CC. (b) The positive CBPE CC is heat-sealed to the other side of the plastic spacer on one edge to create a flexible flap. (c) After adding $ZnBr_2$ electrolyte and the positive electrode, the flap is closed and the remaining three edges are sealed. (d) Current collectors prepared for the scaled bipolar pouch before assembly. A negative CC/plastic spacer assembly (top left), positive CC (middle left), and three bipolar CC/plastic spacer assemblies (right) are shown. The markings on the plastic spacers are to assist with alignment.

Testing configuration. To test individual pouch cells, the sealed pouch was placed between two rigid endplates (Figure 51). The endplates consist of aluminum tape stuck to a glass plate. To improve electrical contact between the aluminum foil and the pouch, the metal is roughened with sandpaper and coated with a thin layer of conductive carbon conductive assembly paste (MG Chem 847-25ML). Pressure is then applied to the full assembly using a pair of small (¾") steel binder clips, and the leads are clipped to the protruding aluminum tape before cell cycling.

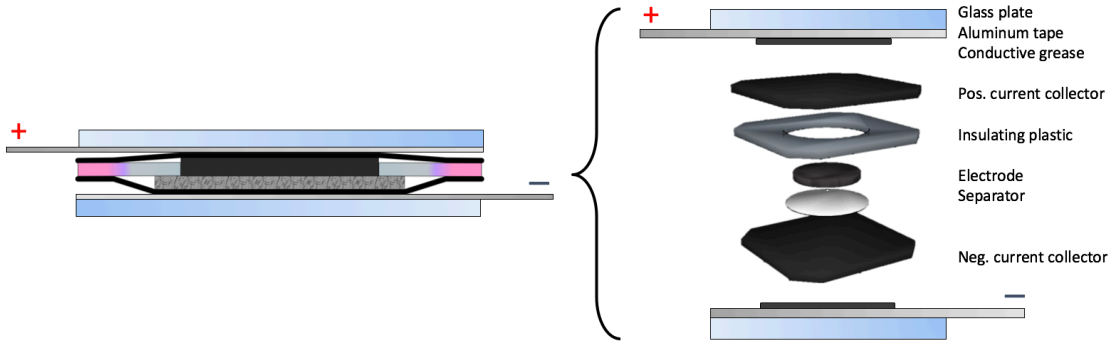

Figure 51. Testing setup for pouch cells. The heat-sealed pouch is placed between glass plates covered in aluminum tape and a carbon conductive paste. External pressure is applied to the entire assembly by a pair of steel binder clips (not shown) acting as compressive springs.

For the scaled bipolar pouch, a similar procedure was followed. As shown in the manuscript, titanium plates were used as endplates instead of aluminium tape on glass. The metal plates were again roughened and covered in conductive carbon paste, and four steel binder clips were used to apply pressure to the stack.

Electrochemical characterization

All linear sweep voltammetry and galvanostatic charge/discharge (GCD) cycling tests were performed at a temperature of 25 ± 1 ºC on a Bio-logic VMP3 potentiostat/galvanostat.

Linear Sweep voltammetry. The linear sweep voltammetry experiments were carried out on a Bio-logic VMP3 potentiostat/galvanostat with a conventional three electrode cell. Test electrolytes included 1 M Na_2SO_4, 1 M H_2SO_4, 1 M NaCl, and 1 M KOH. The reference electrode was Ag/AgCl (CH Instruments, 1 M KCl internal filling solution) for all electrolytes except KOH, which used an Hg/HgO reference electrode (1 M KOH internal filling solution). Candidate current collector materials including 316L Stainless Steel foil (ESPI Metals KNC7823), Nickel foil (MTI EQ-PLIB-NTAB), Titanium foil (STREM Chemicals 93-244), or CBPE (Linqstat XVCF) were used as working electrodes. These electrodes were masked with electrochemical tape (3M-484) to expose only a circular 6-mm-diameter area to the electrolyte. To minimize the effect of

IR drop from poor in-plane conductivity for tests with CBPE, the side of the film not in contact with the electrolyte was laminated to roughened copper foil with conductive carbon conductive assembly paste (MG Chem 847-25ML).

Before each experiment, the masked working electrode was rinsed with isopropanol and then water, and the Pt wire counter electrode was rinsed first with acetone followed by water. Test solutions were purged with N_2 for 10 mins prior to each measurement. Cathodic sweeps were performed from the open circuit potential (E_{OC}) to -2.5 V and anodic sweeps were performed from E_{OC} to 2.5 V. The potential sweeps terminated early if a cutoff condition of 0.5 mA (1.77 mA•cm^{-2}) was reached. For each working electrode/electrolyte combination, three cathodic sweeps were performed first, followed by three anodic sweeps. The third sweeps were plotted for comparison.

Electrochemical characterization of pouch cells. The applied current for GCD cycling tests was normalized to the dry mass (activated carbon, carbon black, and PTFE binder) of the positive electrode. Charging was performed to a capacity limit of 50 mAh/g, 100 mAh/g, or 150 mAh/g. Potential limits were applied for discharging, with V_{min} values of 1 V for single cells and 5 V for the scaled bipolar stack. The following equations are used for calculating device performance (I = applied current, t = time, and V = voltage):

Charge capacity, Q_{ch} (mAh)	$Q_{\text{ch}} = I_{\text{ch}} \cdot t_{\text{ch}}$	(5.1)
Discharge capacity, Q_{dis} (mAh)	$Q_{\text{dis}} = I_{\text{dis}} \cdot t_{\text{dis}}$	(5.2)
Coulombic efficiency, η_{C}	$\eta_{\text{C}} = Q_{\text{dis}}/Q_{\text{ch}}$	(5.3)
Charge energy, E_{ch} (Wh)	$E_{\text{ch}} = \int_0^{t_{\text{ch}}} I_{\text{ch}} \cdot V(t)\, dt$	(5.4)
Discharge energy, E_{dis} (Wh)	$E_{\text{dis}} = \int_0^{t_{\text{dis}}} I_{\text{dis}} \cdot V(t)\, dt$	(5.5)
Energy efficiency, η_{E}	$\eta_E = E_{\text{dis}}/E_{\text{ch}}$	(5.6)
Voltage efficiency, η_{V}	$\eta_V = \eta_E/\eta_C$	(5.7)
Average power, P_{dis} (W)	$P_{\text{dis}} = E_{\text{dis}}/t_{\text{dis}}$	(5.8)

Energy and power reported in the text indicate discharge energy (E_{dis}) and average discharge power (P_{dis}) and are normalized on both a gravimetric and volumetric basis. For gravimetric normalization, specific power and energy are calculated based on the mass of the activated carbon electrode (including the binder and conductive carbon additive) to be consistent with other similar systems reported in the literature. For volumetric normalization, power and energy density are calculated based on the pouch volume. This volume is calculated by multiplying the geometric area of the electrode, A, by the thickness of the pouch (electrode + separator + CBPE CCs), d. This neglects the volume

occupied by the seal around the perimeter of the pouch, but the volume of this region is small and becomes increasingly negligible as the cell scales to larger sizes.

The self-discharge rate was quantified based on the remaining discharge energy as a function of open circuit time, δ. An open circuit energy efficiency, η_{R}, is defined as the ratio of the energy retained after time δ at open circuit to the initial discharge energy and calculated by the following formula:

Open circuit energy efficiency, η_{R} $\quad \eta_{\mathrm{R}}(\delta) = E_{\mathrm{dis}}(\delta)/E_{\mathrm{dis}}(0)$ (5.9)

Resistivity/Conductivity Calculations

Monopolar current collectors. To calculate current collector (CC) requirements for an idealized monopolar cell architecture we devised a model corresponding to the diagram in Figure 52a. It is assumed that the current density, J, across the electrode-CC interface is uniform over the entire cell and that a continuous, highly conductive tab runs across the entire top of the CC to connect it to the device terminals. In an actual cell, tabbing is unlikely to be continuous and there will also be voltage gradients within the CC that cause higher current densities near the tabs and lower current densities further from tabs. However, in the high-rate charge-discharge condition discussed in this chapter, current density

is likely to be limited by the resistance from the electrolyte and electrode, rather than the CC, making the uniform current density assumption reasonable for a first-order analysis.

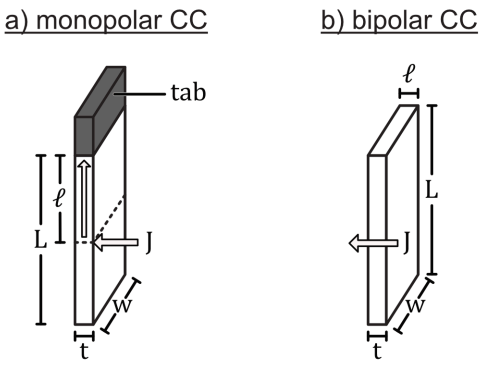

Figure 52. Simplified schematic of monopolar and bipolar current collectors. (a) The parameters for estimating the *IR* drop in (a) a monopolar CC and (b) a bipolar CC. The CC dimensions for both schematics are the height, L, the width, w, and the thickness, t. The current density, J, across the electrode/CC interface is uniform at all points, and each distance ℓ indicates the path length between the points where current enters the CC and the point where it exits through the tab.

The monopolar CC dimensions shown in Figure 52a are its height, L, measured perpendicular to the tab, its width, w, measured parallel to the tab, and its thickness, t. In this configuration current must flow a distance, ℓ, from the point where it enters the CC to the tab. In the CC there is a fixed resistivity, ρ, and the current flows through a cross-sectional area, A, where $A = w \cdot t$. The

contribution to the *IR* drop that is attributed to the monopolar current collector (V_{MCC}) for each value of ℓ is calculated by using the following equation:

$$dV_{\mathrm{MCC}} = dI \cdot R_{\mathrm{MCC}}(\ell)$$

Where R_{MCC} is the resistance of the current collector at a distance ℓ from the tab and *dI* is the current entering the CC at this distance. It is possible to express these values in terms of ℓ:

$$dI = J \cdot w \cdot d\ell$$

$$R_{MCC} = \frac{\rho \cdot \ell}{A} = \frac{\rho \cdot \ell}{w \cdot t}$$

Combining these equations gives:

$$dV_{MCC} = J \cdot w \cdot d\ell \cdot \frac{\rho \cdot \ell}{w \cdot t} = J \cdot \frac{\rho \cdot \ell}{t} d\ell$$

This equation is then simplified and integrated over the entire CC area:

$$V_{MCC} = \int_0^L J \cdot \frac{\rho \cdot \ell}{t} d\ell = \frac{\mathrm{J} \cdot \rho \cdot \mathrm{L}^2}{2t}$$

Finally, for the full cell, the *IR* drop at the transition from charge to discharge (ΔV_{MCC}) is calculated by using $\Delta J = J_{ch} - J_{dis}$. The value for ΔV_{MCC} is doubled to account for two electrodes and CCs in each cell:

$$\Delta V_{MCC} = \frac{\Delta \mathrm{J} \cdot \rho \cdot \mathrm{L}^2}{t}$$

This relationship assumes that electrodes are coated onto only one side of the monopolar CC. Double-sided coating would double *dI* and place more demanding requirements on CC materials.

Bipolar current collectors. The *IR* drop calculation was repeated for bipolar CCs. The bipolar CC dimensions shown in Figure 52b are again the height, L, the width, w, and the thickness, t. The current density, J, across the entire electrode-CC interface is uniform over the entire cell at all conditions for a bipolar cell. In this configuration current flows in the through-plane direction over a distance ℓ, where $\ell = t$. In the CC there is a fixed resistivity, ρ, and the current flows through a cross-sectional area, A, where $A = w \cdot L$. The contribution to the *IR* drop that is attributed to the bipolar current collector (V_{BCC}) is calculated with the following equation:

$$V_{BCC} = I \cdot R_{BCC}$$

Where R_{BCC} is the resistance of the bipolar current collector and I is the current passing through the CC. It is possible to express these values alternately as:

$$I = J \cdot w \cdot L$$

$$R_{BCC} = \frac{\rho \cdot \ell}{A} = \frac{\rho \cdot t}{w \cdot L}$$

Combining these equations gives:

$$V_{BCC} = J \cdot w \cdot L \cdot \frac{\rho \cdot t}{w \cdot L} = J \cdot \rho \cdot t$$

Finally, for the full cell, the *IR* drop at the transition from charge to discharge (ΔV_{BCC}) is calculated by using $\Delta J = J_{ch} - J_{dis}$. The value for V_{BCC} is doubled to account for two electrodes and CCs per cell, then halved to account for each CC being shared between two cells:

$$\Delta V_{BCC} = \Delta J \cdot \rho \cdot t$$

In the manuscript, the derived equations for ΔV_{MCC} and ΔV_{BCC} are used to calculate the maximum resistivity, ρ, a monopolar or bipolar CC material could have (while maintaining an *IR* drop less than ΔV_{CC} at a current density of ΔJ) as a function of cell size, L, for a variety of thicknesses, t. For example, for a cell size of 5 cm with 50-μm-thick current collectors we can apply the condition that the CC *IR* drop contribution be less than 100 mV at a current density of ±100 mA • cm^{-2}. Using the equations for ΔV_{MCC} and ΔV_{BCC} with these values we find that for a monopolar cell the highest acceptable value for ρ is 1.0×10^{-4} Ω•cm and that for a bipolar cell the highest acceptable value for ρ is a substantially higher 100 Ω•cm.

Cost Estimates

Previous studies have compared the relative price of 200-μm-thick sheets of different current collector materials offered in small quantities from specialty suppliers.[7,10] Due to the different cell architecture in this work, we performed a

comparison looking at the *thinnest mass produced foil or film* of each material instead of comparing on a constant-thickness basis. For stainless steel, nickel, and titanium foils this thickness is 25 μm (1 mil), while aluminium foil for battery applications is available at 15 μm. For carbon materials, the thinnest expanded graphite, CBPE, and pyrolytic graphite were 130 μm, 70 μm, and 50 μm, respectively. While lower thicknesses are available for some specialty materials, they are not available in large quantities and tend to be too expensive for use in battery applications.

Reliable data on production *costs* of these materials are difficult to find, so we instead made our best effort to find bulk *pricing* for large rolls (> 10 m^2). The pricing data for CBPE came directly from the manufacturer's website (Caplinq.com). Pricing data for other materials came from Alibaba.com, Allfoils.com, and Graphitematerials.com. There was a large variation in price for the more expensive materials (titanium, nickel, and pyrolytic graphite) and a smaller variation in price for the cheaper materials (expanded graphite, stainless steel, and CBPE), so a ±20% uncertainty is assumed for each material.

Results and Discussion

Electrochemical Stability of Current Collectors

A broadly applicable current collector must withstand wide anodic and cathodic polarization and resist corrosion in neutral, acidic, and basic pH electrolytes. The corrosion protection of metals such as stainless steel (SS), nickel, and titanium derives from the formation of surface passivation layers, which leads to other problems. Passivating metal oxide films are electrically insulating, which causes high interfacial contact resistance between the electrode and current collector.[9] Even in neutral-pH electrolytes, passivated metals are susceptible to pitting corrosion under anodic bias when aggressive anions such as halide salts or sulfates are present.[7,20,21] In other cases the current collector can be stable and still cause cell performance degradation via electrolyte decomposition, especially with metals such as platinum and gold that facilitate water splitting.[4]

We investigated the electrochemical stability window of CBPE and compared it to SS, Ni, and Ti metal current collectors for aqueous devices using linear sweep voltammetry (Figure 53). The electrolytes tested were sodium sulfate, sulfuric acid, potassium hydroxide, and sodium chloride, each representing neutral, acidic, basic, and pitting conditions, respectively. The CBPE material

shows the highest overpotential for hydrogen evolution in all electrolytes tested on the cathodic sweep, indicating wide compatibility with different pH values and electrolyte conditions.

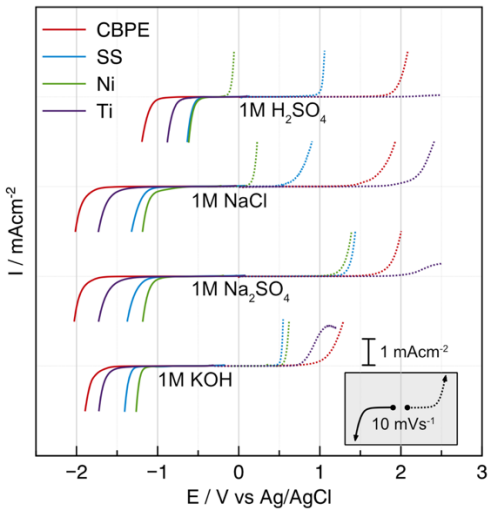

Figure 53. Electrochemical stability of candidate current collectors in different aqueous electrolytes. Linear sweep voltammetry of stainless steel (SS), nickel, titanium , and carbon black/polyethylene composite film (CBPE) reveals the relative stability window of these materials in 1M H_2SO_4, 1M Na_2SO_4, 1M NaCl, and 1M KOH electrolytes. The flat region in the center of each sweep represents the electrochemical stability window. On the cathodic sweep an increase in current represents hydrogen evolution, and on the anodic sweep an increase in current represents oxygen evolution, corrosion, or anodization.

On the anodic sweeps, CBPE also exhibits much higher stability than Ni and SS. In sulfuric acid (1 M H_2SO_4), for example, Ni corrodes immediately and although SS shows some corrosion resistance, its stability limit is almost 1 V

lower than that of CBPE. With chloride present in the electrolyte (1 M NaCl), CBPE is stable to 1.4 V vs. Ag/AgCl well beyond the potential at which Cl^- is oxidized to chlorine gas (Cl_2). In contrast, Ni and SS are susceptible to pitting corrosion under anodic bias when halide salts are present. Titanium appears to have even higher stability on the anodic sweep in some electrolytes, but this electrochemical behavior is likely due to the formation of an oxide passivation layer that would cause a high contact resistance at the electrode/CC interface.

In many aqueous electrolytes, cells can be charged beyond the thermodynamic 1.23 V stability window of water to increase power and energy, provided appropriate current collectors and electrodes are used.[22,23] The electroanalytical study above shows that the CBPE material provides a stability window of ca. 2.5 – 3 V in a variety of aqueous electrolytes, pH values, and pitting conditions. Other materials have much narrower stability windows, suggesting that it is the CC that limits the electrochemical stability window in many cases rather than the electrolyte. The wider stability window with the CBPE composite therefore provides an opportunity to extend operating voltages for further development of new electrodes and electrolytes without limitations from the current collector. For example, the high operating voltages demonstrated elsewhere for aqueous supercapacitors with Li_2SO_4 electrolyte with SS and Au CCs may be worth revisiting with CBPE.[21–23]

Electrical Conductivity – Monopolar versus bipolar cell design

Current collectors must have high electrical conductivity to minimize cell resistance. One often-cited advantage of aqueous rechargeable batteries and pseudocapacitors is the high power (cycling on the order of 100 C or 10 A/g) that is possible due to the excellent ionic conductivity of aqueous electrolytes.[1,24] While these high rates are achievable in coin-type cells, performance will decrease when the same systems are scaled up and the cell design becomes dependent on CC resistivity/conductivity. As a reference, the resistivity, ρ, of several common metallic and carbon-based CC materials are summarized in Table 12.

Table 13. Resistivity of metallic and carbon-based current collectors

	Material	**Resistivity, ρ (Ω • cm)**
Metals	Aluminum Foil*	2.8×10^{-6}
	316L Stainless Steel (SS)	7.4×10^{-5}
	Nickel	7.0×10^{-6}
	Titanium	4.2×10^{-5}
Carbons	Expanded Graphite (EG)	8.0×10^{-4}
	Pyrolytic Graphite (PG)	1.0×10^{-4}
	CBPE	3.5

*Non-aqueous cells only – included for reference

A fundamental challenge with a typical monopolar cell architecture for high power devices is that current flows in-plane in the current collector through a small cross-sectional area (referred to as a "traditional" or "conventional" cell architecture throughout the chapter). As the cell size increases, a correspondingly larger current must flow through the same cross-sectional area, A, and over longer distances, ℓ, significantly increasing ohmic losses (Figure 54a). Therefore, in larger cells, thicker current collectors are necessary to decrease resistance, R, as R is inversely proportional to A. Figure 54c illustrates the maximum allowed resistivity (left axis) and the equivalent minimum allowed conductivity (right axis) of a nominal CC material in a hypothetical high-power device as a function of cell size for several CC thicknesses. The calculation is performed for a case that limits the CC contribution to the IR drop to 100 mV at a current density of ± 100 mA•cm^{-2} (see Materials and Methods). This requirement ensures that during high-rate charge and discharge of a 1 V cell, for example, less than 10% of the total energy is lost to CC ohmic I^2R losses as heat. Under these conditions, in-plane current flow in the conventional cell configuration puts a significant constraint on the allowed resistivity of the CC materials (the resistivity of the CC materials from Table 13 are added to Figure 54c for comparison). From these calculations, it is readily apparent that expanded graphite (EG), for example, is only suitable for small cells (cell size < 2.5 cm). For larger cells, much thicker

EG sheets would be needed, degrading the cell-level volumetric and gravimetric power and energy performance. Nickel, titanium, and stainless steel have better conductivity than EG and can therefore accommodate larger cell sizes before the CCs become prohibitively thick. Although it is stable and corrosion-resistant, CBPE is unusable in a conventional cell format due to its resistivity being ~5 orders of magnitude too high.

To circumvent the insufficient electrical conductivity of CBPE in a conventional cell architecture, a bipolar cell design can be used instead. In this configuration, current flows through-plane over a distance of micrometers to millimeters instead of in-plane over a distance of centimeters, allowing for the current collector material to have higher resistivity and/or lower thickness (Figure 54b). Because CCs are shared between adjacent cells in a bipolar cell stack, a single CC serves as the positive current collector for one cell and the negative CC for its neighbor. This arrangement presents a technical challenge by requiring that the CC material be stable under both anodic and cathodic extremes. This requirement excludes many CC materials from use in a bipolar cell architecture, but the wide electrochemical stability window of CBPE makes it an ideal candidate.

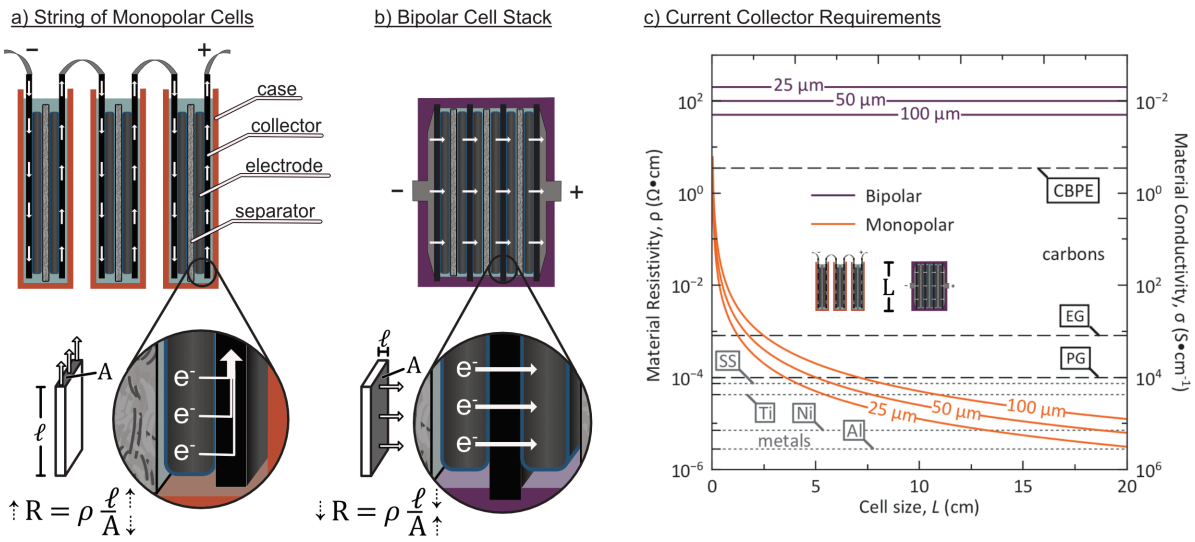

Figure 54. Monopolar and bipolar cell architectures. Series string of monopolar cells showing typical cell components. Current flows in the plane of the current collector to external tabs which connect the cells in the pack. The equation illustrates that resistance, R, of the CCs increases as current travels longer distances, ℓ, or through a smaller area, A. (b) The same cell components arranged in a bipolar cell stack, where current flows directly between cells by traveling in the through-plane direction of a shared bipolar current collector. For cells with equivalent current collector materials, resistance will be lower in the bipolar configuration due to the shorter path length, ℓ, and larger cross-sectional area, A. (c) Current collector requirements for different cell sizes/architectures showing maximum resistivity allowed for a given cell size and CC thickness for monopolar cells (orange curves) and bipolar cells (purple lines). Actual resistivity of metal CC materials (dotted gray lines) and carbon CC materials (dashed black lines) are included for comparison. The calculations assume perfect tabbing and uniform current density with the constraint that CC *IR* drop is ≤ 100 mV at ± 100 mA • cm^{-2}. EG = expanded graphite. PG = pyrolytic graphite. SS = 316L stainless steel.

Repeating the CC resistivity calculations for bipolar architectures (purple lines in Figure 54c) shows that the resistivity of CBPE (3.5 Ω•cm) is significantly better than the required values of 200 or 50 Ω•cm for 25 or 100 μm-thick bipolar CCs, respectively. This confirms that the short path length, ℓ, traveled by current in the bipolar cell design as well as the larger cross-sectional area, A, solve the problems associated with CBPE's low electrical conductivity (Figure 54b). An added benefit of the bipolar configuration is that the current density is uniform at all points in the cell, so the current collector requirements stay constant as the cell scales to larger sizes. This uniform current density also eliminates voltage gradients between the tabbing point and the opposite edge of the current collector found in a monopolar design, producing uniform charging, discharging, and heat generation across the entire electrode.

Areal mass and cost

In electrochemical energy storage, cost and mass must be minimized for all cell components, not just for active materials.[25] For example, if an electrode has a mass loading on the order of 10 mg/cm^2 and a current collector also has an areal mass of 10 mg/cm^2, the effective performance of the electrode is reduced by 50% (or by 33% for double-sided coating), before considering further performance reductions from the mass of electrolyte and other cell components. Thinner CC

materials therefore increase cell-level volumetric/gravimetric performance and also decrease material costs (except for extremely thin specialty materials, where processing costs exceed the savings from using less total material).

Table 14 compares the thickness, cost, and mass of the current collector materials from Table 13 for the thinnest mass-produced form of each material found in the market (details in SI). Although thinner materials are prefereable, thick CCs are sometimes required for large, high-power monopolar aqueous cells, as discussed in the previous section. In this case the realistic areal costs and mass loadings will be much larger than those in Table 14, highlighting the challenge of finding suitable current collectors for high-power aqueous electrochemical energy storage devices.

Table 14. Properties of metallic and coarbon-based current collectors

	Material	Thickness (μm)	Density (g/cm^3)	Areal mass (mg/cm^2)	Cost ($/m^2)
METALS	Aluminum Foil*	15	2.7	4.1	0.6
	316L SS	25	8.1	20.3	1.6
	Nickel	25	8.9	22.3	7.8
	Titanium	25	4.5	11.3	6.2
CARBONS	Expanded Graphite (EG)	130	1.12	14.6	0.9
	Pyrolytic Graphite (PG)	50	2.1	10.5	10.5
	CBPE	70	1.15	8.1	1.6

*Non-aqueous cells only – included for reference

Unlike a conventional monopolar cell architecture, *bipolar designs* decouple some of the current collector requirements and tradeoffs – choosing a thinner material not only improves conductance, but also decreases areal mass and thus cost. This relationship means that for any cell size, the bipolar CC material should be based on the minimum commercially available thickness (the same values presented in Table 14). Figure 55 summarizes the areal cost and areal mass of the different current collectors in the bipolar configuration. Stainless steel, nickel, and expanded graphite have higher areal mass loadings of ~15-20 mg/cm^2, which presents a significant disadvantage for high-power cells with lower electrode mass loadings.[5] Titanium and pyrolytic graphite have lower areal mass loadings of 10-11 mg/cm^2 but cost more (\$6-\$11/m^2, respectively). Of the materials investigated, only the CPBE composite offers both low areal cost and mass (\$1.6/m^2 and 8.1 mg/cm^2, respectively), demonstrating that it is an ideal CC candidate for low-cost, high-performance aqueous cells when incorporated together with a bipolar configuration.

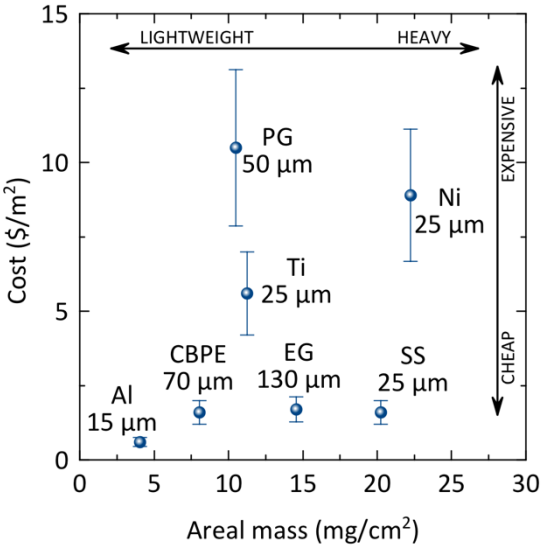

Figure 55. Areal mass and cost for several metallic and carbon-based current collectors. Materials shown are based on the thinnest mass-produced foil or sheet available. Cost estimates are discussed in the SI and plotted with an uncertainty of ± 20%. Although aluminum is unsuitable for aqueous systems, it is shown for reference to indicate the typical mass and cost for a current collector in a non-aqueous energy storage device. EG = expanded graphite, PG = pyrolytic graphite, SS = 316L stainless steel.

Heat-sealed bipolar pouch cells

Another unique property of the CBPE composite material is that the thermoplastic polyethylene is both flexible and heat sealable. Taking advantage of these properties for device engineering, we investigated both individual pouch cells (single CBPE pouch) and stacked bipolar pouch cells (stacked CBPE pouch) where this single composite material serves as the cell packaging, current collector, and seal. This concept is illustrated in Figure 56a, where the cross-

sectional schematic and exploded views show how the CBPE material is directly fused with a polyethylene plastic spacer after assembly, encapsulating a cell stack in a sealed pouch. With both the spacer and CBPE being flexible and heat-sealable, alignment and cell construction are straightforward, and the design can be extended to different cell sizes and electrode geometries.

For a single stand-alone cell (Figure 56a), the CBPE current collectors mainly serve the purpose of protecting metallic endplates from the corrosive aqueous electrolyte. The additional advantages of the design come from its stackable nature, where the total voltage for an n-cell stack equals $n \times V_{cell}$ (Figure 56b). In this configuration, the CBPE films shared between adjacent cells are functioning as true bipolar CCs, and the weight and cost of each are effectively halved relative to the case of a single, stand-alone cell. Similarly, the weight and cost of the single pair of metallic endplates is divided among all of the cells in the stack. With a heat-sealed, bipolar pouch architecture, the CBPE composite should therefore attain a favorable combination of high electrochemical stability, sufficient conductivity, and low cost and weight. In addition, because commercial heat sealers are widely available, CBPE is mass-produced, and the plastic spacers are cut from inexpensive polyethylene, this fabrication process and device architecture can be easily applied to a wide range of electrochemical cells.

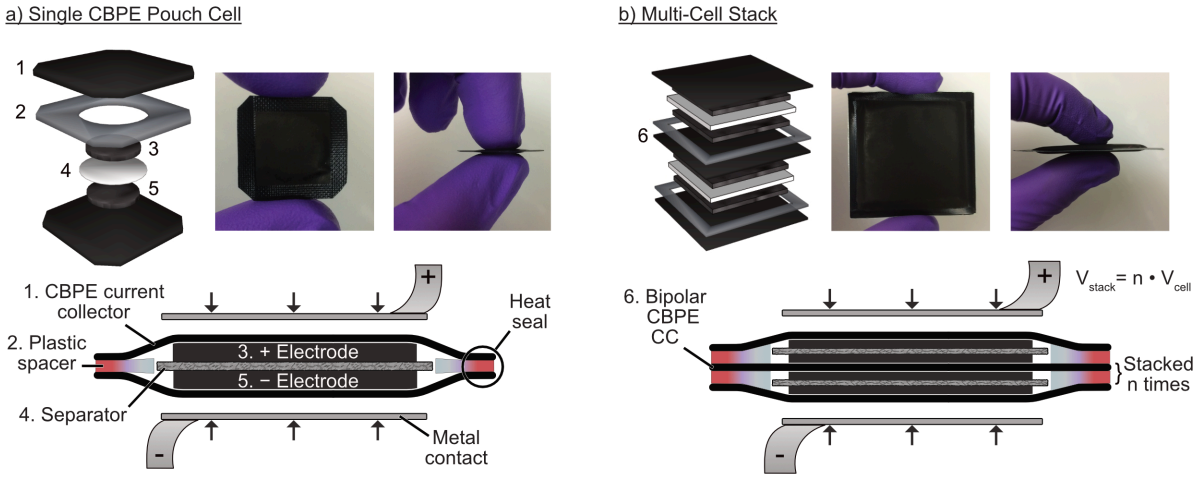

Figure 56. Single and stacked pouch cells. (a) Exploded view, cross-sectional view, and photographs of a single pouch cell. The cell stack, comprised of freestanding electrodes and a separator, is placed between two flexible CBPE current collectors and surrounded by an insulating plastic spacer. The current collectors are heat-sealed to either side of the spacer to seal the cell. (b) Cross-sectional view of an *n*-cell bipolar pouch and an exploded view and photographs of a larger bipolar pouch with 2 cells in series. The photographs in (a) are of a single small pouch cell with round, 11-mm-diameter (300-μm-thick) freestanding electrodes while the photographs in (b) show a larger, bipolar pouch containing two cells in series, each with a pair of square 4 cm × 4 cm (450-μm-thick) freestanding electrodes. These cells contain the pentyl viologen dibromide electrolyte developed in Chapter 3 and deliver the same level of performance achieved with glassy carbon current collectors. The pouch cells are metal-free. Any metal used externally as stack endplates is protected from corrosion as the electrolytes are contained by the CBPE material.

Demonstrating CBPE pouch cells with a Zinc Bromine Battery

To test the utility of pouch cells with CBPE current collectors (CBPE pouch cells) in a demanding application with aggressive aqueous electrolytes, we built (non-flow) aqueous rechargeable batteries with zinc bromide electrolyte. The zinc bromide test electrolyte combines the corrosive bromide anion, an acidic pH, and a wide operating voltage, and therefore provides a challenging system not compatible with metallic current collectors. The battery's basic electrochemistry is summarized below:[13]

Negative: $Zn^{2+} + 2\ e^- \rightleftarrows Zn_{(s)}$	$E°$ = -0.76 V vs. SHE
Positive: $2\ Br^- \rightleftarrows Br_2 + 2\ e^-$	$E°$ = 1.07 V vs. SHE
Overall: $ZnBr_2 \rightleftarrows Zn_{(s)} + Br_2$	***E°* = 1.83 V vs. SHE**

At the negative electrode, zinc has a reduction potential of -0.76 V vs. SHE at its acidic operating range of pH 1 - pH 3.5. This reduction potential is outside of the thermodynamic stability window of water, but zinc possesses a large overpotential for hydrogen gas evolution, minimizing electrolyte decomposition. At the positive electrode, oxidation of bromide to bromine occurs at 1.07 V vs. SHE to give an overall cell potential of 1.83 V for $ZnBr_2$ batteries, higher than

any commercialized aqueous battery systems with the exception of lead-acid batteries (ca. 2.1 V).[26]

Zinc bromine cells are challenged by low Coulombic efficiency and fast self-discharge due to diffusion of Br_3^- across the cell, which readily forms from Br_2 in aqueous electrolytes containing Br^- anions.[27,28] To prevent this, tetrabutylammonium bromide (TBABr) can reversibly complex Br_3^- in a solid phase, $[TBA^+ \cdot Br_3^-]_s$, preventing cross-diffusion (see Chapter 4).[29] However, TBABr is not soluble in concentrated zinc bromide electrolyte because bromozincate anions, $[ZnBr_4]^{2-}$, readily precipitate as an insoluble complex with TBA^+, preventing *ex situ* preparation of $ZnBr_2$/TBABr electrolyte.[30] To solve this problem, the activated carbon positive electrode is pre-soaked in a TBABr solution to pre-adsorb this Br_3^- complexing agent at the surface. Next, the electrode is contacted with a paper separator containing zinc bromide electrolyte, and assembled into a cell. This procedure ensures that when a TBA/bromozincate complex precipitates, both the complex and the TBA^+ it contains are retained in the high-surface-area pores of the electrode (Figure 50). After preparing the cell stack, the full assembly is heat-sealed into a single CBPE pouch cell (Figure 50 and Figure 51). When the full $ZnBr_2$/TBABr cell charges, bromide is oxidized to Br_3^- at the positive electrode, which complexes with pre-adsorbed TBA^+ and forms a solid at the electrode surface. For the negative electrode, zinc is plated

directly from the electrolyte as a solid metal deposit on the CBPE current collector. Both of these processes are reversed upon discharge of the cell (Figure 57). The solid complexation of Br_3^- by TBA^+ significantly slowed self-discharge compared to a $ZnBr_2$ cell without TBABr, increasing energy retention (η_R) from 12% remaining after 6 h at open circuit without TBABr to 75% remaining when TBABr is present. Further, this operating mechanism improves the Coulombic efficiency (CE) at a 1 A/g rate from 92% to 99%.

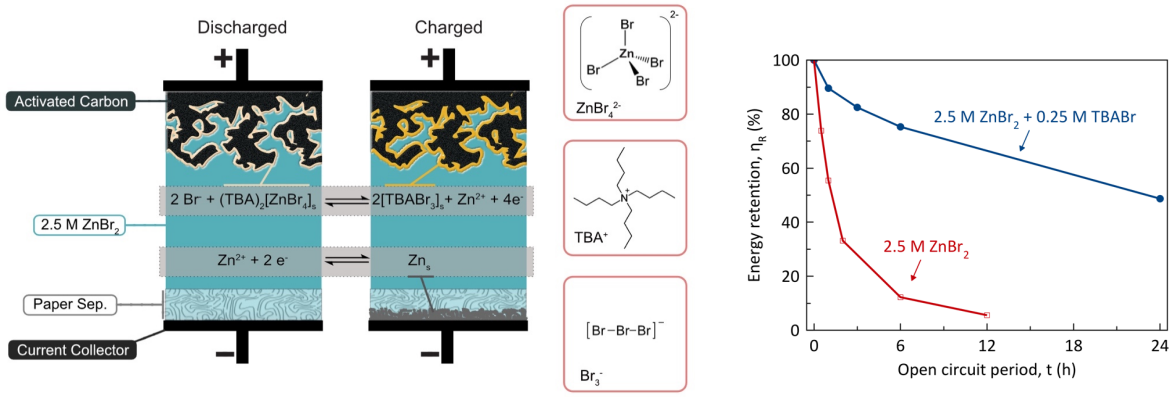

Figure 57. Zinc bromide cell charge/discharge mechanism. (schematic) The cell is assembled in the discharged state. With this electrolyte chemistry, zinc is reversibly plated onto the CBPE negative CC as a zinc metal negative electrode. At the positive electrode, bromide is reversibly oxidized to tribromide and complexed into an insoluble solid with TBA^+. (plot) Self-discharge with and without TBABr – the fraction of the initial discharge energy retained after different periods at open circuit is much higher for cells with TBA complexing agent than for equivalent cells without complexing agent.

The $ZnBr_2$/TBABr cells were charged by galvanostatic cycling at 1 A/g (normalized to the dry mass of the activated carbon positive electrode) to a capacity of 100 mAh/g, and discharged to a set potential of 1 V. A typical GCD profile, shown in Figure 58a, has a low *IR*-drop and a flat charging plateau, reaching almost 1.7 V on the charge and having an average discharge voltage of more than 1.6 V. Long term cycling shows negligible capacity fading over 2000 cycles with a capacity of 100 mAh/g and an additional 500 cycles with a capacity of 150 mAh/g (Figure 58b). To measure energy-power performance and various efficiencies, a series of charge/discharge rate tests was performed from 0.1 A/g to 2 A/g (1 C to 20 C) (Figure 58c). At the most efficient conditions (1C rate), a round-trip energy efficiency of 93% is achieved. Charging was limited to 2 A/g (20 C) or less to prevent the formation of zinc dendrites, but discharge can occur at much higher rates.[16] Therefore, additional discharge rate tests were performed where the cell was charged only at a single rate of 1 A/g (10 C) and discharged at different rates of 1 A/g to 12 A/g (10 C to 120 C). The energy and power densities are summarized on the Ragone plot in Figure 58d.

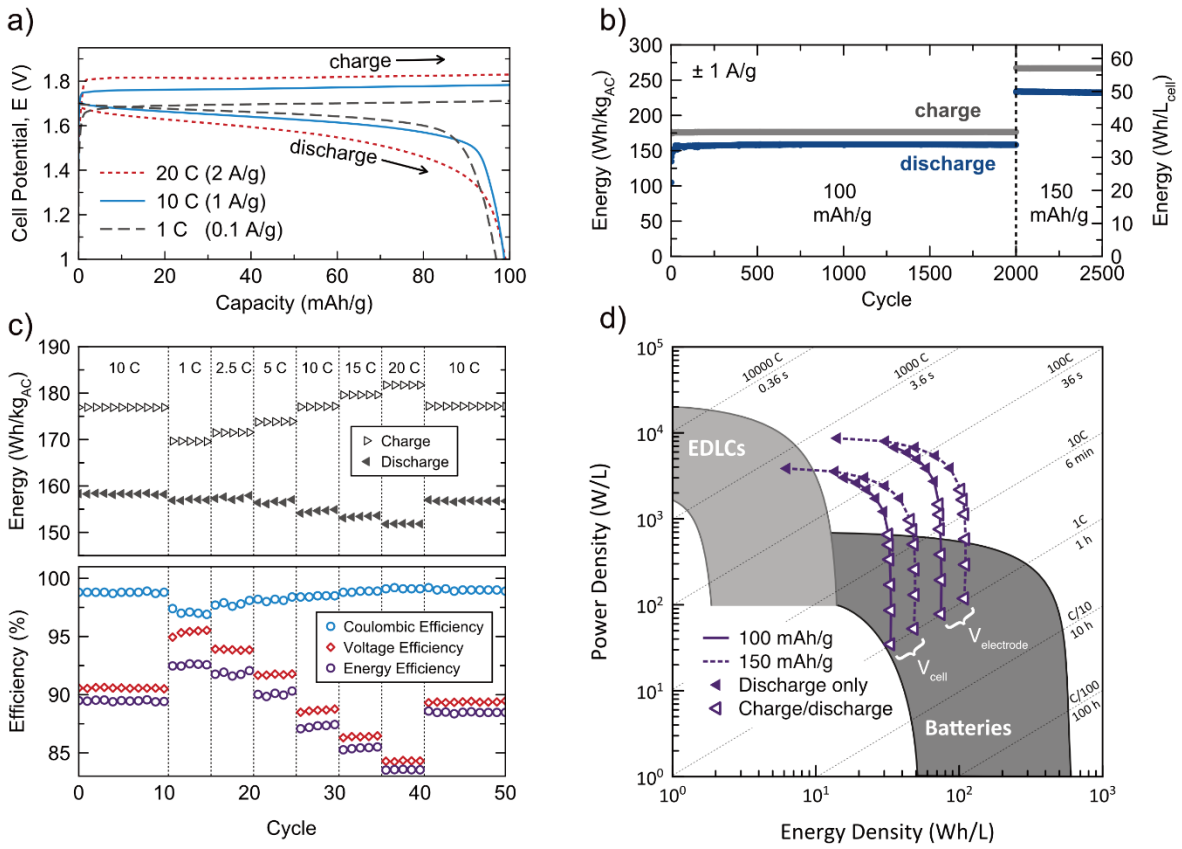

Figure 58. Electrochemical performance data for a $ZnBr_2$/TBABr CPBE pouch cell. (a) Galvanostatic potential profiles at different charge/discharge rates. (b) Cycling stability at a rate of ±1 A/g charged to 100 mAh/g for 2000 cycles and then to 150 mAh/g for an additional 500 cycles. Energies are normalized to the mass of the activated carbon electrode (left axis) and to the full cell volume (right axis) (c) Charge and discharge energy as well as Coulombic, voltage, and energy efficiency at different rates for a cell charged to 100 mAh/g. (d) Ragone plot indicating energy and power densities for a cell charging to 100 mAh/g (solid line) or 150 mAh/g (dashed line). Normalization is to the electrode volume only ($V_{electrode}$) and to the full cell volume (V_{cell}). Open triangles indicate points where the charge and discharge were performed at the same rate (1 C to 20 C) while solid triangles indicate points where charging was limited to 10 C and different high-rate discharges were performed (up to 120 C).

Construction of scaled, bipolar pouch cell stacks

Encouraged by the stable cycling performance of pouch cells with aggressive electrolytes in the single-cell format, we turned our attention towards the development of a bipolar stack. A stacked system has the benefit of reaching the high voltages needed for practical applications, but is more challenging to fabricate. A bipolar pouch comprised of four cells stacked in series was constructed using the same $ZnBr_2$/TBABr chemistry from the individual pouch cells (Figure 59a). The cell stack operates over a voltage range of 6-7 V, and the GCD profile has the same characteristics as that of a single, smaller cell (Figure 59b). Although the scaled, stacked system is more complex than individual cells and contains 25 times more active material, specific energy is unchanged and long-term cycling again shows negligible capacity fading over 1000 cycles with a capacity of 100 mAh/g and an additional 500 cycles with a capacity of 150 mAh/g (Figure 59c). The prototype was then connected to a pair of high-intensity 3 W blue LEDs to show a practical demonstration that requires a much higher voltage and current than a single small test cell can provide (Figure 59d).

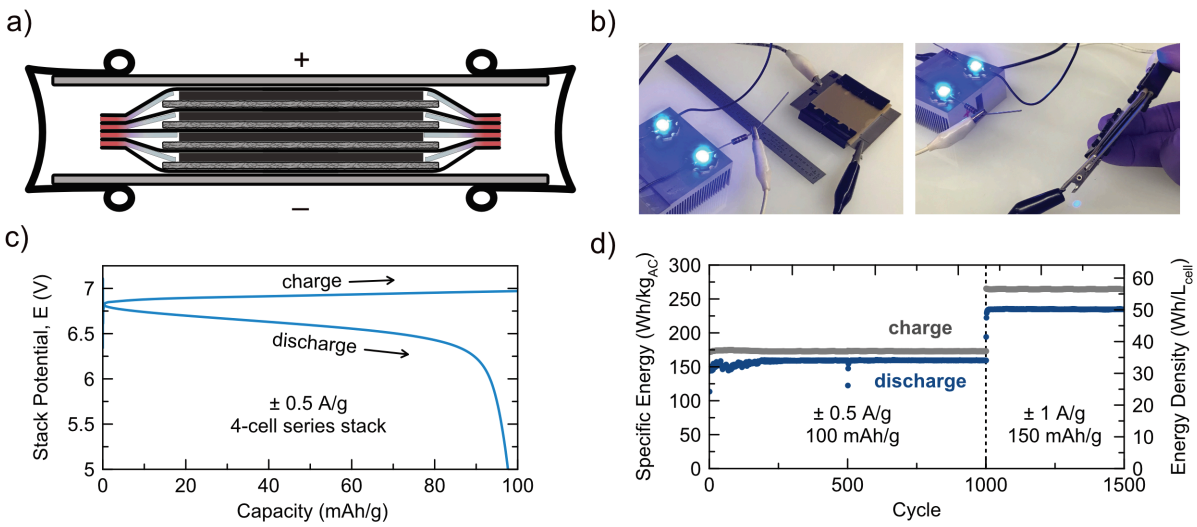

Figure 59. Performance of a scaled, bipolar pouch. (a) Schematic (not to scale) of a 4-cell bipolar pouch cell stack with CBPE current collectors, 2.5 cm × 2.5 cm (265-μm-thick) activated carbon electrodes, and $ZnBr_2$/TBABr chemistry. The cell stack is compressed by four binder clips between a pair of thin titanium plates. (b) Photographs showing the prototype (encased between two 5-cm Ti plates) running a series-connected pair of high-power 3 W blue LEDs. (c) Typical galvanostatic potential profile at 0.5 A/g (normalized to a single electrode). (d) Cycling stability of charge and discharge energy at a rate of ±0.5 A/g (5 C) charged to a capacity of 100 mAh/g for 2000 cycles and then at a rate of ±1 A/g (10 C) charged to a capacity of 150 mAh/g for an additional 500 cycles. Energies are normalized to the mass of all four activated carbon electrodes (left axis) and to the full cell volume (right axis), which includes the electrode, separator, and CBPE current collectors. The cell was rested for several days after cycle 500 and after cycle 1000.

Self-balancing for series-connected pouch cells

The stable cycling of the stacked $ZnBr_2$ system is notable because it indicates that the individual cells remain balanced. In a series-connected pack of monopolar cells, the terminals for each cell are exposed and thus individual cells can be separately charged to their correct capacity, ensuring that the pack remains balanced. In a bipolar stack, however, there is no access to terminals of individual cells, so any cell is vulnerable to being overcharged or overdischarged, damaging the performance of the entire stack.[31] This destructive behavior is not observed in the $ZnBr_2$/TBABr cells in this work because there is an intrinsic self-balancing chemistry available. When cells are overcharged and all pre-adsorbed TBA^+ is utilized in solid complexation, additional Br_3^- generated can escape the positive electrode uncomplexed and diffuse across the cell where it is reduced back to Br^- (Figure 60). This shuttle effect incrementally lowers Coulombic efficiency (CE) as charging capacity increases, so any overcharged cells will have a lower CE (high leakage current) while undercharged cells will have a higher CE (low leakage current). This non-destructive redox-shuttle can be utilized as an effective mechanism to prevent overcharging of individual cells and to balance multiple cells connected in series.[32,33] If one cell in a series stack becomes overcharged, it will enter a condition where the Br^-/Br_3^- redox shuttle develops and forms a temporary internal short circuit until the other cells in the stack reach

the same fully charged state (with equal leakage current). Therefore, this electrochemistry has a built-in mechanism for self-balancing that does not require water splitting (gassing) that would typically be used for a lead-acid battery, or a battery management system (BMS) that would typically be used for lithium-ion packs.

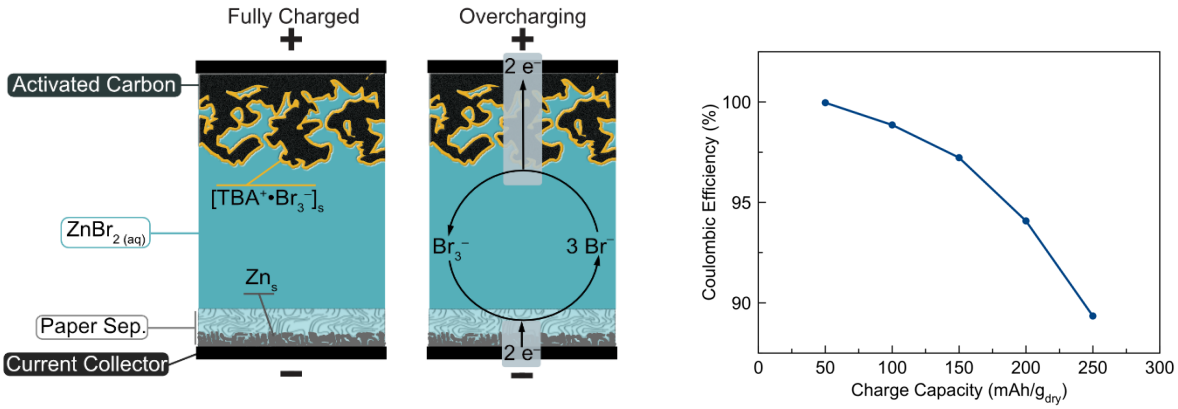

Figure 60. Built-in self-balancing mechanism to prevent overcharging of $ZnBr_2$ cells. (schematic) Overcharging the $ZnBr_2$ chemistry causes uncomplexed tribromide to diffuse across the cell, which creates a temporary internal short circuit. This redox shuttle mechanism can prevent overcharging damage to individual cells and help balance multiple cells when they are connected in series. Note that the electrolyte volume is exaggerated in the schematic. In actual cells, the activated carbon electrode touches the separator and electrolyte only resides in the porous separator and electrode. (plot) Coulombic efficiency versus charging capacity – a $ZnBr_2$/TBABr pouch cell was cycled at 1 A/g to different capacity limits in 50 mAh/g increments. Coulombic efficiency decreases substantially when the cell is overcharged, due to a finite quantity of TBABr complexing agent.

To verify experimentally that series-connected $ZnBr_2$ cells can stay balanced, two individual cells were connected in series and cycled together at 1 A/g to a capacity of 100 mAh/g, as shown in Figure 61a. The cells stayed balanced over 100 cycles, with each cell completing the faradaic plateau at the end of every discharge. The cycling test was then repeated with the cells deliberately offset, where Cell A was initially fully discharged and Cell B was pre-charged to 50 mAh/g. When the two cells were reconnected in series and cycled normally, Cell B would overcharge on each subsequent cycle to ~150 mAh/g (and only discharge back to ~50 mAh/g) while Cell A would operate normally between 0 and 100 mAh/g (Figure 61a). Although the total voltage profile for the 2 cells in series (orange) appears relatively unchanged after the offset, the individual cells deviate significantly from their normal profiles (Figure 61b). Over the course of 50 cycles, however, the cells re-balanced, the potential profiles returned to their initial equilibrium state, and cycling continued normally, indicating that the self-balancing chemistry in the $ZnBr_2$ system is effective.

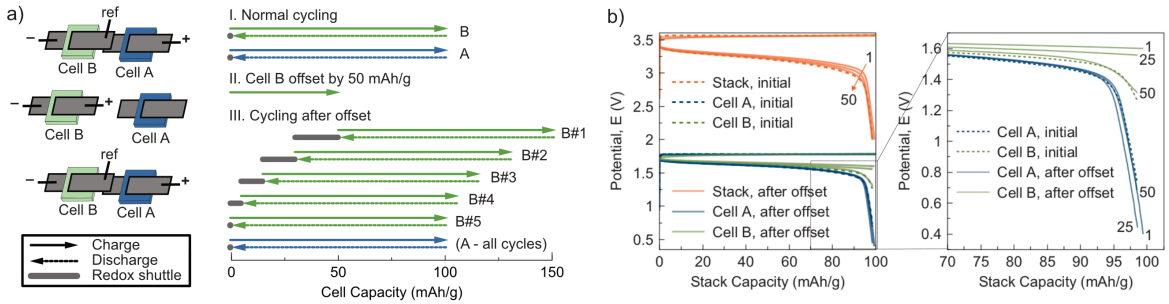

Figure 61. Self-balancing of series-connected $ZnBr_2$ cells. (a) Schematic illustrating an experiment in which two cells, A and B, are connected in series and cycled while the stack potential is measured. The reference lead (Ref) placed at the Cell A/Cell B junction enables the individual cell potentials to be measured. The stack is charged to 100 mAh/g and discharged to 2 V for 100 cycles. After the initial cycles, the cells are intentionally offset so that Cell B overcharges on each subsequent cycle (Cell A is initially fully discharged and Cell B is pre-charged to 50 mAh/g). A hypothetical example is shown where charge/discharge arrows show charge/discharge capacity and bars show additional charge dissipated due to the internal redox shuttles. Cell B rebalances after the offset due to increased internal self-discharge. (b) Outcome of the real self-balancing experiment with $ZnBr_2$ pouch cells. The galvanostatic charge/discharge profile is shown for Cell A, Cell B, and the series A/B stack for the 100th cycle under normal conditions (dashed lines). Cells A and B reach slightly different voltages on the discharge due to both cells being charged to the same capacity despite Cell B having a 7.5% larger electrode. The solid lines indicate the 1st, 25th and 50th cycles after the cells are intentionally offset. The zoomed area of the end-of-discharge for the GCD profiles of Cell A and Cell B shows that Cell A overdischarges and Cell B cannot complete its discharge plateau after the offset. The profiles gradually re-converge to the initial equilibrium state (note 50th cycle overlaps with initial dotted lines) due to self-balancing in the cell stack.

Using the CBPE bipolar pouch format with other aqueous electrochemical energy storage technologies will require different strategies to balance the individual cells. One approach to balancing a bipolar cell stack is to add redox shuttles to the electrolyte that become reduced or oxidized when a cell in the stack approaches an overcharge condition.[31] The choice of the appropriate redox shuttle(s) will depend on the operating potentials of the electrodes and should be carefully considered when incorporated into a new system.

Conclusions

The lack of viable cell designs and the need for low-cost, lightweight, and electrochemically stable current collectors is a major barrier to implementing high-power aqueous energy storage technologies. To address this problem, the heat-sealed bipolar pouch cell design with CBPE current collectors explored in this chapter offers a promising platform for constructing aqueous batteries, supercapacitors, pseudocapacitors, and redox ECs. The electrochemical inertness over a wide range of electrolyte chemistries and the simple assembly with low-cost equipment and consumables make the system attractive for research applications. The pouch cells also use only commercially available materials and are easily modified to accommodate larger electrodes and different geometries, which is important for commercial development. The $ZnBr_2$/TBABr cells deliver battery-level energy density, supercapacitor-level power density, long-term cycling stability, and slow self-discharge to provide a high-performance example of the effectiveness of the CBPE pouch cells with a challenging electrolyte. Based on these results, this cell architecture will find many applications in aqueous electrochemical energy storage.

References

1. Kim, H., Hong, J. & Park, K. Aqueous Rechargeable Li and Na Ion Batteries. *Chem. Soc. Rev.* **114,** 11788–11827 (2014).

2. Yan, J., Wang, Q., Wei, T. & Fan, Z. Recent Advances in Design and Fabrication of Electrochemical Supercapacitors with High Energy Densities. *Adv. Energy Mater.* **4,** 1300816 (2014).

3. Liang, Y. *et al.* Universal quinone electrodes for long cycle life aqueous rechargeable batteries. *Nat. Mater.* **16,** 841–848 (2017).

4. Lukatskaya, M. R. *et al.* Ultrahigh-rate pseudocapacitive energy storage in two-dimensional transition metal carbides. *Nat. Energy* **17105,** 1–6 (2017).

5. Whitacre, J. F. *et al.* An aqueous electrolyte, sodium ion functional, large format energy storage device for stationary applications. *J. Power Sources* **213,** 255–264 (2012).

6. Wu, X. *et al.* Rocking-Chair Ammonium-Ion Battery: A Highly Reversible Aqueous Energy Storage System. *Angew. Chemie - Int. Ed.* **56,** 13026–13030 (2017).

7. Gheytani, S., Liang, Y., Jing, Y., Xu, J. Q. & Yao, Y. Chromate conversion coated aluminium as a light-weight and corrosion-resistant current collector for aqueous lithium-ion batteries. *J. Mater. Chem. A* **4,** 395 (2016).

8. Zuo, W. *et al.* Battery-Supercapacitor Hybrid Devices: Recent Progress and Future Prospects. *Adv. Sci.* **4,** (2017).

9. Wu, H.-C. *et al.* High-performance carbon-based supercapacitors using Al current-collector with conformal carbon coating. *Mater. Chem. Phys.* **117,** 294–300 (2009).

10. Blomquist, N. *et al.* Metal-free supercapacitor with aqueous electrolyte and low-cost carbon materials. *Sci. Rep.* **7,** 1–7 (2017).

11. Dyatkin, B. *et al.* Development of a green supercapacitor composed entirely of environmentally friendly materials. *ChemSusChem* **6,** 2269–80 (2013).

12. Ziv, B. *et al*. Investigation of Graphite Foil as Current Collector for Positive Electrodes of Li-Ion Batteries. *J. Electrochem. Soc*. **160,** A581–A587 (2013).

13. Noack, J., Roznyatovskaya, N., Herr, T. & Fischer, P. The Chemistry of Redox-Flow Batteries. *Angew. Chemie - Int. Ed*. **54,** 9776–9809 (2015).

14. Du, L. & Jana, S. C. Highly conductive epoxy/graphite composites for bipolar plates in proton exchange membrane fuel cells. *J. Power Sources* **172,** 734–741 (2007).

15. Han, P. *et al*. Anticorrosive flexible pyrolytic polyimide graphite film as a cathode current collector in lithium bis(trifluoromethane sulfonyl) imide electrolyte. *Electrochem. commun*. **44,** 70–73 (2014).

16. Banik, S. J. & Akolkar, R. Suppressing Dendrite Growth during Zinc Electrodeposition by PEG-200 Additive. *J. Electrochem. Soc*. **160,** D519–D523 (2013).

17. Easton, M. E., Turner, P., Masters, A. F. & Maschmeyer, T. Zinc bromide in aqueous solutions of ionic liquid bromide salts: the interplay between complexation and electrochemistry. *RSC Adv*. **5,** 83674–83681 (2015).

18. Easton, M. E. *et al*. Factors influencing the formation of polybromide monoanions in solutions of ionic liquid bromide salts. *Phys. Chem. Chem. Phys*. **18,** 7251–7260 (2016).

19. Rallo, F. & Silvestroni, P. Insoluble Polybromides of Quaternary Ammonium Salts and Their Phase-Transitions in the Presence of Aqueous Bromine-Bromide Solution. *J. Electrochem. Soc*. **119,** 1471 (1972).

20. Béguin, F., Presser, V., Balducci, A. & Frackowiak, E. Carbons and electrolytes for advanced supercapacitors. *Adv. Mater*. **26,** 2219–2251 (2014).

21. Ratajczak, P., Jurewicz, K., Skowron, P., Abbas, Q. & Béguin, F. Effect of accelerated ageing on the performance of high voltage carbon/carbon electrochemical capacitors in salt aqueous electrolyte. *Electrochim. Acta* **130,** 344–350 (2014).

22. Gao, Q., Demarconnay, L., Raymundo-Piñero, E. & Béguin, F. Exploring the large voltage range of carbon/carbon supercapacitors in aqueous lithium sulfate electrolyte. *Energy Environ. Sci.* **5,** 9611–9617 (2012).

23. Fic, K., Lota, G., Meller, M. & Frackowiak, E. Novel insight into neutral medium as electrolyte for high-voltage supercapacitors. *Energy Environ. Sci.* **5,** 5842 (2012).

24. Wessells, C. D., Huggins, R. a & Cui, Y. Copper hexacyanoferrate battery electrodes with long cycle life and high power. *Nat. Commun.* **2,** 550 (2011).

25. Gogotsi, Y. & Simon, P. Materials science. True performance metrics in electrochemical energy storage. *Science* **334,** 917–8 (2011).

26. Rajarathnam, G. P. & Vassallo, A. M. *The Zinc/Bromine Flow Battery*. (SpringerNature, 2016). doi:10.1007/978-981-287-646-1

27. Lai, Q., Zhang, H., Li, X., Zhang, L. & Cheng, Y. A novel single flow zinc-bromine battery with improved energy density. *J. Power Sources* **235,** 1–4 (2013).

28. Evanko, B. *et al.* Efficient Charge Storage in Dual-Redox Electrochemical Capacitors through Reversible Counterion-Induced Solid Complexation. *J. Am. Chem. Soc.* **138,** 9373–9376 (2016).

29. Yoo, S. J. *et al.* Fundamentally Addressing Bromine Storage through Reversible Solid-State Confinement in Porous Carbon Electrodes: Design of a High-Performance Dual-Redox Electrochemical Capacitor. *J. Am. Chem. Soc.* **139,** 9985–9993 (2017).

30. Cathro, K. J., Cedzynska, K., Constable, D. C. & Hoobin, P. M. Selection of quaternary ammonium bromides for use in zinc/bromine cells. *J. Power Sources* **18,** 349–370 (1986).

31. Dahn, J., Jiang, J., Moshurchak, L., Buhrmester, C. & Wang, R. L. The drugstore Li-ion cell. *Electrochem. Soc. Interface* (2005).

32. Choi, N. S. *et al.* Challenges facing lithium batteries and electrical double-

layer capacitors. *Angew. Chemie - Int. Ed.* **51,** 9994–10024 (2012).

33. Biswas, S. *et al.* Minimal architecture zinc–bromine battery for low cost electrochemical energy storage. *Energy Environ. Sci.* **10,** 114–120 (2017).

Conclusion

Summary

All electrochemical energy storage research is based on compromise between competing properties. These properties include, but are not limited to: safety, power, energy, cycling stability, and cost. Currently, secondary batteries are used for energy-intensive applications and EDLCs are used for power-intensive applications. A typical off-the-shelf 18650 Li-ion battery and a typical off-the-shelf 100 F EDLC both have approximately equivalent weight, volume, and cost.

The battery has excellent performance in the energy metric but only average performance in the other areas. The EDLC, on the other hand, has ideal characteristics in every metric *except* energy, which is exceptionally low (this in turn negatively impacts cost, as cost per unit energy is more important than cost per cell).

This dissertation summarizes a team effort to understand and optimize redox ECs and other hybrid systems that combine the best aspects of batteries and EDLCs. Our challenge was to demonstrate excellent safety, power, energy, and cycling stability simultaneously in a single, low-cost device. At the beginning of this project, we decided that we would work only with standard activated carbon electrodes in aqueous electrolytes, and that all improvements to the system would come from engineering redox-active electrolytes. There were several advantages to this approach. Limiting the work to only one electrode composition kept the project focused, and using simple electrodes translates to simpler manufacturing and lower costs at later stages in the development of these technologies. Additionally, activated carbon electrodes have exceptionally high surface area, which provides power to the system, while soluble redox couples in the electrolyte offer faradaic charge storage, which provides energy to the system. This pairing eliminates the need for degradation-prone solid-state battery electrodes, improving cycling stability. Finally, the choice to use aqueous

electrolytes is important for safety, lowering the risk of fire and explosion that is a common concern with organic electrolytes.

The fundamental problem with redox ECs is the high self-discharge rate caused by cross-diffusion of redox-active electrolytes in charged cells. This can be addressed with ion-selective separators, but the high cost of these materials is unacceptable. Therefore, we made another decision to use only non-selective paper separators and address the self-discharge issue with electrolyte engineering. Our first efforts to suppress self-discharge without ion-selective separators focused on a search for redox couples that would adsorb strongly to the activated carbon electrodes in the charged state. This approach produced an iodine-based single-redox EC, and later led to the identification of viologen bromide salts as promising redox-active electrolytes for dual-redox ECs (Chapter 2). Detailed investigations revealed that for the viologen bromide system, there is an electroprecipitation mechanism occurring at both electrodes through which redox couples form solid complexes in the charged state that further limit self-discharge (Chapter 3).[††] After exploring this effect, non-redox-active

[††] This effect is similar to the strategy used by Type II electrochromic materials, which rely on reversible electroprecipitation of soluble redox couples to produce colored films on conductive glass. In this case, however, the substrate is a high-surface-area porous carbon electrode rather than a two-dimensional window.

tetrabutylammonium bromide (TBABr) was was added to provide an improved complexing agent for the positive electrode, increasing the amount of viologen available for energy storage (Chapter 4). Finally, to demonstrate that solid complexation as a self-discharge suppression strategy is useful beyond the viologen bromide system, we developed a redox EC/battery hybrid with a $ZnBr_2$/TBABr electrolyte (Chapter 5). Together, these efforts proved that it is possible to design high-performance redox ECs without ion-selective separators.

In addition to self-discharge, the other major problem with redox ECs addressed by this dissertation is stability. Chapter 2 highlights the importance of highly reversible redox couples, and demonstrates that the heptyl viologen bromide system can cycle more than 20,000 times with negligible performance degradation. Chapter 3 identifies solid complexation of bromine as a critical component of cell stability, and shows that a pentyl viologen bromide cell not only has a long cycle life, but can also withstand cycling under reversed polarity. Chapter 4 gives a better mechanistic understanding of how bromine degrades activated carbon electrodes, and offers the TBABr complexing agent as a general solution to this problem. Chapter 5 examines the stability of other cell components (primarily current collectors) that corrode in aggressive aqueous electrolytes and prevent the scaling of redox ECs to practical sizes. The result is a bipolar pouch cell design with carbon/polymer composite current collectors that

enables stable operation of large-format pentyl viologen dibromide and $ZnBr_2$/TBABr cells. Finally, it is shown that solid complexation contributes to stability at the pack/stack level by enabling redox-shuttles to develop when a cell is overcharged, preventing damage to series-connected cells.

All of the electrochemical systems described in this dissertation were engineered to deliver a combination of excellent stability and slow self-discharge. Over the five years it took to complete the project, it was possible to improve both the power and energy density as well. Without changing the electrode design we gradually moved from an EDLC control chemistry to redox ECs, dual-redox ECs, and ultimately a redox EC/battery hybrid by modifying only the composition of the electrolyte. Each iteration realized a significant performance improvement over the last and ultimately produced systems competitive with commercial electrochemical energy storage technologies (Figure 62).

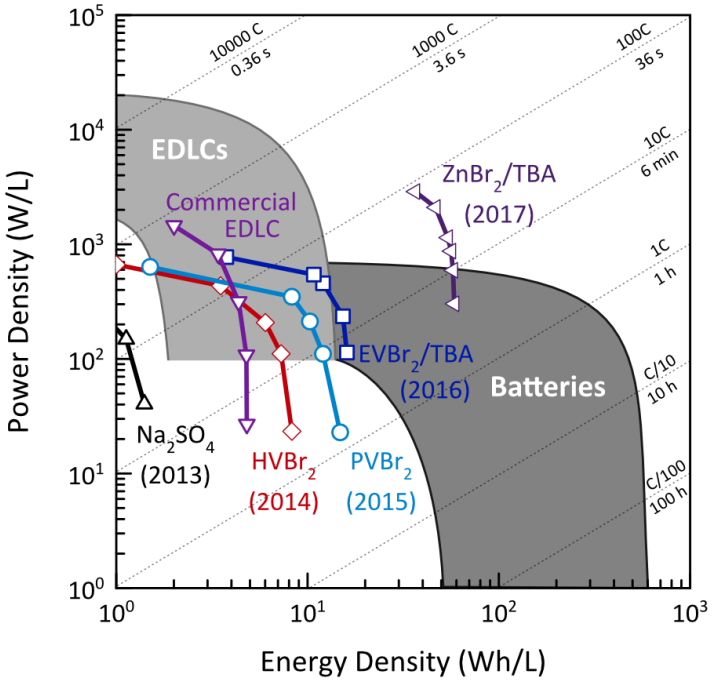

Figure 62. Progression of device-level power and energy density. The Ragone plot illustrates performance improvements over the course of the project for the systems that exhibited both slow self-discharge and long-term cycling stability. These systems include heptyl viologen ($HVBr_2$, Chapter 2), pentyl viologen ($PVBr_2$, Chapter 3), ethyl viologen with tetrabutylammonium bromide ($EVBr_2$/TBA, Chapter 4), and zinc bromide with tetrabutylammonium bromide ($ZnBr_2$/TBA, Chapter 5). An aqueous EDLC (Na_2SO_4 electrolyte) and a commercial organic EDLC (Maxwell) are included for reference.

Future Directions

There are many potential avenues of research that would contribute to the development of improved redox ECs. For example, a redox EC must function over a wide temperature range, but most laboratory experiments are performed at 25 ºC. Lower temperatures cause aqueous electrolytes to freeze or exhibit poor ionic conductivity and higher temperatures accelerate self-discharge and performance degradation, so new approaches are needed to solve these problems. Another outstanding issue is cost and use-case. It is not yet known which applications (electric forklifts, automotive engine start-stop, grid services, etc.) will benefit most from redox ECs. Cost modeling and market analysis will be instructive to identify the opportunities and problems researchers should be focused on. Similarly absent are reliable pack-level production cost estimates for new aqueous electrochemical energy storage technologies. As an example of potentially useful numbers, our preliminary cost and sensitivity analyses for a $ZnBr_2$/TBABr cell in a CBPE bipolar pouch format are presented in Appendix 2.

The simplest way to move a redox EC from the development stage into production is to find a low-cost system that can easily "drop-in" to an existing manufacturing process. This could mean finding redox couples to augment the lower-capacity activated carbon anode of Pb-carbon batteries, or making redox EC electrodes compatible with aqueous lithium or sodium ion batteries. It could

also mean moving beyond aqueous systems to find redox couples that operate in the acetonitrile or propylene carbonate electrolytes currently used for organic EDLCs.

In order to achieve these goals, new redox species should be accessible using organic or inorganic synthetic chemistry. Recent work on designing organic molecules as aqueous redox couples for flow batteries has proven their properties to be highly tunable. Such designer couples could generate new high-performance redox EC systems that address the self-discharge challenge and approach battery-level energy density while providing power and cycle life typically associated with EDLCs.

For aqueous energy storage technologies that cannot easily drop-in to existing cell designs, further development of the CBPE pouch cell format is worthwhile. This format is currently optimized for freestanding electrodes, and it may be difficult to adapt it to other electrodes that are typically cast directly onto a current collector. One way to address this issue would be to coat electrodes onto either side of the separator in a roll-to-roll process, and then put this component into a heat-sealed pouch. Another way to modify the concept could involve eliminating the plastic spacer and the paper separator, and replacing both with a single microporous polyethylene separator. When heat-sealed between CBPE current collectors the pores of the separator would collapse, but only in the region of the

seal (Figure 63). If one of the four sides is left unsealed, there are two isolated pockets that can be filled with electrode slurries before sealing the final side. This would essentially be the inverse of the enveloping technique used to make many Pb-acid batteries now, but with the insertion of electrode slurries instead of plates and grids.

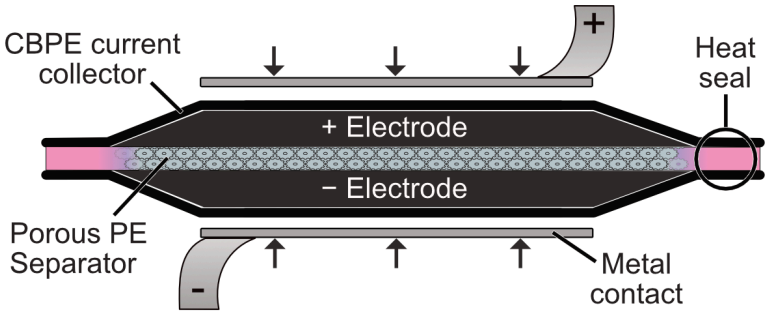

Figure 63. Alternate CBPE pouch cell concept. This schematic shows how the separator and insulating plastic spacer could be integrated into one component by using a microporous polyethylene separator. The micropores of the polyethylene collapse in the region of the heat-seal, making that region impermeable to electrolyte and serving the same function typically addressed by the plastic spacer. This design gives simplified construction, better separation of the two sides of the cell, and better mechanical properties. It may also enable the use of binderless electrode slurries that fill the entirety of the two separated sealed compartments, instead of the typical freestanding electrode films/pellets that must be solid to avoid flowing around the edge of the separator and shorting the cell.

Finally, beyond the realm of engineering and performance optimization, many scientific questions remain surrounding redox ECs. For example, in these systems a better understanding of the electrode-electrolyte interface is needed. It is unknown to what degree the pore structure and surface chemistry of carbon electrodes influence the electroprecipitation mechanisms. Hydrophobicity and surface area appear to be critical, but other factors may contribute as well. The morphology of the solid complexes formed in the charged state is also an open question. Further investigation is needed to determine if the complexes deposit as monolayers, thin films, or aggregates. Such questions are difficult to answer, and will require the synthesis of new electrode materials, the investigation of more quaternary ammonium complexing agents, and the application of new electrochemical techniques. Ultimately, what is learned from these studies can be applied to catholytes other than bromide, anolytes other than the viologens, and electrochemical energy storage technologies other than redox ECs.

Appendix 1

Electrochemical Model

Supercapacitor with Redox-Active Electrolyte

Constants

```
R := 8.314  (*Gas constant in J/molK*)
```

```
T := 298 (*Temperature in K*)
```

```
F := 9.6485 * 10^4 (*Faraday Constant in C/mol*)
```

```
dC := 2.25 (*carbon skeleton density in g/cm^3*)
```

```
CpermAh := 3.6
```

System Variable Inputs

```
cCap := 95 (*Cathode Capacitance in F/g*)
```

```
aCap := 110 (*Anode Capacitance in F/g*)
```

a A -> b B + n e^-
a Br^- -> b Br_2+ n e^-

```
a := 3
```

```
b := 1
```

```
n := 2
```

xX + m e^- -> y Y
x MV^{2+} + m e^- -> y MV^+

```
x := 1
```

```
y := 1
```

```
m := 1
```

```
E0c := 0.7 (*Catholyte standard reduction potential in V vs. SCE*)
```

```
E0a := -0.52(*Anolyte standard reduction potential in V vs. SCE*)
```

```
Eoc := 0.1(*Open circuit voltage in V vs. SCE*)
```

```
Mc := 1.2(*Catholyte molarity in mol/L*)
```

```
Ma := 0.6(*Anolyte molarity in mol/L*)
```

```
me := 47.55(*Electrolyte mass in mg*)
```

```
mc := 8.8(*cathode mass in mg*)
```

```
ma := 9(*anode mass in mg*)
```

```
dE := 1 (*specific gravity of electrolyte*)
```

```
Vmax := 1.4 (*Total device charging voltage*)

Data := Import["/Users/brianevanko/Desktop/Data/1MKBr_05MMVCl2testdata.xlsx"][[1]];
```

Equations

```
rootc := If[a == 3, 3, 1]

roota := If[x == 3, 3, 1]

Vol := me / 1000 / dE / 1000 (*Electrolyte Volume in L*)
```

Cathode

```
Qc[q_] := ((q / F * b / n) / Vol) ^ b /
   ((Mc * Vol - q / F * a / n) / Vol) ^ a (*Reaction Quotient as a function of charge*)

Ec[q_] := (R * T / (n * F) * Log[Qc[q]] + E0c)
 (*Nernst Potential as a function of charge*)

qcf[v_] = q /. Solve[Exp[v - E0c] == Exp[Ec[q] - E0c], q][[rootc]];
(*Faradaic Charge passed as a function of Potential*)

qccap[v_] :=
 cCap * mc / 1000 * (v - Eoc) (*Capacitive Charge passed as a function of Potential*)

qctot[v_] := qccap[v] + qcf[v] (*Total Charge passed as a function of Potential*)
```

Anode

```
Qa[q_] :=
 ((q / F * y / m) / Vol) ^ y / ((Ma * Vol - q / F * x / m) / Vol) ^ x (*Reaction Quotient*)

Ea[q_] :=
 E0a - (R * T / (m * F) * Log[Qa[q]]) (*Nernst Potential as a function of charge*)

qaf[v_] = q /. Solve[Exp[v - E0a] == Exp[Ea[q] - E0a], q][[roota]] ;
(*Faradaic Charge passed as a function of Potential*)

qacap[v_] :=
 aCap * ma / 1000 * (Eoc - v) (*Capacitive Charge passed as a function of Potential*)

qatot[v_] := qacap[v] + qaf[v] (*Total Charge passed as a function of Potential*)
```

Output

```
Vrange := FindRoot[{qatot[xx] - qctot[yy] == 0, yy - xx == Vmax},
   {{xx, Eoc - Vmax / 2}, {yy, Eoc + Vmax / 2}}]

Vmina = xx /. Vrange[[1]] (*Voltage at anode when fully charged*)
```

```
-0.658577
```

```
Vmaxc = yy /. Vrange[[2]] (*Voltage at cathode when fully charged*)
```

```
0.741423
```

```
qcomb[j_] := qatot[xx /. FindRoot[
      {qatot[xx] - qctot[yy] == 0, yy - xx == j}, {{xx, Eoc - j / 2}, {yy, Eoc + j / 2}}][[1]]]

Capacity = qcomb[Vmax] / CpermAh;

mWh = (qcomb[Vmax] * Vmax - (NIntegrate[qctot[xxx], {xxx, Eoc, Vmaxc}] -
       NIntegrate[qatot[yyy], {yyy, Eoc, Vmina}])) /
  CpermAh (*Total Energy Stored in mWh*)
1.08164

% * .95
1.02755

Convc = (qcf[Vmaxc] / F * a / n) / (Mc * Vol) (*Conversion of catholyte*)
0.80513

Conva = (qaf[Vmina] / F * x / m) / (Ma * Vol) (*Conversion of anolyte*)
0.995489

Capacity (*Total Capacity in mAh*)
0.969803

Show[
 ParametricPlot[{qctot[z] / CpermAh + 0.0, z}, {z, Eoc, 1}, PlotLegends → {"Model"}],
 ParametricPlot[{qatot[s] / CpermAh + 0.0, s}, {s, -0.8, Eoc}],
 ParametricPlot[{qcomb[j] / CpermAh + 0.0, j}, {j, 0, 1.4}, PerformanceGoal → "Speed"],
 ListPlot[Data[[All, {1, 2}]], PlotLegends → {"Experimental Data"},
  PlotStyle → Orange], ListPlot[Data[[All, {1, 3}]], PlotStyle → Orange],
 ListPlot[Data[[All, {1, 4}]], PlotStyle → Orange],
 PlotRange → {{0, 2}, {-0.7, 1.5}}, AspectRatio → Full]
```


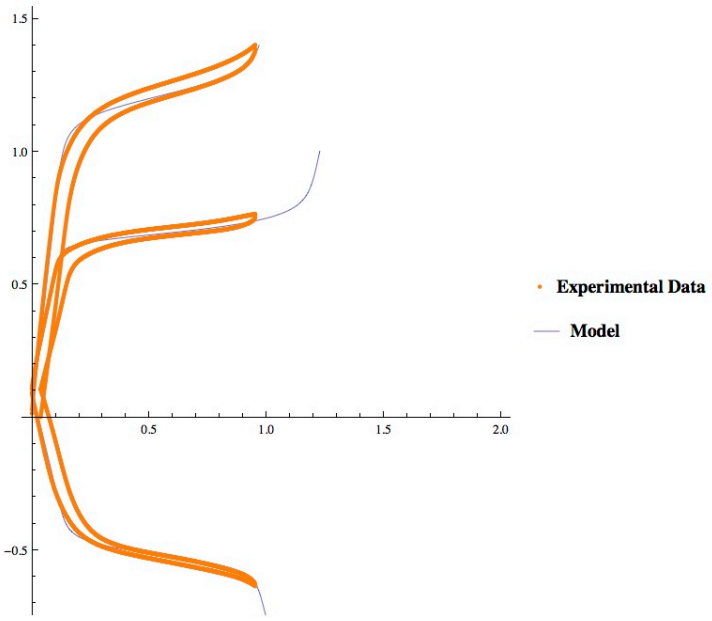

Appendix 2

Cell-level performance, cost, and sensitivity analysis

Cell

Type 1: Swagelok/Coin Cell		
Cell Diameter	1.27	cm
Type 2: Bipolar Pouch		
Mandrel Diameter	pouch	mm
Cell Diameter (mm)	pouch	mm
Cell height (mm)	0.515	mm
Cathode width	2.5	cm
Cathode length	2.50	cm
Anode width	2.50	cm
Anode length	2.5	cm
Cell Volume (cm^3)	0.32	cm^3
Available volume	0.3	cm^3

Conversions

um/cm	10000	
cm/um	0.0001	
Wh/J	0.0002777	
Faraday Constant	9.65E+04	C/mol e-
Coulombs/Ah	3600	
nAvogadro	6.02E+23	

Capacity and Energy Density

Charging Voltage	1.8	V
Rate (/g Carbon in cell)	1	A/g
Discharge/Charge Efficiency	0.89	
Capacity (/gcarbon in cell)	150	mAh/g

Nominal Capacity

Capacitance		
Energy	**0.020**	**Wh**
Charge		
Energy Density (electrode)	260	Wh/kg
Energy Density (Overall)	**27.8**	**Wh/kg**
Discharge		
Capacity	0.018	Wh
Energy Density (carbon in cell)	231	Wh/kg
Energy Density (Overall)	**25**	**Wh/kg**
	56	**Wh/L**

Cell

Cell Type 1 or 2	2	
anode area	6.25	cm^2
cathode area	6.25	cm^2
Sides of CC Coated	1	
Total Stack Thickness	515	um

Electrode

Activated Carbon Fraction	0.9	
Skeleton Density	2.1	g/cm^3
Carbon Black Fraction	0.05	
CB Density	2.1	g/cm^3
Binder Fraction	0.05	
Binder Density	2.2	g/cm^3
Electrode Density	0.47	g/cm^3
Free Volume Fraction	0.777	
Cathode Thickness (1 side)	265	um
Cathode volume	0.166	cm^3
Cathode free volume	0.129	cm^3
Cathode mass	0.0778	g
Anode/Cathode ratio	0	
Anode Thickness (1 side)	0	um
Anode volume	0	cm^3
Anode free volume	0	cm^3
Anode mass	0	g
Total Carbon Mass	0.0778	g

Separator

Thickness (each)	180	um
Porosity	0.7	
Density	0.50	g/cm^3
Separator Volume	0.162	cm^3
Separator Free Volume	0.113	cm^3
Total Mass	0.081	g

Charging/Discharging Time

Number of Desired Cycles	1000	Cycles
Power Density (max)	0.19	kW/kg
Charge/Discharge Current	0.08	A
Current Density	12.5	mA/cm^2
Galvanostatic Cycle Time	0.3	h
Time required for test	13	days

Cell Composition

Component	Mass(g)	Mass%
Electrodes	0.08	10.7
Separator	0.08	11.1
Current Collector	0.05	6.9
Electrolyte	0.48	65.9
Additive	0.04	5.4
Total	**0.73**	100.00

Cell Cost

Component	Cost ($/kWh)	Cost (%)
Activated Carbon	31.11	18.60
Carbon Black	0.24	0.14
Binder	1.08	0.65
Separator	6.94	4.15
Current Collector	55.86	33.39
Zinc bromide	36.38	21.75
NaBr	1.39	0.83
TBABr	10.80	6.46
Case	7.82	4.68
Manufacturing	15.65	9.35
Total Cost	167.28	100.00
	167	**$/kWh**

Current Collector

Material	CBPE	
Anode CC Density	1.15	g/cm^3
Anode CC Thickness	70	um
Anode CC mass	0.025	g
Anode CC volume	0.022	cm^3
Cathode CC density	1.15	g/cm^3
Cathode CC Thickness	70	um
Cathode CC mass	0.025	g
Cathode CC volume	0.022	cm^3
Current Collector mass	0.050	g

Electrolyte

Electrolyte Density	1.48	g/cm^3
Electrolyte Volume	0.324	mL
Electrolyte mass	0.479	g
Electrolyte:Carbon Ratio	6.15	mg/mg
Anolyte		
Salt Molar Mass (ZnBr2)	225	g/mol
Concentration ZnBr2	3	M
Mass ZnBr2	0.218	g
Moles ZnBr2	9.71E-04	moles
Catholyte		
Salt Molar Mass (NaBr)	103	g/mol
Concentration	0.5	M
Mass NaBr	0.017	g
Additive		
Salt Molar Mass (TBABr)	322.4	g/mol
Concentration	3.73E-01	M
Mass TBABr	0.039	g

Material Costs

Component	**Cost ($/Unit)**	**Low**	**High**	**Unit**
Activated Carbon	**8**	5	10	$/kg
Carbon Black	**1.1**	1	5	$/kg
Binder	**5**	4	7	$/kg
Separator	**0.2**	0.1	0.5	$/m^2
Current Collector	**20**	15	25	$/kg
ZnBr2	**3.0**	2	4	$/kg
NaBr	**1.5**	1	2	$/kg
TBABr	**5.0**	3	8	$/kg
Case	**5**	3	7	%
Manufacturing	**10**	5	12	%
Energy Density	**56.0**	65	50	Wh/L
Mass Normalization	2			

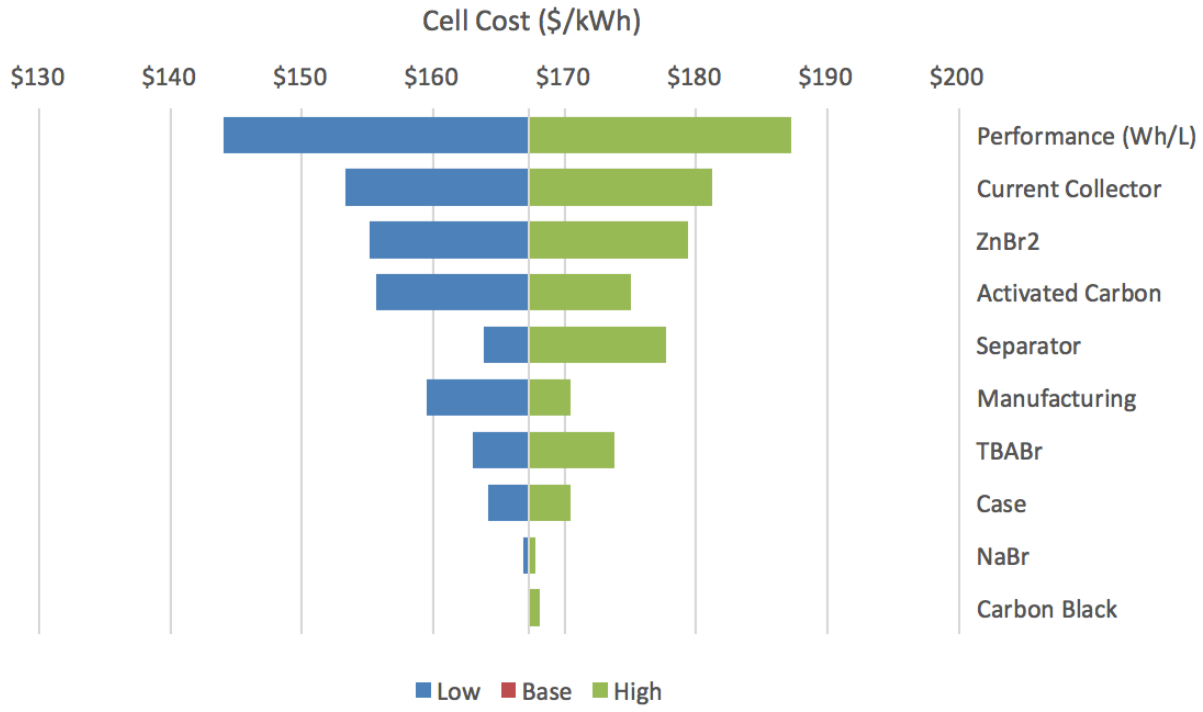
Cell Cost ($/kWh)
$130
$140
$150
$160
$170
$180
$190
$200
Performance (Wh/L)
Current Collector
ZnBr2
Activated Carbon
Separator
Manufacturing
TBABr
Case
NaBr
Carbon Black
Low
Base
High